

University College London

The Characterisation of Performance Limiting  
Defects in 4H-SiC Devices using Density  
Functional Theory

Thesis submitted for the degree of Engineering Doctorate (EngD) by

**Jonathon Philip Cottom**

Supervised by

Prof. Alexander Shluger

University College London

Department of Chemistry

May 2017

# Declaration

---

I, Jonathon Philip Cottom, confirm that the work presented in this thesis is my own. Where information has been derived from other sources, I confirm that this has been indicated in the thesis.

# Abstract

---

This thesis is focused on the atomistic modelling of defects both within silicon carbide (SiC) and at the interface between SiC and silicon dioxide (SiO<sub>2</sub>). These defects are discussed and compared to available experimental data to allow for the identification of performance limiting defects in the current and next generation of 4H-SiC metal oxide semiconductor (MOS) devices.

The results presented throughout this thesis are calculated in the 4H-SiC polytype, which is the most relevant polytype for electronic applications, and as such the devices of interest. These simple bulk models were developed and adapted to produce model 4H-SiC / SiO<sub>2</sub> interface systems. All the models used were tested and calibrated against the available experimental and theoretical data to ensure they were representative of the device regions of interest.

Through the application of density functional theory (DFT) and the models outlined above, defects, both intrinsic and extrinsic, were calculated, allowing for a comparison with electrically detected magnetic resonance (EDMR) measurements to be made. EDMR and to a lesser extent EPR provide a powerful tool for defect identification, providing a magnetic, symmetric and atomistic picture of a defect from a single technique. This allowed the dominant recombination defect in N-implanted pn-junctions to be identified as the neutral N<sub>C</sub>V<sub>Si</sub>, giving atomistic meaning to the unidentified signal from N-implanted devices. The effect of the anneal on forming this and other defects is described, allowing the accumulation and observation of the N<sub>C</sub>V<sub>Si</sub> to be understood. Without this mechanistic understanding, it was impossible to explain how the N<sub>C</sub>V<sub>Si</sub> is able to persist into the fully processed devices when thermodynamically more stable defects did not.

Before these calculations could be conducted, an interface model that was appropriate for the devices of interest was required. This was achieved through the comparison of electron energy loss spectroscopy (EELS) and DFT calculations, allowing an interface that is abrupt, but stepped, to be described. Using this model, the combination of EDMR and DFT calculations was then applied to the problem of defect identification at the SiC / SiO<sub>2</sub> interface. This approach allowed the P<sub>bc</sub> (and dual-P<sub>bc</sub>) to be identified as the dominant interface defect in the current generation of devices.

These results provide an atomistic meaning to the experimentally observed signals, allowing the defects linked to the suboptimal device performance to be identified. This makes it possible to envisage a design paradigm to be based upon the knowledge of the target defect, and the processes by which they form, guiding and enhancing the synthetic approach. Ultimately, this approach has the potential to allow SiC (and any other material it is applied to) to reach its full technological potential.



# Acknowledgements

---

I would like to take opportunity to offer my thanks and gratitude to those people whose help and friendship were valuable beyond measure during my studies. Firstly, I am hugely grateful for the support and encouragement provided by my supervisor Alexander Shluger, whose guidance throughout my studies was extremely valuable. I would also like to thank the rest of the Shluger group for vigorous scientific debate, allowing new ideas to be explored and developed. I'd like to thank Gernot Gruber, Gregor Pobegen and Thomas Aichinger for providing me with the opportunity to collaborate closely on interesting technological challenges. Giving the experimental imperative for my work allowing each part to become more than it would have been in isolation.

I'd like to thank the Centre for Doctoral Training in Molecular Modelling and Materials Science, the EPSRC, and Infineon, for funding this work. I also extend thanks to the Materials Chemistry Consortium and UCL Research Computing for providing the computational resources that made this work possible.

Finally, I'd like to thank Emilia and my family for their unwavering support, encouragement, and inspiration.

*To my little Oooooos...*

# Table of Contents

---

<b>Abstract</b>	<b>3</b>
<b>Acknowledgements</b>	<b>5</b>
<b>List of Publications</b>	<b>13</b>
<b>List of Abbreviations</b>	<b>14</b>
<b>List of Tables</b>	<b>15</b>
<b>List of Figures</b>	<b>17</b>
<b>Chapter 1</b>	<b>27</b>
1.1 Introduction	27
1.2 Structure	27
1.3 Physical Properties	29
1.4 Crystal Growth	31
1.5 Doping	34
1.6 The SiC / SiO <sub>2</sub> Interface	36
1.6.1 Oxidation	36
1.6.2 SiC / SiO <sub>2</sub> Interface States (D <sub>it</sub> )	38
1.6.3 Interface Morphology	40
1.6.3.1 Post Oxidation Anneal and Passivation	40
1.7 Defects in SiC	42
1.7.1 Bulk Defects	44
1.7.1.1 Antisites	45
1.7.1.2 Interstitials	45

## Table of Contents

---

1.7.1.3 Vacancies	46
1.7.2 Nitrogen Defects	49
1.7.2.1 Nitrogen Donor ( $N_C$ )	50
1.7.2.2 Donor Pair ( $N_x$ )	50
1.7.2.3 Nitrogen Vacancy Centre ( $N_C V_{Si}$ )	51
1.7.3 Interface Defects	51
1.7.3.1 C-Cluster Models	52
1.7.3.2 Silicon Vacancy ( $V_{Si}$ )	53
1.7.3.3 Carbon Dangling Bond ( $P_{bc}$ )	54
1.8 Summary	54
<b>Chapter 2</b>	<b>57</b>
2.1 Introduction	57
2.2 Theoretical Methodology	58
2.2.1 Density Functional Theory	58
2.2.1.1 Gaussian Plane Waves Method (GPW)	60
2.2.1.1.1 Localised Basis Sets	60
2.2.1.1.2 Plane Wave Basis Sets	61
2.2.1.1.3 Application to the Gaussian Plane Wave Method	63
2.2.1.1.4 Gaussian Augmented Plane Wave Method (GAPW)	64
2.2.1.2 Exchange-correlation functionals: LDA, and GGA	64
2.2.1.3 Self-Interaction Error and Hybrid Functionals	66
2.2.1.4 The Generalised Koopmans' Condition	68
2.2.2 Optimisation Approaches	70
2.2.2.1 Geometry Optimisations: Conjugate Gradients	70
2.2.2.2 Broyden–Fletcher–Goldfarb–Shanno Algorithm	71

2.2.2.3 The Relaxation of Lattice Parameters: Pulay Stress and the Equation of State Method	72
2.2.2.4 Transition States	73
2.2.3 Vibrational Frequency Analysis	74
2.2.4 Boundary Conditions and Modelling Defects in Solids	74
2.2.4.1 Supercells for Defect Calculations	75
2.3 <i>Experimental Methodology</i>	78
2.3.1 Electrically Detected Magnetic Resonance (EDMR)	78
2.3.2 Electron Paramagnetic Resonance – EPR	79
2.3.3 Hyperfine Interaction	80
2.3.4 Electron-Electron Interaction: Zero Field Splitting	82
2.3.5 Spin Dependent Recombination	82
2.3.6 Bipolar Amplification Effect (BAE)	84
2.3.7 Electron Energy Loss Spectroscopy / Energy Loss Near Edge Spectroscopy (EELS / ELNES)	84
<b>Chapter 3</b>	<b>85</b>
3.1 <i>Introduction</i>	86
3.2 <i>Experimental Methods</i>	87
3.2.1 Experimental Parameters	90
3.3 <i>Computational Details</i>	91
3.3.1 Defect Calculations	91
3.3.2 Probabilistic treatment of HF parameters	92
3.4 <i>Experimental Results: Performed by G. Gruber</i>	95
3.5 <i>Theoretical Results</i>	96

## Table of Contents

---

3.5.1 Nitrogen Interstitial ( $N_i$ )	97
3.5.2 Substitutional Nitrogen – $N_C$ and $N_{Si}$	99
Nitrogen Vacancy Complexes	101
3.5.3 $N_C C_{Si}$	104
3.5.4 Defect shortlist ( $N_C V_{Si}$ , $N_{Si} V_C$ and $N_C C_{Si}$ )	106
3.5.4.1 $N_C V_{Si}$	107
3.5.4.2 $N_{Si} V_C$	108
3.5.4.3 $N_C C_{Si}$	109
3.6 Comparison Between Theory and Experiment	110
3.7 Conclusion	113
<b>Chapter 4</b>	<b>115</b>
4.1 Introduction	116
4.2 Methodology	120
4.3 Results	123
4.3.1 Defect Formation Energies	123
4.3.2 Energy Barriers	126
4.3.3 Diffusion Behaviour	129
4.4 Conclusion	132
<b>Chapter 5</b>	<b>135</b>
5.1 Introduction	136
5.2 Experimental Details	138
5.3 Experimental Results: Performed by G. Gruber	140
5.3.1 EELS Interface Description	142
5.4 Theoretical Methodology	147

<i>5.5 Theoretical Results</i> _____	149
5.5.1 Simulation of the EELS Spectra _____	149
5.5.2 Interface Model _____	155
<i>5.6 Conclusion</i> _____	159
<b>Chapter 6</b> _____	<b>161</b>
<i>6.1 Introduction</i> _____	162
<i>6.2 Experimental Methods: Performed by G. Gruber</i> _____	164
6.2.1 Sample Preparation and Characterisation _____	164
6.2.2 Experimental Parameters _____	165
<i>6.3 Computational Details</i> _____	165
6.3.1 Defect Calculations _____	165
<i>6.4 Experimental Results: Performed by G. Gruber</i> _____	166
6.4.1 Angular Dependence _____	167
6.4.2 Hyperfine Structure _____	168
<i>6.5 Theoretical Results</i> _____	170
6.5.1 Initial Considerations _____	170
6.5.2 Interface Defects _____	171
6.5.2.1 Silicon Vacancy _____	172
6.5.2.2 Carbon Dangling Bond ( $P_{bc}$ ) _____	175
6.5.2.3 Dual Carbon Dangling Bond (Dual- $P_{bc}$ ) _____	178
<i>6.6 Comparison between Theory and Experiment</i> _____	181
<i>6.7 Conclusion</i> _____	189
<b>Chapter 7</b> _____	<b>191</b>
<i>7.1 Summary</i> _____	191

*Table of Contents*

---

<i>7.2 Future Work</i>	<i>192</i>
<b>Bibliography</b>	<b>194</b>
Appendix A	212
Appendix B	220
Appendix C	226



# List of Publications

---

The work described in this thesis is based upon the following papers:

**J. Cottom**, G. Gruber, G. Pobegen, M. Koch, P. Hadley, T. Aichinger, A.L. Shluger.

“Recombination centers in 4H-SiC investigated by electrically detected magnetic resonance and *ab initio* modelling” *Journal of Applied Physics*, 119-18, 2016

**J. Cottom**, G. Gruber, G. Pobegen, T. Aichinger, A. L. Shluger, "Identifying Performance Limiting Defects in Silicon Carbide pn-Junctions: A Theoretical Study", *Materials Science Forum*, Vol. 858, pp. 257-260, 2016

**J. Cottom**, G. Gruber, G. Pobegen, T. Aichinger, A. L. Shluger, “Defect Diffusion and Interaction During Annealing of N-implanted 4H Silicon Carbide Devices” *Submitted to Physical Review Applied*

G. Gruber, R. Meszaros, **J. Cottom**, G. Pobegen, M. Koch, P. Hadley, T. Aichinger, D. Peters. “Carbon dangling bonds at the Si-face 4H-SiC / SiO<sub>2</sub> interface”, *Submitted to Applied Physics Letters*

**J. Cottom**, G. Gruber, G. Pobegen, T. Aichinger, A. L. Shluger, “Recombination centers at the 4H-SiC / SiO<sub>2</sub> interface investigated by electrically detected magnetic resonance and *ab initio* modelling”, *Manuscript in preparation*.

**J. Cottom**, G. Gruber, G. Pobegen, T. Aichinger, A. L. Shluger, “The interface morphology of 4H-SiC / SiO<sub>2</sub> deposited oxides described by EELS and *ab initio* modelling”, *Manuscript in preparation*.

# List of Abbreviations

---

**AIM:** Atoms in Molecules

**CG:** Conjugate Gradient

**CTL:** Charge Transition Level

**DFT:** Density Functional Theory

**DLTS:** Deep Level Transient Spectroscopy

**DOS:** Density of States

**EDMR:** Electrically Detected Magnetic Resonance

**EELS:** Electron Energy Loss Spectroscopy

**EPR:** Electron Paramagnetic Resonance

**GGA:** Generalised Gradient Approximation

**KS:** Kohn-Sham

**LDA:** Local Density Approximation

**LPAW:** Linear Augmented Plane-Wave

**NCPP:** Norm-Conserving Pseudopotentials

**PAW:** Projector Augmented Wave

**PBE:** Generalised gradient approximation density functional developed by Perdew, Burke, and Ernzerhof

**PDOS:** Projected Density of States

**SD:** Steepest descent

**SIMS:** Secondary Ion Mass Spectrometry

**USPP:** Ultrasoft pseudopotentials

**VASP:** Vienna *Ab-Initio* Simulation Package

**VSEPR:** Valence Shell Electron Pair Repulsion

# List of Tables

---

- Table 1.1. Band gaps, lattice constants (a and c), stacking sequence, and space group of different SiC polytypes.[1], [6]\_\_\_\_\_ 29
- Table 1.2. Comparison of properties of 4H-SiC and some competitor materials. [1], [7] \_\_\_\_\_ 30
- Table 2.1. Isotropic abundance of elements of interest for SiC based devices. \_\_\_\_ 81
- Table 3.1. Calculated HF splitting constants  $a_k$  for the most reasonable candidate defects in their different paramagnetic charge states. The values were calculated using the pcj-1 basis-set, with the HSE06 functional.  $a_{C1}$  refers to the equivalent atoms 1NN C shell,  $a_{Si2}$  to the 2NN Si shell, and  $a_{C3}$  to the 3NN C shell. The values are averaged for all atoms in the same shell. \_\_\_\_\_ 110
- Table 4.1. Formation energies for the listed defects in the neutral charge state. Where appropriate, the effect of chemical potential is illustrated from C-Rich to Si-Rich. \_\_\_\_\_ 124
- Table 4.2. Table of activation barriers for the defect rearrangements, rotations, combinations and bulk diffusion. The 0 K energy barrier is compared to the 2000 K Gibbs free energy for each of the reaction pathways of interest. \_\_\_\_\_ 126
- Table 5.1. Electrical characterisation of the TEM samples as measured by G. Gruber. These measurements highlight the dramatic effect the POA has upon the performance of the device. \_\_\_\_\_ 139
- Table 5.2. Comparison between the various interface descriptors for the O<sub>2</sub> and NO annealed interfaces. \_\_\_\_\_ 146

## List of Tables

---

Table 5.3. Peak position extracted from the magnitude of the arrows in Figure 5.9.	151
Table 6.1. Electrical characterisation as conducted by G. Gruber, describing devices that are wildly different from an electronic perspective.	164
Table 6.2. Principal $g$ -factors from the tilt series in Figure 6.1.	168
Table 6.3. Average HF splitting's of the shortlisted defects for the defect centre and concentric shells moving radial outwards. In the $V_{Si}$ case there are 3 x $C_1$ , 12 x $Si_2$ and 18 x $C_3$ the $C_3$ contribution tends to average to 0. The $P_{bc}$ has 1 x $C_1$ , 3 x $Si_2$ , and 8 x $C_3$ . The $P_{bc}^2$ has 2 x $C_1$ , 6 x $Si_2$ and 16 x $C_3$ .	185

# List of Figures

---

- Figure 1.1. 2D illustration of the common SiC polytypes. The repeating units (A, B and C) are shown along the bottom. The stacking of hexagonal and cubic layers is shown on the y-axis. \_\_\_\_\_ 28
- Figure 1.2. Schematic view of the step-growth mechanism in SiC facilitated by the approximately  $4^\circ$  off-angle growth direction. This has the effect of eliminating polytypic inclusions, leaving only a single option for new molecules to be added. \_\_\_\_\_ 32
- Figure 1.3. The ubiquitous  $D_{it}$  plot showing, the density of interface traps ( $D_{it}$ ) as a function for energy above the valance band ( $E_V$  – right hand side). Then various conduction band minima ( $E_C$ ) are indicated as is the differences observed for  $n$ -type and  $p$ -type dopants. The figure is taken from [31], with permission. \_\_\_\_\_ 39
- Figure 2.1. Schematic overview of supercell method in relation to defect calculation. \_\_\_\_\_ 75
- Figure 2.2. Schematic view of Zeeman splitting. \_\_\_\_\_ 79
- Figure 3.1. Schematic view of the experimental SDR set-up, the sample is placed in the field and the current ( $I$ ) is measured as a function a function of field. \_\_\_\_\_ 88
- Figure 3.2. Experimental SDR result, the offset in the centre line between the parallel and perpendicular directions describes the degree of anisotropy between the principle axis. \_\_\_\_\_ 96
- Figure 3.3. Combined formation energy plot for the puckered (dashed red line) and split (solid blue line) interstitial. \_\_\_\_\_ 97

## List of Figures

---

- Figure 3.4. Representation of the split and puckered interstitial in the 0 and -1 charge states respectively. The blue is Si, brown is C and the white N. In each case on the left is a perspective view followed by the view along the x, y and z axis. \_\_\_\_\_ 98
- Figure 3.5. Spin density plot of the 0 charge state of the split interstitial, showing the majority of the spin centred upon the C atom. \_\_\_\_\_ 99
- Figure 3.6. Formation Energy plot for the  $N_C$  and  $N_{Si}$  defects. The solid line showing the  $N_C$  defect and the dashed line the  $N_{Si}$ . \_\_\_\_\_ 99
- Figure 3.7. Geometry of the lowest energy charge states of the  $N_C$  and  $N_{Si}$  defects, +1 and neutral respectively. The blue is Si, brown is C and the white N. In each case on the left is a perspective view followed by the view along the x, y and z axis. \_\_\_\_\_ 100
- Figure 3.8. Combined formation energy plot for the  $N_C V_{Si}$  and the  $N_{Si} V_C$ . The red line corresponds to the  $N_C V_{Si}$  and the blue line to  $N_{Si} V_C$ . \_\_\_\_\_ 101
- Figure 3.9. Configuration of the neutral  $N_C V_{Si}$  and the +2  $N_{Si} V_C$ . The blue is Si, brown is C and the white N. In each case on the left is a perspective view followed by the view along the x, y and z axis. \_\_\_\_\_ 102
- Figure 3.10. Spin density plot for the accessible paramagnetic states of the defect short list. From left to right; the  $N_{Si} V_C^{+2}$ , showing the spin density centred on the N, the  $N_C V_{Si}$  in the 0 and -1 charge state with the spin density distributed between 3  $sp^3$  hybridised C-dangling bonds, finally the  $N_C V_{Si}$  in the -2 charge state where there is only spin density on a single C-dangling bond. \_\_\_\_\_ 104

- Figure 3.11. Formation energy plot for the  $C_{Si}N_C$  defect, illustrating the formation energy and most favourable charge state for a given Fermi level position. \_\_\_\_\_ 105
- Figure 3.12. Configuration of the  $N_C C_{Si}$  in the neutral charge state. The blue is Si, brown is C and the white N. In each case on the left is a perspective view followed by the view along the x, y and z axis. \_\_\_\_\_ 105
- Figure 3.13. Combined formation energy plot showing the  $N_C C_{Si}$ ,  $N_C V_{Si}$  and the  $N_{Si} V_C$ . The lowest accessible charge states at a given Fermi level position are indicated by the bold lines (black). \_\_\_\_\_ 107
- Figure 3.14. Spin density plot for the neutral charge state of the  $N_C V_{Si}$ . \_\_\_\_\_ 108
- Figure 3.15. The spin density of the  $N_{Si} V_C$  in the +2 charge state. \_\_\_\_\_ 109
- Figure 3.16. Spin density of the  $N_C C_{Si}$  in the neutral charge state. \_\_\_\_\_ 109
- Figure 3.17. Simple comparison of the experimental and theoretical hyperfine parameters for the shortlisted defects. \_\_\_\_\_ 111
- Figure 3.18. Comparison between the  $N_C V_{Si}^0$  calculated spectra and the experimental spectra. In the hh configuration. \_\_\_\_\_ 112
- Figure 3.19. Improved spectra calculated using the larger pcj-3 basis set and implicit treatment of the 4 distinct defect configurations (hh, kk, hk, and kh).\_ 113
- Figure 4.1. Schematic view of implantation and anneal, giving an overview of the defects that can be envisaged as being created during implantation. The processing runs from left to right, starting from defect free stoichiometric 4H-SiC. After implantation, a large number of defects are formed including, but not limited to, the above. Finally, after annealing these defects combine, or rearrange to give the defects observed in the processed devices. C-Brown, Si-Blue, N-White. \_\_\_\_\_ 117

## List of Figures

---

Figure 4.2. Formation energies as a function of Fermi level position for the main defects of interest. \_\_\_\_\_ 125

Figure 4.3. a) The defect rearrangement mechanism, either C / N, is displaced along the Z-axis from a C-site to a Si-site or vice versa. b) Mechanism of interstitial vacancy combination, equally valid for interstitial migration in the absence of the adjacent vacancy. The barrier observed relates to passing through the plane of Si (middle picture), in the case of interstitial migration the barrier is substantially higher than in the defective case. C-Brown, Si-Blue. \_\_\_\_\_ 127

Figure 4.4. Barriers for interconversion highlighting the asymmetric nature of the transition. Relating to a) the  $N_{Si}V_C$  conversion to the  $N_CV_{Si}$  (reaction number 15 in Table 4.2), and b) the conversion of the  $V_{Si}$  to the  $V_C C_{Si}$  (reaction number 5 in Table 4.2). \_\_\_\_\_ 129

Figure 4.5. Diffusion behaviour of the key defect configurations as a function of temperature. The reactions have been grouped into those with similar diffusion coefficients as indicated. This shows the interstitial rotations (i) have the lowest diffusion coefficients, followed by the vacancy interstitial combinations (ii), and finally the defect rearrangements (iii). The bulk interstitial migration, reactions 1 and 3 from Table 4.2 have been omitted having diffusion coefficients orders of magnitude lower than the defects shown. \_\_\_\_\_ 130

Figure 5.1. BF image of the  $O_2$  annealed sample (a) and the NO annealed sample (b), both treatments appear to show a relatively abrupt interface, which is



- extensively stepped. These steps are then comprised of smaller steps down to single bilayer in size. \_\_\_\_\_ 140
- Figure 5.2. An illustration of how the bilayer steps were counted to give a descriptor of the balance between the macro / micro steps for each of the anneals used. \_\_\_\_\_ 141
- Figure 5.3. Comparison between the step bunching of an NO passivated interface (green) and an unpassivated interface (blue). The steps were counted by inspection from the contrast TEM images as illustrated in Figure 5.3. 141
- Figure 5.4. Contrast TEM image indicating the region from which the EELS spectra are taken, the spatial drift marked on the left indicates the effect of the beam and why correcting for this is important. All pixels at a given distance from the interface are averaged, this relates to the short length of the spectrum image box. \_\_\_\_\_ 143
- Figure 5.5. EELS profiles of the O<sub>2</sub> annealed device (a), and the NO annealed device (b). In each plot the transition from SiC to SiO<sub>2</sub> proceeds from right to left. The C and O signals are well resolved, whereas it is important to note the N is not, and as such is hard to draw definite conclusions from, aside from it only being detectable near the interface. The above scans were taken across the [0001] interface. \_\_\_\_\_ 144
- Figure 5.6. EELS profiles of the contrast, C, O, N, and Si profiles for the O<sub>2</sub> annealed (a) and the NO annealed (b). The Si shift is now included, all of the profiles have been rotated so the absolute transition length can be compared. With the exception of N, all of the profiles are clearly describing the same transition. \_\_\_\_\_ 145

Figure 5.7. Schematic view of the clusters used to approximate the abrupt interface motifs. From  $\text{SiO}_2$  through to  $\text{SiC}$ , with a stepped increase in C-concentration from left to right. \_\_\_\_\_ 148

Figure 5.8. (a) The experimental EELS data for the  $\text{SiC} / \text{SiO}_2$  interface showing the silicon L-edge, carbon and oxygen K-edges. The lines between the marked  $\text{SiC}$  and  $\text{SiO}_2$  lines represent 2 Å steps across the interface. (b) shows a zoomed in view of the Si- $L_{2,3}$  edge and the fine structure that will form the basis of the comparison between the theoretical and experimental data. \_\_\_\_\_ 150

Figure 5.9. Schematic representation of the clusters (above) that could be expected to be found at an abrupt  $\text{SiC} / \text{SiO}_2$  interface, the label below illustrates the interface motif that is being mimicked. The dashed lines are to give an impression of the shift between configurations and are not there to suggest any connection between them. The vertical line represents the energy difference between the core Si-2p states and the s/p\* states. 151

Figure 5.10. Experimental spectra with the calculated peak position overlaid for  $\text{SiC}$  and  $\text{SiO}_2$ , the green line represents the interface case, being equidistant between the two and exhibiting properties of both. The peak position indicated above relates the energy difference between the ground and excited states as indicated by the vertical line in Figure 5.9. \_\_\_\_\_ 152

Figure 5.11. A schematic view of the experimental EELS spectrum deconvoluted using the motifs shown in Figure 5.9. \_\_\_\_\_ 153

Figure 5.12. The schematic interface motifs translated from the small clusters described in Figure 5.7. Each of these are then combined to produce and

- interface model for defect calculations along the lines of the models described by Devynck *et al.*[234] \_\_\_\_\_ 155
- Figure 5.13. a) The fixed connection scheme that allows for the connection of oxides of varying thickness. These oxides are H-terminated along with the C-face of the SiC and the top-face of the oxide. b) a schematic view of the connection scheme where  $\text{Si}^3$  relates a triple bridged  $\text{O}_3\text{SiO}$ ,  $\text{Si}^2$  is the double bridged  $\text{O}_2\text{SiO}_2$ , and  $\text{Si}^1$  is the single  $\text{OSiO}_3$  as shown in figure 5.12 c) A schematic view of the band offset between SiC and  $\text{SiO}_2$  for a 16 Å oxide thickness. This diagram is produced from the projected density of states for each of the SiC bilayers, maintaining the same spacing into the oxide, giving an indication of the band opening from SiC to  $\text{SiO}_2$ . These points have then been connected by a smooth line. \_\_\_\_\_ 158
- Figure 6.1. a) [11-20] ( $0^\circ$ ) to [0001] ( $90^\circ$ ), b) [1-100] ( $0^\circ$ ) to [0001] ( $90^\circ$ ). Data courtesy of G. Gruber. \_\_\_\_\_ 167
- Figure 6.2. A comparison of the HF-interactions of the dominant defect observed with EDMR as a result of the various passivation treatments. a) Shows the EDMR spectra of the indicated devices with a microwave power of < 10 mW. b) Gives the same spectra with a microwave power of  $\approx 1$  W and has the effect of broadening out the features. \_\_\_\_\_ 169
- Figure 6.3. A schematic illustration of the  $g$ -tensor shift between the previously measured interface and oxidation defects. Illustrating the similarity in HF and the offset in  $g$ -value between the literature values. \_\_\_\_\_ 170
- Figure 6.4. Schematic view of the  $V_{\text{Si}}$  and the  $P_{\text{bC}}$  that are initially considered for comparison with the EDMR measurements. 1)  $V_{\text{Si}}$  on a terrace, 2)  $P_{\text{bC}}$  at

a terrace, 3)  $P_{bc}$  on a step edge, 4)  $V_{Si}$  in the layer beneath the interface.

The blue circles represent Si, the black represent C, and red O. \_\_\_\_\_ 172

Figure 6.5. a)  $V_{Si}$  in the neutral charge state at the SiC / SiO<sub>2</sub> interface, b) HOMO state of the  $V_{Si}$  showing the in phase and out of phase combination of the correlated C-dangling bonds, c) LUMO state of the same defect. \_\_\_\_ 173

Figure 6.6. Projected density of states plots for the  $V_{Si}$  defect in the a) neutral doublet, b) neutral quartet, c) -1-singlet, d) -1-triplet, e) -2-doublet, f) -3-singlet. The 0 on the x-axis indicates the position of the highest energy electron, those states above the 0 position are unoccupied while those below are occupied. The positive y-values relate to the  $\alpha$ -spin channel, while the negative y-values relate to the  $\beta$ -spin channel. The 4H-SiC band gap is indicated by the non-greyed out area, indicating the number and occupation of the localised gap states associated with the  $V_{Si}$ . \_\_\_\_\_ 174

Figure 6.7. Formation energy plot for the interface  $V_{Si}$ , showing the CTL for charge states of interest. \_\_\_\_\_ 175

Figure 6.8. DOS plots for the a) neutral doublet, and b) the negative singlet. The 0 on the x-axis indicates the position of the highest energy electron, those states above the 0 position are unoccupied while those below are occupied. The positive y-values relate to the  $\alpha$ -spin channel, while the negative y-values relate to the  $\beta$ -spin channel. The 4H-SiC band gap is indicated by the non-greyed out area, indicating the number and occupation of the localised gap states associated. The black line represents the C-PDOS and the red line the Si-PDOS. \_\_\_\_\_ 176

Figure 6.9. Formation energy plot for a single  $P_{bc}$  in configuration a from Figure 6.10a.  
 \_\_\_\_\_ 177

Figure 6.10. The dual- $P_{bc}$  can exist in two forms, that can be viewed as being a result of the stepped interface structure (a), or a result of partial oxidation (b). In each case O is red, Si blue, and C brown. \_\_\_\_\_ 179

Figure 6.11. PDOS plots for the a) 0-singlet, b) 0-triplet, c) -1-doublet, and d) -2-singlet. The 0 on the x-axis indicates the position of the highest energy electron, those states above the 0 position are unoccupied while those below are occupied. The positive y-values relate to the  $\alpha$ -spin channel, while the negative y-values relate to the  $\beta$ -spin channel. The 4H-SiC band gap is indicated by the non-greyed out area, indicating the number and occupation of the localised gap states associated. The black line represents the C-PDOS and the red line the Si-PDOS. \_\_\_\_\_ 180

Figure 6.12. Formation energy plot for the double dangling bond defect (dual- $P_{bc}$ ).  
 \_\_\_\_\_ 180

Figure 6.13. The effect  $P_{bc}$  local strain environment has on the calculated HF interaction. The above values sit in a tight range of  $a_c = \pm 4$  G and  $a_{Si} = \pm 2.5$  G. \_\_\_\_\_ 182

Figure 6.14. HF interaction for the interface  $V_{Si}$  in the neutral and negative charge states showing a similar  $a_{Si}$  regardless of charge state. In the case of the  $a_c$  a more pronounced shift is observed of approximately  $\pm 5$  G between the charge states. \_\_\_\_\_ 183

Figure 6.15. HF interactions for the two charge states of the dual- $P_{bc}$ , neutral triplet ( $P_{bc} 2-2$ ) and negative doublet ( $P_{bc} 2$ ). \_\_\_\_\_ 184

## List of Figures

---

Figure 6.16. A comparison of the EDMR spectra of candidate defects to the EDMR spectrum from the O<sub>2</sub> annealed sample detailed in Figure 6.2 and Table 6.1. \_\_\_\_\_ 187

Figure 6.17. A plot of the min-max C-HF interactions, along with the dual-P<sub>bc</sub> showing an excellent agreement with the observed experimental data. In addition, the secondary features within the C-HF match the magnitude and intensity of the max-min P<sub>bc</sub> values. \_\_\_\_\_ 189

# Chapter 1

## Introduction

---

### 1.1 Introduction

Silicon Carbide (SiC) is a wide band gap semiconductor that has long been viewed as offering the potential to revolutionise the market place for high-power, high-frequency and high-temperature electronic devices. The potential for this comes by virtue of the many favourable properties of SiC; wide bandgap, high thermal conductivity, high breakdown field, high saturated drift velocity, and a thermal and chemical robustness. [1]

SiC-based technologies, while having great potential, require development before this inherent potential can be realised. This is manifested in sub-optimal device characteristics, resulting in poor channel mobility and premature device breakdown. These issues are a result of the inherent defects present within SiC, and this is particularly true of the SiC / SiO<sub>2</sub> interface. When compared to the Si / SiO<sub>2</sub> system, the defect concentration observed at the interface is at least an order of magnitude higher. Understanding the structure and geometry of these defects is critical in developing a clear picture of the performance limitations of SiC devices.

### 1.2 Structure

Silicon carbide is built up of SiC<sub>4</sub> (CSi<sub>4</sub>) tetrahedra with Si and C being 4-coordinate species bonded via sp<sup>3</sup>(states of mixed s and p character) hybridised covalent bonds. There is a small negative polarisation towards C, owing to its higher electronegativity. This results in C being the anion-like species within SiC, and Si being cation-like, when an ionic view of the system is taken.

SiC exhibits polytypism, which is illustrated in Figure 1.1, along with some of the most common polytypes. Polytypism is strictly speaking the ability of SiC to crystallise into one of several crystal structures, by varying the arrangement of the two-dimensional cell along the c-axis. These SiC bilayers consist of the two-dimensional hexagonal unit cell, which varies in the third dimension giving rise to the observed polytypism through changing the layering ABA or ABC *et cetera* to build up the hcp structure as illustrated in Figure 1.1. This leads to the possibility that different polytypes belong to different lattice types and space groups, and at present over 250 polytypes have been identified. [1]–[4]

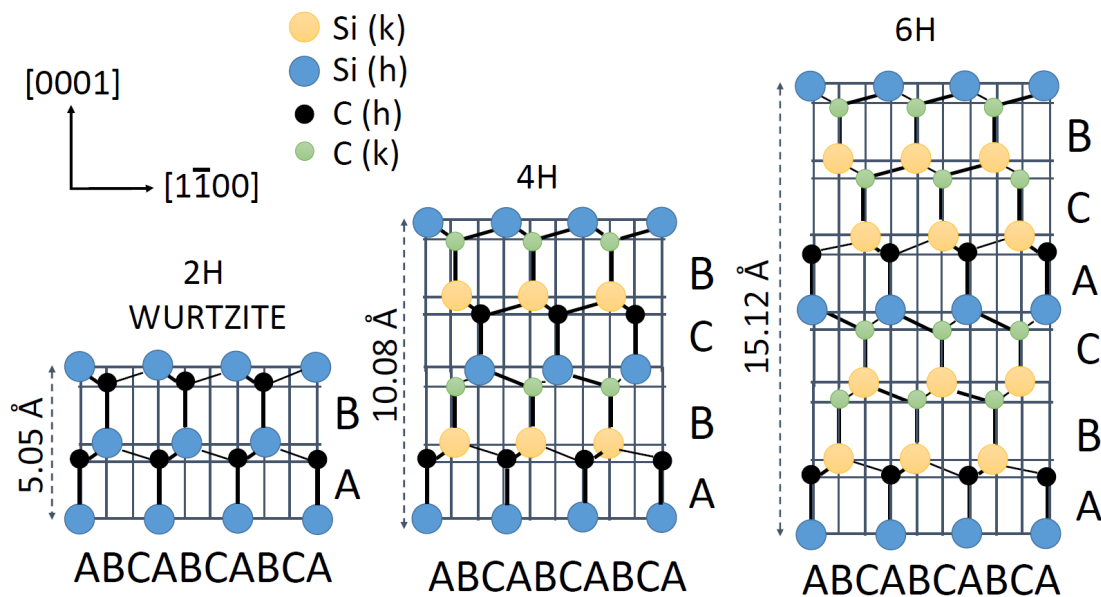


Figure 1.1. 2D illustration of the common SiC polytypes. The repeating units (A, B and C) are shown along the bottom. The stacking of hexagonal and cubic layers is shown on the y-axis.

Polytypism has a marked effect on the electronic and optical properties of SiC, illustrated below in Table 1.1. From a device perspective, 4H is the most relevant polytype, having both a wide bandgap, and with synthetic methods in place to grow



large single crystals.[1], [5] The bandgap widens as the hexagonal character increases, with 2H having the widest bandgap. 2H comprises entirely of hexagonal sites. The physical properties and chemical inertness are shared by all polytypes. The energy between the various polytypes is extremely small, leading to issues when regions of one polytype are incorporated into another. A full discussion of this is covered in Section 1.4.

Table 1.1. Band gaps, lattice constants (a and c), stacking sequence, and space group of different SiC polytypes.[1], [6]

	2H-SiC	4H-SiC	6H-SiC
Band Gap (eV)	3.33	3.26	3.02
Lattice Constant (a) / Å	3.078	3.078	3.078
Lattice Constant (c) / Å	5.048	10.053	15.110
Stacking Sequence	AB	ABCB	ABCACB
Space Group	$C_{6v}^4-P6_3mc$	$C_{6v}^4-P6_3mc$	$C_{6v}^4-P6_3mc$

### 1.3 Physical Properties

Silicon carbide has several properties, as outlined above, that makes it particularly suited for power electronic applications. In Table 1.2, a comparison of the properties of 4H-SiC contrasted against what can be viewed as competitor materials for post Si microelectronics is presented.

Table 1.2. Comparison of properties of 4H-SiC and some competitor materials. [1], [7]

Property	Si	GaAs	4H-SiC	GaN	Diamond
Bandgap (eV)	1.12	1.43	3.26	3.45	5.45
Breakdown Field ( $\times 10^5$ Vcm <sup>-1</sup> )	3	4	32	30	57
Thermal Conductivity (W cm <sup>-1</sup> K <sup>-1</sup> )	1.5	0.46	4.9	1.3	22
Electron Drift ( $\times 10^7$ cm s <sup>-1</sup> )	1.0	1.0	2.2	2.2	2.7
Electron Mobility (cm <sup>2</sup> V <sup>-1</sup> s <sup>-1</sup> )	1500	8500	700-1200	900-1250	2200
Melting Point (°C)	1420	1240	2830	2500	4000

From Table 1.2, the potential advantages of SiC when compared to the more traditional semiconductor materials such as Si and GaAs, for high power and high frequency applications are evident. The wide bandgap in SiC results in an intrinsic carrier concentration many times smaller than Si and GaAs, which allows for higher temperature operation. SiC devices have a typical operation window as high as 400 °C, but have been shown to be operational at temperatures up to 600 °C.[8], [9] The high breakdown field in SiC, an order of magnitude higher than in Si and GaAs, allowing a SiC layer of equivalent thickness to endure at a much higher voltage. In the case of SiC devices, blocking voltages well in excess of 10 kV are typical and substantially higher than in the equivalent Si-devices.[1] The high thermal conductivity of SiC allows for excellent heat shedding properties, and therefore SiC is often used as a substrate. Finally, the high saturated electron drift velocity allows for high frequency operation to be supported.[10]

The properties outlined above paint a compelling picture for 4H-SiC based devices. A closer inspection of Table 1.2 shows that diamond, and to a lesser extent GaN, offer superior properties in every respect. In both cases, there are currently

unresolved synthetic and growth challenges, limiting the application of these devices. It should, however, be noted that both of these areas are the subject of intense interest and study.[7] The processing of SiC has an often overlooked advantage. In having SiO<sub>2</sub> as its native oxide, in common with Si, a great many processing steps are the same or are easily adapted. This 'shortcut' has resulted in SiC based technologies being successfully commercialised in the form of Schottky diodes, metal oxide semiconductor field effect transistors (MOSFETs), and LEDs.

## 1.4 Crystal Growth

A good review of the various methods of crystal growth for SiC is provided by Presser *et al.*[1] There are a number of challenges to overcome before high quality single crystals of SiC can be grown, with the very properties outlined above, while desirable in a device, result in challenges for crystal growth. The lack of a cheap and simple growth method was one of the principle hindrances when it came to the development of SiC based technologies. In addition to the synthetic challenges, the growth rates for SiC crystals are orders of magnitudes slower than their Si counterpart.[1] The most reliable method to produce SiC wafers commercially was found to be seeded sublimation, where a seed crystal is placed at the top of a reaction vessel and the reagents are heated to  $\geq 2000$  °C driving them towards the seed where they crystallise. This is commonly known as physical vapour transport (PVT).[1], [11]–[13] The crystal is typically tilted by a few degrees from the [0001] direction to minimise polytypic inclusion that have the potential to render a wafer useless from a device perspective.[11] By including a growth angle, polytypic inclusion is minimised as there is only one favoured growth direction, and is shown in Figure 1.2. This gives rise to growth propagating along the steps, with more layers being added as this proceeds.

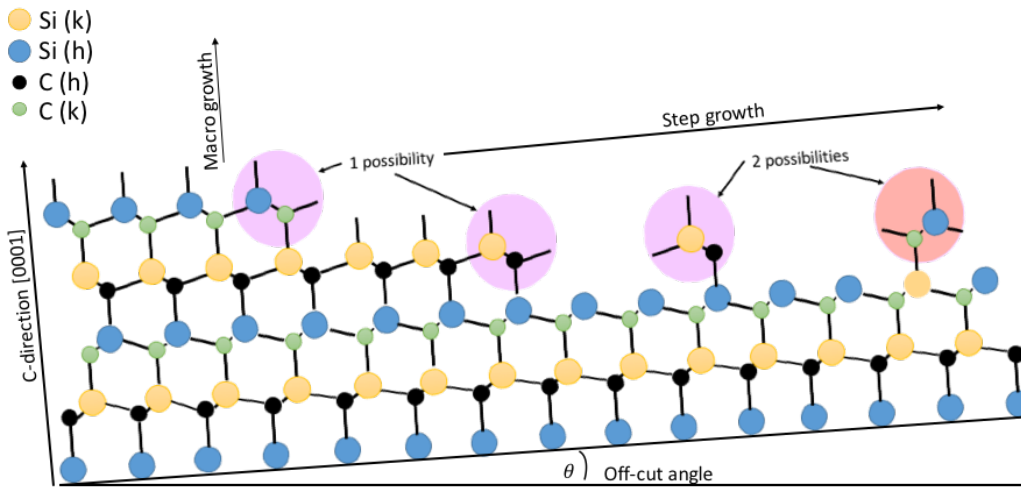


Figure 1.2. Schematic view of the step-growth mechanism in SiC facilitated by the approximately  $4^\circ$  off-angle growth direction. This has the effect of eliminating polytypic inclusions, leaving only a single option for new molecules to be added.

Even with state-of-the-art growth methods there are still challenges to overcome, with a high concentration of extended growth defects being present:

- i. **Void**s – Macroscopic defect, hexagonal voids parallel to the [0001] surface vary in size from nm to more than  $500\mu\text{m}$ . They result from poor crystal-seed/seed-holder interface, and migrate in the growth direction once a critical size has been achieved. These faults are greatly reduced by improving crystal-seed/seed holder interface.[1], [14]
- ii. **Polytypic Inclusions** – Formed due to the small stacking fault energy, different polytypes may occur during SiC growth. As more than one polytype can exist at a given temperature, absolute control of the growth environment becomes key when growing large single crystals. Wafer edges are particularly prone to these faults as the key parameters are hard to control.

These inclusions can act as nucleation sites for micropipes and screw-type dislocations.[1], [15]

- iii. **Low-angle Boundaries** – PVT grown SiC has the tendency to form a pronounced domain structure (mosaicity). It is often blamed on spiral growth and the interaction between two growth centres, although it is important to note that the origin is not well understood. [15]
- iv. **Graphitisation and Silicon droplets** – Graphitisation denotes the presence of excess carbon within the gas phase during SiC PVT growth, and can be caused by a higher vapour pressure of Si or a non-stoichiometric carbon source material/seed. The opposite is true for the formation of Si droplets.[1]
- v. **Micropipes** – Hollow tube shape defects, preferentially directed parallel to the c-axis with very little observed deviation from it. Where faceted growth occurs, micropipes are almost perfectly aligned with the c-axis (non-faceted growth micropipes are observed with a certain angle with respect to the c-axis.) In addition to these, small randomly orientated micropipes are observed. A shift in the orientation of the growth direction has been shown to eliminate micropipes at the cost of an increase in the number of stacking faults. The diameter of micropipes varies from a few nm to in excess of 5  $\mu\text{m}$ . The mechanism of micropipe formation is not well understood, although it has been proposed that sublimation processes may be responsible for surface micropipe formation, something that has yet to be confirmed. The presence of micropipes, both internally and more critically at the surface, has a negative impact on device operation and lifetime. A micropipe density of

below  $15 \text{ cm}^{-3}$  is required for the operation of most devices. Wafers with a micropipe density of below  $1 \text{ cm}^{-3}$  are standard, whereas wafers free of micropipes have been grown via the modified Lely method.[11], [16], [17]

- vi. **Stacking Faults** - Are primarily found on the basal plane along the [1120] direction in 4H-SiC. These are believed to be induced by local stresses, these stress related defects are often found near micropipes. The mechanism of fault formation is not related to the initial stages of single crystal growth, as only a few stacking faults are generated at the seed/crystal interface. Polytype and growth direction has a large effect; stacking fault concentration 6H-SiC [1120] is one hundred times higher than the [0001] face in terms of stacking faults. The [0001] grown crystals produce a much lower percentage stacking faults. Stacking faults can lead to the inclusion of different polytypes. Stacking faults also have the potential to create localised electronic states by inducing a quantum well like structure.[1]

These defects have largely been managed, and have only a limited impact on the performance of devices, with their respective concentrations being kept below the thresholds by modifications to the synthetic method. However, in so doing the cost and complexity of the synthetic process has been increased.

## 1.5 Doping

Doping allows the conductivity of a semiconductor to be tuned, and this is achieved *via* the introduction of impurity atoms. These impurity atoms introduce states in the semiconductor bandgap either close to the conduction band edge (*n*-doping), or close to the valance band edge (*p*-doping). Thus, increasing the concentration of electrons and holes respectively. There are a variety of techniques available to allow the

introduction of dopants. In many semiconductors, this is diffusion driven allowing *n*- and *p*-doped regions to be easily formed. In the case of SiC, this is not possible due to the very low diffusion coefficients for the dopant atoms leading to essentially immobile atoms.[1] For this reason, SiC relies on implantation to achieve doping. However, there are inherent issues with implantation, involving as it does high kinetic energies resulting in a large amount of lattice damage. This requires high temperature anneals (typically 1700+ °C) to repair the damage, while moving the dopant atoms from interstitial positions to the active sites.[18] This leaves the system in many cases far from thermodynamic equilibrium and leads to a number of unintended consequences. A mechanistic picture of which is presented in chapter 4. Typical dopant concentrations fall in the range  $10^{16} \text{ cm}^{-3}$  to  $10^{19} \text{ cm}^{-3}$ .[1]

The most common *p*-type dopant is aluminium as it offers a favourable combination of high solubility in SiC with a low ionisation energy. In general, any group III element could be used, with boron, aluminium and gallium widely discussed in the literature along with beryllium from group II. The *p*-type dopants substitute at the Si-site, in the case of aluminium denoted as Al<sub>Si</sub>. The hexagonal and cubic sites are non-equivalent, showing as they do different ionization energies 198 meV for the hexagonal (h) site and 201 meV for the cubic site.[19] Al-doping is typically achieved *via* implantation with dopant deactivation via defect complex formation being less of a problem than for the *n*-type dopants.[20], [21]

In the case of *n*-type doping, all group V elements can be used to *n*-dope SiC, nitrogen is the most common *n*-dopant used in device applications.[22], [23] Nitrogen is favoured offering as it does a low ionisation energy and low mass. *n*-dopants substitute at the C-site forming N<sub>C</sub> in the case of nitrogen. The same site inequivalence that is observed for the *p*-type dopants is seen, with the ionisation

energy of the h site being 61 meV, while the c site is 125 meV.[19], [24] As with Al-doping, N-doping is typically achieved *via* implantation. The carrier concentration saturates above a N-concentration of approximately  $5 \times 10^{19} \text{ cm}^{-3}$  due to dopant deactivation.[25], [26] There have been a variety of dopant deactivation mechanisms suggested in the literature, centring around either dimer or small cluster models, or vacancy dopant defect complexes. These complexes shift the desired shallow donor states out of target range either deep into the bandgap or the conduction band, rendering the dopant inert.[27] In addition, they may introduce deep states that can have a negative impact in terms of channel mobility, device reliability and breakdown. [28], [29] This is discussed and forms part of the motivation for chapters 3 and 4, and will be discussed in greater detail in those sections.

## 1.6 The SiC / SiO<sub>2</sub> Interface

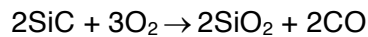
To turn SiC from a lump of semiconductor into a transistor, such as a MOSFET, a gate oxide is required. As highlighted above SiC has a stable native oxide, whereas for the other wide bandgap semiconductors (Table 1.2) it would require a deposited oxide to be added, complicating the synthetic process. The native oxide for SiC is SiO<sub>2</sub>, and can be grown by thermal oxidation, either wet or dry. The oxide layer produced has similar properties to those grown of Si. The main difference is the quality of the SiC / SiO<sub>2</sub> interface, showing many more orders of magnitude interface defects ( $D_{it}$ ) than observed in Si / SiO<sub>2</sub> system.[30], [31] This is generally accepted to be the reason for the low mobility in SiC MOSFET devices.[32]–[36]

### 1.6.1 Oxidation

Both Si and SiC have SiO<sub>2</sub> as the native oxide the clear difference with the SiC system is the presence of C. During the oxidation process the Si-C bond needs to be broken



and the liberated C removed from the oxide. This results in a higher thermal budget being required for the oxidation of SiC than for Si, and additional complications are introduced in the SiC case showing as it does a strong dependence of growth rate and crystal orientation. [1], [37] The fastest oxidation is seen on the C-face, the Si-face has the slowest and stoichiometric a-face has an intermediate rate, these are all far below the oxidation rates seen in Si / SiO<sub>2</sub>. [1], [37] The bulk oxidation process is understood as shown below:



The Si atoms are oxidised to give SiO<sub>2</sub>, the target oxide, at the same time CO is formed and diffuses out of the oxide, along with a minority population of CO<sub>2</sub>. Any CO / CO<sub>2</sub> molecules that are not completely removed from the oxide would be expected to remain in the oxide. [38] This has often been discussed in terms of carbon excess at the interface, either in the form of C-clusters, C-interstitials or partial oxidation products. This has been studied using a variety of approaches both theoretical and experimental with graphitic layers, sub-stoichiometric layers and C-dimers all being postulated. This C-excess has long been used to explain the various defect states that make up D<sub>it</sub>. [31], [39]–[46] Recent Electron Energy Loss Spectroscopy (EELS) and secondary ion mass spectrometry (SIMS) studies have called this assumption into question, showing no appreciable carbon excess at or in the vicinity of the interface. [47]–[50]

The ‘dry’ oxidation mechanism shown above produces an interface with an unacceptably high defect concentration for device applications. Most oxides for device applications are formed *via* chemical vapour deposition (CVD). In this process, a carrier gas made up of the target (SiO<sub>2</sub>) precursors is deposited on the substrate and go on to form the oxide. These precursors are activated either *via* plasma ignition or

heat. The main benefit of CVD is that the need to diffuse C away from the oxidation front is removed, and by extension a source of the excess carbon (either real or imagined).[1] However, it should be noted that the oxides formed by deposition alone are only weakly bonded to the SiC surface and result in a highly defective interface, hence making a limited thermal oxidation vital to improve the oxide adhesion and interface quality. This is typically achieved in a post deposition anneal under differing atmospheres (N<sub>2</sub>, NO).[36], [51], [52] Consequently, an interface that has been shown to offer enhanced channel mobility's when compared to those produced exclusively by thermal oxidation is obtained.[53]

### **1.6.2 SiC / SiO<sub>2</sub> Interface States (D<sub>it</sub>)**

The seminal work that described and characterised the interface defects in SiC was presented in 1997 by Afanas'ev *et al.*[31] The ubiquitous plot from this work is reproduced in Figure 1.3 and shows the experimental techniques that describe the various defect states that make up the D<sub>it</sub>.

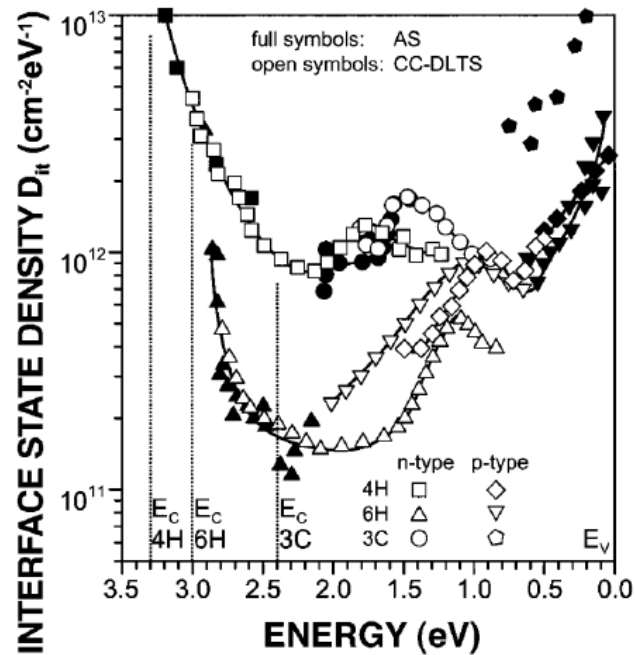


Figure 1.3. The ubiquitous  $D_{it}$  plot showing, the density of interface traps ( $D_{it}$ ) as a function for energy above the valance band ( $E_v$  – right hand side). Then various conduction band minima ( $E_c$ ) are indicated as is the differences observed for  $n$ -type and  $p$ -type dopants. The figure is taken from [31], with permission.

From Figure 1.3, it is clear that the  $D_{it}$  can be split into three regions, those close to the band edges and those deep states around the mid-gap region. States near the conduction band minimum (CBM) and valence band maximum (VBM) band edges have a dramatic effect on the  $n$ -channel and  $p$ -channel devices respectively, limiting as they do electron and hole transport.[53], [54] The deep states are envisaged to act as recombination centres, which reduce carrier lifetime and as a result limit the mobility. The states of interest from a device perspective are those close to the conduction band and the deep states, being as the typical commercial SiC-MOSFET is an  $n$ -channel device.[36], [53], [55], [56]

For the shallow states next to the conduction band, Afanas'ev *et al.* applied image force calculations to obtain an estimate as to the physical location of these

defects with respect to the channel. These calculations described traps close to the interface on the oxide side, out to approximately 2 nm, as such these defects are commonly known as near interface traps (NITs).[31], [57] While these calculations are by their very nature a simplification, these results have been reproduced and are widely accepted as the location of the NITs. The morphology of the interface complicates the picture and a full discussion of this is presented in chapter 5. An atomistic picture for the NIT has so far proved elusive, in spite of SiO<sub>2</sub> being one of the most heavily studied materials for the last 20 years.[45], [58]–[61]

### **1.6.3 Interface Morphology**

#### **1.6.3.1 Post Oxidation Anneal and Passivation**

The high defect concentration highlighted in the previous section highlights the need for an efficient passivation scheme. This was required before SiC could become useful from a device perspective. In the case of the Si / SiO<sub>2</sub> system, the dominant interface defect is the silicon dangling bond (P<sub>b</sub> centre), this defect can be efficiently passivated by hydrogen. Recent studies have shown that the concentration of H is critical as a H-mediated depassivation mechanism has recently been described.[62] In the case of SiC, the picture is more complicated with a H-passivation appearing to affect some defects while leaving other unchanged.[31] Through the development process, NO was identified as an effective passivation agent offering a significant reduction in D<sub>it</sub> across the whole bandgap.[33], [36], [63], [64] The mechanism of N passivation is currently unknown, although it has been suggested that N might remove excess interface C, based upon the early assumption that there is an excess of C in the vicinity of the interface.[57], [64] Additionally, it has been observed that NO passivation could lead to the introduction of N within the interface region, acting as a

shallow donor in effect *n*-doping the interface.[65], [66] Resulting in the same shallow donor states described above. The final missing piece from the passivation perspective is the N-interaction with the interface defects, the effect on the  $D_{it}$  is clear while the defects passivated and the atomistic picture of the passivated defects is far from understood. As with the oxidation, there is also a crystal orientation dependence observed for the passivation, with a higher mobility being observed for the a-face than the Si-face post passivation. This has been taken as an indication that the a-face has a higher concentration of reactive sites for N-incorporation.[49], [65]

Electron Energy Loss Spectroscopy (EELS), Tunnelling electron microscopy (TEM), secondary ion mass spectrometry (SIMS), X-ray photoelectron spectroscopy (XPS) and energy-dispersive x-ray spectroscopy (EDS) have all shown a N intensity centred on the interface tailing off rapidly into the oxide.[49], [67]–[72] Recent work has expanded upon this picture showing that the N is strongly bound to the SiC side of the interface (without penetrating into SiC), persisting even after the oxide has been etched away.[49], [69], [70] This shows the N to be distributed in a layer of around 1 nm in concentrations approximately equivalent to an atomic layer.[69] Various TEM and EELS studies have suggested N-passivation in effect reduces the interface ‘thickness’ *via* a limited reconstruction of the interface.[42], [48] It should, however, be noted that other studies have reported no effect, or in fact the opposite trend, adding to the confusion. The most recent studies that represent the current state of the art, show no evidence of any surface reconstruction, or any alteration in the surface morphology as a result of NO passivation. [49], [50], [73]

Rozen *et al.*[37] showed that N concentration saturates after a few hours with no additional concentration increase observed after 3 hours.[74] In addition, very high N concentrations have been shown to increase the number of ‘fast’ interface

states.[74], [75] This is suggestive of several competing pathways for nitradation, some of the minority pathways giving rise to states that are sub-optimal from a device perspective. Additionally, it has been shown that by varying the passivation time for the NO anneal to optimise one parameter negatively impacts another. This has led to the suggestion that a multistep approach, utilising NO followed by some other treatments, has the potential to offer further improvements in device performance. This has been demonstrated through the combination of NO and H anneals, and results in an improvement in the mobility, unfortunately this process led to unforeseen reliability issues.[76] Other novel annealing processes have been suggested using  $\text{POCl}_3$ , which have shown promise at the expense of introducing reliability issues. Developing an atomistic picture of the passivation mechanisms and the defects passivated is of critical importance in identifying a more efficient passivation regime. This remains an ongoing challenge.[34], [77], [78]

## **1.7 Defects in SiC**

As the previous sections have highlighted, defects play an important role in the challenges currently facing SiC-based devices. These defects effect both the device performance in terms of the discussed poor mobility and the reliability leading to premature breakdown. A variety of experimental techniques have been used to describe the defects within the bulk, surface and interface regimes in SiC-based samples (not necessarily devices). These techniques include, but are not limited to, deep level transient spectroscopy (DLTS),[31] vibrational spectroscopy,[79] Raman spectroscopy (including surface Raman),[79] photoluminescence (PL),[80] positron annihilation spectroscopy,[80] and EPR (including related techniques).[80]–[82] A challenge with the experimental results has always been relating the signals observed

with one technique to those observed in another. This has led to a great deal of debate and disagreement, which in places is still ongoing.

In tandem with the experimental measurements, *ab initio* calculations have been extensively deployed to describe the various point defects within the SiC bulk at varying levels of theory. Initially, these techniques were used to characterise simple point defects within SiC, comparing formation energies and accessible charge states with little attempt to correlate these with experimental techniques.[83]–[85] Through a process of refinement on both the theoretical and the computational resource side, comparison between theory and experiment has become possible. Providing a potent tool with which to shed light on the atomistic structure of performance / reliability limiting defects.[57], [86]–[88]

Among the most powerful experimental techniques for the study of defects in the solid state are those based around EPR. These techniques allow multiple data points to be obtained, describing the defect symmetry, chemical environment, and orbital occupied. Many defects have been studied using these techniques, identifying defects within the bulk, interface and surface regimes.[89]–[92] While the atomistic picture of these defects is not always clear or agreed upon, the utilisation of *ab initio* simulations has greatly improved the situation.[28], [86], [93], [94] It should at this stage be made clear that while EPR and related techniques offer some clear advantages, they are only applicable for the study of paramagnetic defects. The result of this is that only a partial picture of the defects within a sample can be obtained, as the number and concentration of diamagnetic defects cannot be probed. In the case of wide band gap materials such as SiC, defects tend to have multiple accessible charge states.[28], [95] The stability of these states is governed by the Fermi level position, hence once this coincides with a paramagnetic state of a given defect it will

be visible to EPR. This is described by the relative formation energies of the various charge states as a function of Fermi level position as covered in chapter 2.

There are several comprehensive reviews that cover defects in SiC from varying perspectives along with EPR parameter tables from assigned and unassigned defects. In addition, thanks to the similarities between SiC and diamond, there is a growing interest in the potential of utilising both intrinsic and extrinsic defect for qubit applications.[96] This has motivated a renewed interest in the NV-centre like defects that have shown promise in this area.[97]–[100] This section presents the current understanding of the defect systems in the bulk, as a result of N-implantation, and at the interface, drawing together the available experimental and theoretical works in each case.

### 1.7.1 Bulk Defects

The defects discussed here will be limited to intrinsic bulk defects and limited defect complexes. These defects can be categorised as something missing (a vacancy), something added (an interstitial), or something in the wrong position (an antisite). In addition, rearrangements and aggregations of these point defects into more complex structures are frequently described in the literature.[101] These are included here as they are typically considered together with the simple atomic defects. Some of these defects are electrically active and envisaged to play an important role in limiting device performance. Torpo *et al.*[83] described what has become the standard approach for calculating defect formation energies in SiC using the Northrop and Zhang formalism.[102] In this approach, the chemical potential for the C-rich limit is taken from diamond, with Si-rich being taken from crystalline Si, linked by the  $\mu_{\text{SiC}} = \mu_{\text{C}} + \mu_{\text{Si}}$ .



By convention all defects are compared at  $\Delta\mu = 0$  (stoichiometric) case, assuming to have been formed from the defect free bulk.[83]

#### 1.7.1.1 Antisites

The antisite defects represent either a carbon at a silicon site ( $C_{Si}$ ) or a silicon at a carbon site ( $Si_C$ ). In addition, these sites can either be of cubic or hexagonal symmetry. [83], [101], [103], [104] With both Si and C being 4-valent, each is able to occupy the other one's site, maintaining the  $\approx T_d$  symmetry in the neutral charge state. The  $C_{Si}$  defect has a formation energy of  $\approx 3.5$  eV, with the hexagonal site being slightly higher in energy  $\approx +0.1$  eV.[83], [101] The same trend is observed for the  $Si_C$  although the formation energies are approximately 0.5 eV higher at around 4 eV.[83] The C-C bond lengths are approximately 10% shorter than the Si-C bond length leading to an inward relaxation of the neighbouring C-atoms. In the  $Si_C$  case the opposite is true, the Si-Si bond length being  $\approx 15\%$  longer leading to an outward relaxation. In the case of the higher charge states of the  $Si_C$ , the  $T_d$  symmetry is broken and a Jahn-Teller distortion with  $\approx C_{3v}$  symmetry is found.[83], [87] The  $C_{Si}$  has been shown to only be stable in the neutral charge state, with the (+/0) and (0/-) charge transition levels (CTL) being degenerate with the VBM and CBM respectively. The  $Si_C$  has both the +1 and the 0 accessible with a (+/0) CTL at approximately 0.25 eV leaving the neutral charge state favoured for the rest of the SiC band gap.[87], [90], [103], [105]

#### 1.7.1.2 Interstitials

The interstitial defects can take one of two configurations either as a split interstitial sharing the lattice site or for certain charge states it is favourable to break the split

interstitial and form puckered configuration with the interstitial atom moving away from the shared lattice site.[85], [106] The formation energies reported fall into the range of 7.0-9.0 eV in the neutral charge state with the silicon interstitial ( $\text{Si}_i$ ) sitting approximately 1 eV higher than the carbon equivalent. The  $T_d$  symmetry of C / Si site is reduced to  $C_{2v}$  symmetry that have two degenerate configurations. The (+/0) CTL is approximately +0.5 eV above the VBM, the (0/-) CTL is at approximately 2.2 eV above the VBM. Both the +1 and the 0 charge state have the split interstitial as the lowest energy configuration while for the -1 and higher negative charge state the puckered configuration is favoured.[85], [107] The  $\text{Si}_C$  was incorrectly assigned to the E16 EPR peak before *ab initio* studies allowed the error to be identified and corrected.[104]

### 1.7.1.3 Vacancies

The carbon vacancy ( $V_C$ ) has a formation energy in the range of 4.0-4.5 eV, which is one of the lowest formation energies leading to a high defect concentration. The defect geometry has a strong site dependence resulting in a different structure for the k-site and h-site defect. The four 3-coordinate nearest neighbour Si atoms show an inward relaxation to form a long-range interaction at 2.7 Å (comparable with 2.3 Å).[83], [96] The k-site shows a Jahn-Teller distortion that breaks the symmetry of the  $sp^3$  orbital, resulting in a lowering of the point symmetry to  $C_{1h}$ , the h-site retains the  $C_{3v}$  symmetry of defect. There are a number for charge states that are accessible in the 4H-SiC band gap, the associated CTL are (++): 1.64 eV (h), 1.67 eV (k), (+/0): 1.84 eV (h), 1.75 eV (k), (0/-): 2.71 eV (h) 2.80 eV (k), (-/-): 2.79 eV (h), 2.74 eV (k).[83], [108] The  $V_C^+$  and the  $V_C^-$  have both been observed using EPR with electron

irradiated 4H-SiC samples.[95], [109], [110] These peaks were labelled EI5 and EI6, with EI5 being assigned to the  $V_C^+$ , the EI6 was incorrectly believed to be the  $Si_C$ . [111], [112] The assignment of the EI5 was confirmed and the mistaken assignment was corrected through *ab initio* calculations allowing the  $V_C^-$  to be assigned to the EI6 peak.[95] The  $V_C$  has also been assigned as being responsible for the  $Z_{1/2}$  peak on the basis of comparative EPR and DLTS studies.[113] This assignment has been supported by limited *ab initio* calculations comparing the Kohn-Sham levels and the CTL with DLTS spectra.[113] Agreement in the case of the  $Z_{1/2}$  centre is not without problems, being as the  $V_C$  related deep level should be visible to EDMR and has yet to be observed.

The silicon vacancy ( $V_{Si}$ ) has a significant formation energy of approximately 8-8.5 eV, which is significantly higher than the  $V_C$ . [83], [96], [106] Regardless of these energetic hurdles the  $V_{Si}$  has been widely studied both theoretically and experimentally. In the neutral charge state, the 3-coordinate carbon atoms exhibit an outward relaxation as unlike the  $V_C$  the C-atoms are unable to form a significant interaction at this range. This leaves the four weakly correlated dangling bonds pointing towards the vacancy, resulting in the favouring of the high spin states resulting in  $T_d$  symmetry ( $V_{Si}^-$  and  $V_{Si}^0$ ) and  $C_{3v}$  ( $V_{Si}^{-2}$ ). [83], [90] In the case of SiC, C represents the anionic species. The  $V_{Si}$  favours the negative charge states with CTL at (0/-) 1.24 eV (k), 1.30 eV (h), (-/-) 2.47 eV (k) 2.58 eV (h), (--/--) 2.74 eV (k) 2.85 eV (h). [83], [106], [114], [115]  $V_{Si}^-$  has been observed and characterised using EPR, no zero-field splitting is observed although the closely related  $T_{V_{2a}}$  centre exhibits a pronounced zero-field splitting. The  $T_{V_{2a}}$  centre has been assigned to the  $V_{Si}^-$ , in a lower symmetry environment, after initially being thought to belong to the neutral

charge state.[82], [90], [116], [117] This assignment is far from established with serious doubts being raised, requiring further study before the question is settled. [118], [119] The high spin ground states of  $V_{Si}$  have promoted interest from the quantum computing community from the potential qubit perspective.[99], [118], [119]

Theoretical studies have shown that the  $V_{Si}$  is only stable in  $n$ -type, and is metastable in undoped and  $p$ -type SiC, where it has been shown to reconstruct to  $C_{Si}V_C$  with a barrier of 1.6 eV.[114] The  $T_d$  symmetry of the  $V_{Si}$  is broken resulting in a doubly degenerate defect of  $C_{1h}$  symmetry. This is caused by the inability of C to occupy the Si-site causing it to relax back into the plane of the nearest neighbour (NN) C-atoms. There are additionally four inequivalent configurations based upon the  $kk$ ,  $hh$ ,  $hk$ , and  $kh$  variants, and the mixed symmetry sites are triply degenerate.[85], [101] The CTL picture is similar to the  $V_C$ , ( $++/+$ ) 1.24 eV, ( $+/0$ ) 1.79 eV, ( $0/-$ ) 2.19 eV. Both the  $C_{Si}V_C^+$  and the  $C_{Si}V_C^-$  have been observed with EPR and have been suggested as candidates for the E14 centre, although this assignment is no longer favoured. [87], [120] The E14 centre is thought to be related to the  $V_CV_C C_{Si}$ . It is important to note that these observations were made in samples prepared using 2 MeV electron irradiation followed by a high temperature anneal to enhance the defect concentration.[111], [121]

The divacancy ( $V_CV_{Si}$ ) is the final intrinsic defect to consider, it is made up of a  $V_{Si}$  and a  $V_C$  at neighbouring sites. As with the  $C_{Si}V_C$  there are four defect arrangements relating to the  $hh$ ,  $kk$ ,  $hk$  and  $kh$ . The mixed symmetry defects are triply degenerate as before.[84] The unrelaxed defect exhibits  $C_{3v}$  symmetry, relaxation breaks symmetry and results in a  $C_{1h}$  symmetry. These defects have high formation energies, in the range of 7.75 – 8.5 eV, coupled to unusually high binding energies of

3.8 – 4.4 eV.[101], [122]–[124] As the divacancy is not favoured from a thermodynamic perspective, once formed, either by defect migration or directly as the result of implantation, they are stable to dissociation. The  $V_C V_{Si}$  shows a strong site dependence for the CTL positions, all of the defects have the +1, -1 and -2 charge states accessible with the hh and kk defects having the neutral charge states in addition. The (+/0) sits at approximately 0.5 eV, (0/-) at 0.9 eV and the (-/-) at 1.8 eV for the hh / kk configurations. In the case of the hk / kh configurations, a negative-U effect is observed with CTL at (+/-) 0.6 eV, (-/-) 1.9 eV. [122]–[124] The neutral triplet (S=1) configuration has been observed with EPR showing a strong zero field splitting in all configurations.[97], [123], [125] This has led to interest from the quantum computing community along with the  $V_{Si}$ .[97], [125] Additionally, the divacancy has been suggested as an implantation defect and can act as a vector for dopant deactivation.[126]

### 1.7.2 Nitrogen Defects

As discussed in section 1.6.3.1, N is the most common *n*-type dopant for 4H-SiC, having the lowest ionisation energy. As highlighted, doping is typically achieved by implantation, which is a destructive process that leads to a high degree of lattice damage. The subsequent post-implantation anneals are intended to move the dopant to the C-site while repairing the lattice damage. As is to be expected, the desired dopant activation pathway is one of many possible pathways, and these competing pathways lead to dopant deactivation.[25]–[27] Many theoretical studies have examined these potential mechanisms of dopant deactivation, starting from the early tight binding models through to the result presented in chapter 4. These studies have described a range of mechanisms that can be broadly divided into vacancy and interstitial migration mechanisms. As is common in other semiconductors, the barriers

for the vacancy migration are higher than those for interstitial migration.[93], [126]–[129] These defects have been observed experimentally using EPR. Assigning these signals to a given defect has proven challenging as a high degree of disorder is inherent in post implantation.[130]

#### 1.7.2.1 Nitrogen Donor ( $N_C$ )

The  $N_C$  centre is the objective of implantation forming the shallow donor state, sitting at the C-lattice site. The N-dopant assumes the  $T_d$  symmetry of the host site in the positive charge state, assuming  $C_{3v}$  symmetry in the neutral charge state. The formation energy is approximately 0.5 eV in the neutral charge state. This defect has the distinction of being one of the first characterised with EPR, by Woodbury and Ludwig in 1961.[131] The strong site dependence observed in the experiment is supported by theoretical modelling of the  $N_C(k)$  showing a 1:1:1 triplet with a N-hyperfine of 18 G, the  $N_C(h)$  site shows a vastly reduced N-hyperfine < 1G.[132], [133]

#### 1.7.2.2 Donor Pair ( $N_X$ )

When the EPR spectra of N-implanted samples are measured, a related defect of low intensity appears with the identified  $N_C$  centre discussed above. This defect is only observed in heavily implanted samples and from the EPR appears strongly correlated to the  $N_C$  centre. The  $N_X$  centre is understood to be two correlated  $N_C$  centres on inequivalent sites.[93], [133], [134] More recent studies have identified a small zero-field splitting confirming the theoretical prediction of a triplet ( $S=1$ ) ground state.[135] This gives rise to a triplet defect that appears singlet-like on first inspection. There is still a degree of debate as to the atomistic picture of the  $N_X$  centre, with a high degree

of anisotropy observed experimentally that has yet to be explained by any of the proposed models.[130]

### 1.7.2.3 Nitrogen Vacancy Centre ( $N_C V_{Si}$ )

The  $N_C V_{Si}$  forms a family of defects that are of interest from a dopant deactivation and implantation damage perspective.[93], [96], [100] The  $N_C V_{Si}^0$  will be discussed in detail in chapter 3, having been identified in N-implanted *pn*-junctions.[28] The formation energy in the neutral charge state is approximately 1 eV, with a binding energy of 3.5 eV. In general, the  $N_C V_{Si}$  centre has  $C_{3v}$  or  $C_{1h}$  symmetry and show the same site dependence as described above. The CTL are (0/-) 1.4 eV, (-/--) 2.6 eV, (-/--) 3.0 eV.[28], [96], [136] As is common for the  $V_{Si}$  based defects, the weak correlation between C-dangling bonds leads to a proclivity for high spin ground states. This defect, along with the related  $(N_C)_x V_{Si}$  ( $x=2-4$ ), has been suggested as one of the main culprits that lead to dopant deactivation.[126], [127]

Bardeleben *et al.*[100] used proton irradiated N-doped samples and optical pumping to study the  $N_C V_{Si}^-$ , this was then compared to theoretical calculations. Allowing the centre to be identified on the basis of the pronounced zero-field splitting of 900 G, along with the N-hyperfine.

### 1.7.3 Interface Defects

The intrinsic and dopant defects described above have been extensively studied from both an experimental and theoretical perspective. This allows a good understanding of where the assignments highlighted above agree and where they break down. This has led to vigorous debate around the competing models for the various experimental centres. The same is not true in the interface system where there is a far greater range in the experimental observations. This is in part due to the fact that at the

interface, a larger number of structural motifs are possible than in the bulk or doped-bulk case. Leading to a situation where all surfaces are not all created equal, adding to the experimental challenge of defect identification and hindering comparison with the theoretical results. However, in spite of these challenges, two main schools of thought have been developed for the nature of these interface defects. The first, and oldest, was centred around the expectation that there would be a carbon excess at the interface. This led to the development of a number of C-cluster models that developed in C-dimer models that have been discussed in section 1.7.3.1 and have been used at various times to explain the observed  $D_{it}$ . The competing school of thought holds that the dominant interface defect is based upon various flavours of the Si-vacancy, and in the latest generation of devices appears to be supported by SIMS, TEM, and XPS data that shows no C-excess at the interface. Additionally, the EPR and EDMR spectra recorded show a strong anisotropy that challenges the assumption of a C-interlayer like structure that the early C-cluster models were built upon. It should be noted however that interface preparation techniques have been evolving at the same time as the experimental and theoretical accuracy have been refined. This opens up the possibility that one model is suitable for a specific interface, whereas the other best describes another.

### 1.7.3.1 C-Cluster Models

The early TEM and SIMS studies along with kinetic studies suggested that there was a C-accumulation at the interface.[1], [31], [39], [115], [137] This motivated the first wave of theoretical studies that described C-clusters of various sizes in a SiC / Monolayer SiO<sub>2</sub> system.[45], [138]–[140] The first discovery of these studies was that only the smallest clusters represented stable minima, seeming to discount the



possibility of a C-rich ‘graphitic’ interlayer.[44], [45], [138] As a result, the models were refined to a variety of C-dimers, either  $sp^2$  or  $sp^3$  hybridised. These studies showed that the various configuration produced gap states that correlated with the  $D_{it}$  peaks observed experimentally.[138]

### 1.7.3.2 Silicon Vacancy ( $V_{Si}$ )

The  $V_{Si}$  has been proposed as an important interface defect[141], [142], following on from its identification as one of the dominant bulk SiC defects.[82] This effort has been spearheaded by extensive work from the Lenahan group, having used EDMR to measure similar spectra in a variety of SiC MOSFETs.[91], [141]–[143] All of these defects show similarities with the bulk  $V_{Si}$  centre, however, it should be highlighted that the assignment is not without issue. The signals for both the ‘fast-passage’ measurements and conventional EDMR have been assumed to show the same defects, whereas an alternative interpretation based upon the shift in g-tensor and HF splitting is that in fact two defects are being probed as a function of measurement timescale.[144]–[147] Additionally, the high isotropy reported seems to be at odds with the assignment of the interface defect which has been shown to have significant anisotropy. Theoretical studies question the stability of the  $V_{Si}$  in the  $p$ -type devices, as it is unstable to rearrangement at the annealing temperatures.[114] What can be stated with confidence is that the  $V_{Si}$  defect plays a role close to the interface as identified by the ‘fast-passage’ measurements.[145] What is far from clear is whether or not it is one of the dominant defect types.

### 1.7.3.3 Carbon Dangling Bond ( $P_{bc}$ )

The  $P_{bc}$  centre was described by Cantin *et al.*[148]–[150] in oxidised porous samples, showing a strong angular dependence as would be predicted from the differently orientated surface terminations present in the sample. [148]–[150] These defects have additionally been observed in EDMR measurements at a single surface termination. [141], [151]–[153] A recent study of Anders *et al.*[154] concluded that dangling bonds play a minor role at the interface in MOSFET devices. This is based upon the expectation that H-passivation would lead to a dramatic reduction in  $P_{bc}$  concentration, where only a small reduction in certain  $D_{it}$  is seen after H-treatment.[155] This leaves the role of the  $P_{bc}$  in limbo, clearly observed at the interface although it is unclear if it is critical to device performance. A refinement of this picture is presented in chapter 5 giving an insight into this issue and those of the  $V_{Si}$ .

## 1.8 Summary

The attractive SiC material properties that first prompted the attention of the device community has led to intense interest for the last 20 years. This interest and focused study have allowed a great many of the manufacturing challenges to be overcome, leading to the realisation of commercial SiC based devices. As highlighted in the previous sections, this story is far from over with many challenges centring around the SiC / SiO<sub>2</sub> interface still to be overcome. The defect picture in the bulk and as a result of implantation is more developed, with many of the important performance limiting defects identified.[25], [29], [126], [127], [156]–[158] At the interface, this is far from the case with a number of defects described and identified, but little clarity on which ones are important from a performance perspective. To further complicate the

picture, there are several apparently contradictory observations, particularly those TEM studies that have aimed to describe the interface structures.[41], [159], [160] Part of this confusion is derived from specific sample preparation that results in a non-physical interface from a device perspective.[1] This has led to the suggestion of graphitic region being at the interface, which are only seen in a single set of observations.[1], [79] Theoretical calculations showed that these structures were at best metastable configurations and it is widely accepted to be a result of sample preparation. This is a recurring theme of sample preparation over time between those studies that use lab bench samples and those that use devices (device wafers), and always causes problems of comparability between works. The lab bench samples tend to produce enhanced or new defect signals being as they are implanted, irradiated and annealed to maximise defect concentration. In the case of samples based upon device wafers, the opposite is true, where every possible treatment is undertaken to minimise the defect concentration.

The synthetic effort has shown that a post oxidation NO treatment passivates the interface traps leading to a marked (approximately 1 order of magnitude) reduction in the concentration of electrically active defect states.[161] This made it possible for commercial 4H-SiC MOSFETs to be realised. There are still questions that remain unanswered in this area, like why some of the trap states are never passivated regardless of NO concentration, passivation time, or temperature. This is suggestive of a site or steric limitation that prevents efficient passivation of a small percentage of the defect states. This is hampered by the absence of any mechanistic information where the passivation mechanism is concerned, and leaves the prospect for significant device improvement by understanding the passivation process and refining the process.

This thesis is motivated by the challenges outlined in this chapter. While a great deal has been achieved, much is still to be accomplished. In this work, this is realised in a controlled manner, where at each stage the complexity of the problem at hand is increased. Chapter 3 starts using EDMR and *ab initio* calculations to positively identify a defect that has long been known to exist in N-implanted *pn*-junctions. Chapter 4 explores the diffusion behaviour of defects in the bulk context to offer an insight into why some defects survive to be observed, while others do not. Chapter 5 explores the nature of the SiC / SiO<sub>2</sub> interface using a combination of EELS and theoretical calculations. Finally, chapter 6 takes the interface model developed in chapter 5, and the approach described in chapter 3, and applies them to the problem of defect identification at the 4H-SiC / SiO<sub>2</sub> interface. This approach has allowed a variety of performance limiting defects to be identified. At the same time, the power of combining theoretical calculations with a variety of experimental techniques, where a meaningful comparison can be made, is unequivocally illustrated.

# Chapter 2

## Methodology

---

### 2.1 Introduction

This chapter introduces the methods used throughout this project, by describing firstly the theoretical methods, and secondly, the experimental techniques to which the theoretical calculations are compared. Deviations from the general methods presented here are highlighted in the individual chapters, and dealt with in the relevant sections. The modelling of point defects within bulk crystals and at the interface between materials provides a significant modelling challenge.

The principal method employed throughout this project is density functional theory (DFT), which will be utilised for the bulk of the theoretical methodology. This allows for comparison to the experimental measurements discussed in chapter 1. DFT is introduced and the different approaches within DFT are discussed and contrasted. Then, a discussion of how these concepts are applied to defects in the solid state *via* periodic boundary conditions follows. This finally leads us on to a consideration of geometry optimisation of ground or transition states, vibrational frequency analysis, and density of states plots. These approaches are utilised in the Vienna *ab initio* simulation package (VASP), and CP2K codes.

For the experimental methodology, the focus is electrically detected magnetic resonance (EDMR), as this is the main point of comparison between theory and experiment. Without a detailed understanding of EDMR, there is always the risk of stumbling into uninformed and unfounded assignments.

## 2.2 Theoretical Methodology

### 2.2.1 Density Functional Theory

In 1964, Hohenberg and Kohn (H-K) suggested a new solution to circumvent the need to solve the many-body problem posed by the Schrödinger equation, providing information on the physical and electronic properties of a material.[162] It is an *ab initio* method in principle requiring no additional parameters aside from those inherent in the material being studied. The first H-K theorem states that there is a one-to-one mapping of the density,  $\rho(\mathbf{r})$ , of a system to its external potential. The result of this is that all of the properties of a given system can be determined from its density, and the total energy of the system can be expressed as a functional of its density:

$$E[\rho(\mathbf{r})] = E^T[\rho(\mathbf{r})] + E^V[\rho(\mathbf{r})] + E^H[\rho(\mathbf{r})] + E_{XC}[\rho(\mathbf{r})], \quad (2.1)$$

where  $E^T[\rho(\mathbf{r})]$  is the kinetic energy,  $E^V[\rho(\mathbf{r})]$  is the potential energy,  $E^H[\rho(\mathbf{r})]$  is the Hartree energy, and  $E_{XC}[\rho(\mathbf{r})]$  is the exchange-correlation energy of the system. Expressing the energy as a functional of its density reduces a many-body problem to one that depends upon three spatial variables of the density. The  $E_{XC}[\rho(\mathbf{r})]$  term in equation 2.1 includes all the many-body effects that are not included in the other energy terms. The second H-K theorem states that the ground state density of the system is that which minimises the energy of the system:

$$E[\rho(\mathbf{r})] \geq E_0 \text{ for } \rho(\mathbf{r}) \neq \rho_{gs}(\mathbf{r}) \quad (2.2)$$

$$E[\rho(\mathbf{r})] = E_0 \text{ for } \rho(\mathbf{r}) = \rho_{gs}(\mathbf{r}),$$

where  $\rho_{gs}(\mathbf{r})$  is the ground state density and  $E_0$  is the ground state energy. Therefore, by minimising equation 2.1, the ground state energy and density is found.

From equation 2.1, the total energy of the system can be calculated from its 3-dimensional density. However, due to a lack of a good approximation for  $E^T[\rho(\mathbf{r})]$ ,

these calculations are unable to produce accurate results. Kohn and Sham (KS) developed a solution to this through the introduction of a system of non-interacting electrons (Kohn-Sham system), which have the same density as the real system of interacting electrons.[163] As the KS system is non-interacting, the wave function can be written as a Slater determinant:

$$\Psi_{SD}(\mathbf{r}_1, \dots, \mathbf{r}_N) = \frac{1}{\sqrt{N!}} \begin{bmatrix} \psi_1(\mathbf{r}_1) & \dots & \psi_N(\mathbf{r}_1) \\ \vdots & \ddots & \vdots \\ \psi_N(\mathbf{r}_N) & \dots & \psi_N(\mathbf{r}_N) \end{bmatrix}, \quad (2.3)$$

where  $\psi_1(\mathbf{r}_1)$  are the single particle orbitals.[164] The electron density is then obtained for these orbitals using the Born interpretation of the wave function:

$$\rho(r) = \sum_i^N |\psi_i(\mathbf{r})|^2 = |\Psi|^2 \quad (2.4)$$

The total energy of the system is then evaluated as an expectation value of the Hamiltonian of this wave function. An external potential,  $v_{eff}$  is chosen to reproduce the actual ground state density from the KS system. The total energy of the system is given by

$$E_{gs} = \langle \Psi_{gs}[\rho] | \hat{H} | \Psi_{gs}[\rho] \rangle \quad (2.5)$$

where

$$\hat{H} = \frac{\hbar^2 \nabla^2}{2m} + v_{eff} \quad (2.6)$$

and

$$v_{eff} = v_{ext}(\mathbf{r}) + v_{Hartree}(\mathbf{r}) + v_{xc}(\mathbf{r}) = v_{ext}(\mathbf{r}) + \int d\mathbf{r}' \frac{\rho(\mathbf{r}')}{|\mathbf{r} - \mathbf{r}'|} + \frac{\delta E_{xc}[\rho]}{\delta \rho(\mathbf{r})}, \quad (2.7)$$

where  $v_{ext}$  is the electron-ion interaction,  $v_{Hartree}$  is the electron-electron potential, and  $v_{xc}$  is the exchange-correlation potential. The single particle orbitals can then be determined using the Kohn-Sham formulation of the Schrödinger equation:

$$\left(-\frac{\hbar^2 \nabla^2}{2m} + v_{eff}(\mathbf{r})\right) \psi_i(\mathbf{r}) = \varepsilon_i \psi_i(\mathbf{r}), \quad (2.8)$$

where  $v_{eff}(\mathbf{r})$  is the effective potential,  $\psi_i(\mathbf{r})$  is the KS orbital, and  $\varepsilon_i$  is the eigenvalue of the KS orbital.[163] Equation 2.8, is one of a series of equations that are solved self-consistently starting from an initial guess for the electron density, which is inserted into the effective potential. Once the new density converges with that from the previous step, the KS equations have converged and as such the ground state density obtained.

### 2.2.1.1 Gaussian Plane Waves Method (GPW)

In a DFT calculation, the KS orbitals are described within a set of basis functions. The two functions typically used for solving the KS equations are either local or plane wave functions. Each approach has inherent advantages and disadvantages, the GPW approach makes use of the advantages of each technique to improve computational efficiency.[165]

#### 2.2.1.1.1 Localised Basis Sets

The logic that localised basis sets follow seems intuitive, the basis sets being a set of atomically centred functions. The original functions that were used were Slater-type orbitals (STO's), that have the following form (equation 2.9)

$$\chi_{STO}(r, \theta, \phi) = AY_l^m(\theta, \phi)r^{n-1}e^{-\zeta r}, \quad (2.9)$$

where  $Y_l^m$  is a spherical harmonic,  $A$  is a normalisation constant and  $\zeta$  defines the function's radial extent. STO's show the correct exponential decay behaviour moving away from the nucleus. The issue with STO's arises from determining the overlap integrals between orbitals centred on different atoms, lacking as it does a convenient analytical form. This is typically tackled numerically on a grid, leading to a drastic



increase in computational expense. While they represent the original solution to the problem, the limitations when applied to molecular systems and beyond have limited their use.

A solution to the computational challenges provided by STO's was found in using Gaussian-type orbitals (GTO's), which have the following form:

$$\chi_{GTO}(r, \theta, \phi) = AY_l^m(\theta, \phi)r^l e^{-\xi r^2}, \quad (2.10)$$

GTO's simplify the computational problem associated with STO's being as they are based upon Gaussian functions, and the product of two Gaussian functions is a Gaussian, and as such readily integrated analytically. The problem lies in the fact that unlike STO's, they do not reproduce the correct decay behaviour. This is improved by forming contracted GTO's that approximate STO's as linear combinations of primitive GTO's. Additionally, GTO's can suffer due to the incomplete nature of the basis set.

#### 2.2.1.1.2 Plane Wave Basis Sets

Plane waves are used as basis sets as they are robust to the atomic species and positions. The periodic nature makes them a logical choice of basis set when describing a periodic system, and a converged plane wave basis set in principle represents a complete basis. This method allows the calculation of the Hartree potential and the exchange correlation potential in reciprocal space, where they are more efficiently evaluated.

The free electron wave function is described by a plane wave  $\Psi \sim e^{i\mathbf{k}\cdot\mathbf{r}}$  where the points with a constant value form a plane perpendicular to the vector  $\mathbf{k}$ . From this a wave function of one electron moving in a periodic potential ( $\Psi_{i,\mathbf{k}}(r)$ ) is the same as that of the free electron ( $e^{i\mathbf{k}\cdot\mathbf{r}}$ ) only modulated by the function  $f_{i,\mathbf{k}}(r)$  (equation 2.11).

$$\Psi_{i,\mathbf{k}}(\mathbf{r}) = f_{i,\mathbf{k}}(\mathbf{r})e^{i\mathbf{k}\cdot\mathbf{r}} \quad (2.11)$$

The function,  $f_{i,\mathbf{k}}(\mathbf{r})$  has the same periodic character as the crystal, meaning that  $f_{i,\mathbf{k}}(\mathbf{r})$  has the same value when the input argument is  $\mathbf{r}$  or any translational vector  $\mathbf{T}$  with the same periodicity as the crystal.  $f_{i,\mathbf{k}}(\mathbf{r})$  can be expanded as a series of vectors  $\mathbf{G}$  in the reciprocal lattice

$$f_{i,\mathbf{k}}(\mathbf{r}) = \sum_{\mathbf{G}} C_{i,\mathbf{k},\mathbf{G}} e^{i\mathbf{G}\cdot\mathbf{r}}, \quad (2.12)$$

where the vectors  $\mathbf{G}$  are defined by the expression  $e^{i\mathbf{G}\cdot\mathbf{T}} = 1$ . By inspection of the above equations, it is clear that the solutions for  $\mathbf{G}+\mathbf{k}$  are identical to  $\mathbf{k}$ . It is therefore sufficient to find solutions only for the values of k-points in the first Brillouin zone, which is the primitive cell in reciprocal space.

Several methods exist for providing an array of k-points. Two of the most common are the Monkhorst-Pack method,[166] which generates a set of special k-points in the Brillouin zone, and the improved tetrahedron method, which divides the cell in reciprocal space into tetrahedra.[167]

As previously stated, a given wave function can be expressed as an expansion of plane waves by substituting equation 2.11 into equation 2.12, giving equation 2.13.

$$\Psi_{i,\mathbf{k}}(\mathbf{r}) = \sum_{\mathbf{G}} C_{i,\mathbf{k}+\mathbf{G}} e^{i(\mathbf{k}+\mathbf{G})\cdot\mathbf{r}} \quad (2.13)$$

The description of the wave function can only be viewed as complete when described by an infinite set of plane-waves. In practice, for plane-waves of high kinetic energy the coefficients ( $C_{i,\mathbf{k}+\mathbf{G}}$ ) tend towards zero. Therefore, in practice, only those plane-waves with kinetic energy  $\hbar^2/2m |\mathbf{k} + \mathbf{G}|^2$  below a given cut-off are included. The problem of solving the Kohn-Sham equations is thus reduced to finding a set of  $C_{i,\mathbf{k}+\mathbf{G}}$

that minimises the energy, as the wave function ( $\Psi_{i,\mathbf{k}}(\mathbf{r})$ ) is dependent upon the plane-wave coefficients ( $C_{i,\mathbf{k}+\mathbf{G}}$ ).

### 2.2.1.1.3 Application to the Gaussian Plane Wave Method

In the hybrid GPW method, the electrons in the system are split into those close to the nucleus that do not change much during the calculation, the core electrons, and those that sit far from the nucleus and are involved in chemical reactions and bonding, the valence electrons. The core electrons are replaced with a pseudopotential, which provides a smoothly varying density that can easily be mapped from the basis set to a plane wave basis set.[168] Gaussian functions effectively reproduce the nuclear cusp behaviour, due to the smoothly varying pseudopotential fewer plane waves are required. This allows for simpler mapping of the density from a Gaussian to a plane wave basis set. CP2K makes use of Goedecker-Teter-Hutter (GTH) pseudopotentials, separable dual-space Gaussian pseudopotentials. This type of pseudopotential is separated into local and non-local parts, describing optimal decay properties in both real and Fourier space.[169] This allows for a computationally efficient implementation without sacrificing accuracy. The KS equation (2.1) within these two basis sets is then calculated as:

$$E[\rho] = \sum_{\mu\nu} P^{\mu\nu} \left\langle \psi_{\mu}(\mathbf{r}) \left| -\frac{1}{2} \nabla^2 \right| \psi_{\nu}(\mathbf{r}) \right\rangle + \langle \psi_{\mu}(\mathbf{r}) | V_{loc}^{PP} | \psi_{\nu}(\mathbf{r}) \rangle + \langle \psi_{\mu}(\mathbf{r}) | V_{nl}^{PP} | \psi_{\nu}(\mathbf{r}) \rangle + 2\pi\Omega \sum_{\mathbf{G}} \frac{\rho^*(\mathbf{G})\rho(\mathbf{G})}{G} + \int \varepsilon_{xc}(\mathbf{r}) d\mathbf{r}, \quad (2.14)$$

where  $P^{\mu\nu} \left\langle \psi_{\mu}(\mathbf{r}) \left| -\frac{1}{2} \nabla^2 \right| \psi_{\nu}(\mathbf{r}) \right\rangle$  is the kinetic energy,  $\langle \psi_{\mu}(\mathbf{r}) | V_{loc}^{PP} | \psi_{\nu}(\mathbf{r}) \rangle + \langle \psi_{\mu}(\mathbf{r}) | V_{nl}^{PP} | \psi_{\nu}(\mathbf{r}) \rangle$  are the local and non-local parts of the pseudopotential,  $2\pi\Omega \sum_{\mathbf{G}} \frac{\rho^*(\mathbf{G})\rho(\mathbf{G})}{G}$  is the Hartree energy, and  $\int \varepsilon_{xc}(\mathbf{r}) d\mathbf{r}$  is the exchange-correlation energy. The density within a Gaussian basis set is used to calculate the kinetic and potential energies analytically *via* Gaussian product theory making this a relatively

simple problem. The density in a plane wave basis set allows for efficient calculation of the Hartree energy using fast Fourier transforms.

This method leads to a significant reduction in computational cost allowing significantly larger systems to be considered than would be possible using either basis set in isolation. The GPW method is used throughout the calculations presented in this thesis as implemented in the Quickstep module of the CP2K code.[170]

#### 2.2.1.1.4 Gaussian Augmented Plane Wave Method (GAPW)

In the Gaussian Augmented Plane Wave (GAPW) method, the auxiliary plane wave basis set is as described for the GPW method, but is augmented with primitive periodic Gaussians (building blocks of the contracted Gaussians described above). The simulation cell is then divided into non-overlapping, spherical regions centred upon the nuclear positions, and the internuclear positions. The insight that led to the development of the GAPW method was that the internuclear electron density changes only gradually, and can therefore efficiently be represented by a limited number of plane waves. The opposite, however, is true in the vicinity of the nuclei where the density oscillates (substantially), and is therefore more efficiently represented by localised basis sets.[170]

#### 2.2.1.2 Exchange-correlation functionals: LDA, and GGA

This section is concerned with the two levels of approximation to the exchange-correlation energy that are commonly used; local density approximation (LDA),[171] and the generalised gradient approximation (GGA).[172], [173] The simplest approximation, LDA, is based upon the free electron gas (jellium). The LDA exchange-correlation energy is calculated using equation 2.15

$$E_{xc}^{LDA} = \int d^3r \rho(r) \varepsilon_{xc}^{LDA}, \quad (2.15)$$

where  $\varepsilon_{xc}$  is the exchange-correlation energy per particle in the uniform electron gas. In this approximation, the energy only depends upon the density at each point, hence the ‘local’. This approach performs well for systems that have limited density variation, so are well described by the free electron gas, for example metals. In general, LDA functionals tend to over-bind, resulting in an underestimate of the lattice constants and an overestimate of the bulk moduli. Furthermore, LDA is of limited use for describing localised defect states in solids, as it significantly underestimates the bandgaps of semiconductors, by as much as 50%. [174], [175]

The main failing of the LDA approximation, is its inability to account for inhomogeneity in the density. To overcome this failing, GGA was developed. GGA accounts for density inhomogeneity by adding terms that depend upon not only the density, but also its gradient ( $\nabla\rho(r)$ ) (equation 2.16).

$$E_{xc}^{GGA}[\rho] = \int d^3r (\rho(r), \nabla\rho(r)) \quad (2.16)$$

There are multiple implementations to allow the above to be achieved, and they are all motivated by the same imperative, and as such behave similarly. Some of the most widely used GGA functionals in the solid state community are those based around the Perdew-Burke-Ernzerhof functional (PBE). [172], [173], [176], [177] The results obtained using GGA functionals offer a substantial improvement over those from LDA for the majority of systems (excluding metals where LDA performs well). The issues of bandgap underestimation and the problems of describing localised defect states still remain. For both LDA and GGA, this is due to self-interaction error and is covered in the next section along with hybrid functionals.

### 2.2.1.3 Self-Interaction Error and Hybrid Functionals

The shortcomings identified in the previous section are due to the self-interaction error (SIE) that originates in the Hartree term (equation 2.17).

$$E^H[\rho] = \int dr' \frac{\rho(\mathbf{r})\rho(\mathbf{r}')}{|\mathbf{r} - \mathbf{r}'|} \quad (2.17)$$

The SIE comes about from this term failing to vanish for one-electron systems giving an unphysical Coulombic repulsion. This is due to the fact that the electron sees the repulsion from an average of all of the electrons, including itself. Depending upon the system studied, the manifestation of this problem is more or less serious. For crystals, where the one electron orbitals can be well described by delocalised Bloch-states, SIE does not lead to an unphysical description of the system. However, for systems that have strongly localised d- or f-states, or for defect systems that tend to introduce localised defect states, the SIE can introduce serious problems. In these cases, SIE leads to the favouring of an unphysical description of the system. Several solutions have been proposed to account for SIE. Hybrid functionals are one of the most common methods employed to address this issue and is discussed in detail below.

Becke's insight was that as HF theory does not suffer from SIE, due to the cancellation of the diagonal terms in the exchange and Coulomb integrals, that through mixing a percentage of the HF exchange with that from DFT, the situation could be improved. This was accomplished in the form of the global hybrid functional (equation 2.18)

$$E_{XC}^{Hyb} = a_{Hyb} E_X^{HF} + (1 - a_{Hyb}) E_X^{DFT} + E_C^{DFT}, \quad (2.18)$$

where  $a_{Hyb}$  is the fraction of the exact exchange employed.[178]–[180] This approach offers marked improvements on the structural and more significantly electronic

description when compared to LDA and GGA. Initially, this approach was limited to molecular systems purely from a computational cost perspective, although improvements both from an implementation and method perspective have addressed this.

Range-separated hybrid functionals, and local hybrid functionals are two methods that are employed to retain the accuracy while reducing the computational cost. The Heyd-Scuseria-Ernzerhof (HSE) screened exchange functional has been used extensively to describe solid state systems, and it has been shown to perform very well for semiconductors.[181], [182] The functional affects how short-range Fock exchange is computed and is split into long- and short-range components through breakdown of the Coulomb operator (equation 2.19).

$$\frac{1}{|\mathbf{r} - \mathbf{r}'|} = \frac{\text{erfc}(\omega, |\mathbf{r} - \mathbf{r}'|)}{|\mathbf{r} - \mathbf{r}'|} + \frac{\text{erf}(\omega, |\mathbf{r} - \mathbf{r}'|)}{|\mathbf{r} - \mathbf{r}'|} \quad (2.19)$$

The first term on the right hand-side of equation 2.19 relates to the short-range component, the second is long-range, and the  $\omega$  defines the range separation (empirically determined). Using equation 2.19, the following form of the exchange-correlation functional (equation 2.20) is obtained:

$$E_{XC}^{Hyb} = a_{Hyb} E_X^{HF,SR} + (1 - a_{Hyb}) E_X^{DFT,SR} + E_X^{DFT,LR} + E_C^{DFT} \quad (2.20)$$

The saving in computational cost is derived from the fact that the HF exchange is only evaluated for the short-range component. In the case of HSE, the PBE functional is used for the DFT components. As previously stated, HSE has been shown to perform very well for solid states systems producing results comparable with the global hybrids at a fraction of the cost.

As the computational cost of hybrid functional calculations can be extremely high, to reduce the cost of the HF exchange integrals, various strategies have been

devised such as the resolution of the identity (RI) and the auxiliary density matrix method (ADMM).[183] The ADMM method is implemented in CP2K and is used for hybrid functional calculations throughout this work. It constructs a reduced density matrix using an auxiliary basis, the HF exchange is determined from this, vastly reducing the number of calculations required. The auxiliary basis set has the following form (equation 2.21a):

$$\psi' = \sum_{\mu} C_{\mu i} \psi'_i(r), \quad (2.21a)$$

$$P^{\mu\nu} = \sum_i C_{\mu i} C_{\nu i}, \quad (2.21b)$$

where  $\psi'$  is the wave function of the reduced auxiliary basis set,  $C_{\mu i}$  is the orbital coefficient, and  $\psi_i(r)$  is the orbital. The density matrix is then constructed from these coefficients, which are the result of minimising the square difference between the wave functions of the original and auxiliary basis set (equation 2.21b). This allows the HF exchange energy ( $E_x^{HF}[\rho]$ ) to be calculated as follows:

$$E_x^{HF}[\rho] = E_x^{HF}[\rho'] + (E_x^{HF}[\rho] - E_x^{HF}[\rho']), \quad (2.22)$$

$$E_x^{HF}[\rho] \approx E_x^{HF}[\rho'] + (E_x^{DFT}[\rho] - E_x^{DFT}[\rho']), \quad (2.23)$$

where the HF exchange energy is  $E_x^{HF}[\rho']$ , and the  $E_x^{DFT}[\rho]$  is the GGA (DFT) exchange energy. The assumption inherent in ADMM is that the difference in exchange energy calculated using the full and auxiliary basis sets for both HF and DFT is the same (equations 2.22 & 2.23). This allows for a substantial saving in the computational cost associated with hybrid functional calculations.

#### 2.2.1.4 The Generalised Koopmans' Condition

It is clear that in the utilisation of hybrid functionals to correct the delocalisation induced by SIE, a variable parameter has to be chosen. This parameter is the



percentage of exact exchange ( $a_{Hyb}$ ) that is to be used. It is widely accepted that selection of this parameter is not universal and has a material impact in the properties obtained for a given system. There are a number of methods in the literature that have been used to justify the selection of  $a_{Hyb}$ . In broad terms, they can be broken down into those that are empirically fitted, and those that are fitted theoretically. The most widely known and utilised functional in the literature, B3LYP, is an example of a functional that has been empirically fitted. In the case of B3LYP,  $a_{Hyb}$  was fitted to minimise the error associated with the thermochemical data of a small molecular calibration set, yielding a value of 0.2.[184] On the theoretically fitted side, PBE0 is fitted using perturbation theory giving a value of 0.25.[185]

By plotting the total energy as a function of the fractional number of electrons in the system between integer points linear behaviour should be observed. In the case of Hartree-Fock methods the function is generally concaved favouring a localisation on a single site. In the case of GGA and LDA, the opposite is generally true with the function tending to be convex, therefore the energy is lowered by delocalisation, hence favouring that solution. The correct behaviour is linear, giving a constant gradient between integer points, with discontinuities at the points.

Janak's theorem states that the gradient of the total energy function is equal to the highest occupied eigenvalue. Putting this together with the requirement for linearity gives a statement resembling Koopmans' theorem in HF theory (equation 2.24).

$$E(N + 1) - E(N) = \epsilon_i, \quad (2.24)$$

where  $N$  is the number of electrons in the system, and  $\epsilon_i$  is the eigenvalue of the orbital populated.[186]

## 2.2.2 Optimisation Approaches

This section is focused on the methods utilised to allow the atomic positions and the lattice parameters to be relaxed. These methods rely upon the minimisation of the electronic energy and the inter-nuclear Coulombic energies at 0 K.

### 2.2.2.1 Geometry Optimisations: Conjugate Gradients

The conjugate gradients (CG) methods is one of the various methods that is deployed to find the minimum of a multi-variable function. When applied to the problem of relaxing the atom positions, the energy function ( $E(R)$ ) and its gradient with respect to the atom position  $R$ , the force ( $F$ ) acting on the atoms is given by  $-\partial E(r)/\partial R$ , and it is minimised to solve the Hellmann-Feynman theorem for the system of study.

The CG method is based upon the steepest descent (SD) algorithm, where the atoms are moved in the direction of  $F$ . The SD method evaluate  $E(R)$  along a line at regular intervals between two points. For a starting point  $R_i$ , the new position  $R_{i+1}=R_i+b_i F(R_i)$ , where  $b_i$  is chosen to give an  $F(R_{i+1})\cdot F(R_i)=0$ . The new gradient  $F(R_{i+1})$  is perpendicular to the previous line, the procedure is repeated in the direction of  $R_{i+1}$  until the minimum is located. The first step of the SD and CG techniques is the same, in the CG method successive displacements can take any direction, this can be expressed as:

$$R_{m+1} = R_m + b_m S_m \quad (2.25)$$

The search vector  $S_m$  now contains information from the gradient and the search direction of the previous step (equation 2.26).

$$S_m = F(R_m) + \gamma_m S_{m-1} \quad (2.26)$$

The scalar coefficient,  $\gamma_m$ , is zero for  $m=1$  and is defined by Fletcher and Reeves as equation 2.27.[187]

$$\gamma_m = \frac{F(R_m) \cdot F(R_m)}{F(R_{m-1}) \cdot F(R_{m-1})} \quad (2.27)$$

The advantage of the CG method when compared to the SD method is that it is able to drastically reduce the number of search steps required to locate the minimum of the energy function. In the CG approach, search directions that are optimally independent from one another are utilised.

### 2.2.2.2 Broyden–Fletcher–Goldfarb–Shanno Algorithm

The Broyden–Fletcher–Goldfarb–Shanno (BFGS) method was proposed as means of solving nonlinear optimisation problem in a more efficient manner than the CG method outlined above.[188] In the BFGS (and other quasi-Newtonian methods), the Hessian matrix is not directly evaluated, but instead it is approximated by updates from the gradient evaluations. The BFGS method (L-BFGS, limited memory variant), is well suited to the efficient treatment of large multi-dimensional problems (equation 2.28).

$$B_k p_k = -\nabla f(x_k), \quad (2.28)$$

where  $p_k$  defines the search direction,  $B_k$  is the approximated Hessian matrix updated at each stage, and  $\nabla f(x_k)$  is the gradient of the function evaluated at  $x_k$ . A line search in the direction of  $p_k$  locates the next point of evaluation  $x_{k+1}$ . The approximate Hessian matrix is then updated at  $k$  via matrix addition (equation 2.29).

$$x_{k+1} = x_k + \alpha_k p_k \quad (2.29)$$

$\alpha_k$  defines the step size and is determined in the first step in the direction found in the first step. For subsequent steps  $s_k = \alpha_k p_k$ , with the quasi-Newton condition enforced  $y_k = \nabla f(x_{k+1}) - \nabla f(x_k)$ , this is all put together to give:

$$B_{k+1} = B_k + \frac{y_k y_k^T}{y_k^T s_k} - \frac{B_k s_k s_k^T B_k}{s_k^T B_k s_k} \quad (2.30)$$

$f(x)$ , is the function to be minimised. In the first step,  $B$  is the gradient, further steps being refined by  $B_k$ .

It is important to note that the above techniques assume there is a single minimum associated with the given energy function. Where there are several minima, the minimum located in the basin where the search starts will be located. Due to this shortcoming, the inability to move between basins necessitates the searching of configurational space. This ensures the configuration being studied is a meaningful minimum as opposed to a metastable configuration.

### **2.2.2.3 The Relaxation of Lattice Parameters: Pulay Stress and the Equation of State Method**

While the relaxation of local geometries is covered in the previous section, each functional gives a variation in bond length, which by extension leads to lattice parameters being dependent upon functional. With this in mind, the fixing of the cell parameters can in effect lead to the describing of a geometrically excited state.

When both atom positions and lattice parameters are being relaxed, Pulay stress may arise.[189] This error comes about from the plane wave basis set being incomplete with respect to changes in volume. This means that both the energy cut-off and size of the reciprocal cell define the number of basis functions. The volume variation that occurs during the optimization of the lattice parameters, changes the number of plane waves in the basis set for a given energy cut-off. The effect of this error is to introduce a positive non-zero pressure, or stress that tends to decrease the volume. This is typically remedied by setting the cut-off energy 30% higher than required for energy convergence, as this is typically enough to converge the stress tensor. However, the higher cut-off has an impact on the computational time required.

An alternative approach, that avoids the Pulay stress, is to carry out a constant volume relaxation where only the ion positions and cell shape is allowed to relax. This keeps the basis set constant and removes the above issues induced by volume variations by repeating this at a number of volumes and fitting the points to a cubic equation of state, the minimum of which gives the equilibrium volume of the cell.

#### **2.2.2.4 Transition States**

The transition state is the minimum energy path (MEP) between two local minima, and defines the reaction coordinate for a given transition (reaction). The barrier height gives the adiabatic energy cost for a given reaction to occur, which for elementary reactions is equal to the activation energy.

There are a variety of methods designed to tackle the problem of finding the MEP, the two that will be focused on here are climbing image nudged elastic band (CI-NEB),[190], [191] and the improved dimer method (IDM).[192] The CI-NEB is based upon the nudged elastic band method, where a series of replica images along the reaction coordinates (band) are created and kept equidistant during the relaxation through the addition of spring forces between the images.[193], [194] An optimisation of all images except the initial and final is carried out, using the residual minimisation method-direct inversion in the interactive subspace (RMM-DIIS). This is a quasi-Newton method based on the forces and stress tensor in which the norm of the residual vector is minimised through diagonalization of the inverse Hessian matrix. In the CI-NEB approach, the method is refined to give an improved description of the saddle point with the same (or fewer) images. The highest energy image is freed from the spring constraints and the force along the tangent is inverted to allow this image to maximise its energy along the band and minimise it in all other directions.

The IDM method is implemented in VASP and CP2K. This algorithm identifies a transition state from only the initial configuration. Through identifying the negative vibrational mode that defines the reaction coordinate, a dimer axis is identified and followed to give the transition state.[195]

### **2.2.3 Vibrational Frequency Analysis**

For any ground state, the gradient of each vibrational mode is equal to zero, the second derivatives are positive, indicating that all of the vibrational modes are real. In the case of transition states, one of the frequencies is imaginary, which defines the reaction coordinate. In practical terms, the second derivative from the energy gradients variation is calculated numerically from small displacements of each atom. The Hessian matrix is determined from the forces, its eigenvalues are the vibrational frequencies, and the eigenvectors are the vibrational normal modes of the system.

### **2.2.4 Boundary Conditions and Modelling Defects in Solids**

The approximations and methods highlighted in the previous sections provide the tools to optimise and analyse the structures of interest. Practically, these methods are size limited to systems of no more than a 1000 – 2000 atoms. While improvements in computational resources have drastically improved this picture, 10 years ago it would be unthinkable to tackle systems of more than a few hundred atoms. This situation, while sufficient for molecular systems in the gas phase, fall far short of the  $10^{23}$  atoms that would be appropriate in the macroscopic context.

There are a number of approaches that are used to treat large scale solid systems, the principle technique involves taking advantage of the periodic nature of crystalline solids. This has the advantage of allowing a small region made up of one

or more unit cells to be extended, then *via* Bloch theorem, to calculate the electronic structure of the infinite solid.[196]

#### 2.2.4.1 Supercells for Defect Calculations

One of the main challenges when calculating defects within the confines of periodic models is that of an artificially high defect concentration. Taking advantage of periodic boundary conditions, the primitive cell can be repeated to generate large supercells that are then themselves repeated, allowing defects to be added to larger cells, leading to a marked decrease in defect concentration. If a defect was introduced to the primitive cell, which in the 4H-SiC case contains 8 atoms, the application of the periodic boundary conditions would map that defect into every neighbouring cell in three dimensions giving an unrealistically huge defect concentration (one in every eight atoms). By generating supercells, the defect concentration is reduced which in the 3x3x3 example shown schematically in Figure 2.1 would relate to a 96-atom cell for 4H-SiC giving a vastly reduced defect concentration (although still very high). The supercell size is selected to allow the defect relaxation to be described within the simulation cell ensuring that the final structure is not constrained.

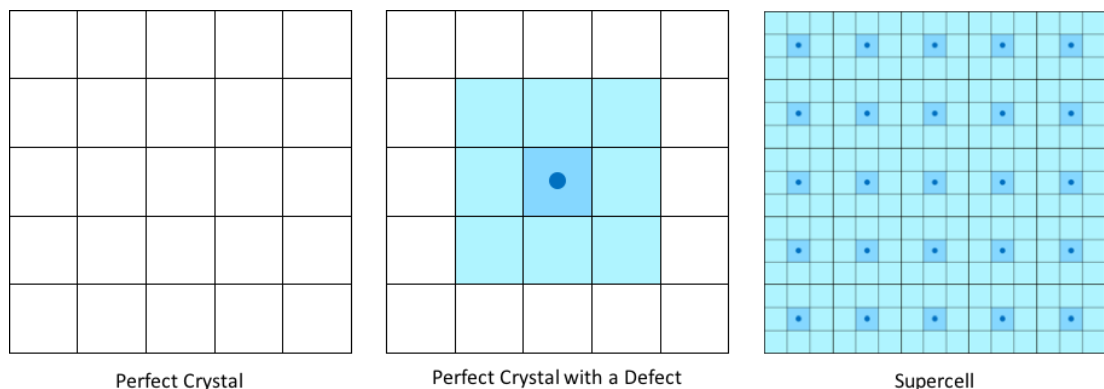


Figure 2.1. Schematic overview of supercell method in relation to defect calculation.

A further level of complexity is introduced when charged defects are to be considered. These arise due to the long-range nature of the Coulomb potential, where an unphysical interaction between the defect and its periodic image can be introduced. The principle quantity of interest in defect calculations is the defect formation energy ( $E_f$ ), as this can be used to infer defect concentration assuming equilibrium has been reached.  $E_f$  is the energy required to create an isolated defect in charge state  $q$ :

$$E_f(q) = E_D(q) + \sum n_s \mu_s - E_{bulk}(q) + q(\mu_e + E_v) + E_{corr}, \quad (2.31)$$

where  $E_D$  is the total energy of the supercell containing the defect, the sum is the energy of the removed or added species  $s$ ,  $n_s$  the number of species  $s$ ,  $\mu_s$  is the chemical potential of species  $s$ ,  $\mu_e$  is the electron chemical potential (Fermi Level),  $E_v$  is the potential alignment, and  $E_{corr}$  is a correction term.[96], [102]

There are two major errors that result from the use of periodic boundary conditions, and these must be corrected if accurate defect energies are to be obtained. These errors are image-charge interactions and differences in the reference electrostatic potential. The correction of these problems has led to numerous correction schemes, and vigorous debate as to the best method for a given system type.

The simplest correction scheme of this type is a Madelung type correction proposed by Leslie and Gillian, which is derived from the screened Coulomb interaction between point charges.[197] This idea was extended by Makov and Payne (MP), and until recently was the most common method for correcting the image charge interaction.[198] The correction ( $\Delta E_{MP}$ ) takes the simple Madelung term and adds an additional term to account for the multipole expansion



$$\Delta E_{MP} = \frac{q^2 \alpha_M}{2\epsilon L} + \frac{2\pi q Q_s}{3\epsilon L^3}, \quad (2.32)$$

where  $\alpha_M$  is the Madelung constant of the super lattice,  $\epsilon$  is the dielectric of the material,  $Q_s$  is the second radial moment of the charge density, and  $L$  is cell length. The MP scheme has been shown to perform well for molecular systems, but the MP scheme has a tendency to overestimate the magnitude of the correction (to the first order approximation). This overestimation comes about from the fact that  $Q_s$  does not take into account the screening response of the dielectric.

The solution to this overestimation was proposed by Lany and Zunger ( $\Delta E_{LZ}$ ), which has largely become the standard for the correction of image charge interactions.[199] To the first order it is given as

$$\Delta E_{LZ} = [1 + C_{sh}(1 - \epsilon^{-1})] \frac{q^2 \alpha_M}{2\epsilon L}, \quad (2.33)$$

where  $C_{sh}$  is the shape factor and depends only upon the shape of the supercell, and the dielectric of the material. An alternative approach was proposed by Freysoldt, Neugebauer, and van de Walle, consideration of this scheme is beyond the scope of this work as the LZ method has been successfully used for the SiC system and allows for comparison with the existing literature.

To correct for the shift in electrostatic potentials due to the divergence of the Madelung sum in charged cells, for a given supercell calculation, the average value of the electrostatic potential is set to zero. This leads to the introduction of an arbitrary constant that is not constant between charge states. This is corrected for by inspection, either via comparison of ions in the defect and bulk region to give an estimation of the shift. Alternatively, the potential shift can be gauged by inspection of the core-levels of ions far from the defect for the neutral and charged systems. It is

important to note that these methods should yield the same value for the potential alignment.

## 2.3 Experimental Methodology

This work was motivated by the need to understand defects within the device context, and to achieve this and allow for a comparison with theory, experimental measurements of the systems of interest were required. The main source of comparison between the experimental and theoretical calculations within this thesis will be EDMR, offering an insight into the defects that persist in fully processed devices, and as such impact device performance and reliability. Additionally for the interface systems, electron energy loss spectroscopy (EELS) was used to describe the atomic composition across the SiC / SiO<sub>2</sub> interface. An overview of EDMR, and more generally spin dependent recombination, and EELS is given here.

### 2.3.1 Electrically Detected Magnetic Resonance (EDMR)

An electronic state that has an inequivalent number of spin-up ( $\alpha$ ) and spin down ( $\beta$ ) electrons is called paramagnetic defects, and have a net interaction with magnetic fields. In 1945, Zavoisky showed that the interaction of these unbalanced spins with an applied field could be measured yielding structural information on the paramagnetic states.[200], [201] From this point, electron paramagnetic resonance (EPR) was born and has over the intervening period been developed into a powerful method for probing reactive intermediates, transition metal complexes, and point defects in solids. One of the major challenges and limitation inherent in EPR in the solid state is that of signal deconvolution, with multiple overlapping signals being probed in a single measurement that then require untangling. In addition to this, EPR has always been limited by the detection limit of approximately  $10^{10}$  defects, making

the study of small samples and minority defect populations challenging.[202] In response to this, optically detected magnetic resonance and EDMR have been developed.[203], [204] The relevant comparison throughout this thesis is the spin dependent recombination (SDR) variant of EDMR, offering vastly improved sensitivity, theoretically up to single defect resolution and selectivity. Further area selectivity is gained from only those defects in the path of the current being probed, which is of particular advantage when surface or interface defects are of interest, but in conventional EPR would be overshadowed by the bulk signal.[205]–[207] This section is intended to give the reader an overview of the experimental techniques that form the basis of the comparison presented in this work.

### 2.3.2 Electron Paramagnetic Resonance – EPR

The EPR signal derives from the Zeeman splitting of the electron spin,  $S=1/2$  and  $m_s=+1/2$  or  $-1/2$ , by an external magnetic field  $B_0$ , the magnetic moment is aligned parallel or anti-parallel to the field. Each orientation has a different energy due to  $E=m_s g_e \mu_B B_0$  where  $g_e$  is the electron  $g$ -factor,  $\mu_B$  is the Bohr magneton. From this the splitting of energy levels is directly proportional to the applied field, illustrated in Figure 2.2.

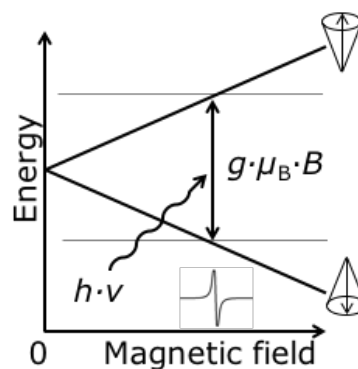


Figure 2.2. Schematic view of Zeeman splitting.

An unpaired electron can move between the energy levels either by absorbing or emitting a photon of energy  $h\nu$  such that  $\Delta E=h\nu$ . The  $g$ -factor gives information about the local electronic structure of the paramagnetic centre. The unpaired electron responds to both the applied field and any local magnetic fields, a combination of these give  $B_{eff}$ , the effective field experienced by an electron. As  $h\nu=g\mu_B B_0$  the variation in  $g$  compare to  $g_e$  holds critical information. An electron's spin magnetic moment is constant, and any variation must be due to spin-orbit coupling. The mechanism of spin-orbit coupling is well understood; the magnitude of the change gives information on the molecular orbital containing the unpaired electron.

### 2.3.3 Hyperfine Interaction

Hyperfine (HF) coupling is the interaction of an electron's magnetic moment, with neighbouring nuclear spins, gives rise to a multi-line spectra and characteristic splitting patterns.[208] There are two mechanisms by which this can occur:

1. Fermi Contact – When the  $\Psi(r)$  does not vanish at the nuclear position (s-states), direct contact interaction, no angular dependence.

$$A_s = \frac{\mu_0}{4\pi} \cdot \frac{8\pi}{3} \cdot (g_n \cdot \mu_N) \cdot (g_e \cdot \mu_B) \cdot |\Psi(0)|^2 \quad (2.34)$$

2. Dipolar Interaction – The wave function has an angular dependence and vanishes at the nuclear position (p / d / f – functions)

$$A_p = \frac{\mu_0}{4\pi} \cdot \frac{2}{5} \cdot (g_n \cdot \mu_K) \cdot (g_e \cdot \mu_B) \cdot \left\langle \frac{1}{r^3} \right\rangle \langle 3\cos^2\theta - 1 \rangle \quad (2.35)$$

If both contributions are present, equation 2.36 is valid.

$$A = A_s + A_p \cdot (3\cos^2\theta - 1) \quad (2.36)$$

In gases and liquids, only the isotropic ( $A_s$ ) is observable, as rapid tumbling averages the anisotropic components to 0. In the solid state, site symmetry is important, and for cubic sites only  $A_s$  is retained. In general, one can write

$$A^2 = A_{XX}^2 \cdot \sin^2\theta \cdot \cos^2\Phi + A_{YY}^2 \cdot \sin^2\theta \cdot \sin^2\Phi + A_{ZZ}^2 \cdot \cos^2\theta, \quad (2.37)$$

where  $\theta$  and  $\Phi$  are the angles between the coordinate system axis and the tensor principle axis. The pattern of the splitting is itself instructive give information on the nuclear spin and number of magnetically equivalent nuclei contributing to a given splitting. In the case of nuclear spin, the number of lines is given by  $2I+1$ . This is then summed over the number of magnetically equivalent nuclei.

The final piece of information that can be derived from the magnitude of the HF peaks is the isotopic abundance of the species responsible when scaled relative to the centre line. This is of particular use when identifying the atomistic make up of a given defect, as the isotopic abundances of spin active ( $S>0$ ) isotopes is constant. Table 2.1 below shows the relative abundances of a number of species of interest.

Table 2.1. Isotopic abundance of elements of interest for SiC based devices.

Isotope	Isotopic Abundance / %	Nuclear Spin / I
<sup>1</sup> H	99.99	1/2
<sup>13</sup> C	1.11	1/2
<sup>14</sup> N	99.63	1
<sup>27</sup> Al	100	5/2
<sup>29</sup> Si	4.67	1/2

When all of this information is considered together a detailed picture of the atoms that make up a given defect can be obtained.

### 2.3.4 Electron-Electron Interaction: Zero Field Splitting

Similar to the HF interaction described above, the zero field splitting arises from the interaction of an unpaired electron with the magnetic moment of a neighbouring electron (equation 2.38).[209]

$$\mathcal{H}_{ee} = \mathcal{H}_{dd} + \mathcal{H}_{ex} \quad (2.38)$$

where  $\mathcal{H}_{ee}$  is the electron-electron coupling Hamiltonian,  $\mathcal{H}_{dd}$  is the electron dipole-dipole interaction, and  $\mathcal{H}_{ex}$  is the electron exchange interaction.  $\mathcal{H}_{dd}$  (equation 2.39) is only relevant for the states of  $S > 1$ , and  $\mathcal{H}_{ex}$  describes the difference between the  $S=0$  and  $S=1$  and their respective order.

$$\mathcal{H}_{dd} = S \cdot D \cdot S \quad (2.39)$$

$$D = \frac{\mu_0}{8\pi} (g\mu_B)^2 \left\langle \frac{3r_i r_j - \delta_{ij} r^2}{r^5} \right\rangle \quad (2.40)$$

Here,  $S$  is the spin parameter ( $S=S_1+S_2$ ), and  $D$  is the electron quadrupole matrix. This relates to one electron placed at the origin and then integrated over all the positions of the second. As previously stated, this describes the energy between the triplet and singlet states at zero magnetic field.

### 2.3.5 Spin Dependent Recombination

To combat the detect limit inherent with EPR highlighted above, EDMR, and more specifically spin dependent recombination (SDR) were developed to overcome this shortcoming. In EDMR the changes in the current are observed as a function of field position. In these techniques, various spin dependent processes affect the conductivity of the sample, such as spin dependent scattering, spin dependent tunnelling, and SDR.[207] The particular strength of SDR is that it allows the study of fully processed devices, rather than specially prepared samples. In this technique,

little sample preparation is required as biasing is used to selectively probe the device region of interest.

The SDR technique was first introduced by Lepine in 1972. [205] This work offered the insight that by monitoring the photocurrent in Si devices in an EPR apparatus, the spectrum can be measured with a high signal-to-noise ratio.[205] This was understood in terms of a portion of the recombination current being spin dependent. The initial model was based upon Shockley-Read-Hall recombination *via* a paramagnetic state in the band-gap.[55], [56] This model, while qualitatively reasonable, predicted a far smaller current change than observed.

A more developed picture was proposed by Kaplan *et al.*[206] which gave an improved description of the observed current change. This spin-pair model considers a situation where an electron and a hole are captured by two different paramagnetic states in the bandgap. The electron and hole have to be in close proximity in order to interact and to be considered a spin-pair. The recombination occurs with the electron filling the empty state or the hole filling the electron space, the total spin of the system can be  $S=0$  or  $S=1$ , which is crucial for recombination. As spin must be conserved after recombination, a singlet state is allowed as such recombination is rapid when compared to the triplet state.[206] This results in a higher population of triplets with respect to singlets under steady state conditions. When resonance occurs, a spin flip is induced, transforming a portion of the triplet states into singlets that allow more states to recombine. This is detected as a current change, observable in SDR with the EPR parameters of the defect state of interest. In theory, both the donor (electron) and acceptor (hole) state can be probed, in practice one of the states tends to dominate.[207], [210]

### **2.3.6 Bipolar Amplification Effect (BAE)**

This technique is described by Aichinger and Lenahan, and is related to the SDR technique described above.[211] It was demonstrated that by adapting the (SDR) biasing scheme dramatic improvements in the signal to noise ratio can be achieved. This approach results in a change in current many orders of magnitude greater than in gated diode SDR at resonance.

### **2.3.7 Electron Energy Loss Spectroscopy / Energy Loss Near Edge Spectroscopy (EELS / ELNES)**

An insight into the local chemical environment can be gained from the inelastic scattering of electrons passing through the sample, EELS measures this energy distribution to probe the chemical environment of the interacting atoms. The energy measured relates to the inelastic scattering of the electron beam, the majority of the electrons pass through without interacting with the sample. In the case where the inelastically scattered the electron ionises a core electron, the energy lost is equal to the ionisation energy, of an electron from a core level to a conduction band state, and as such acts as a probe of the unoccupied density of states of the material. The relative positions of these states are extremely sensitive to the local chemical environment allowing EELS to act as a probe of the chemical bonding environment.[212]



# Chapter 3

## Nitrogen defects in N-Implanted *pn*-junctions

---

### Abstract

In this chapter, defects in N-implanted *pn*-junctions are identified by comparing EDMR measurements with extensive *ab initio* calculations. The defect identification is based upon the defect symmetry and the form of the hyperfine (HF) structure. A full description of how an accurate spectrum can be generated from the theoretical data by probabilistic treatment of the individual HF contributions is described. This approach is illustrated with a defect observed in nitrogen implanted silicon carbide. Nitrogen implantation is a high energy process that gives rise to a high defect concentration. The majority of these defects are removed during the dopant activation anneal, shifting the interstitial nitrogen to the desired substitutional lattice sites, where they act as shallow donors. EDMR shows that a deep-level defect persists after the dopant activation anneal. This defect is characterized as having a  $g_{\parallel}=2.0054$  and  $g_{\perp}=2.0006$ , with pronounced hyperfine shoulder peaks with a 13 G peak to peak separation. The  $N_C V_{Si}$  centre is identified as the persistent deep-level defect responsible for the observed EDMR signal and the associated dopant deactivation.

### 3.1 Introduction

As discussed in section 1.5, in *n*-type 4H-SiC, nitrogen is the most feasible shallow donor impurity due to its low mass and low ionization energy.[18] In order to form *n*-doped regions, nitrogen is typically incorporated by ion implantation and substitutes preferentially at the carbon site.[94], [126], [158] For the N substitutional donor ( $N_C$ ) there is a slight difference in ionisation energy dependent on whether it sits at the quasi-hexagonal site (60 meV) or in the quasi-cubic site (120 meV).[19], [22] In device regions where high conductivity is desired, particularly high nitrogen doping concentrations are required.

As the nitrogen concentration can exceed the donor concentration, it has been suggested that not all implanted nitrogen impurities occupy the desired substitutional lattice sites, where they act as shallow donors.[157] It has been postulated that nitrogen may form silicon nitride clusters or complexes with intrinsic crystal defects. In addition to deactivating dopants, impurity defect complexes may also introduce deep levels in the SiC band gap, which can act as recombination centres and limit the performance of SiC devices. Theoretical and experimental investigations have shown that nitrogen is able to interact with silicon vacancies ( $V_{Si}$ ), carbon vacancies ( $V_C$ ), divacancies ( $V_C V_{Si}$ ) and vacancy clusters to form either  $N_C V_{Si}$  or  $N_{Si} V_C$ . The fully passivated  $(N_C)_4 V_{Si}$  defect, which is an electrically passive defect, has been suggested as a candidate for dopant deactivation.[126]

In previous EPR studies performed on N-doped SiC, the spectra were dominated by the shallow  $N_C$ . [93], [132], [134], [135] Some studies reported on an additional smaller signal of a defect with smaller concentration, called the  $N_X$  centre. [93], [133]–[135] This defect has been assigned to closely correlated  $N_C$  dopant

pairs. There is only one study applying conventional EPR in order to measure a nitrogen-complex.[100] This identification was made on the basis of a large zero-field splitting resulting from the spin  $S=1$  of the defect, which was identified as the negatively charged NV-centre ( $N_C V_{Si}^-$ ). In the study of Aichinger *et al.*, the spectra of deep levels caused by N-implantation were unambiguously measured using the spin dependent recombination (SDR) technique.[130] A well resolved spectrum was measured in N-implanted SiC devices, which was not observed in epitaxially grown devices. A very similar defect was also observed in another SDR study on *pn*-junctions in bipolar junction transistors.[146] Small scale theoretical modelling appeared to assign the observed spectrum to the substitutional N next to a C antisite ( $N_C C_{Si}$ ), although this assignment is in question.[128] The basis of the concern arises from discrepancies in the magnitudes of the hyperfine (HF) peaks and that the symmetry of the experimentally observed defect seems at odds with the assignment of  $N_C C_{Si}$ .

In this chapter, the SDR spectra from an N implanted *pn*-junction are compared with extensive *ab initio* simulations and detailed probabilistic treatment of the calculated hyperfine parameters. This allows the atomistic structure of the dominant defect to be identified. These results demonstrate that the nitrogen at a carbon site next to a silicon vacancy  $N_C V_{Si}$  centre is the persistent deep-level defect responsible for the observed SDR signal and the associated dopant deactivation defect.

## 3.2 Experimental Methods

Electrically detected magnetic resonance (EDMR) makes it possible to investigate performance limiting defects directly on fully processed devices, *eg* a *pn*-junction.

Here we use SDR, a subset of EDMR where a recombination current is used to measure the transitions between the Zeeman levels of paramagnetic recombination centres in the studied sample.[146], [205], [213] The technique is most sensitive to paramagnetic defects close to the middle of the band gap, as they are the most efficient recombination centres.[55], [56], [213], [214]

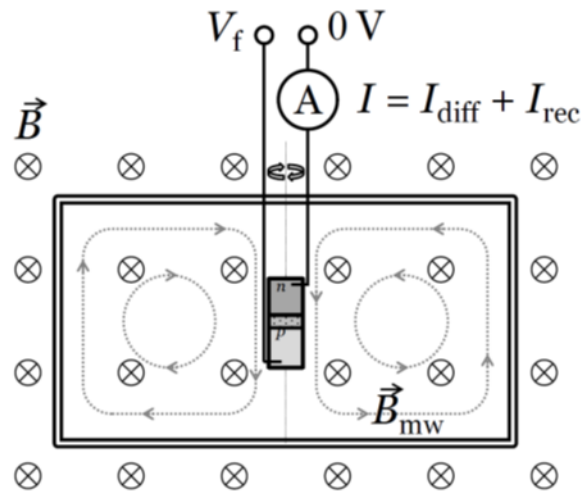


Figure 3.1. Schematic view of the experimental SDR set-up, the sample is placed in the field and the current ( $I$ ) is measured as a function a function of field.

Figure 3.1 shows a schematic of how SDR is performed. A  $pn$ -junction is forward biased so that electrons and holes are injected into the depletion region of the junction. The total current ( $I$ ) through the  $pn$ -junction is a sum of a diffusion current ( $I_{diff}$ ) and a recombination current ( $I_{rec}$ ). The recombination component of the current depends on the density of recombination centres in the depletion region of the junction, which can capture electrons and holes, and allows them to recombine. The device under test is put in a microwave cavity where a quasi-static external magnetic field  $B$  is applied. As this magnetic field interacts with the electron spins the recombination rates are lowered.[206] Additionally, a microwave field is applied of which the magnetic component  $B_{mw}$  interacts with the spins. When resonance occurs,

the recombination rates are enhanced and a change in the current ( $\Delta I$ ) can be observed.[205], [206] The resonance condition is

$$h\nu = g\mu_B \left( B_{res} + \sum_{k=1}^n a_k m_k \right) \quad (3.1)$$

where  $h$  is the Planck's constant,  $\nu$  is the microwave photon frequency,  $g$  is the Lande-factor,  $\mu$  is the Bohr magneton,  $B_{res}$  is the resonant applied magnetic flux density,  $a_k$  is the HF splitting constant at atomic site  $k$ ,  $m_k$  is the magnetic nuclear spin quantum number at atomic site  $k$ , and  $k$  sums over the atoms that make up the defect.[81]

One way to identify a defect is to analyse the  $g$ -factor, which is influenced by the local environment of a specific defect. Even when a strong resonance peak is observed in an experiment, it is not always obvious what the microscopic structure of the defect is. While  $g$  can be calculated for a candidate defect, a precise calculation is very challenging.[215] However, the observed angular dependence of  $g$  must match the symmetry of the defect.

Another way to identify a defect is to examine the additional structure caused by the HF interaction. The sum over HF constants in equation 3.1 shifts the field where the resonance occurs and adds satellite peaks to the spectrum. Every atom with a non-zero nuclear spin on a site where the electron density is non-negligible adds a contribution to the HF structure. As the unpaired electron wave function can extend over the nearest neighbour (1NN), the second nearest neighbour (2NN) and even the third nearest neighbour (3NN) shells, there may be many contributions to the sum. Paired with the fact that SDR spectra are often broadened, this can make the interpretation more difficult.[128], [130]

Theoretical modelling combined with accurate probabilistic consideration of the calculated HF interactions can be used to identify the defect responsible for the observed SDR spectra, as discussed below.

### 3.2.1 Experimental Parameters

A 4H-SiC *pn*-junction formed by heavy N-implantation (doping of  $5 \times 10^{17} \text{ cm}^{-3}$ ) and an Al-implantation of a similar dose was studied. The sample received a standard dopant activation anneal at 1800°C. The measurements were recorded by Gernot Gruber using a method similar to Aichinger *et al.*[130] To measure SDR, a forward bias of 2.35 V was applied, in this regime the recombination current is high and a good signal-to-noise ratio can be obtained. The sample was measured at room temperature with an X-band EPR spectrometer at a microwave frequency of  $\nu \approx 9.402$  GHz and a microwave power of  $\approx 50$  mW. The magnetic field was calibrated using a 2,2-diphenyl-1-picrylhydrazyl standard and a Drusch nuclear magnetic resonance magnetometer. The current was measured with a Stanford Research SR570 current amplifier and a Stanford Research SR830 lock-in-amplifier. For the lock-in amplification a magnetic field modulation of 0.5 G was applied in order to avoid any line broadening by over-modulation and to obtain the best resolution of the HF side peaks. The modulation frequency was  $\approx 900$  Hz. Due to the use of lock-in amplification, all spectra were recorded as  $d/d_B$  vs.  $B$ . Multiple scans were averaged to improve the signal-to-noise ratio.

### 3.3 Computational Details

DFT calculations were performed using the CP2K code, and the functionals selected for the calculations were PBE and HSE06. These functionals were utilized with the DZVP-MOLOPT-SR-GTH and the TZVP-MOLOPT-GTH basis sets. All parameters were converged to 0.01 meV per formula unit. This led to the selection of a  $5 \times 4 \times 2$  orthorhombic supercell (480 atoms  $15 \text{ \AA} \times 16 \text{ \AA} \times 20 \text{ \AA}$ ), with a single k-point (Appendix C). This formed the basis for all calculations allowing for the defect relaxation to be contained within the simulation supercell.

The HF parameters were calculated using the GAPW approximation in the CP2K code. The basis-sets selected for geometry optimization are not appropriate for the calculation of hyperfine parameters, as an explicit description of the core electrons is required, hence an all electron basis set is required. To ensure the best description of the core electrons, extensive calibration and testing of several basis-sets was conducted using a variety of test systems.[216] The best accuracy was obtained from the pcj family of basis-sets with an error of  $\pm 6$  G in the pcj-0 case,  $\pm 3$ G for pcj-1 and  $\pm 1$  G for pcj-2 and  $\pm 0.3$  G for pcj-3. As a result of these calibration tests, the pcj-1 basis set was selected as giving the best balance of accuracy to computational time.

#### 3.3.1 Defect Calculations

The above parameters and supercells were used for all defect calculations. Initially, the neutral charge states were calculated and from the number of occupied and unoccupied gap states, the accessible charge states for a given defect were inferred and calculated. The defect formation energy ( $E_f$ ) was calculated using the standard formalism of Northrup and Zhang.[102] This neglects the temperature dependent portion of the free energy of formation, ( $\Omega_f = E_f - TS$ ) which includes phonon effects that

are challenging to calculate. While  $E_f$  dominates at low temperatures, the entropy term (S) can have a marked effect on  $\Omega_f$  at elevated temperatures. Explicit consideration is beyond the scope of this chapter, but is considered in chapter 4, here  $E_f$  is assumed to approximate  $\Omega_f$  as:

$$E_f(q) = E_D(q) + \sum n_s \mu_s - E_{bulk}(q) + q(\mu_e + E_v) + E_{corr}. \quad (3.2)$$

$E_D$  is the calculated total energy of the defect containing supercell, the sum is the energy of the removed or added species  $s$  calculated through the number of species  $s$  ( $n_s$ ), and the chemical potential of species  $s$  ( $\mu_s$ ).  $\mu_e$  is the electron chemical potential (Fermi Level),  $E_v$  is the potential alignment, and  $E_{corr}$  is the correction term.[96], [102]

It is important to note that the lowest energy charge state for a given  $\mu_e$  assumes that the system has reached thermodynamic equilibrium, which may not always be the case. With this in mind, formation energies give useful information about the relative concentrations for a given series of defects. The chemical potentials are treated in accordance with the method outlined by Torpo *et al.*[83] with 1/2 of N<sub>2</sub> molecule total energy used for the  $\mu_N$ . The finite size charge corrections are applied according to the scheme of Lany and Zunger,[199] with consideration of the anisotropic nature of the supercell using the methodology of Murphy and Hine.[217]

### 3.3.2 Probabilistic treatment of HF parameters

In order to simulate a spectrum, the magnitude of the hyperfine splitting and their relative intensities need to be described for all of the defect atoms. Rewriting equation 3.1 reveals the resonance field  $B_{res}$  for a given configuration of  $n$  atoms as

$$B_{res} = B_0 - \sum_{k=1}^n a_k m_k. \quad (3.3)$$



The term  $B_0 = h\nu/g\mu_B$  is simply the resonance field without HF interactions and marks the centre of the spectrum. For a given defect, many different configurations of the  $m_k$  values of the  $n$  atoms are possible, each resulting in a different HF interaction term in equation 3.1. At a nitrogen site,  $m$  can take on the values -1, 0, or 1, assuming that 100% of the nitrogen is  $^{14}\text{N}$  which has a nuclear spin of 1. At a carbon site,  $m=0$  for a  $^{12}\text{C}$  isotope and  $m=\pm\frac{1}{2}$  for a  $^{13}\text{C}$  isotope. At a silicon site,  $m=0$  for the  $^{28}\text{Si}$  and  $^{30}\text{Si}$  isotopes and  $m=\pm\frac{1}{2}$  for the  $^{29}\text{Si}$  isotope. Therefore, every atomic site has three possible spin states with a respective probability. As the isotopes are randomly placed around the defect, for  $n$  atoms there are  $3^n$  possibilities to consider. Each of these will shift the centre of the Lorentzian peak and the experimentally observed result will be a sum of all of these resonance peaks. In an experiment, the weighted sum of all lines due to the individual configurations is measured. The intensity  $P$  of each individual line is given by the product of the probability  $p_{k,m_k}$  for each atom at site  $k$  to have a certain spin state

$$P = \prod_{k=1}^n p(\text{atom}_k, m_k) \quad (3.4)$$

with  $p(\text{N}, \pm 1)=1/3$ ,  $p(\text{C}, 0)=0.989$ ,  $p(\text{C}, \pm\frac{1}{2})=0.0055$ , and  $p(\text{Si}, 0)=0.953$ ,  $p(\text{Si}, \pm\frac{1}{2})=0.0233$ . The resulting line at the position  $B_{res}$  can be represented by a Lorentzian lineshape  $L \propto P/(\Gamma^2 + B - B_{res})^2$  with  $\Gamma$  being a parameter linked to the line width via  $W_{PP} = 2/\sqrt{3}\Gamma$ . The experiments are performed with a lock-in amplifier and the measured signal is the sum of the derivatives of the Lorentzians. The resulting contribution of one set of  $n$  atoms with their respective spin states  $m_k$  can be represented by a derivative Lorentzian line given by

$$L'(B; B_{res}; \Gamma) = \frac{-P(B - B_{res})}{[\Gamma^2 + (B - B_{res})^2]^2}. \quad (3.5)$$

To simulate a complete spectrum, it is necessary to sum over all  $3^n$  permutations of the  $m_k$  of the  $n$  atoms. The equation that describes the full spectrum can be written as

$$L'_{total} = \sum_{i_1=1}^3 \sum_{i_2=1}^3 \dots \sum_{i_n=1}^3 \left( - \prod_{k=1}^n p(atom_k, m_k) \frac{B - B_0 + \sum_{k=1}^n a_k m_{k,i_k}}{[\Gamma + (B - B_0 + \sum_{k=1}^n a_k m_{k,i_k})^2]} \right). \quad (3.6)$$

The defects considered contain up to about 30 individual atoms interacting with the unpaired electron. Simulating the full spectrum including all lines therefore requires enormous computational resources and is not practical. Fortunately, many of the configurations are improbable and can be neglected. For instance, it is exceedingly unlikely that all of the carbon atoms in the neighbourhood of the defect are  $^{13}\text{C}$  isotopes. By setting a minimum probability  $P_{min}$  to be considered one can dramatically reduce the number of lines that are actually calculated. Subsequently we consider only lines with a higher abundance than  $P_{min}=10^{-7}$  when generating the simulated spectra. In order to prevent memory problems, the  $3^n$  atoms are split into smaller subsets where all combinations of nuclei resulting in a smaller probability than  $P_{min}$  are filtered out. In a second step, the remaining sets are combined and again a filtering step is applied. In the end, the total of  $3^n$  lines to be plotted are reduced by many orders while still >99% of the total spectrum is simulated. The advantage of this method is that every splitting constant of every atom can be considered individually, rather than using an average value. Also very small contributions are considered even though they do not result in resolved features. However, they can add broadening to

the line and influence the resulting line shape, which otherwise may not be well represented.

### 3.4 Experimental Results: Performed by G. Gruber

The recorded spectra with the crystalline  $c$ -axis oriented parallel to the magnetic field  $B$  ( $c \parallel B$ ) and with  $c$  oriented perpendicular to  $B$  ( $c \perp B$ ) are shown in Figure 3.2. The former corresponds to  $B$  applied in the [0001] direction and the latter to  $B$  in the [1-100] direction, respectively. The measured  $g$ -values are  $g_{c \parallel B} = 2.0054$  and  $g_{c \perp B} = 2.0006$ . The spectra are rotationally symmetric about the crystalline  $c$ -axis with some small deviations (likely due to the  $4^\circ$  off-axis growth) within experimental error. The spectrum with the magnetic field applied in the [11-20] direction is equivalent to [1-100] and is therefore not shown. The spectrum with  $c \parallel B$  is slightly sharper, which can be explained by the hexagonal crystal structure and more defect atoms being equivalent in this direction. There is a small anisotropy in the HF interaction as the main side features in the  $c \parallel B$  direction is split into two sets of lines in the  $c \perp B$  direction. It is likely that this is due to equivalent sites in the former direction being inequivalent in the latter.

For simplicity, all of the following discussions are focused on the  $c \parallel B$  spectrum. The spectrum contains a strong centre line with a peak-to-peak linewidth of  $W_{pp} \approx 3.8$  G and several HF side peaks. The most pronounced peaks are at approximately  $\pm 6.5$  G left and right of the centre line. Due to their high relative intensity, the lines are likely either to be due to the HF interaction of one N atom, as suggested by Aichinger *et al.*[130], or due to multiple Si atoms, as they can in sum have a significant abundance as well. A second pair of HF lines with much smaller relative intensity is found at approximately  $\pm 21$  G and is likely due to  $\approx 3$  C atoms. No

more lines with a larger splitting than the ones mentioned were observed in the region  $\pm 600$  G away from the centre line. In the following sections, we use theoretical modelling of the defect structures and compare them to the SDR spectra in order to identify the responsible defect.

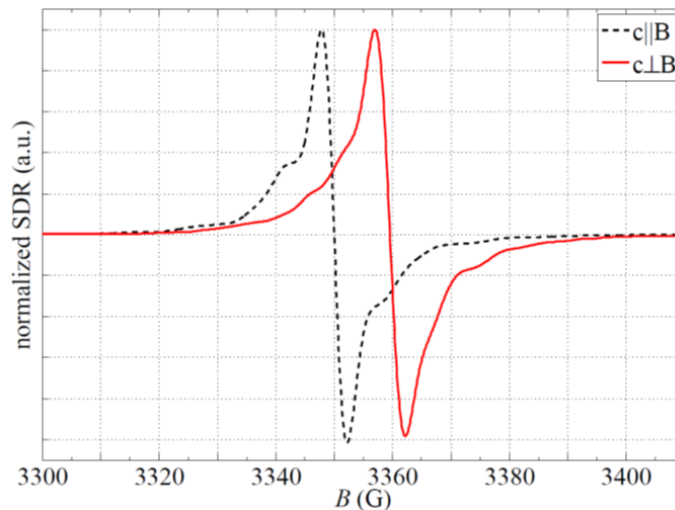


Figure 3.2. Experimental SDR result, the offset in the centre line between the parallel and perpendicular directions describes the degree of anisotropy between the principle axis.

### 3.5 Theoretical Results

As the defect of interest is only observed in N-implanted devices, therefore, the initial calculations are concerned with defects containing N either at a substitutional site or as a defect complex, these are  $N_C C_{Si}$ ,  $N_C V_{Si}$ ,  $N_{Si} V_C$ ,  $N_{Si}$ ,  $N_C$ , and  $N_i$ . [85], [86], [93], [101], [126], [127], [156], [158] These defects are considered in all of the accessible charge states and form the defect 'long list', these are then compared to the experimentally observed SDR signal described above. The general properties of which are discussed below, these were then assessed further on the basis of accessible paramagnetic gap states and formation energy, which leaves the defect 'short list' containing the lowest energy accessible paramagnetic states for each

distinct defect configuration. These states would be visible to SDR and should hence be investigated further.

### 3.5.1 Nitrogen Interstitial ( $N_i$ )

The N interstitial can exist in the split interstitial and puckered configuration just as observed with the  $C_i$ , the favoured conformation being determined by charge state.

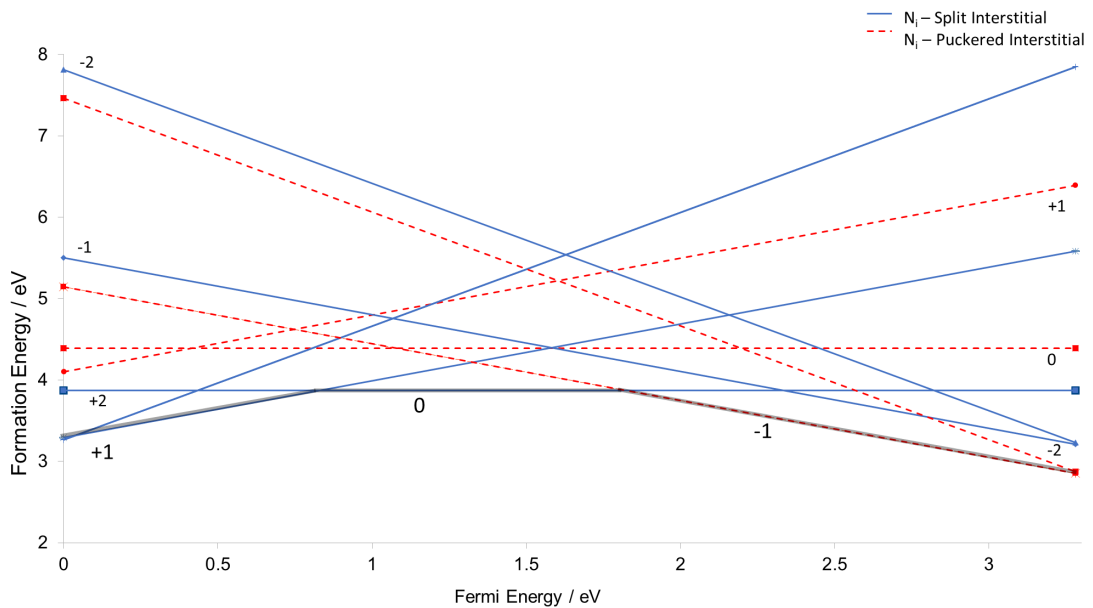


Figure 3.3. Combined formation energy plot for the puckered (dashed red line) and split (solid blue line) interstitial.

From Figure 3.3, it is clear that the N interstitial favours the split interstitial configuration from the VBM to approximately mid-gap, and for the remainder of the SiC bandgap the puckered configuration is favoured. In terms of charge transitions we see the +2/+1 transition at  $\sim 0.05$  eV, +1/0 at 0.8 eV and the 0/-1 at 1.75 eV (along with a change in configuration).

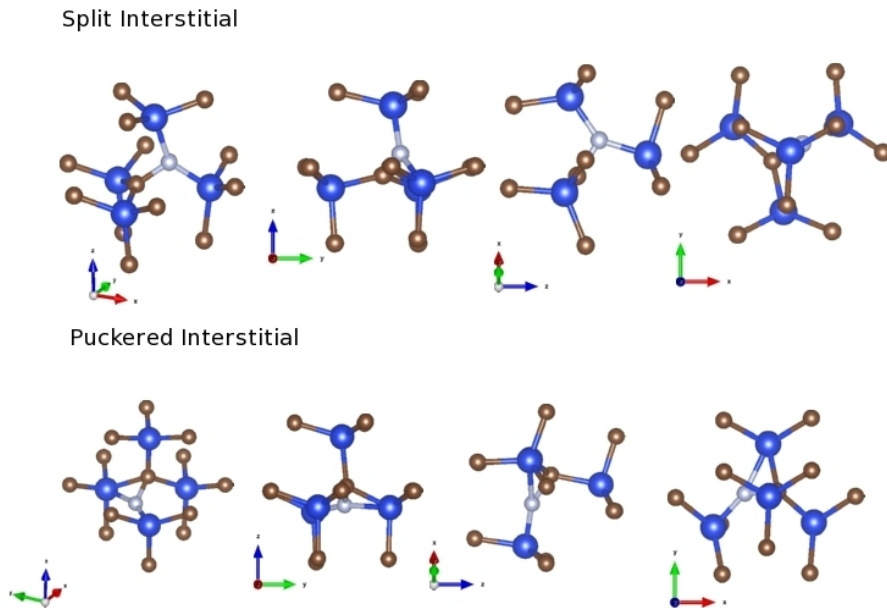


Figure 3.4. Representation of the split and puckered interstitial in the 0 and -1 charge states respectively. The blue is Si, brown is C and the white N. In each case on the left is a perspective view followed by the view along the x, y and z axis.

In the split interstitial in all charge states, the lattice site is shared between the N-C unit with each being bonded to two Si and each other. The bond length of the N-C unit is 1.30 Å, which is indicative of an  $sp^2$  bonding arrangement, N-Si bonds are 1.77 Å, which is in the range expected, as is the 1.83 Å of C-Si bond. There is an outwards distortion, as the N-C unit takes up more space than a single C atom. The bond length shifts, although small, an outward relaxation of the lattice that extends to the NN distance results. In the positive and neutral charge states, this arrangement is favoured. In the puckered interstitial, the N has moved down into the plane of the Si, in so doing the C is distorted as well, leading to a lengthening of one of the previously equal C-Si bonds. The N-C bond length is approximately consistent between the split and the puckered configuration 1.40 Å. Only the neutral charge state is paramagnetic

and would be visible to EDMR, and the unpaired electron is centred on the C atom, shown in Figure 3.5.

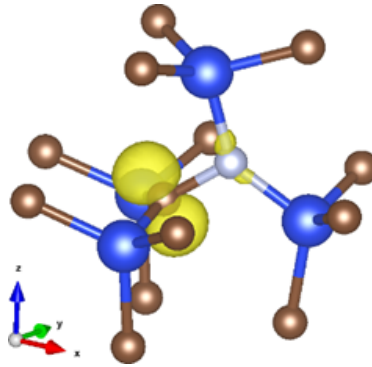


Figure 3.5. Spin density plot of the 0 charge state of the split interstitial, showing the majority of the spin centred upon the C atom.

### 3.5.2 Substitutional Nitrogen – $N_C$ and $N_{Si}$

The  $N_C$  is the target for N implantation with nitrogen sitting at the carbon site acting as an *n*-type dopant. As previously stated, the N is introduced *via* ion implantation with kinetic energies of the order of keV, which can conceivably displace both the intended C and the Si, as such both cases have been considered.

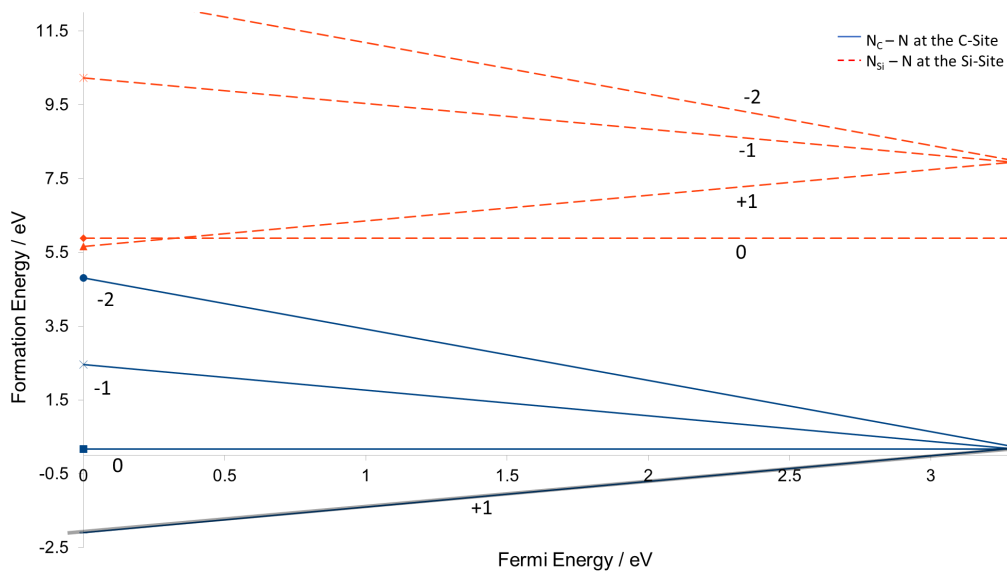


Figure 3.6. Formation Energy plot for the  $N_C$  and  $N_{Si}$  defects. The solid line showing the  $N_C$  defect and the dashed line the  $N_{Si}$ .

These defects have been widely studied and characterised with particular focus on the  $N_C$  shallow donor, the aim being to increase the dopant concentration. It is interesting to note that in the study of Bockstedte *et al* (2003), above a critical N concentration ( $c_s$ ) the concentration of the other defects shows a marked increase. In the high N concentration regime, the  $N_x$  ( $N_C$  pair) defect becomes favoured. These defects have been included here for completeness, as they are not expected to contribute to the observed EDMR signal. The justification for this is an absence of any localised gap states in required mid-gap region, which would not be visible to EDMR. In addition, the +1 charge state is favoured, which is not paramagnetic. The  $N_{Si}$  defect does have localised gap states shown in Figure 3.6, the unpaired electron being confined to the 3-coordinate C, with a small contribution from the N. This defect has been primarily discounted on the basis of formation energy required a precursor  $V_{Si}$  to form.

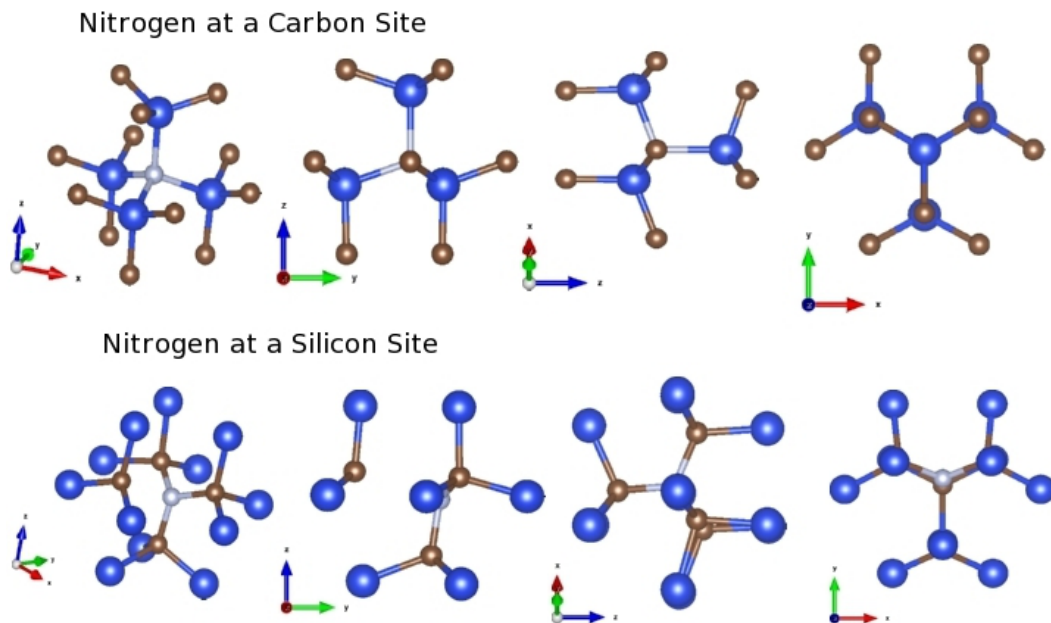


Figure 3.7. Geometry of the lowest energy charge states of the  $N_C$  and  $N_{Si}$  defects, +1 and neutral respectively. The blue is Si, brown is C and the white N. In each case on the left is a perspective view followed by the view along the x, y and z axis.



### Nitrogen Vacancy Complexes

Nitrogen can interact with either a pre-existing divacancy ( $V_C V_{Si}$ ) sitting either at the  $V_C$  or the  $V_{Si}$ , alternatively the N can substitute for one of the 3-coordinate vacancy atoms (Si or C).

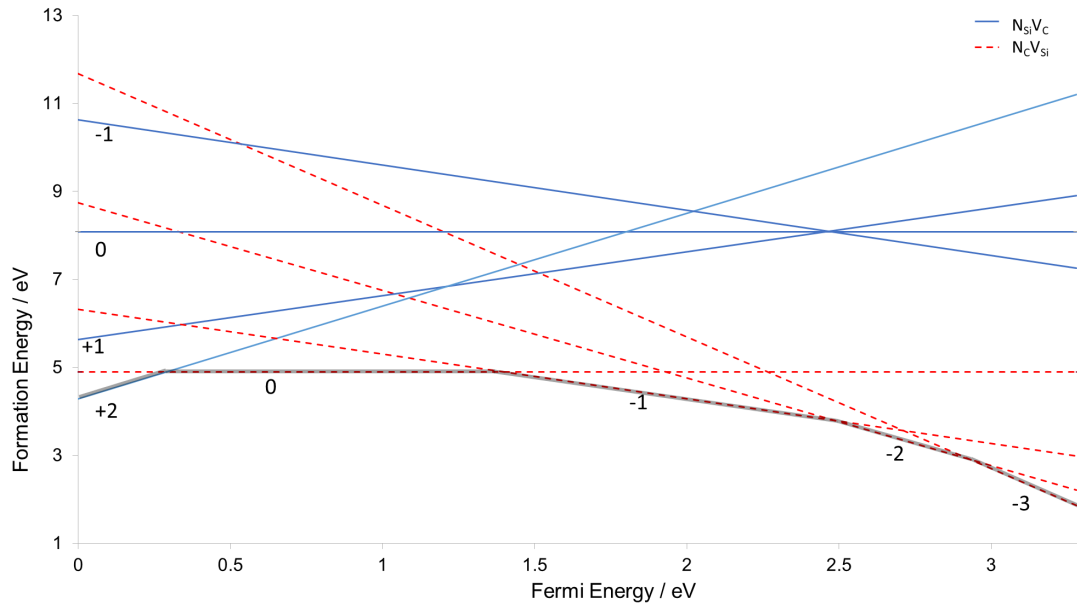


Figure 3.8. Combined formation energy plot for the  $N_C V_{Si}$  and the  $N_{Si} V_C$ . The red line corresponds to the  $N_C V_{Si}$  and the blue line to  $N_{Si} V_C$ .

In terms of the geometric arrangements of the two defect configurations shown in Figure 3.9, there are marked differences with the N being much more easily accommodated on the C site. This results in the N capping one of the 3-coordinate dangling bonds of the  $V_{Si}$ . The Si-N bond length is 1.79 Å and the N-C\* bond length is 1.75 Å. This similarity leads to little strain induced in the structure from the introduction of N at the C site. The bonding picture changes to a defect of  $C_{3v}$  symmetry with 3 carbon dangling bonds. The relaxation propagates in the same manner as the  $V_{Si}$  in the direction defined by the 3 carbon dangling bonds, with the bulk bond length being returned within  $\sim 7$  Å. In the N direction, the bulk SiC bond

length is reinstated after the next neighbour (NN) shell. The defect wave function is centred upon the 3-coordinate C, the tails of which propagate back as far as the NNNN neighbour shell. As there is little correlation between the three C\*, the doublet and quartet states are separated by only 0.08 eV.

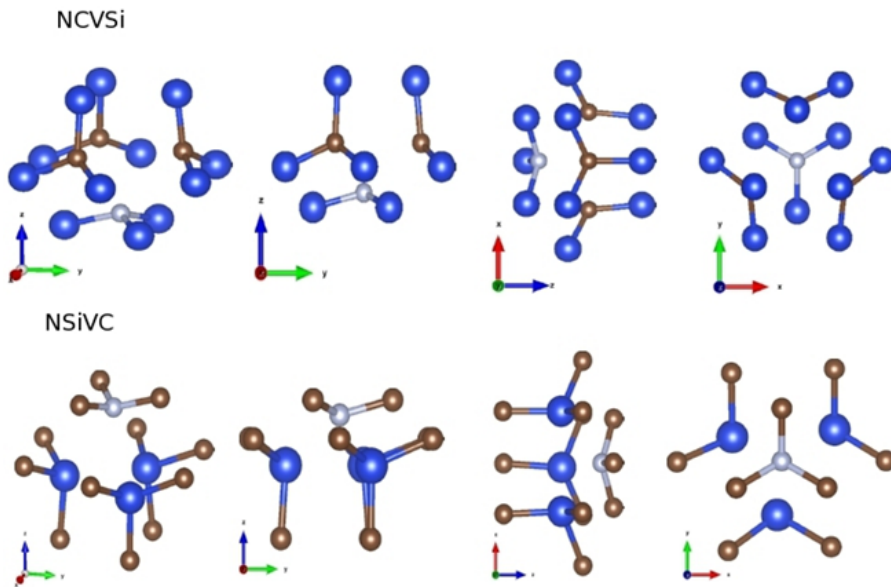


Figure 3.9. Configuration of the neutral  $N_C V_{Si}$  and the +2  $N_{Si} V_C$ . The blue is Si, brown is C and the white N. In each case on the left is a perspective view followed by the view along the x, y and z axis.

As the Fermi energy is increased towards the conduction band of SiC, gradually higher negative charge states become accessible, the 0/-1 transition at ~1.3 eV, -1/-2 at 1.8 eV and -2/-3 at 2.9 eV. This relates to each of the 3 carbon dangling bonds being converted to a carbanion. The even charge states are paramagnetic in the low spin state (doublet), the -1 charge state has a high spin (triplet) ground state. The result is that for the majority of the SiC bandgap the  $N_C V_{Si}$  defect is paramagnetic, and hence visible to EDMR. In the neutral charge state this gives a formation energy of +4.82 eV compared to the perfect bulk and -3.5 eV compared to the divacancy.

The  $N_{Si}V_C$  defect appears markedly different from the  $N_CV_{Si}$ , with the N-C bond being significantly shorter than the N-Si bond. Incorporating the N at the silicon site result in a significantly more distorted structure. The N is forced back into the plane of the C atoms, leading to a more planar arrangement than the  $N_CV_{Si}$  shown in Figure 3.10. This distortion of the N-C bond, leads to a repulsive interaction with the nitrogen lone pair, resulting in non-bonding N states within the SiC bandgap. This is in contrast to the  $V_C$  where the 3 coordinate Si are able to pair forming two long range Si-Si interactions. This is only possible for two of the 3-coordinate Si leaving one lone Si dangling bond in the neutral charge state. In the +2 charge state the spin density is centred on the N, the +1 charge state sees the ionisation of the Si dangling bond. This is shown in the spin density plot, Figure 3.10. The  $N_{Si}V_C$  is only favoured in the p-type regime close to the valence band (VB), with only the +2 charge state being accessible for 0.4 eV next to the VB. The neutral vacancy has a formation energy significantly higher than the  $N_CV_{Si}$  at 8.02 eV compared to the pure bulk, it is interesting to note, however, that the neutral charge state is -0.5 eV when compared to the divacancy. This raises the possibility that the  $N_{Si}V_C$  defect may be formed *via* implantation either directly in the +2 charge state or the neutral charge state is formed followed by a charge capture event.

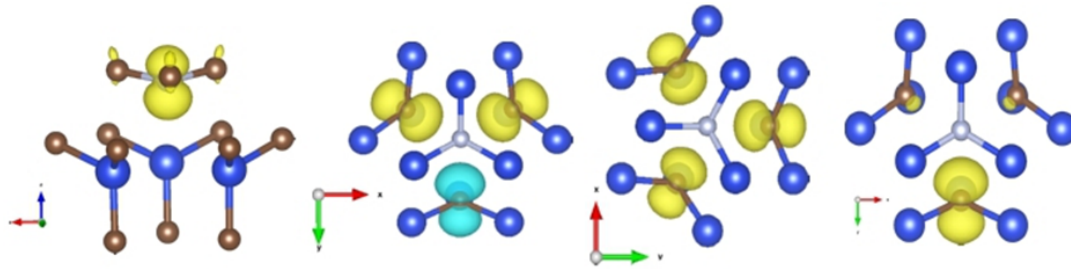


Figure 3.10. Spin density plot for the accessible paramagnetic states of the defect short list. From left to right; the  $N_{Si}V_C^{+2}$ , showing the spin density centred on the N, the  $N_CV_{Si}$  in the 0 and -1 charge state with the spin density distributed between 3  $sp^3$  hybridised C-dangling bonds, finally the  $N_CV_{Si}$  in the -2 charge state where there is only spin density on a single C-dangling bond.

### 3.5.3 $N_C C_{Si}$

From Figure 3.11 it is clear that the  $N_C C_{Si}$  has the +1-charge state favoured for the first half of the SiC bandgap until +1.6 eV where the neutral charge state is favoured. As with the previous defects where N sits at the C site, the N-C bond length is 1.78 Å and the N is accommodated with little distortion to the lattice. The C-C bond length is substantially shorter at 1.57 Å, leading to an inward relaxation of the neighbouring C atoms showing an extended distortion out to the NNN shell. This forms a near planar C radical with respect to the neighbouring C. In the neutral defect the unpaired electron sits on the 3 coordinate carbon within a p-type orbital. In the +1 charge state the unpaired electron is lost forming a planar carbocation, the +1 charge state is not paramagnetic, and as such would be invisible to EDMR.

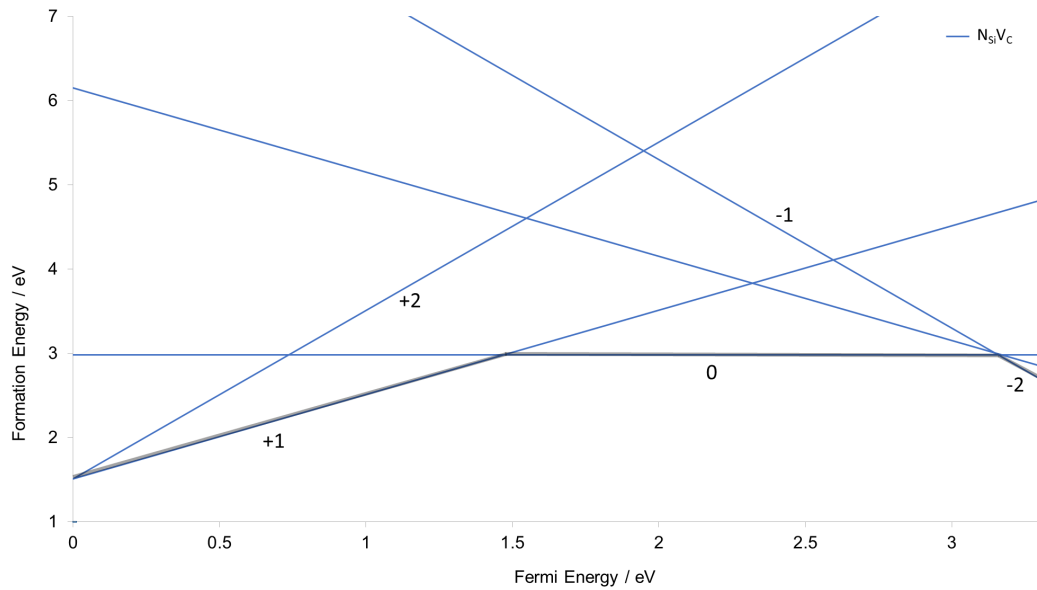


Figure 3.11. Formation energy plot for the  $C_{Si}N_C$  defect, illustrating the formation energy and most favourable charge state for a given Fermi level position.

This defect represents the local minimum on the N-defect potential energy surface, and has a formation energy  $\sim 1$  eV lower than any of the other defects examined in the neutral charge state. The only point to note is that for this defect to be present a high energy precursor state must be present ( $V_{Si}$ ).

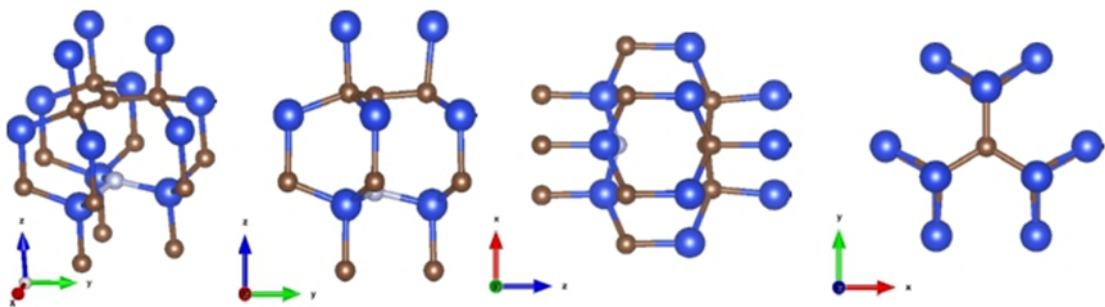


Figure 3.12. Configuration of the  $N_C C_{Si}$  in the neutral charge state. The blue is Si, brown is C and the white N. In each case on the left is a perspective view followed by the view along the x, y and z axis.

#### 3.5.4 Defect shortlist ( $N_C V_{Si}$ , $N_{Si} V_C$ and $N_C C_{Si}$ )

From the long list of N-containing defects the majority can be discounted on the basis of lack of accessible paramagnetic defect states. This leaves the shortlist of defects presented here that have the required paramagnetic states that would be visible to EDMR. The formation of these defects is easily within the energetic span provided by the implantation process and subsequent dopant activation anneal.

The  $N_C V_{Si}$  has gained a degree of recent attention from a quantum computing perspective. It has been proposed that the  $N_C V_{Si}^{-1}$  defect,[96], [98], [136] among some other point defects in SiC, has the potential to act as a qubit.[96]–[99], [119], [122], [218]–[220] These properties have been extensively catalogued and compared to the diamond NV centre, an existing qubit system.[96], [136], [218], [219], [221] Figure 3.13 shows the formation energies of the defects on the short list. The defect configurations are shown in Figure 3.14, Figure 3.15, and Figure 3.16 for the  $N_C V_{Si}$ ,  $N_{Si} V_C$ , and  $N_C C_{Si}$  defects, respectively. The  $N_C V_{Si}$ , and  $N_{Si} V_C$  are clearly related, whereas the  $N_C C_{Si}$  is very different, with a carbon antisite precursor being required.

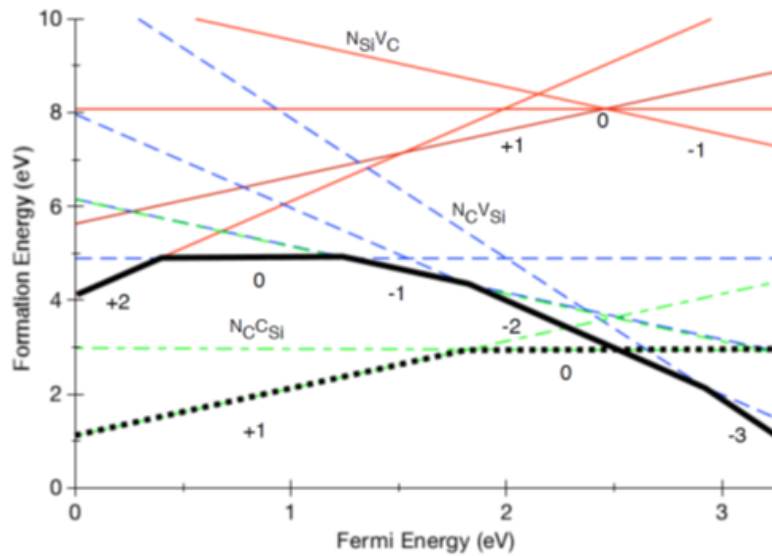


Figure 3.13. Combined formation energy plot showing the  $N_C C_{Si}$ ,  $N_C V_{Si}$  and the  $N_{Si} V_C$ . The lowest accessible charge states at a given Fermi level position are indicated by the bold lines (black).

#### 3.5.4.1 $N_C V_{Si}$

The  $N_C V_{Si}$  (Figure 3.14) is accessible in the 0, -1, and -2 charge states (Figure 3.13). The neutral charge state has a doublet ground state with a quartet state being only 0.10 eV higher in energy. The defect has  $C_{3v}$  symmetry with three  $sp^3$  hybridized carbon dangling bonds. The defect-induced lattice deformation propagates in the same manner as in the  $V_{Si}$  in the directions defined by the 3 carbon dangling bonds, with the bulk bond length being recovered within  $\approx 7 \text{ \AA}$ . As there is little correlation between the three carbon dangling bonds, the doublet and quartet states are separated by only 0.10 eV.

As defined above the  $N_C V_{Si}$  defect is paramagnetic and hence visible to SDR at most Fermi energy positions within the SiC band gap. However, for the -1 charge state a large zero-field splitting due to the electron-electron coupling has been reported.[100] The respective lines were not observed in the SDR measurements,

which seems to rule out this charge state. Additionally, the -2 charge state shows a significant directional dependence with the spin density centres on a single C-atom.

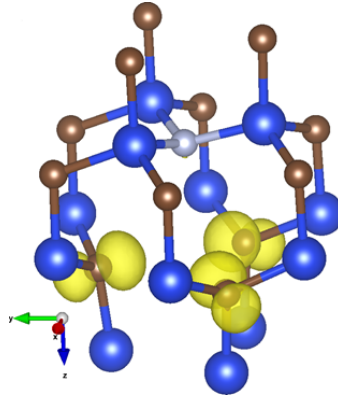


Figure 3.14. Spin density plot for the neutral charge state of the  $N_C V_{Si}$ .

#### 3.5.4.2 $N_{Si} V_C$

In the accessible +2 charge state, the spin density is centred almost entirely (>99%) on the N. The +1 charge state sees the ionization of the Si dangling bond. The  $N_{Si} V_C$  is only favoured in the heavily *p*-type regime close to the valence band (VB), with only the +2 charge state being accessible for 0.4 eV next to the VB. This defect is only accessible in a Fermi energy range next to the VB and would not be expected to be observable with SDR. In addition, when considering the symmetry of the defect over all sites ( $T_d$ ) it does not provide the required anisotropy. Therefore, it can be discarded as a potential candidate.



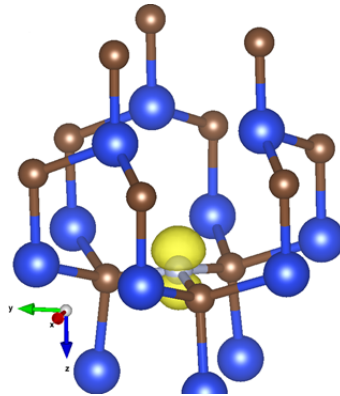


Figure 3.15. The spin density of the  $N_{Si}V_C$  in the +2 charge state.

### 3.5.4.3 $N_C C_{Si}$

For completeness  $N_C C_{Si}$  is considered representing the rearrangement of the silicon vacancy to form the vacancy antisite pair. In the neutral defect state, the unpaired electron sits on the 3 coordinate C within a p-type orbital. In the +1 charge state the unpaired electron is lost forming a planar carbocation, the +1 charge state is not paramagnetic and thus invisible to SDR.

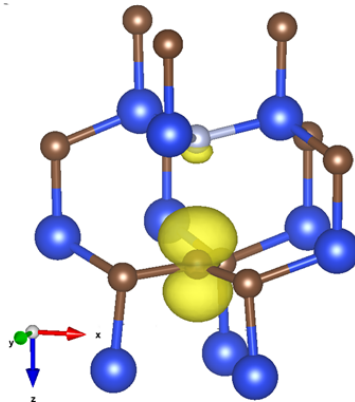


Figure 3.16. Spin density of the  $N_C C_{Si}$  in the neutral charge state.

Before considering the hyperfine parameters of shortlisted defects, we note that the symmetries of the defects discussed above seems to rule out both the  $N_C C_{Si}^0$  and  $N_{Si}V_C^{+2}$ . The experimentally observed defect shows a pronounced rotational

symmetry about the crystal c-axis along with an anisotropy with respect to the crystal c-axis. Both the  $N_C C_{Si}^0$  and the  $N_{Si} V_C^{+2}$  defects can be approximated by the  $C_\infty$  point group, but when considered in every possible orientation this gives a defect of  $T_d$  symmetry, which lacks the required anisotropy with respect to the c-direction.

### 3.6 Comparison Between Theory and Experiment

The HF parameters of the most reasonable defects complexes with their paramagnetic deep level charge states are shown in Table 3.1.

Table 3.1. Calculated HF splitting constants  $a_k$  for the most reasonable candidate defects in their different paramagnetic charge states. The values were calculated using the pcj-1 basis-set, with the HSE06 functional.  $a_{C1}$  refers to the equivalent atoms 1NN C shell,  $a_{Si2}$  to the 2NN Si shell, and  $a_{C3}$  to the 3NN C shell. The values are averaged for all atoms in the same shell.

Defect	$a_N$ (G)	$a_{C1}$ (G)	$a_{Si2}$ (G)	$a_{C3}$ (G)
$N_C V_{Si}^0$	0.8	39.9	10.7	6.7
$N_C V_{Si}^{-1}$	1.0	45.6	8.9	4.6
$N_C V_{Si}^{-2}$	0.8	46.7	9.2	6.1
$N_C C_{Si}^0$	11.2	39.9	10.7	6.7

This table only contains averaged values for the equivalent atoms that have significant HF splitting constants. However, they can be used to create an accurately simulated spectrum according to equation 3.1 in order to compare theory to experiment. Figure 3.17 shows the simulated spectra compared to the experimental spectrum.

It is quite clear that the  $N_C V_{Si}$  defect, especially in the neutral charge state, is a much better candidate than the  $N_C C_{Si}$ . The  $N_C C_{Si}$  centre does not closely match the experimental spectrum. This simulation was performed with averaged,  $a_k$ , values including the errors outlined above. The pronounced 1:1:1 triplet of this defect is ruled out as a candidate defect, leaving the  $N_C V_{Si}$  in its different charge states as the only candidate.

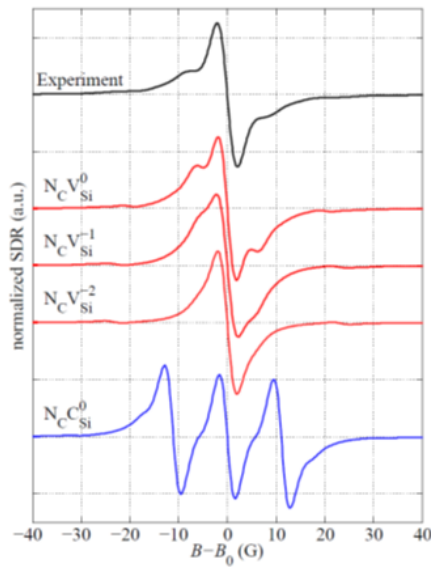


Figure 3.17. Simple comparison of the experimental and theoretical hyperfine parameters for the shortlisted defects.

The  $N_C V_{Si}^0$  shows the best agreement between theory and experiment as it is the only one with pronounced Si side shoulders. For this reason, a more detailed theoretical treatment of this charge state has been performed. An important point that has been left out so far is the fact that the N atom can sit in four different sites with respect to the  $V_{Si}$ . Additionally, the  $V_{Si}$  can sit in a quasi-cubic (k) or quasi-hexagonal (h) site. Therefore, a total of four different configurations (kk, kh<sub>1,2,3</sub>, hh, hk<sub>1,2,3</sub>) are possible, each with a slightly different formation energy and electronic structure. In order to improve the simulation of the resulting spectrum each of the eight defect configurations was calculated separately. The resulting  $a_k$  values for every atom of every configuration were used explicitly in the simulations of the spectra, rather than their average values. All of this data can be found in Appendix A. The eight resulting spectra have been simulated and added together. Their individual contributions were weighted with their respective Boltzmann factors corresponding to their formation

energies. The resulting complete spectrum is compared to the experimental spectrum in Figure 3.18.

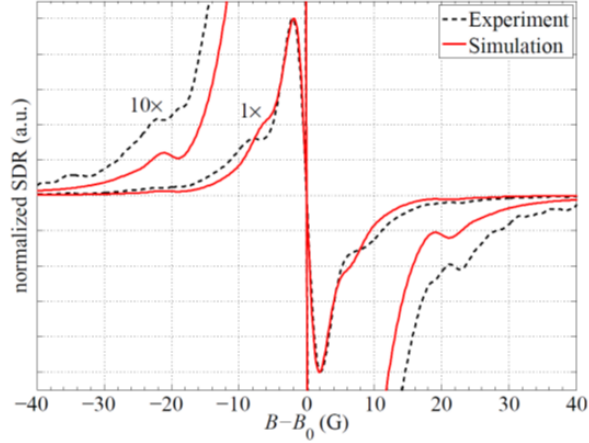


Figure 3.18. Comparison between the  $N_C V_{Si}^0$  calculated spectra and the experimental spectra. In the hh configuration.

The  $\pm 21$  G lines are very well matched by the three 1NN C atoms while their  $a_k$  values are marginally underestimated. The  $\pm 13$  G lines are well represented by the 2NN Si atoms, especially in terms of their relative intensity. However, the  $a_k$  values fall  $\pm 2.5$  G short. The calibration tests illustrated that the pcj-1 basis set used to calculate the  $a_k$  value has an error of  $\approx 3$  G.

In the case of the calibration calculations it was clear that an improved description of the HF parameters could be obtained with the pcj-2/3 basis-sets. In order to demonstrate the basis-set effect, which is observed in the calibration set, the  $N_C V_{Si}^0$  was calculated with the pcj-3 basis-set. This in effect shrinks the discrepancy between the simulated and experimental measurements. As these calculations are very time intensive, they could not be performed on all eight sites. Only the ground state (hh) site of the  $N_C V_{Si}^0$  was calculated for comparison and the difference between pcj-1 and pcj-3 was gauged. This gives confidence that the trends suggested by the

calibration set are observed, and falls well within the defined error for a given basis-set. The result is a defect with identical symmetry but with the 1NN C and 2NN Si HF splitting increased by  $\approx 2.5$  G. Adding this shift to the  $a_k$  of all sites results in the improved simulated spectrum shown in Figure 3.19 which demonstrates an excellent match between theory and experiment.

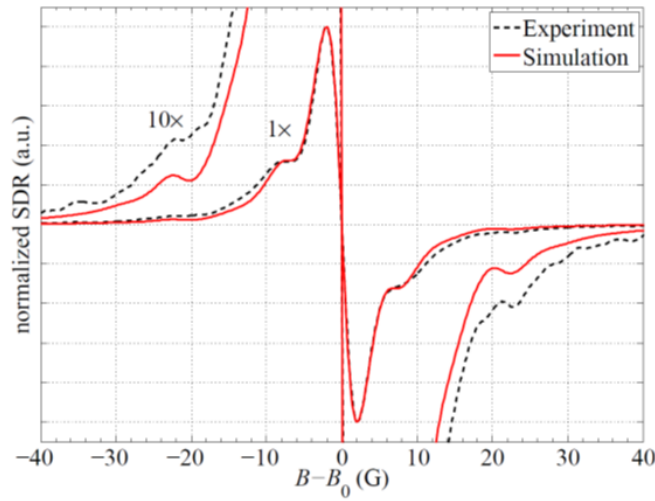


Figure 3.19. Improved spectra calculated using the larger pcj-3 basis set and implicit treatment of the 4 distinct defect configurations (hh, kk, hk, and kh).

In a very recent study of N-implanted SiC, the  $N_C V_{Si}^{-1}$  defect was identified using EPR measurements and theoretical modelling.[136] In agreement with this study, we show that this defect has smaller Si HF splitting than the  $N_C V_{Si}^0$ . The large zero-field splitting observed by Bardeleben *et al.* was not observed.[100]

### 3.7 Conclusion

We combined SDR measurements with extensive DFT calculations to identify the best candidate of an unknown defect in a 4H-SiC *pn*-junction which was formed by heavy N implantation (doping of  $5 \times 10^{17} \text{ cm}^{-3}$ ) and an Al implantation of a similar dose. SDR measurements were used to identify a 'fingerprint' of the defect of interest, guiding

DFT calculations. From the long list of defects, the selection was narrowed down on the basis of accessible paramagnetic states, formation energy, symmetry, and hyperfine parameters.

Starting from a list of nitrogen-containing defects in 4H-SiC,  $N_C C_{Si}$ ,  $N_C V_{Si}$ ,  $N_{Si} V_C$ ,  $N_C N_{Si}$ , and  $N_i$ ; it was possible to identify  $N_C V_{Si}$  as the dominant defect measured by SDR in N-implanted SiC. This defect comes in eight conformations, which all can exist in 3 charge states. The electron densities of the unpaired electron for these 24 cases were calculated and further the hyperfine coupling constants were determined. This made it possible to compute the hyperfine structure of the defects. While billions of lines contribute to the hyperfine structure, it was possible to sort out the few thousand lines that make the most important contribution on the basis of their respective probabilities. The observed anisotropy of the SDR spectrum describes a defect which is rotationally symmetric around the crystal  $c$ -axis and anisotropic with respect to the  $c$ -direction. This is reproduced in the  $C_{3v}$  symmetry of the calculated  $N_C V_{Si}$  defect. Therefore, we conclude that the  $N_C V_{Si}^0$  centre is the defect responsible for the observed SDR spectrum.

Although the  $N_C V_{Si}$  is identified as one of the deep-level defects responsible for dopant deactivation, this does not exclude the existence of other diamagnetic defects that may also be responsible for dopant deactivation. The next chapter looks at the process of nitrogen and defect diffusion in more detail.

# Chapter 4

## Defect Diffusion During the Annealing of N-implanted 4H-SiC

---

### Abstract

Annealing of defects resulting from nitrogen implantation of SiC-based devices has long been a topic of interest and relevance for device regions that require high nitrogen concentration, such as the source-drain region of MOSFETs or the cathode of diodes. In chapter 3, a combination of EDMR measurements and *ab initio* simulations were employed to identify a  $N_C V_{Si}^0$  centre in fully processed devices that have undergone various post-implantation anneals. In this chapter, the kinetic basis for the absence of the  $N_C C_{Si}$  centre is illustrated. This is predicted to be a much more thermodynamically stable defect than the  $N_C V_{Si}^0$  centre, which is not observed in EPR or EDMR measurements. Previous calculations ascribe a distinct 1:1:1 triplet with a hyperfine splitting of 11 G to the  $N_C C_{Si}$ . To explore this observation, the mechanisms of  $N_i$  and  $C_i$  diffusion are studied, along with an extensive study of the defect-interstitial interactions in 4H-SiC. The predicted energy barriers for the bulk diffusion of  $N_i$  and  $C_i$  of 2.6 eV and 2.9 eV, respectively, and the associated diffusion coefficients show that they have limited mobility even during the high temperature anneal. Despite the low barriers for the transformation of the  $N_C V_{Si}$  into  $N_C C_{Si}$ , the need for a defined precursor coupled to the limited mobility of  $N_i$  and  $C_i$  hinders the transformation

process. This mechanistic picture shows categorically why  $N_C V_{Si}$  is observed when the lower energy  $N_C C_{Si}$  is not. Knowledge of persistent defects, and the processes by which they form, are of vital importance in developing more efficient annealing regimes.

## **4.1 Introduction**

Identifying defects in semiconductor devices and the mechanisms by which they form is of key importance for optimizing device performance. To form n-doped regions, N is incorporated in 4H-SiC by ion implantation, and substitutes preferentially at the carbon site, rather than the silicon site.[18], [126], [158], [220] This is described in detail in chapter 1.5. Implantation is, however, a highly destructive process, involving high kinetic energies leading to a significant amount of lattice damage, which in turn results in the formation of many defects, such as those described in chapters 1 and 3. A high temperature dopant activation anneal is typically employed with the dual purpose of 'healing' lattice damage and moving interstitial N from interstitial positions to the C-lattice sites. A schematic overview of how the process is envisaged to occur is given in Figure 4.1. Implantation generates a large number of defects, which are then annealed out to give relatively few stable defects that persist in devices.



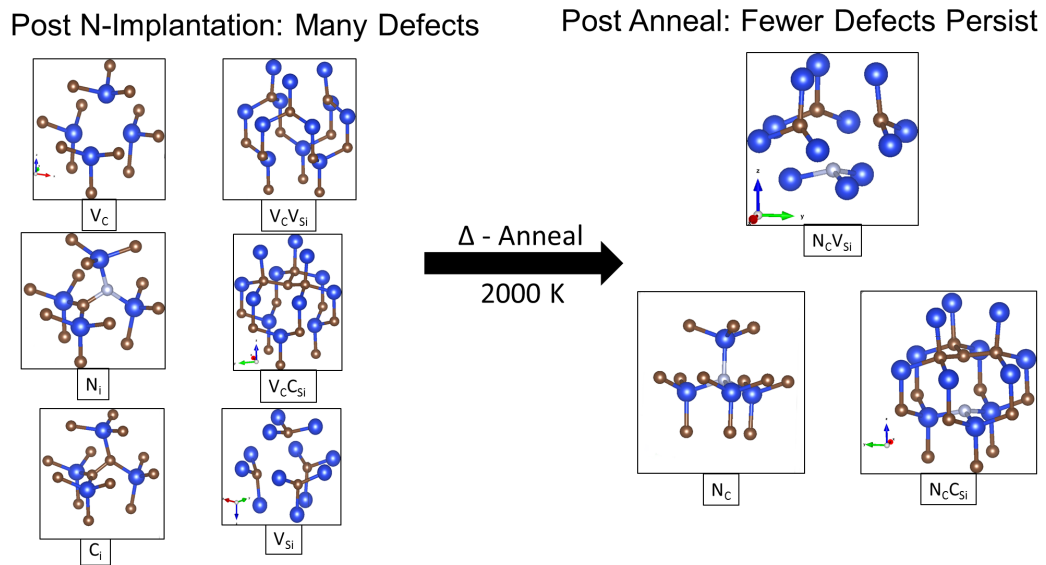


Figure 4.1. Schematic view of implantation and anneal, giving an overview of the defects that can be envisaged as being created during implantation. The processing runs from left to right, starting from defect free stoichiometric 4H-SiC. After implantation, a large number of defects are formed including, but not limited to, the above. Finally, after annealing these defects combine, or rearrange to give the defects observed in the processed devices. C-Brown, Si-Blue, N-White.

These defects are typically experimentally observed using DLTS, EPR, and EDMR. EPR measurements offer an insight into the structure and atomistic makeup of the defect of interest. EDMR offers the prospect of single defect selectivity, which has always hampered EPR studies in samples with a high number of defects, such as post implantation. EDMR provides the additional benefit of being performed on fully processed devices, so no special sample preparation is required and therefore cannot be responsible for the defects observed. This faculty has been used to achieve atomistic defect identification by Cochrane *et al.*[145], Tuttle *et al.*[128] and more recently by Cottom *et al.*[28], [29] using the combination of theoretical calculations and EDMR measurements.

Previous theoretical studies of SiC have focused on the mechanisms of interstitial and vacancy diffusion. This has been used as a means of explaining, or predicting, interstitial clustering, vacancy clustering, and dopant deactivation. These studies have outlined a number of mechanisms including, but not limited to, interstitial diffusion *via* either next neighbour or neighbour hops.[115], [126], [127], [222] In addition, the migration and clustering of vacancies have been a focus of study, with direct (next neighbour hopping) and an antisite mechanisms being proposed.[115], [127] Consistent with other covalent systems, the barriers for vacancy diffusion are higher than those observed for the interstitial migration for a given Fermi level position. Rauls *et al.* found a carbon interstitial diffusion barrier of 2.6 eV, while the lowest vacancy migration barrier was 3.2 eV.[127], [222]–[224] The picture is complicated by the particularly strong binding energies for both interstitials and vacancies, which has led to the suggestion that these structures accumulate during the anneal. As a result, various cluster models have been proposed to explain the defects observed by a variety of experimental techniques. However, linking these structures to the experimental observations remains a challenge.[115], [140], [225], [226]

Theoretical and experimental investigations have shown that nitrogen is able to interact with silicon vacancies ( $V_{Si}$ ), carbon vacancies ( $V_C$ ), divacancies ( $V_C V_{Si}$ ), and vacancy clusters to form either  $N_C V_{Si}$  or  $N_{Si} V_C$ . The fully passivated  $(N_C)_4 V_{Si}$  defect, which is also electrically passive, has been suggested as a candidate for dopant deactivation.[126] Identification of the shallow  $N_C$  dopants[93], [132], [134], is widely accepted along with the  $N_x$  centre.[93], [134], [135] A recent study using a combination of *ab initio* calculations and EDMR measurements identified the  $N_C V_{Si}^0$  as discussed in chapter 3, with the  $N_C V_{Si}^{-1}$  being identified in specially prepared

samples after optical excitation.[100] These defects are created as a result of defect diffusion and reactions during anneal. However, why some defects persist in processed devices and some others do not is still unclear. In particular, why the  $N_C V_{Si}$  defect is observed and the lower energy  $N_C C_{Si}$  defect is not formed in any significant concentration remains a mystery.[28], [126], [127] From a thermodynamic perspective the opposite would be expected, with a large population of  $N_C C_{Si}$  with respect to  $N_C V_{Si}$ . This is in accordance with the previous literature where the  $N_C C_{Si}$  is demonstrated to have a substantial binding energy, while being significantly lower in energy than either the  $N_C V_{Si}$  or the  $C_{Si} V_C$ , which are the suggested precursors.[85], [126]

In this chapter, the picture described in chapter 3 is developed to examine how the  $N_C V_{Si}$  may be formed, diffuse, and interact. Building upon the previous work outlined above, the defect geometries, barriers for their diffusion, and transformation are calculated using a hybrid DFT functional, HSE06, in large supercells. The starting point is the previously identified  $N_C V_{Si}$  defect, along with a number of intrinsic and extrinsic defect complexes that are envisaged to result from implantation. These defects are then linked *via* an interstitial diffusion mechanism to probe the barriers for inter-conversion. This is shown schematically in Figure 4.1, where the system is envisaged to start (pre-implantation) as defect free 4H-SiC. After implantation, a large number of defects are formed, which then anneal to give the surviving defects observed by EPR/EDMR. This chapter builds a picture of defect evolution during annealing, deriving a mechanistic picture for the formation of the observed  $N_C V_{Si}$ , when the related and more thermodynamically stable  $N_C C_{Si}$  is not.[28], [126], [130]

## 4.2 Methodology

The DFT calculations were performed using the CP2K code, and the PBE and HSE06 density functionals. Due to the computational cost associated with non-local HSE06 functional calculations the auxiliary density matrix approximation (ADMM) was employed, as it offers a significant time saving. These functionals were used with the DZVP-MOLOPT-SR-GTH and the TZVP-MOLOPT-GTH basis-sets and the GTH-pseudopotential. This led to the selection of a 5 x 3 x 2 orthorhombic 4H-SiC supercell (480 atoms: 15 Å x 16 Å x 20 Å). The converged plane wave cut-off was set to 600 Ry. All geometry optimizations were performed using the Broyden-Fletcher-Goldfarb-Shanno (BFGS) optimizer. This formed the basis for all calculations in this chapter, allowing for the defect relaxation to be contained within the simulation supercell. All defect characteristics were converged to 0.01 meV per formula unit (Appendix C).

The adiabatic transition barriers were calculated using the climbing-image nudged-elastic-band (CI-NEB) method, with 10 images along the band. The images were generated by a linear interpolation between the initial and final states in the first instance. It was found that employing a pre-optimization with the PBE functional reduced the required number of optimization steps needed to converge the subsequent HSE06 structure. This offered a substantial saving of computational time, and was employed in all of the defect calculations.

The choice of chemical potential requires careful consideration as it will have a marked effect on the results obtained. Conceptually, it is related to the growth conditions, which in the case of 4H-SiC can range from silicon rich to carbon rich, with the extreme limits being taken from cubic silicon and diamond, respectively, ( $\mu_{Si} \leq \mu_{Si}^{Bulk}$ ,  $\mu_C \leq \mu_C^{Bulk}$ ). As the values of  $\mu_{Si}$  and  $\mu_C$  cannot be exactly determined, they can

only be described in terms of  $\mu_{SiC} = \mu_{Si} + \mu_C$ ,  $\mu_{SiC}$  is the energy per formula unit (SiC), which allows a range of chemical potentials to be described from Si-rich to C-rich within the limits defined above. This is in accordance with the method described by Torpo *et al.*[83] Additionally,  $\frac{1}{2}$  of an N<sub>2</sub> molecule DFT total energy is used for the  $\mu_N$ .

In the case of growth, the importance of chemical potential is clear, and the variation between the defined limits can be seen as making various defects more or less favoured dependent upon the prevailing conditions. For instance, the carbon vacancy (V<sub>C</sub>) defect has a higher formation energy at the C-rich limit (Table 4.1). In the case of equilibrium processes, the implications of the above are well defined. However, when considering non-equilibrium processes, such as implantation, the picture is more complex. In this case, as the nitrogen is introduced by implantation, the consideration of various N-partial pressures is inappropriate and as such  $\mu_N$  is fixed. It is assumed that the pre-implantation starting material is stoichiometric and no material is lost during the implantation. Therefore, the stoichiometric ( $\Delta\mu=0$ ) values of the formation energy are reported and discussed, with an illustration of the effect of variations in chemical potential being included for completeness only (Table 4.1).

Finite size charge corrections are applied according to the scheme of Lany and Zunger (equation 2.33), with consideration of the non-cubic nature of the supercell using the methodology of Murphy and Dines. From the above, the 0 K formation energies are calculated. The defect formation energy (equation 2.31) approach presented in section 2.2.4.1 neglects the temperature ( $T$ ) dependent portion of the free energy of formation ( $\Omega_f = E_f - TS$ ), which includes phonon effects. However, at temperatures above 0 K the Gibbs free energy is required,

$$\Omega_f = E_f + U_{vib} - TS, \quad (4.1)$$

where  $U_{vib}$  is vibrational energy, and  $T$  is temperature. For most cases, the 0 K approximation is sufficient, however, as the dopant activation anneal is a high temperature process ( $T > 2000$  K), these effects can no longer be neglected and may reasonably be expected to have a meaningful impact on both the accessible vibrational modes, and by extension the entropy.

The vibrational entropy is calculated following the method described in the work of Scheffler and Dabrowski,[227] then applied to SiC in the work of Rauls *et al.*[115]  $U_{vib}$  is calculated using

$$U_{vib} = k_B \sum_{i=1}^{3N} \left\{ \frac{\hbar\omega_i}{\exp(\hbar\omega_i/k_B T) - 1} + \frac{1}{2} \right\} \hbar\omega_i. \quad (4.2)$$

By extension the vibrational entropy  $S_{vib}$  can be derived from the expression of  $U_{vib}$  equation 4.2, giving

$$S_{vib} = k_B \sum_{i=1}^{3N} \left\{ \frac{\hbar\omega_i}{k_B T} \left[ \exp\left(\frac{\hbar\omega_i}{k_B T}\right) - 1 \right]^{-1} - \ln \left[ 1 - \exp\left(\frac{-\hbar\omega_i}{k_B T}\right) \right] \right\}. \quad (4.3)$$

To allow  $U_{vib}$  and  $S_{vib}$  to be calculated, the vibrational spectra of all stationary points and transition states need to be calculated. These calculations were conducted using CP2K until all of the vibrational modes are converged. This gives a series of vibrational frequencies ( $\omega_i$ ), which can be substituted into the above equations 4.2 and 4.3. Following this procedure, the Gibbs free energies can be calculated by substituting the values of  $S$  and  $U$  obtained in each case into equation 4.1.

To discuss the diffusion behaviour of the defects, the diffusion coefficients are calculated from the minima, and connecting transition states, using the Arrhenius relationship

$$D = D_0 \exp\left(\frac{-E_a}{k_B T}\right), \quad (4.4)$$

where  $D$  is the diffusion coefficient,  $D_0$  is the maximum diffusion coefficient (infinite  $T$ ), and  $E_a$  is the energy barrier.  $D_0$  is obtained using

$$D_0 = \frac{d^2 \omega}{2} p \exp\left(\frac{\Delta S}{k_B}\right), \quad (4.5)$$

in this case,  $\Delta S$  is the entropic difference between the start and the transition state,  $p$  is the probability of finding a vacancy or interstitial at the neighbouring site (for direct diffusion  $p=1$ ),  $d$  is the distance between the initial and final structures, and  $\omega$  is the attempt frequency, which by convention is approximated by the Debye frequency ( $\omega_{D_{SiC}} = 1.6 \times 10^{13} \text{ s}^{-1}$ ). [115]

## 4.3 Results

### 4.3.1 Defect Formation Energies

Initially, the various intrinsic and extrinsic defects that have been observed experimentally, postulated theoretically, or identified through a combination of the two, are considered. In addition, a number of potential defects have been included for completeness, although this is not to suggest that they persist in the device. The defects considered are  $C_i$ ,  $N_i$ ,  $C_{Si}$ ,  $N_{Si}$ ,  $N_C$ ,  $V_C$ ,  $V_{Si}$ ,  $V_C V_{Si}$ ,  $N_C C_{Si}$ ,  $N_C N_{Si}$ ,  $N_{Si} V_C$ , and  $N_C V_{Si}$ .

Table 4.1. Formation energies for the listed defects in the neutral charge state. Where appropriate, the effect of chemical potential is illustrated from C-Rich to Si-Rich.

Defect	Formation Energy / eV (C-Rich, $\Delta\mu=-\Delta H$ )	Formation Energy / eV ( $\Delta\mu=0$ )	Formation Energy / eV (Si-Rich, $\Delta\mu=\Delta H$ )
$N_C V_{Si}$	-	4.9	-
$N_{Si} V_C$	-	7.8	-
$N_C N_{Si}$	-	3.9	-
$N_C C_{Si}$	2.6	2.9	3.2
$V_C C_{Si}$	6.9	7.2	7.5
$V_C V_{Si}$	-	7.8	-
$V_{Si}$	7.8	8.1	8.4
$V_C$	4.4	4.1	3.8
$N_{Si}$	5.3	5.6	5.9
$C_{Si}$	2.9	3.6	4.2
$N_i(NC)$	-	3.8	-
$C_i(CC)$	5.3	5.6	5.9

The defect formation energies referenced to the defect free bulk (Table 4.1) demonstrate a wide range of values ranging from 3-8 eV. The highest energy configurations relate to the Si-based defects, which have been studied extensively.[58], [101], [115], [124], [126], [158], [228] They are provided for completeness and comparison with the results of the previous work.[93], [115], [127], [158] It is important to reiterate at this stage that the formation energy picture assumes that the system has reached thermodynamic equilibrium, which in the case of implantation damage is far from assured. Complementary to Table 4.1, which compares the neutral charge states, a plot of the formation energies as a function of Fermi level position is shown in Figure 4.2.



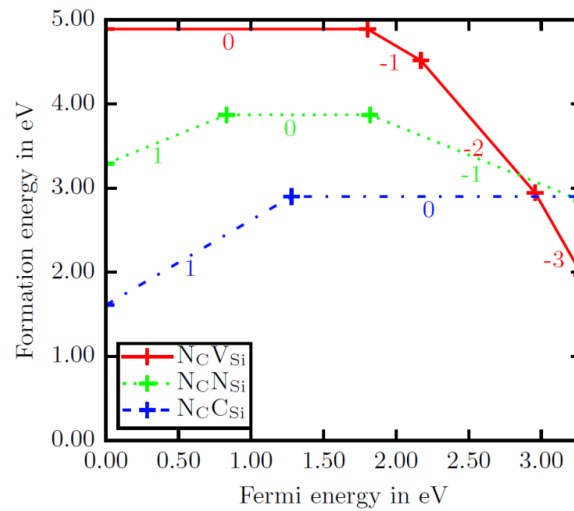


Figure 4.2. Formation energies as a function of Fermi level position for the main defects of interest.

Figure 4.2 shows the formation energies as a function of the Fermi energy position for the  $N_C V_{Si}$ ,  $N_C N_{Si}$ , and the  $N_C C_{Si}$  defects, giving an insight into the charge state that is most favoured in a given region of the band gap. The  $N_C C_{Si}$  and the  $N_C N_{Si}$  defects are of particular interest, as they provide an important reference with which to compare the N defects. Both defects can be viewed as being related to the identified  $N_C V_{Si}$ , with either the C or the N sitting at the silicon vacancy site. The defects favour the +1 charge state from the VBM to +1.0 eV ( $N_C N_{Si}$ ), and +1.35 eV ( $N_C C_{Si}$ ), at which point the neutral charge state is favoured for the rest of the 4H-SiC band gap for the  $N_C C_{Si}$ . Above +2.0 eV, the  $N_C N_{Si}$  is most stable in the -1 charge state. The  $N_C C_{Si}$  defect is paramagnetic in the neutral and even charge states, while the  $N_C N_{Si}$  defect is paramagnetic in the odd charge states. At this stage, it should be observed that in the band gap window of interest, the  $N_C N_{Si}$  would be diamagnetic and hence not be expected to be observed *via* EPR / EDMR.[28], [130]

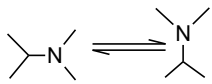
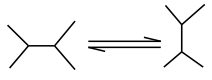
The results presented above clearly beg the question as to why the  $N_C C_{Si}$  defect, which has the formation energy approximately 2 eV lower than the identified  $N_C V_{Si}$  defect, is not observed in any of the EPR/EDMR measurements in spite of

having paramagnetic states resonant with the device Fermi level. The answer lays in the mechanism of formation of these defects discussed below.

### 4.3.2 Energy Barriers

The energy barriers for the reactions outlined in Table 4.2 are calculated using the approach outlined in section 4.2, NEB calculations for each of the relevant configurations were conducted with the lowest energy in each case being recorded in Table 4.2. These values are then used to calculate the Gibbs free energy in each case.

Table 4.2. Table of activation barriers for the defect rearrangements, rotations, combinations and bulk diffusion. The 0 K energy barrier is compared to the 2000 K Gibbs free energy for each of the reaction pathways of interest.

Reaction	Activation Energy / eV	Gibbs Free Energy (2000 K) / eV
1. N <sub>i</sub> to next site	2.6	2.1
2. N <sub>i</sub> rotated	0.5	0.4
		
3. C <sub>i</sub> to next site	3.0	2.5
4. C <sub>i</sub> rotated	0.6	0.5
		
5. V <sub>Si</sub> → C <sub>Si</sub> V <sub>C</sub>	1.6	1.4
6. C <sub>i</sub> + N <sub>C</sub> V <sub>Si</sub> → N <sub>C</sub> C <sub>Si</sub>	0.4	0.35
8. C <sub>i</sub> + V <sub>C</sub> V <sub>Si</sub> → V <sub>Si</sub>	0.7	0.65
9. N <sub>i</sub> + V <sub>C</sub> V <sub>Si</sub> → N <sub>Si</sub> V <sub>C</sub>	0.9	0.8
10. N <sub>i</sub> + V <sub>C</sub> V <sub>Si</sub> → N <sub>C</sub> V <sub>Si</sub>	0.6	0.5
11. N <sub>i</sub> + V <sub>Si</sub> → N <sub>Si</sub>	0.5	0.4
12. C <sub>i</sub> + N <sub>C</sub> V <sub>Si</sub> → N <sub>C</sub> C <sub>Si</sub>	0.6	0.65
13. N <sub>i</sub> + N <sub>C</sub> V <sub>Si</sub> → N <sub>C</sub> N <sub>Si</sub>	0.9	0.85
14. N <sub>C</sub> V <sub>Si</sub> → N <sub>Si</sub> V <sub>C</sub>	4.5	4.1
15. N <sub>Si</sub> V <sub>C</sub> → N <sub>C</sub> V <sub>Si</sub>	1.2	0.8

The reaction pathways considered have been limited to those that directly link to interstitial migration and the interaction between interstitials and the  $N_C V_{Si}$ . This still provides a great many possibilities. The simplified starting point developed here assumes that, as a result of implantation, a series of vacancies and interstitials are created, as shown schematically in Figure 4.1. Then during the anneal they go on to form various combinations. In particular,  $N_C V_{Si}$  can be viewed as forming *via* the following mechanism:  $N_i + V_C V_{Si} \rightarrow N_C V_{Si}$  or *via*  $N_i + V_C V_{Si} \rightarrow N_{Si} V_C$ , followed by  $N_{Si} V_C \rightarrow N_C V_{Si}$ , assuming the interstitial is in the neighbouring site to the vacancy. Either pathway results in the formation of the  $N_C V_{Si}$ . To consider the vacancy interstitial behaviour as well as the bulk diffusion, a series of barriers were calculated, as outlined in Table 4.2. The range of energy barriers covered is extensive, from the easily accessible (0.4 eV) to the inaccessible (4.5 eV).

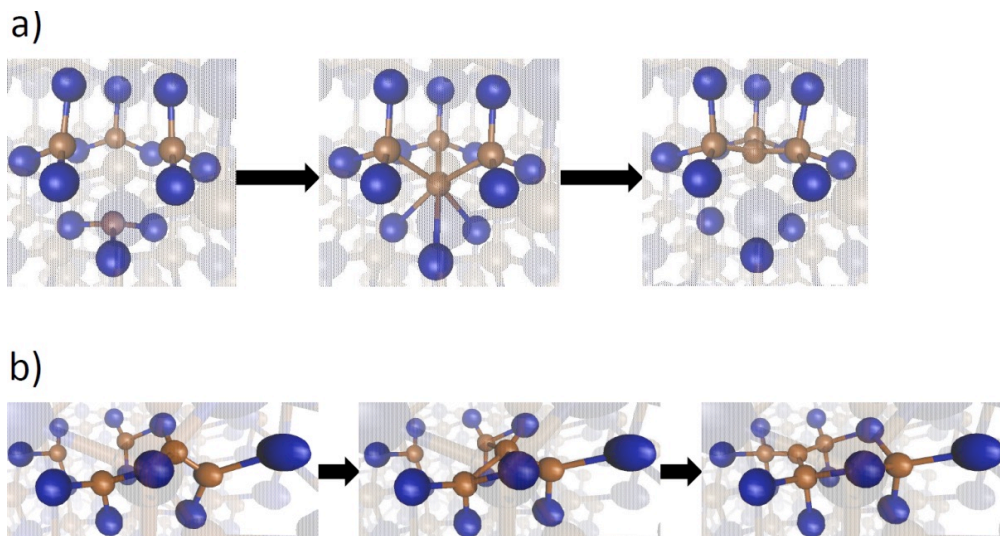


Figure 4.3. a) The defect rearrangement mechanism, either C / N, is displaced along the Z-axis from a C-site to a Si-site or vice versa. b) Mechanism of interstitial-vacancy combination, equally valid for interstitial migration in the absence of the adjacent vacancy. The barrier observed relates to passing through the plane of Si (middle picture), in the case of interstitial migration the barrier is substantially higher than in the defective case. C-Brown, Si-Blue.

The transition states can be broadly grouped into 4 mechanisms: (1) bulk interstitial migration; (2) the rearrangements ( $N_C V_{Si} \rightarrow N_{Si} V_C$ ,  $V_{Si} \rightarrow V_C C_{Si}$ ) (Figure 4.3a); (3) defect interstitial recombination ( $N_i + V_C V_{Si} \rightarrow N_{Si} V_C$ ,  $C_i + N_C V_{Si} \rightarrow N_C C_{Si}$ ) (Figure 4.3b); and (4) defect rotations.

Firstly, in the bulk context, the interstitial rotations switch between two iso-energetic structures with barriers of 0.6 eV and 0.5 eV for nitrogen and carbon, respectively. The second interstitial mechanism relates to the bulk migration of C and N, with the barriers of 2.9 eV and 2.6 eV, respectively. In the case of the  $N_C V_{Si}$  and  $V_{Si}$  rearrangements, the picture is made more complicated by asymmetric barriers for the forward and reverse reactions. However, one can see that the forward reaction  $N_{Si}$  to  $N_C$  is hugely favoured with a barrier of 1.2 eV (reaction 14) for the forward reaction, and 4.5 eV (reaction 13) for the back reaction. This suggests that, if the  $N_{Si} V_C$  is formed in the neutral charge state, the defect will be converted to the  $N_C V_{Si}$  conformation during the post implantation anneal. Likewise, this is true for the interconversion of the  $V_{Si} \rightarrow C_{Si} V_C$ , with a 1.6 eV barrier in the forward direction, and a 2.8 eV in the reverse. This asymmetry is shown in Figure 4.4, and leads to the favouring of one conformation. Hence, the result is that the process can be viewed as being unidirectional, which leads to an effective zero population in the highest energy configuration.

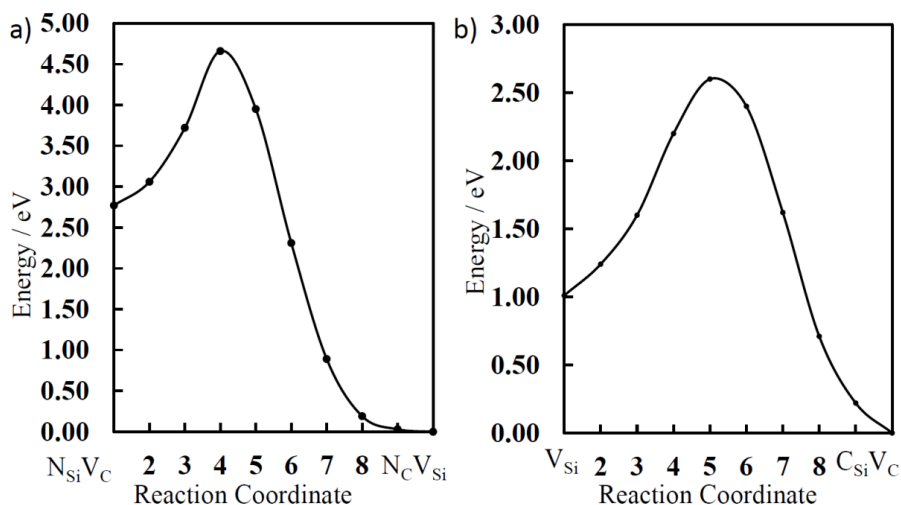


Figure 4.4. Barriers for interconversion highlighting the asymmetric nature of the transition. Relating to a) the  $N_{Si}V_C$  conversion to the  $N_CV_{Si}$  (reaction number 15 in Table 4.2), and b) the conversion of the  $V_{Si}$  to the  $V_C C_{Si}$  (reaction number 5 in Table 4.2).

The final set of the calculated barriers relate to the combination (reactions 6-12) of a migrating interstitial species with the various vacancies (di-vacancies) outlined in Table 4.2. These barriers are significantly reduced when compared to the bulk migration (2.6 eV compared to as low as 0.5 eV). It is evident from both Table 4.1 and Table 4.2 that the minima on the defect potential energy surface relates to the  $N_C C_{Si}$  and the  $N_C N_{Si}$ , coupled to low activation barriers once the migrating species have arrived at the defect. As a result, in both cases, subject to sufficient mobile interstitials,  $N_C V_{Si}$  would be expected to be converted to one of the above conformations.

### 4.3.3 Diffusion Behaviour

Taking the stationary points calculated initially, and illustrated in Table 4.1, together with the related transition states in Table 4.2, the diffusion coefficients for each of the forward and reverse reactions can now be calculated, using equations 4.4-5.

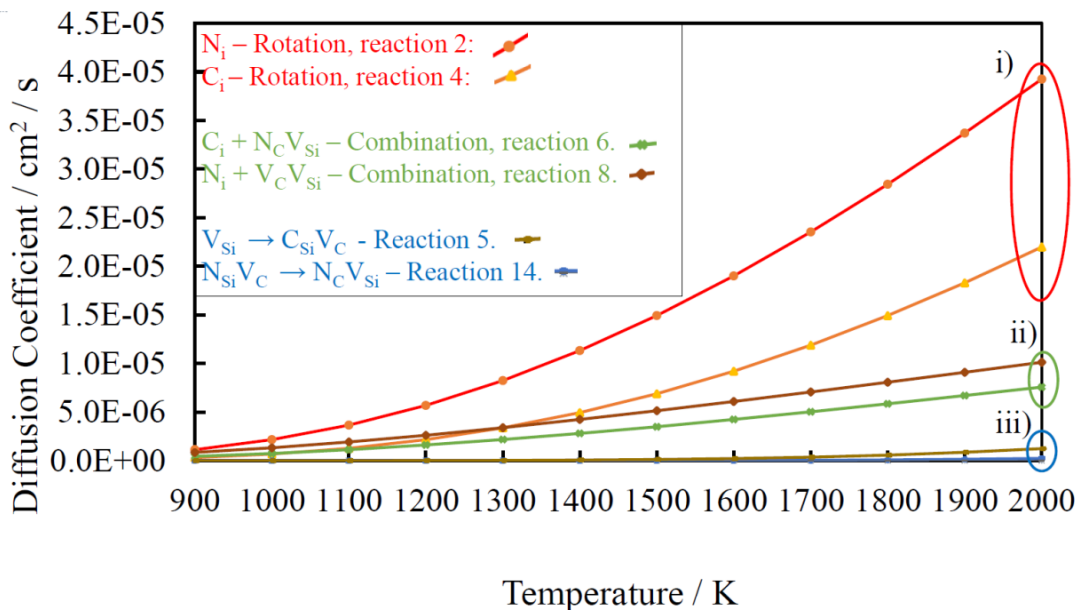


Figure 4.5. Diffusion behaviour of the key defect configurations as a function of temperature. The reactions have been grouped into those with similar diffusion coefficients as indicated. This shows the interstitial rotations (i) have the lowest diffusion coefficients, followed by the vacancy interstitial combinations (ii), and finally the defect rearrangements (iii). The bulk interstitial migration, reactions 1 and 3 from Table 4.2 have been omitted having diffusion coefficients orders of magnitude lower than the defects shown.

In accordance with the trends suggested by the activation barriers alone, it is clear that there are processes that occur (i) very rapidly, (ii) rapidly, (iii) moderately, and (iv) slowly. In particular, interstitial rotations happen extremely rapidly, as illustrated in Figure 4.5. Both take place an order of magnitude more rapidly than any of the competing processes. The recombination between a neighbouring interstitial and a vacancy occurs rapidly too, and relates to either "healing" the lattice, or moving a dopant to the target site. However, the processes of defect rearrangement (14:  $N_{Si}V_C \rightarrow N_C V_{Si}$ , 5:  $V_{Si} \rightarrow C_{Si}V_C$ ) are substantially slower, with diffusion coefficients smaller than either of the above. These processes would still be expected to be accessible within the temperature and time scale of anneal. Additionally, due to the asymmetric nature of the barriers involved, once the defects have converted, they can

be viewed as being fixed in the final configuration. The bulk interstitial migration is several orders of magnitude slower than any of the above processes at the temperature and time-scale of anneal.

The final piece of information that can be extracted is the diffusion length, which gives an estimation of the maximum distance a given species can travel within the annealing time. In the case of interstitial rotations (1 & 3), vacancy interstitial combinations (6-12), and defect rearrangements (5, 13 & 14), this has no significant meaning. These processes are either fixed in the case of defect rotations or involve a single step, in the case of vacancy interstitial combinations.

In the case of bulk interstitial migration, the diffusion length is meaningful. Using 30 minutes as the annealing time, one finds values of 5 nm and 9 nm for the  $C_i$  and the  $N_i$  diffusion length, respectively. This simple estimation of the diffusion length represents a maximum value, tending to overestimate the 'distance travelled'. The typical dopant concentrations are between  $10^{14}$ - $10^{16}$   $\text{cm}^{-3}$  with an upper limit of  $10^{19}$   $\text{cm}^{-3}$ . Assuming the N-dopants are homogeneously distributed, this gives the N-N separation between 200 nm and 5 nm. Hence, for typical N-concentrations the bulk interstitial migration is limited, however, at the high dopant concentration scenario, the interstitial diffusion would be expected to contribute to defect mix.

It is interesting to note that Kimoto *et al.*[229] demonstrated a marked decrease in interstitial concentration as a function of distance from the surface, in the same distance the concentration of carbon vacancies is observed to increase.[229], [230] This is seen in samples treated with an oxidative anneal, which is understood to introduce mobile  $C_i$  in the vicinity of the surface, these  $C_i$  then diffuse into SiC where they combine with  $V_C$  leading to the observed reduction in the  $Z_{-1/2}$  and  $EH_{6/7}$  DLTS

peaks.[229]–[232] This observation suggests that the barriers associated with interstitial diffusion are far lower in the surface like regime, aiding interstitial diffusion. As the material becomes bulk like, the diffusion becomes limited and the interstitial concentration is observed to rapidly decrease. A parallel can be drawn in the case of implantation described here. There is a dramatic reduction in the migration barrier in the vicinity of vacancies and vacancy complexes, resulting in greatly enhanced interstitial diffusion. This appears to be consistent with the same effect being observed by Kimoto *et al.* after C-implantation.[229]–[233]

#### 4.4 Conclusion

Summarizing the processes outlined and discussed above, a number of points are evident. Firstly, during the post implantation anneal, a great many processes are accessible and occurring rapidly. This leads to the observed ‘healing’ of the lattice where neighbouring interstitial atoms combine with vacancies, either implantation induced or otherwise. In tandem with these processes, the conversion of defects into more stable configurations is also occurring, and, through the asymmetry of the barriers involved, leads to a near zero population of the high energy conformations. The higher barrier for  $C_i$  when compared with  $N_i$  gives rise to the diffusion lengths of 5 nm and 9 nm respectively, therefore  $N_i$  is the more mobile interstitial. The question posed above as to why the  $N_C V_{Si}$  is observed, whereas the lower energy  $N_C C_{Si}$  is not, can be now addressed by considering the results described in Table 4.2:

- i) When the  $N_i$  is in the vicinity of the divacancy, regardless of the site the interstitial initially sits at, the  $N_C V_{Si}$  is either generated directly (Table 4.2, reaction 8), or *via* the  $N_{Si} V_C$  followed by the inter-conversion (Table 4.2, reactions 9 and 14).



- ii) The interaction of the  $C_i$  with the divacancy can give rise to either the  $V_{Si}$  or the  $C_{Si}V_C$ . With the higher energy  $V_{Si}$  being rapidly converted into the  $C_{Si}V_C$ .
- iii) Direct substitution of the 3-coordinated C that make up the  $V_{Si}$ , with a  $N_i$  has a significant barrier in excess of 3.0 eV. The barrier for defect inter-conversion to form the vacancy antisite pair is half that of direct substitution (reaction 15, Table 4.2).
- iv) The interaction of the interstitials with mono-vacancies gives rise to either healing of the lattice, the N-donor,  $C_{Si}$  or the  $N_{Si}$ . In the context of vacancy complex formation, these defects act as a sink for interstitials, reducing the concentration of interstitials that are available to react.
- v) Assuming that the formation of divacancies results from an implantation process, the formation of the  $N_C V_{Si}$  takes place directly *via* the interaction of the  $N_i$  with a nearby divacancy. These defects then accumulate in the device because they are stable to dissociation at the annealing temperatures. This gives a strong driver on the route to the experimentally observed  $N_C V_{Si}$  defect.

However, before the  $N_C C_{Si}$  defect can be formed, one of two precursors need to be present. The mechanism by which such precursors,  $C_{Si}V_C$  or  $N_C V_{Si}$ , can be formed is outlined above. To move from the precursors to the  $N_C C_{Si}$  and the  $N_C N_{Si}$ , an additional interstitial is required. Since  $N_i$  has a lower barrier for diffusion, this would tend to favour the formation of the diamagnetic  $N_C N_{Si}$  at the expense of the  $N_C C_{Si}$ . As a result, neither defect is expected to be found in a significant concentration, which may explain the experimental observations.

In considering the diffusion behaviour, the thermal budget of the anneal is 2000 K for 30 minutes. In the confines of the above conditions, it is clear that long range bulk interstitial diffusion is limited, and in this context the conversion of the  $N_C V_{Si}$  to either the C or N substituted variety can be understood. As there is a relatively low probability of finding a vacancy or vacancy complex with two neighbouring interstitials, without bulk diffusion, the population of the  $N_C C_{Si}$  and the  $N_C N_{Si}$  will always be very small (tending towards 0). Without bulk diffusion, the combination of isolated interstitials with the above complexes cannot occur. Therefore, the local minima on the PES that  $N_C C_{Si}$  and  $N_C N_{Si}$  represent, are never attained in significant concentrations, thus remaining below the detection threshold and not observed.

Thus, this chapter presents a mechanistic understanding of why the  $N_C V_{Si}$  is observed after the post implantation anneal, where the lower energy  $N_C C_{Si}$  is not. The lack of a favourable direct substitution mechanism (reaction 15) and limited interstitial diffusion give rise to the formation and accumulation of the  $N_C V_{Si}$ . To complete this picture, an understanding of the interplay between the competing mechanisms described here, and the vacancy diffusion mechanisms explored elsewhere, would be instructive. This would allow a combined dynamic picture to be presented along with the associated stable defect configurations.

# Chapter 5

## Building a Realistic SiC / SiO<sub>2</sub> Interface Model

---

### Abstract

In this chapter, EELS spectra and *ab initio* simulations are used to describe the interface of the current generation of SiC / SiO<sub>2</sub> MOSFETs, allowing for a description of the atomistic composition of this interface to be elucidated. This is then applied to the building of an interface model that can be used to study the performance limiting defects in the current generation of 4H-SiC MOS devices. This moves away from a reliance upon the picture presented in the literature, to allow different interface preparations are considered, allowing a device specific picture to be developed. This develops the picture from the devices based upon thermal oxides of the older generation of devices to the current deposited oxides.

The interface characterised here is best described as abrupt, but stepped, transitioning without any of the interlayers that have been posulated and discussed in the literature. These spectra are then deconvoluted using a combination of abrupt interface motifs, using the relative peak positions. The identified motifs are subsequently tessellated to create a full-size interface system that is used for defect modelling and identification in chapter 6. This produces a defect free interface that well reproduces the experimental band offset, and allows the flexibility of a variable oxide thickness.

## **5.1 Introduction**

As discussed in chapter 1.6, the current understanding of the SiC / SiO<sub>2</sub> interface is limited at best, with several competing models proposed, each supported by apparently contradictory experimental results. These models split broadly into three categories, (i) SiC<sub>x</sub>O<sub>y</sub> type interlayer models, (ii) carbon cluster / dimer interlayer models, and (iii) finally an abrupt interface with 'roughness'. As this thesis is motivated by the identification of defects within the current generation of SiC devices, the nature of these interfaces is of critical importance. Several TEM studies have described interface thicknesses of 1.5 nm – 25 nm, some with an apparent interlayer of undetermined composition, and some without any evidence of an interlayer. [42], [49] However, what is common between all of these studies, is that in some distance there is a transition from SiC to SiO<sub>2</sub>, and there is a rapid shift from a Si L<sub>2,3</sub>-edge of SiC character to one of SiO<sub>2</sub> character.[48] This shift typically occurs within 1 – 2 nm. How the broadness of this transition is to be gauged will be further discussed in section 5.3 and Figure 5.1. These studies have attempted to correlate the interface thickness with the mobility, with some studies finding a positive correlation between interface roughness and mobility, [42], [48] while others have shown the opposite negative correlation. [49], [72] This has been put down to sample preparation and the measurement technique used.[50] These apparently contradictory results suggest that thickness alone is insufficient as a descriptor of the interface, as the description of what constitutes thickness is not always comparable between studies. The picture is further complicated by variations in lamella preparation and differences between the experimental set-ups used.

In light of the inconsistencies in the existing literature highlighted above, the only reliable solution was to perform STEM / TEM measurements on the samples of interest. As with the experimental work presented in chapters 3 and 6, G. Gruber designed and performed the experimental work. These measurements were conducted by M. Dienstleder and C. Gspan at the Austrian Centre for Electron Microscopy and Nanoanalysis (FELMI-ZFE) as part of an ongoing research project. The subsequent electronic characterisation of the parent samples was conducted by G. Gruber and a full description can be found in reference.[73] As opposed to the work presented throughout this thesis, which is concerned with defect identification, the objective of this study was to identify a topological picture of the interface. From a theoretical standpoint, it is vital to have a robust model of the interface before defects can be considered within an interface context.

In the literature, a variety of interfaces have been used to study defects. The earliest, and simplest, approaches were presented by Knaup *et al.*[45] and involved adding a monolayer / bilayer of H-terminated oxide to the [0001] surface of SiC. This proved surprisingly robust for a variety of defects at or just below the interface. The observed problems arose from the flexibility associated with the monolayer leading to unphysical relaxations when defects were directly at the interface, or those involving large relaxations, were considered. This was refined by adding a thicker oxide of either  $\alpha$ -quartz or later amorphous SiO<sub>2</sub>. The question of interface connection scheme was most successfully tackled by Devynck *et al.* [234], [235] before this work, the interface bonding morphology was always artificially strained by the use of a single motif that leads to an increase in interface bonding density. All of these studies have had various problems of limited cell size due to the computation cost involved, making

it hard to systematically compare the various models. However, the most reliable results have been obtained from the models described by Devynck *et al.* incorporating an amorphous oxide and 8 bilayers of SiC. This was shown to reproduce the experimental band offset for 4H-SiC / SiO<sub>2</sub> with reasonable accuracy. To allow for comparison between the measured EDMR spectra and theoretical simulations, a reasonable model of the interface is required as the hyperfine interaction is directly affected by the defect geometry, which is impacted by the strain at the interface and the connection scheme.

## **5.2 Experimental Details**

As highlighted in the introduction, several contradictory results have been reported in the literature, and this is best understood by different samples giving wildly different results. This uncertainty has necessitated the study of the system of interest directly to allow a robust description of, in this case, the interface to be obtained. This understanding is vital from a defect identification stand point, allowing the assumptions inherent in the models to be justified. The samples were prepared from fully processed 4H-SiC MOS capacitors formed on a *p*-doped substrate. These samples are identical to those in which defects are measured and identified in chapter 6. The only difference in sample preparation derived from different POA, one receiving the industry standard NO anneal, while the other was just annealed in an O<sub>2</sub> atmosphere. This resulted in samples with wildly different electronic properties. These are summarised in Table 5.1.

Table 5.1. Electrical characterisation of the TEM samples as measured by G. Gruber. These measurements highlight the dramatic effect the POA has upon the performance of the device.

Sample	$\mu_{LF} / \text{cm}^2 \text{V}^{-1} \text{s}^{-1}$	$D_{it} / \text{cm}^{-2} \text{eV}^{-1}$
O <sub>2</sub> anneal	0.2	$2.3 \times 10^{12}$
NO anneal	17.6	$2.9 \times 10^{11}$

To prepare the samples for TEM study, a chemical etch removed the metallisation, after which thin lamellas were cut out using a focused ion beam (FIB – FEI NOVA200). These lamellas were then prepared to give a [1-100] viewing direction. This direction is selected as it is parallel to the step bunching that results from the off-axis growth. The final preparation step involves the thinning of the lamellas by ion polishing using a Fischione 1040 NanoMill ion mill. These steps resulted in a sample of approximately 20 – 50 nm thickness.

The measurements were performed using a FEI Titan<sup>3</sup> G2 60-300 transmission electron microscope with a C<sub>s</sub> probe corrector facilitating high resolution STEM imaging. These measurements were taken using the STEM mode with an acceleration voltage of 300 keV and a spatial resolution of 0.7 Å. A selection of detectors allows for bright field (BF), annular dark field (ADF), and high angle annular dark field (HAADF) imaging. The EELS measurements were performed using the ‘Dual EELS’ mode, which allows for the simultaneous recording of the zero-loss peaks and the energy loss region. These spectra were recorded in a box across the SiC / SiO<sub>2</sub> interface. The energy dispersion of the measurements was 0.25 eV and the pixel size was 0.25 nm. To correct for spatial drift during long measurement times, a post processing drift correction was applied.

### 5.3 Experimental Results: Performed by G. Gruber

From the contrast images shown in Figure 5.1 for both the O<sub>2</sub> and NO annealed interfaces, it is evident that both interfaces appear ‘sharp’, with no hint of an interlayer or extensive mixing such as described in previous papers. In the 20 nm images, both interfaces show a highly-stepped interface with macro steps-extending over tens of nanometres. These macro-steps originate as a result of step bunching. From the higher resolution images it is clear that the macro steps are comprised of a varying number of bilayer steps.

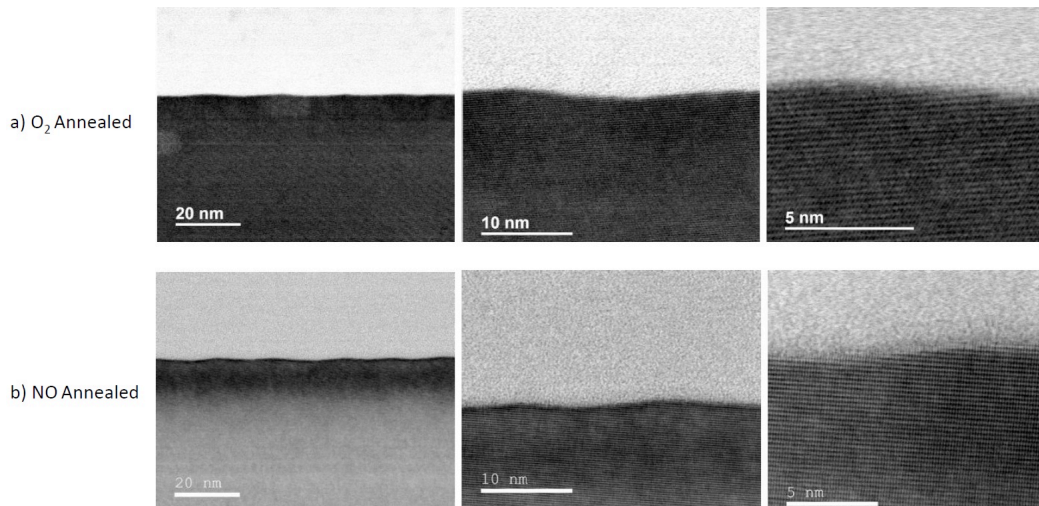


Figure 5.1. BF image of the O<sub>2</sub> annealed sample (a) and the NO annealed sample (b), both treatments appear to show a relatively abrupt interface, which is extensively stepped. These steps are then comprised of smaller steps down to single bilayer in size.

In an attempt to correlate the number of macro / micro steps observed to a given anneal, G. Gruber used the high-resolution images to count the number of micro steps that make up each macro step. An example of how this can be visualised is shown in Figure 5.2, this is possible as the bilayers in SiC are clearly resolved.



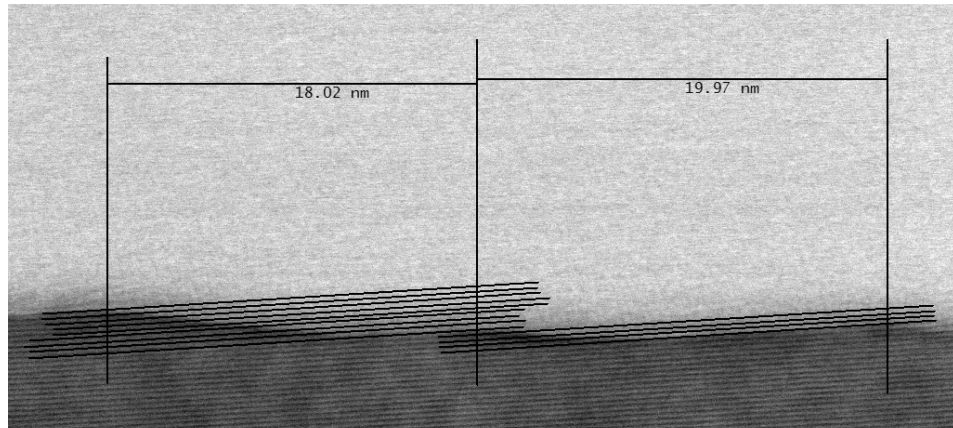


Figure 5.2. An illustration of how the bilayer steps were counted to give a descriptor of the balance between the macro / micro steps for each of the anneals used.

Taking the approach schematically illustrated in Figure 5.2, this was applied to a wide area on both of the interfaces to allow any similarities and differences to be identified. This would start to form the basis of any morphological argument for the differences between the two samples described in Table 5.1 and shown in Figure 5.3.

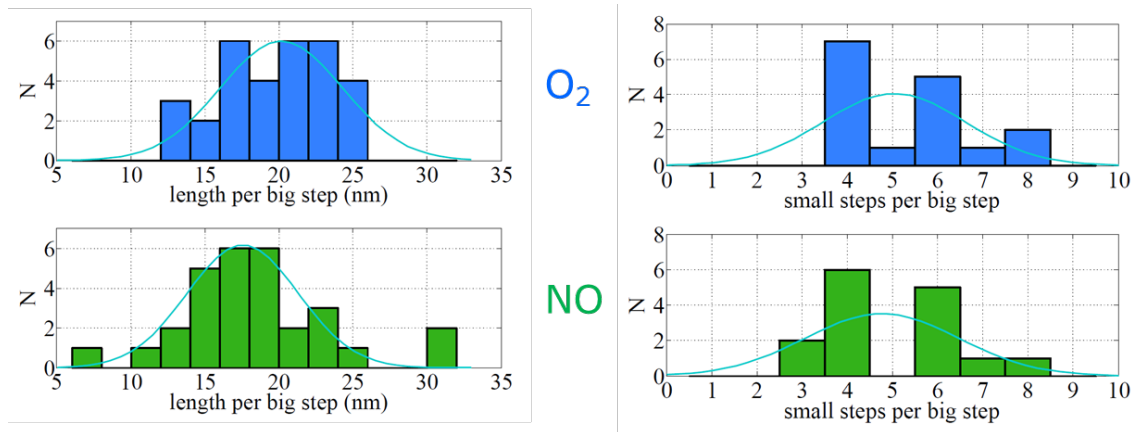


Figure 5.3. Comparison between the step bunching of an NO passivated interface (green) and an unpassivated interface (blue). The steps were counted by inspection from the contrast TEM images as illustrated in Figure 5.3.

As a result, it can be seen that both interfaces are highly disordered showing near continuous stepping along the interface. Additionally, the interface structures

described appear to be rough but sharp, with no evidence for an interlayer or extensive mixing. This work was able to find no meaningful difference between the two interfaces on the basis of the interface morphology obtained from the contrast TEM images. Therefore, it is hard to envisage how interface morphology can be responsible for the observed mobility differences outlined in Table 5.1. This leads to the conclusion that the poor mobility must be due to interface point defects that would not be resolved in the contrast TEM images.

This provides the first information for the construction of an interface model, stepping is extensive although the interface itself appears abrupt, supporting a model along the lines of those described by Devynck and Pasquarello.[234], [235] To probe the chemical environment at the interface, EELS measurements were performed on the samples outlined above.

### **5.3.1 EELS Interface Description**

The picture developed in the previous section shows tantalising hints of the nature of the 4H-SiC / SiO<sub>2</sub> interface, but it lacks the fine detail to be relied upon in isolation when it comes to constructing a realistic interface. To add a description of the chemical bonding environment while moving across the interface, EELS measurements were utilised. The additional benefit of this technique is that, in accordance with the method described in chapter 2, these spectra can be deconvoluted and simulated allowing for a direct comparison between the theory and the experiment.

The EELS study was performed on the samples outlined above, with the objective being to describe the interface thickness. Additionally, to confirm that in accordance with recent studies, no C-excess is present at the interface of these

devices, and finally to locate the N in the interface context. The Z-contrast from the HAADF detectors, the C, Si, O, and N ionisation edges and the Si-L<sub>2,3</sub> edge were recorded in accordance with the generally accepted method of Taillon *et al.*[48] The measurements were taken in a predefined 2D box with pixels of equivalent position above the interface being averaged to reduce the noise observed. This was then repeated at 5 sites across the interface and averaged again, illustrated schematically in Figure 5.4.

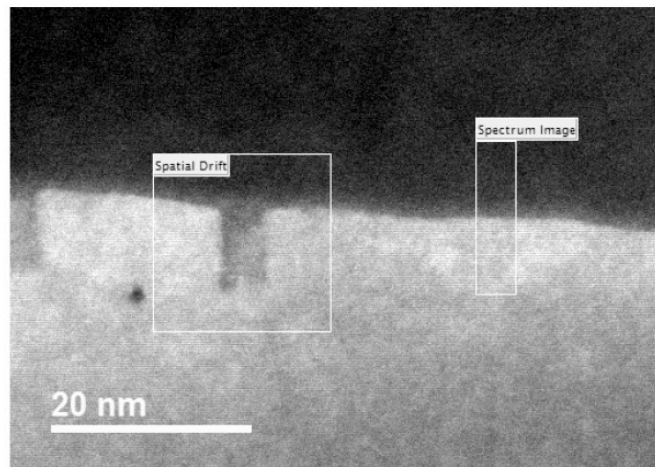


Figure 5.4. Contrast TEM image indicating the region from which the EELS spectra are taken, the spatial drift marked on the left indicates the effect of the beam and why correcting for this is important. All pixels at a given distance from the interface are averaged, this relates to the short length of the spectrum image box.

From the images obtained, the normalised C and N profiles were compared to obtain an estimation of the interface thickness. The initial intention had been to include the shift of the Si-L<sub>2,3</sub> edge, but the noise in the signal complicated this, making it difficult to obtain a meaningful estimation of the thickness. These plots are shown in Figure 5.5.

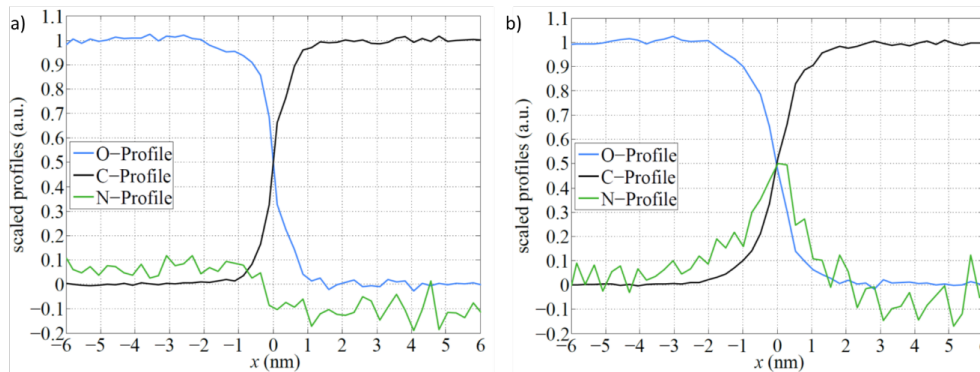


Figure 5.5. EELS profiles of the O<sub>2</sub> annealed device (a), and the NO annealed device (b). In each plot the transition from SiC to SiO<sub>2</sub> proceeds from right to left. The C and O signals are well resolved, whereas it is important to note the N is not, and as such is hard to draw definite conclusions from, aside from it only being detectable near the interface. The above scans were taken across the [0001] interface.

The first thing evident from Figure 5.5 is the clear lack of any C-excess near the interface, this is in accordance with the most recent studies and removes the C-cluster / C-dimer models of the interface from consideration.[36], [47], [48], [50] The shift from SiC to SiO<sub>2</sub> is extremely rapid with the bulk of the transformation occurring in  $\approx 1$  nm, with the tails extending much further before the bulk behaviour is recovered. This transition will be broadened by averaging effects, taking multiple pixels at multiple locations, due to a spatial resolution that is unable to avoid or account for the roughness of the interface. The effect being that in the interface region when the pixels of a given distance are averaged, some will be at the interface, and some will be next to the interface. Averaging these together will give the impression of an interface which is broader than in reality. When considering the N-peak (Figure 5.3b), it is important to note that the N-concentration is right at the detection limit, and as such is only barely resolvable from the noise in the signal. What is clear is that the only significant concentration can be observed in the region of the interface. Any further

interpretation of the exact position and shape of the peak would be akin to see patterns in static and should be treated with extreme caution.

The results for the Si-L<sub>2,3</sub> edge are shown in Figure 5.6. As discussed above, the data is noisier, which derives from how the chemical shift is determined. The edge position is defined as the inflection point of the ionisation edge, which is found by numerical differentiation. This leads to an amplification of noise in the signal, and hence an increased uncertainty in the edge position. It is however, important to note that the C, O and Si, all describe an interface of similar thickness.

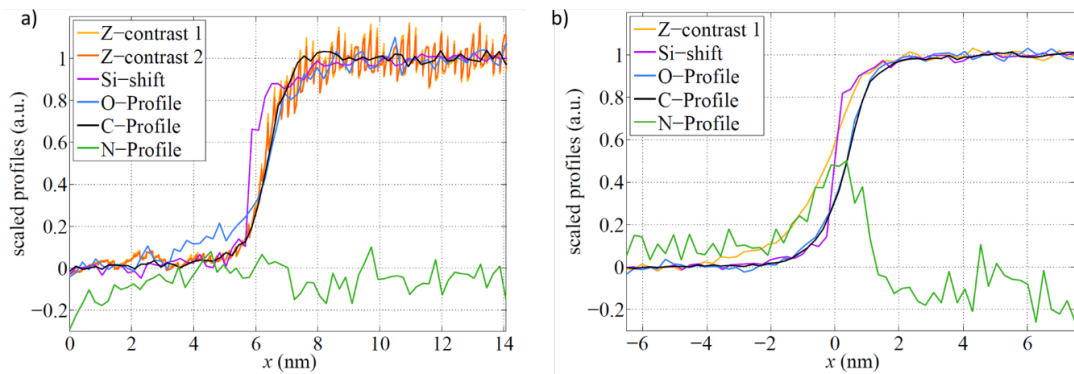


Figure 5.6. EELS profiles of the contrast, C, O, N, and Si profiles for the O<sub>2</sub> annealed (a) and the NO annealed (b). The Si shift is now included, all of the profiles have been rotated so the absolute transition length can be compared. With the exception of N, all of the profiles are clearly describing the same transition.

While treatment of the Si-L<sub>2,3</sub> edge shift is problematic, from an interface thickness method as suggested by Taillon *et al.*[48] for comparison with theoretical calculation, only the ionisation edge is required and so these effects are not material. Putting all of the above together, an estimation of the interface thickness provided by each proxy is shown in Table 5.2.

Table 5.2. Comparison between the various interface descriptors for the O<sub>2</sub> and NO annealed interfaces.

	C -profile / nm	O-profile / nm	Si-profile / nm	Z-contrast / nm
O <sub>2</sub> anneal	2.7	3.3	2.4	4.2
NO anneal	3.0	3.7	3.2	5.4

From Table 5.2, it is interesting to note that, regardless of the descriptor selected, the O<sub>2</sub> anneal leads to a sharper interface. This is unexpected, as traditionally the sharpness of the interface has been correlated to mobility, and sharper interfaces predicted to give better mobility. From the morphology investigation, this result is not entirely unexpected as, from section 5.3, interface morphology was unable to explain the observed mobility differences.

Putting all of the above together allows an experimental description of the interface to be elucidated. This will then form the basis of, and be tested using, theoretical calculations to allow a realistic representation of the interfaces of interest to be constructed. The first observation from the contrast image was the lack of any extended interlayer, either based around C-clusters or an extended SiC<sub>x</sub>O<sub>y</sub> layer, as had been previously observed.[47], [48], [50], [67], [72], [74], [148] The second observation from the contrast TEM was that there was no meaningful difference between the O<sub>2</sub> and the NO annealed samples in terms of interface morphology. This has the implication that, at least for these devices, there is no correlation between interface morphology and channel mobility. From an interface modelling perspective, this removes from consideration any extended interlayer models and suggests an abrupt, but stepped interface.

From the EELS measurements, a similar picture is presented with an interface that is rough to between 2 – 4 nm. As touched upon, the method of averaging employed above will have the effect of exaggerating the interface thickness so these should be viewed as describing an upper limit.[212] In addition to this, how the ‘tails’ of the various profiles should be treated is not yet clear. This is in accordance with recent studies that have looked at the interface thicknesses for other systems.[41], [47], [159] Finally, to put any significance on the N-profile, beyond the fact that it is located at the interface, is problematic and as such is avoided. A full description can be obtained from [73]. The C, Si and O profiles confirm the observations of an interface without any C-interlayer. The above description forms the ‘fingerprint’ of the interface that guides the modelling described in the next section.

## 5.4 Theoretical Methodology

To allow for a comparison with the EELS spectra described in the previous section, a series of calculations were conducted. These calculations were carried out in accordance with the methodology described by Pippel *et al.*[236] In this approach, the Si-L<sub>2,3</sub> shift is described for a variety of interface motifs, which are then compared with the experimental spectrum. These interface motifs are initially approximated by small clusters representing the structures that could be envisaged to be found at an abrupt interface. In selecting these motifs, it was assumed the valency of each of the interface species is maintained. Although the XPS data describes an oxygen deficient interface, the model constructed from this data will be used to study individual defects in isolation, and hence it is important that it is defect free. The selected clusters are shown schematically in Figure 5.7.

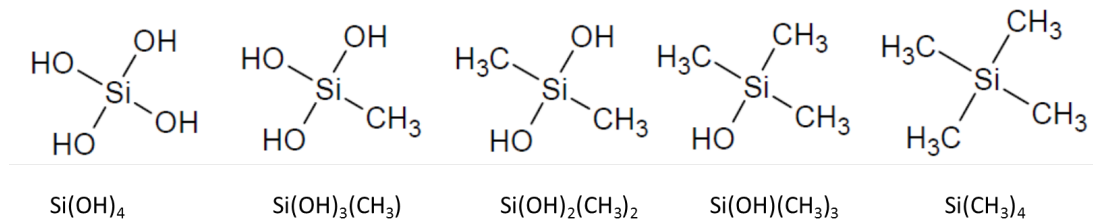


Figure 5.7. Schematic view of the clusters used to approximate the abrupt interface motifs. From SiO<sub>2</sub> through to SiC, with a stepped increase in C-concentration from left to right.

The clusters shown in Figure 5.7 are used to calculate the electronic environment using DFT, as implemented in the Gaussian09 code,[237] with a 6-311++G\* basis set and the PBE0 functional. This approach was selected as performing well for molecular C / Si systems and being comparable with the parameters used for the periodic calculations. The main difference being the selection of the PBE0 functional as opposed to HSE06. This change was made as HSE06 degenerates down to PBE0 as the mixing parameter ( $\omega$ ) approaches 0, as would be the case for the clusters above.

The Si-L<sub>2,3</sub> edge is made up of transitions from the Si-2p to the antibonding s\*, p\* and d\* states. For tetrahedral systems, the transitions of interest are described by the optical selection rule ( $\Delta l = \pm 1$ ) resulting in p → s\*, p → d\*, additionally in this case p → p\* transitions are allowed by the parity selection rule. The energetic difference between the unoccupied and occupied states gives an estimation of the Si-L<sub>2,3</sub> shift for each of the clusters that can be compared with the experimental peak onset.

To confirm the results obtained from the molecular cluster calculations, small scale periodic calculations were conducted using the method of Pickard *et al.* [215] This is implemented in the optados module of the CASTEP code,[238] allowing the simulation of the Si-L<sub>2,3</sub> edge. The simulations were performed in a 96 atom SiC cell,



and a 72 atom SiO<sub>2</sub> cell, these cells were selected to eliminate any interaction between core-holes in accordance with the method described by Pickard *et al.*[215]. The calculations were performed with a converged plane wave cut-off of 600 eV and the HSE06 functional, with the simple models calibrated against the above molecular representations of the interface motifs (calculated with PBE0). Tests were performed to gauge the shift in the core level eigenvalues between the clusters and the periodic systems, in each case the shift was found to be minimal < 0.2 eV. This represents less than 0.1 % disagreement in the methods, and demonstrates that the core levels are sensitive to the ligand environment, while the shift between periodic and non-periodic only has a minimal effect.

## 5.5 Theoretical Results

### 5.5.1 Simulation of the EELS Spectra

The approach described above with the motifs shown in Figure 5.7, is used to describe an abrupt transition from 4H-SiC to SiO<sub>2</sub>. The L<sub>2,3</sub> edge relates to an excitation from the 2P<sup>1/2</sup> and the 2P<sup>3/2</sup> states of in this case Si, this acts as an extremely sensitive probe of the chemical environment of a given species. These can then be directly compared to the Si-L<sub>2,3</sub> shown in Figure 5.8b as the interface is traversed from SiC to SiO<sub>2</sub>.

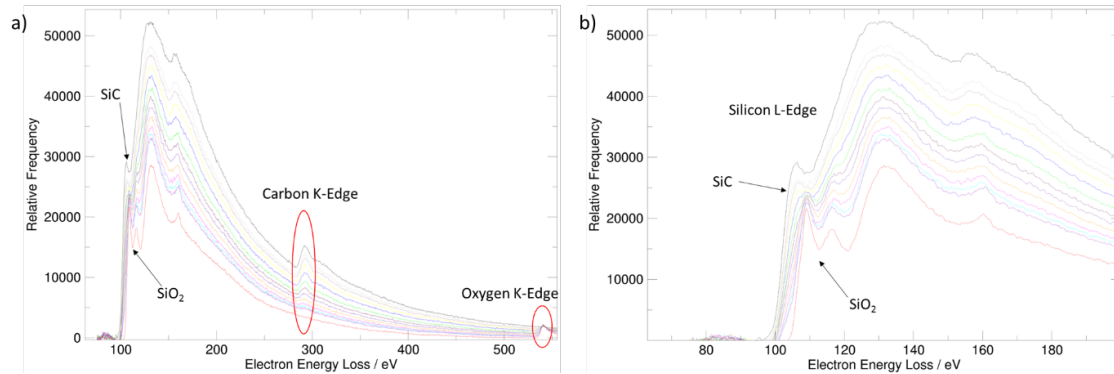


Figure 5.8. (a) The experimental EELS data for the SiC / SiO<sub>2</sub> interface showing the silicon L-edge, carbon and oxygen K-edges. The lines between the marked SiC and SiO<sub>2</sub> lines represent 2 Å steps across the interface. (b) shows a zoomed in view of the Si-L<sub>2,3</sub> edge and the fine structure that will form the basis of the comparison between the theoretical and experimental data.

From Figure 5.8a, a number of things are instantly evident. Firstly, the C and O K-edges show that there is no extensive intermixing, being as they are only observed on the SiC and SiO<sub>2</sub> sides of the interface. On the basis of the form and position of the C- (and O-) K-edge it is clear that none of the motifs typically associated with SiC<sub>x</sub>O<sub>y</sub> glasses are observed. Key amongst the absent features are the sharp peak at approximately 285 eV relating to the C-O motif, the double peak at  $\approx$  280 eV relating to the C=C, and the multiple peaks starting at 294 eV relating to sp<sup>3</sup> C-C. Secondly, Figure 5.8b shows a zoomed in view that highlights the fine structure as the single SiC peak is split into the double peak observed in SiO<sub>2</sub>. These differences will form the basis of the comparison with experiment along with the shift in the peak position. The peak position shift is due to the opening of the band gap from SiC (3.26 eV) to SiO<sub>2</sub> (8.9 eV).

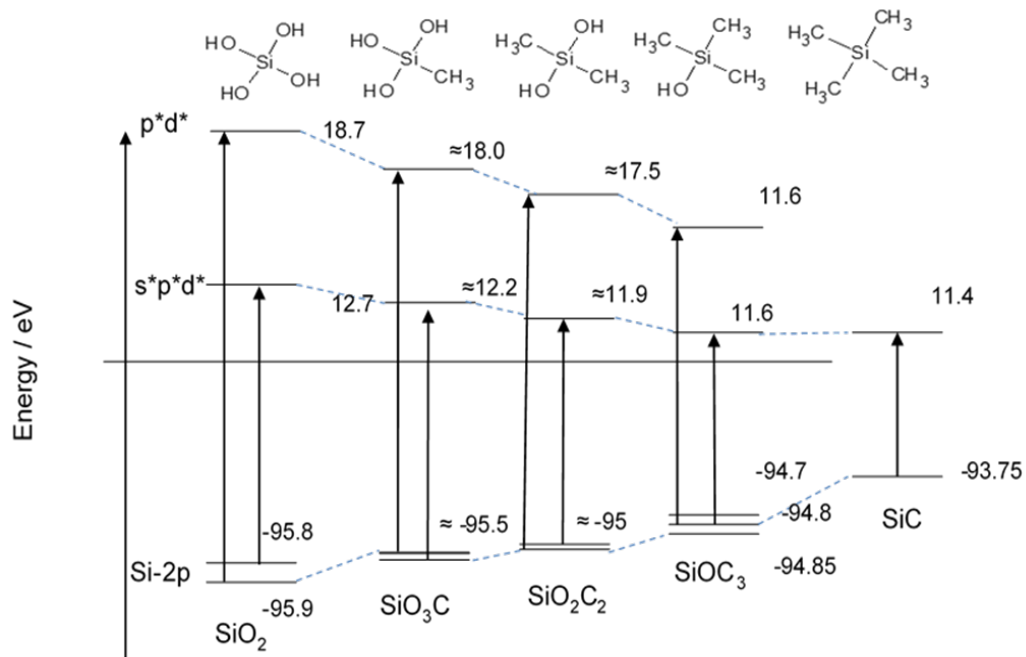


Figure 5.9. Schematic representation of the clusters (above) that could be expected to be found at an abrupt SiC / SiO<sub>2</sub> interface, the label below illustrates the interface motif that is being mimicked. The dashed lines are to give an impression of the shift between configurations and are not there to suggest any connection between them. The vertical line represents the energy difference between the core Si-2p states and the s/p\* states.

Table 5.3. Peak position extracted from the magnitude of the arrows in Figure 5.9.

	SiO <sub>2</sub>	SiO <sub>3</sub> C	SiO <sub>2</sub> C <sub>2</sub>	SiOC <sub>3</sub>	SiC
First Peak Position	108.6	107.7	106.9	106.4	105.15
Second Peak Position	114.6	113.5	112.5	109.6	

Figure 5.9 shows the positions of the states that make up the Si-L<sub>2,3</sub> edge and starts to allow a comparison with the experimental data to be made. The origin of the dual peak observed in the SiO<sub>2</sub> signal can now be understood, as can its absence from the SiC signal. The splitting of the 2p levels is far smaller than the experimental linewidth, and as such cannot be observed and will only add to the broadening in a minimal fashion. The simplest comparisons are made with the pure phases as shown in Figure 5.10.

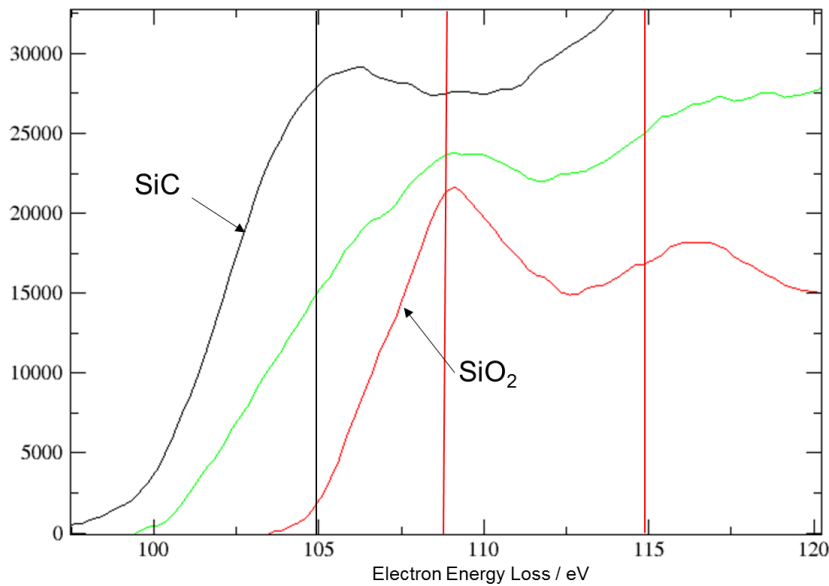


Figure 5.10. Experimental spectra with the calculated peak position overlaid for SiC and SiO<sub>2</sub>, the green line represents the interface case, being equidistant between the two and exhibiting properties of both. The peak position indicated above relates the energy difference between the ground and excited states as indicated by the vertical line in Figure 5.9.

From Figure 5.10 it is clear that the calculated and experimental peak positions show good agreement, as is to be expected as the EELS spectra of many Si based materials have been extensively studied using this approach. It is possible to reproduce the entire spectra by adding varying degrees of Lorentzian and Gaussian broadening, and this has in many cases been used as an additional fitting parameter. For the pure phases, this approach can be argued to be justified, but in the case of an interface, it complicates the picture when several configurations are to be considered together. As such, only the peak positions are indicated in this case to show which features can be accounted for by the various motifs. This is in accordance with the method described by Pippel *et al.*[236] where only the magnitude of the transition, as shown by the length of the vertical lines in Figure 5.9 and listed in Table

5.3, are considered. This line length represents the energy difference between the 2p eigenvalues and those of the antibonding states of the ‘conduction’ band (LUMO states).

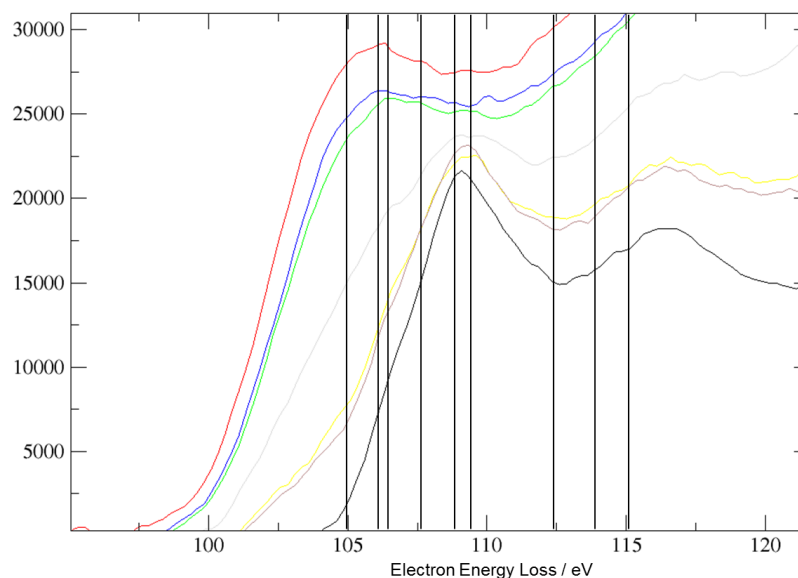


Figure 5.11. A schematic view of the experimental EELS spectrum deconvoluted using the motifs shown in Figure 5.9.

From Figure 5.11, features from both SiC and SiO<sub>2</sub> become more or less pronounced as the interface is traversed from one material to the other. This intermediate region varies from those regions on the SiC or SiO<sub>2</sub> side of the interface that exhibit a high degree of the features associated with the pure phase. The degree of this mixing is most clearly observed in the shift of the SiO<sub>2</sub> edge onset that is evident in the yellow and brown lines in Figure 5.11. This shows a pronounced shift with respect to the SiO<sub>2</sub> edge within 2 – 4 Å of the SiO<sub>2</sub> side of the interface, this length is approximately 1 – 2 bilayers. The same pattern is observed on the SiC side of the interface, with the secondary SiO<sub>2</sub> peak at approximately 115 eV, apparent as a broad peak that sharpens into the recognisable peak. As highlighted in the experimental

section 5.3, the lines on Figure 5.9 are averaged over multiple pixels at a fixed height with respect to the interface. This can have a dramatic effect on the profile of the interface when applied to a stepped interface, the SiC and SiO<sub>2</sub> sides of the interface being well described and the stepped features appearing to be broadened as motifs of SiC / SiO<sub>2</sub> character are mixed. This leads to a smearing out of the interface, combining step and non-step features, in effect artificially broadening the interface. Thus, this method of averaging across a stepped interface would tend to represent the maximum thickness that could be expected.

The observations made above and shown schematically in Figure 5.11, indicate that the interface of interest can be described using motifs from an abrupt interface but stepped interface. It is critical at this stage to reiterate that, due to the large variety seen in the literature, these results are only valid for the samples, and by extension the MOSFETs, from which they were derived and that are studied here. In this context, the interface can be understood as being abrupt and heavily stepped, these bilayer steps then bunch together to form macro steps of 10s of nanometres. The theoretical simulation of the EELS Si-L<sub>2,3</sub> supports this view, with the main features of the observed spectra being able to be deconvoluted using only the motifs from an abrupt interface. This interface description can then be applied to the construction of interface model of the interface to ultimately allow defects to be considered in the interface context. The failure of the traditional linear interpolation based approaches is due to the complexity of the connection schemes, associated with a ternary system that simply cannot be captured by this approach.

## 5.5.2 Interface Model

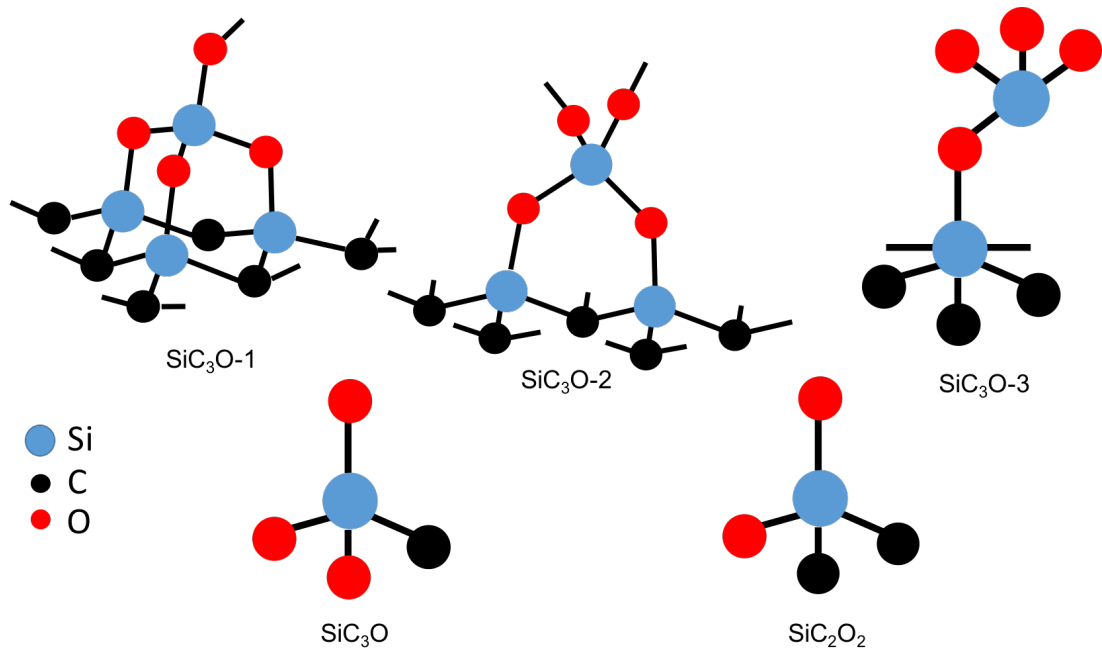


Figure 5.12. The schematic interface motifs translated from the small clusters described in Figure 5.7. Each of these are then combined to produce an interface model for defect calculations along the lines of the models described by Devynck *et al.*[234]

Using the experimental and simulation work described in the first part of this chapter, it is now possible to describe the interface in the devices of interest. This allows an abrupt interface model to be constructed building upon the earlier work of Devynck *et al.*[234], [235] This periodic slab model is constructed using connection motifs outlined in Figure 5.12, which are then combined to give a fixed connection scheme on the SiC [0001] surface. The bottom C-face is then H-terminated, while the top face is connected to a H-terminated amorphous oxide of variable thickness. A converged vacuum gap of 40 Å is added to prevent periodic images from interacting.

Before the above model can be constructed, the problem is broken down into 3 parts, the 4H-SiC, the amorphous oxide, and the interface between the two. The 4H-SiC is described by the 5 x 3 x 2 orthorhombic cell introduced in chapter 3, this

cell is extended in the z-direction to create two surfaces, the [000-1] and the [0001] (Appendix C). The [0001] surface will become host for the interface while the C-face ([000-1]) is hydrogen terminated. This cell was selected as it allows a significant 'bulk' region to be incorporated without resorting to fixing a large number of atoms, which becomes particularly important when considering defects at or just below the interface. Where extensive fixing can limit the relaxation and lead to distortions in defect geometries.

To capture the amorphous nature of the oxide a MD-melt quench was employed using the BKS force field and the LAMMPS code.[239] This is in accordance with the method described by Devynck *et al.*, a cooling rate of 5 K / ps was used as this has been shown to perform reliably when producing amorphous oxides using this method.[235] Giving reasonable structural motifs, a defect free oxide, within the expected density range. Structurally the bulk oxide produced using this method has a Si-O bond length of 1.61 Å ( $\sigma=0.02$  Å), a Si-O-Si bond angle of 143° ( $\sigma=15^\circ$ ), and a O-Si-O bond angle of 110° ( $\sigma=7^\circ$ ). This is in accordance with the bond length and angle distributions reported in the work of Devynck *et al.*[234] and critically in the original work of van Beest *et al.*[240], giving confidence in the description of the oxide produced.

The final and most challenging part of the puzzle is the connection between the 4H-SiC and the oxide. In the model presented here the simulation cell is fixed to the bulk xy-lattice parameter of 4H-SiC. This approach results in the interface strain being accommodated entirely by the oxide, which in the case of a deposited oxide is reasonable. In the case of device oxides the deposition is followed by a limited anneal making this an assumption that it's important to highlight. To connect the oxide to the



4H-SiC a monolayer of oxide is added to the Si-face which is then H-terminated. The scaled (to reflect the Si-O bond length) H-positions are then mapped onto oxygen positions in the amorphous oxide, which are themselves fixed. This produces a robust means of ensuring the oxide and 4H-SiC are always able to be connected. This is shown schematically in Fig 5.13a and b, as in each case the connection scheme is fixed any variations in the arrangement of the motifs shown in Fig 5.12 must be considering discretely. In the final step the ReaxFF force field and 1000 K is used to release any residual strain present in the interface system. The final structure is then relaxed using CP2K with a TZVP-MOLOPT basis set, GTH type pseudopotentials, and the HSE06 functional as described in detail in chapter 3.3. Structurally the interface shows a Si-C bond length of 1.86 Å, and a Si-O bond length of  $1.63 \pm 0.01$  Å, this effect can be understood in the same terms as the elongated Si-O bonds (contracted Si-C bonds) observed in the Si/SiO<sub>2</sub> sub-oxide, resulting from a shift in the Si electronegativity. The bond angles sit in a wider range, Si-O-Si: 120 – 140°, and C-Si-O: 104 – 116°, these distortions relative to the bulk values relate to the accommodation of strain at the interface, this mismatch is accommodated within 5 Å when the bulk values are obtained.

This results in an interface model that ensures each of the species involved is fully coordinated removing the problem of an unrealistic dangling bond concentration. As discussed, the strain is entirely born by the oxide with the *xy*-parameters being fixed to the bulk value of SiC. Step bunching is not explicitly treated in this case due to cell size limitations, although the cell is of sufficient size to allow step like motifs to be considered. This leads to a model of the interface that reproduces the SiC / SiO<sub>2</sub> band offset to <10% (Figure 5.13c), and gives a band gap free of defect states. It is

of critical importance for the study of individual defects to have an interface free of defect states, and while this is not necessarily physical it allows for the individual defects to be studied in isolation.

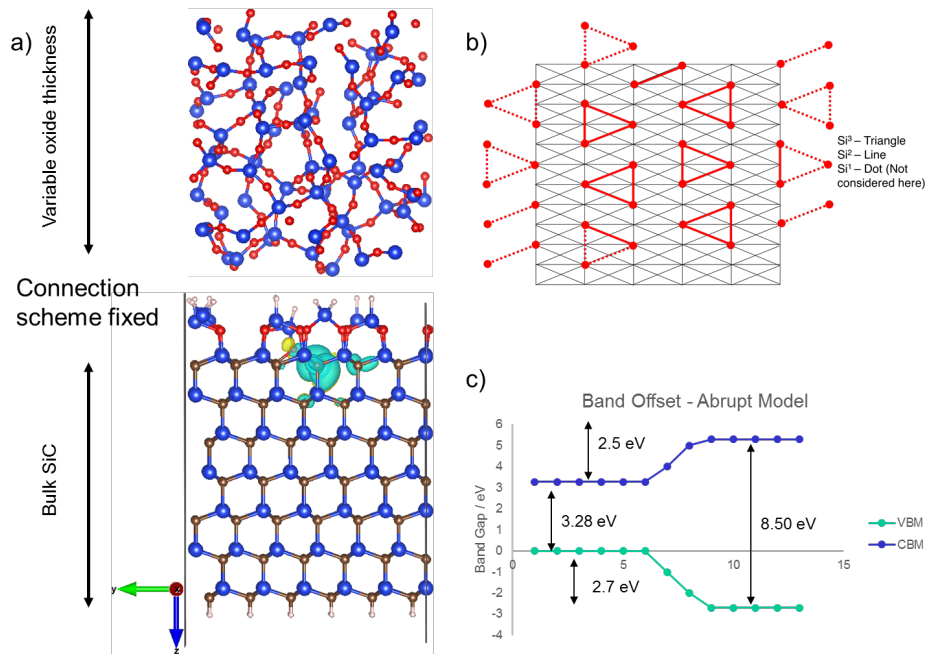


Figure 5.13. a) The fixed connection scheme that allows for the connection of oxides of varying thickness. These oxides are H-terminated along with the C-face of the SiC and the top-face of the oxide. The yellow and blue lobes indicate the spin density of an interface C-vacancy. b) a schematic view of the connection scheme where Si<sup>3</sup> relates a triple bridged O<sub>3</sub>SiO, Si<sup>2</sup> is the double bridged O<sub>2</sub>SiO<sub>2</sub>, and Si<sup>1</sup> is the single OSiO<sub>3</sub> as shown in figure 5.12 c) A schematic view of the band offset between SiC and SiO<sub>2</sub> for a 16 Å oxide thickness. This diagram is produced from the projected density of states for each of the SiC bilayers, maintaining the same spacing into the oxide, giving an indication of the band opening from SiC to SiO<sub>2</sub>. These points have then been connected by a smooth line.

Figure 5.13a shows the interface model with the fixed connection scheme allowing for the interchange of pre-prepared oxides of varying thickness. Figure 5.13b shows a schematic view of the interface, giving an overview of how the motifs illustrated in Figure 5.12 are tessellated to produce an abrupt defect free interface.

Figure 5.13c shows the progression of the CBM and VBM from the bulk across the interface into the oxide. This allows a controlled system into which the individual defect will be considered and discussed in chapter 6.

## 5.6 Conclusion

This chapter is motivated by the need to define the nature of a system before meaningful study can be undertaken. In the same way as in chapter 3 (and 6), EDMR is used to elucidate a defect ‘fingerprint’. Here EELS is used to produce a description of the interface that can be compared with *ab initio* simulations. This was applied to the SiC / SiO<sub>2</sub> interface, allowing a picture of the interface of interest to be developed. In the absence of this, a vital part of the picture is missing and any defect identification will be speculative without the required context to anchor it to a given device. Therefore, it is of critical importance to have a means of describing the system of interest.

The combination of EELS and *ab initio* simulations provides a powerful tool with which to probe the nature of the interface allowing for a description of the atomistic composition and a direct comparison between the two. Vivaly for this work, it moves away from a reliance upon the often-contradictory picture presented in the literature, allowing for a device specific picture to be developed. This confirms the experimental picture of an abrupt, but heavily stepped interface. The spectra recorded across the SiC / SiO<sub>2</sub> interface can be deconvoluted through a combination of abrupt interface motifs, based upon their relative peak positions, and from this a comparison is obtained without the need for fitting.

The suggested motifs are then tessellated to create a full-size interface system that can be used for defect modelling and identification in chapter 6. This produces a

defect free interface that well reproduces the experimental band offset, and allows the flexibility of a variable oxide thickness. The most important implication is that this approach allows for the study of defects in a context that mimics the device environment. In situations where there is a high degree variability based upon preparation, it is vital to know that the models used are appropriate.

These interfaces, while being representative of the interface of interest, are also a huge simplification. The transition from SiC to SiO<sub>2</sub> is achieved in a single layer without any consideration of the continuous stepping that is prevalent in the TEM images. Additionally, the step bunching that goes on to form the macro steps is on a scale that could not be considered using electronic structure methods. These details are not captured by the model presented here, as they arise from strain at the SiC side of the interface and the off-angle growth. To improve this picture, these structures need considering and would form a logical refinement of the model presented here.

# Chapter 6

## Interface Defect Identification

---

### Abstract

This chapter is a culmination of the work presented in this thesis, combining the approach to defect identification described in chapter 3, with the interface model developed for these n-channel MOSFETS outlined in chapter 5. The site selectivity of EDMR is utilised to probe the dominant recombination defect at the 4H-SiC / SiO<sub>2</sub> interface. This has long been a question that has resulted in vigorous debate with two main schools of thought emerging on the matter, assigning the defect either to the V<sub>Si</sub> as favoured by Lenahan *et al.*[145], or to the dangling bond (P<sub>bc</sub>) as suggested by Cantin *et al.*[148]

Through the comparison between experimental EDMR measurements and *ab initio* calculations, the performance limiting recombination defect observed with EDMR in the current generation of nMOSFET's is identified as a combination of the P<sub>bc</sub> and the dual-P<sub>bc</sub> defects. These defects match the symmetry, HF, and isotopic abundance observed in the experimental spectrum. This defect is found within technologically relevant samples and supports the initial assessment of Gruber *et al.*,[73], [241] and illustrates that the defect identified by Cantin *et al.*[148] in oxidised porous samples persists in the current generation of nMOS devices.

## 6.1 Introduction

One of the remaining challenges for SiC MOSFETs is the poor channel mobility, which remains significantly below the bulk mobility. In addition, threshold voltage instabilities are ubiquitous in modern SiC MOSFETs. It is well established that there is a high density of interface traps present at the SiC / SiO<sub>2</sub> interface of the most common polytypes and that passivation can be achieved by nitridation, particularly by post oxidation anneals (POAs) in nitric oxide (NO) atmosphere. However, there is no clear consensus on what the dominant electrically active defects are. Important interface defects in Si MOSFETs have been identified with EPR many years ago, but for SiC this is not the case. Numerous studies have aimed for an identification of those defects by means of EPR and EDMR, as summarized in the work of T. Umeda *et al.*[70], [90], [95], [153]

Three defect models are relied upon to explain these interface defects, C-clusters, V<sub>Si</sub>, and dangling bond (P<sub>bC</sub>). The C-cluster model has already been excluded based on the EELS measurements detailed in Chapter 5. This leaves the V<sub>Si</sub> and the P<sub>bC</sub>. The P<sub>bC</sub> centre is described and characterised in a series of EPR studies on oxidized porous SiC by J.L. Cantin *et al.* The angular dependence of the differently oriented dangling bonds at the various interfaces was determined to be  $g_{\parallel}=2.0023$  when the magnetic field ( $B$ ) is applied in the symmetry axis of a dangling bond and  $g_{\perp}=2.0032$  in the perpendicular direction. The hyperfine (HF) parameters for the P<sub>bC</sub> centre were  $a_{C\parallel} \approx 80$  G, and  $a_{C\perp} \approx 40$  G for the central C atom and  $a_{Si} \approx 13$  G for the neighbouring Si atoms. The negatively charged V<sub>Si</sub> defect has been identified by EPR in bulk SiC long ago revealing an isotropic  $g$ -factor of  $g \approx 2.0028$ . The HF parameters due to the four neighbouring C atoms are  $a_{C\parallel} \approx 28$  G with  $B$  applied in the

symmetry direction of the unsaturated C bond and  $a_{C-} \approx 10.5$  G in the perpendicular direction, as well as  $a_{Si} \approx 3$  G for the twelve next neighbour Si atoms.

Several EDMR studies linked the observed defect to the  $V_{Si}$  defect, predominantly based on the isotropic  $g$ -factor.[145] Where information is provided, it appears these studies were performed on interfaces produced by thermal oxidation. The study by C.J. Cochrane *et al.* could resolve the HF structure of the  $V_{Si}$  using application of *fast passage* EDMR.[145] The *fast passage* technique was pioneered by Hyde and Weger in the 1960's and relates to a scan rate of sufficient speed that the electron spins are not able to relax between modulation sweep cycles.[242], [243] However, while this study identified the  $V_{Si}$  as the defect observed by *fast passage* EDMR, the other referenced studies used a conventional detection scheme (without *fast passage*) and showed a dramatically different HF spectrum. This is suggestive of a time component to the measurement resulting in different defects probed as a result of the EDMR approach employed. In a recent work, M.A. Anders *et al.* attempt to rule out the presence of dangling bond defects at the SiC / SiO<sub>2</sub> interface.[154] This conclusion is based upon the assumption that the observed defect is the  $V_{Si}$  defect and not the dangling bond. This appears to neglect anisotropy shown in the  $g$ -tensor along with the selective focus on the fast passage results without any explanation. In this chapter, the EDMR spectra obtained from a variety of 4H-SiC  $n$ -channel MOSFETS are presented (measurements performed by G. Gruber[73]), and from these a defect fingerprint is extracted and then compared with the EPR parameters of the calculated defect shortlist.

## 6.2 Experimental Methods: Performed by G. Gruber

### 6.2.1 Sample Preparation and Characterisation

The samples considered in this chapter cover the most common passivation techniques and interface preparations. The O<sub>2</sub> and NO samples (Table 6.1) are those characterised and simulated in Chapter 5. The N<sub>2</sub>O treatments are included for completeness as they are commonly suggested as an alternative passivation scheme to NO.

Table 6.1. Electrical characterisation as conducted by G. Gruber, describing devices that are wildly different from an electronic perspective.

Sample (Anneal)	$\mu_{LF} / \text{cm}^2 \text{V}^{-1} \text{s}^{-1}$	$V_{th} / \text{V}$	$D_{it} / \text{cm}^{-2} \text{eV}^{-1}$
Thermal (N <sub>2</sub> O)	0.006	22.8	-
Deposited (O <sub>2</sub> )	0.2	20.3	$2.3 \times 10^{12}$
Deposited (N <sub>2</sub> O)	2.2	19.5	$1.7 \times 10^{12}$
Deposited (NO)	17.6	14.5	$2.9 \times 10^{11}$

Table 6.1 shows that the devices of interest are, from an electronic perspective, extremely different. The processing has a marked influence on the mobility ( $\mu_{LF}$ ), threshold voltage ( $V_{th}$ ), and density of interface traps ( $D_{it}$ ). This is in accordance with the previous literature, describing an inverse relationship between  $D_{it}$  and  $\mu_{LF}$ . The NO treated sample gives the highest mobility, with the lowest density of interface traps. This interface represents the closest to the state of the art. Chapter 5 describes the SiC / SiO<sub>2</sub> interfaces with TEM and EELS, these techniques describe an interface that shows no morphological dependence upon passivation regime. The above (Table 6.1) illustrates that, while this is the case from an electrical perspective, these are very different.



### 6.2.2 Experimental Parameters

All measurements were performed using the BAE biasing scheme of EDMR.[211] The source-to-body diode was forward biased at  $V_{sb}=-3.5$  V. All measurements were performed at room temperature with a microwave frequency of  $f_{mw}=9.4022$  GHz, and a magnetic field modulation of  $f_{mod}=900$  Hz.[73]

### 6.3 Computational Details

DFT calculations were performed using the CP2K code, and the functionals selected for the calculations were PBE and HSE06. These functionals were utilized with the DZVP-MOLOPT-SR-GTH and the TZVP-MOLOPT-GTH basis sets. All parameters were converged to 0.01 meV per formula unit. The orthorhombic interface cell used in these simulations is described in Chapter 5. This formed the basis for all calculations allowing for the defect relaxation to be contained within the simulation supercell (Appendix C).

The HF parameters were calculated using the GAPW approximation in the CP2K code. The basis-sets selected for geometry optimizations are not appropriate for the calculation of hyperfine parameters, as an explicit description of the core electrons and hence an all electron basis set is required. Using the approach outlined in chapter 3, the exception being that as a result of improvements in the CP2K code and the computation resources available, the pcj-3 basis set was selected for these calculations.

#### 6.3.1 Defect Calculations

The above parameters and supercells were used for all defect calculations. Initially, the neutral charge states were calculated and from the number of occupied and unoccupied gap states, the accessible charge states for a given defect were inferred

and calculated. The defect formation energy ( $E_f$ ) was calculated using the standard formalism of Northrup and Zhang[102], as described in chapter 3. As explicitly considered in chapter 4,  $E_f$  neglects the temperature dependent portion of the free energy of formation ( $\Omega_f = E_f - TS$ ), which includes phonon effects that are challenging to calculate. While  $E_f$  dominates at low temperatures, the entropy term can have a marked effect at elevated temperatures. However, explicit consideration is beyond the scope of this chapter, and here  $E_f$  is assumed to approximate  $\Omega_f$  as defined in equation 3.2. Formation energies give useful information about the relative concentrations for a given series of defects. In the case of defects in the interface context, the deposition / oxidation process is not expected to leave a system that has reached thermodynamic equilibrium. As a result, the most useful information that is gleaned is the CTL and as a result where the paramagnetic states are in the 4H-SiC bandgap.

The HF calculated are treated in accordance with the methods outlined in section 3.3.2 with all the contributions being considered and treated probabilistically. This allows a spectrum to be simulated for comparison with the experimental results.

## **6.4 Experimental Results: Performed by G. Gruber**

In the first instance, the relative signal intensities of the samples of interest were investigated to allow the optimum gate voltage ( $V_g$ ) to be identified for a given device. Initially, the angular dependence of the signal is measured giving important information on the defect symmetry, this is followed by consideration of the HF interactions along the principle symmetry axis (parallel and perpendicular to the c-axis).

### 6.4.1 Angular Dependence

The angular dependence of the signal of interest gives information on the symmetry of the defects, and additionally it allows for a comparison between devices. These tilt series are shown in Figure 6.1, and allow for the device to be rotated in the field along the directions indicated. There is only a single orientation of the device with the thermal oxide (Figure 6.1a – brown line) and this is only included for completeness, as it can be expected to have a significantly different interface morphology than the devices characterised in chapter 5. Representing as it does a previous generation of the technology. For the NO sample, only a few points are recorded as extensive averaging was required to determine the  $g$ -factor.

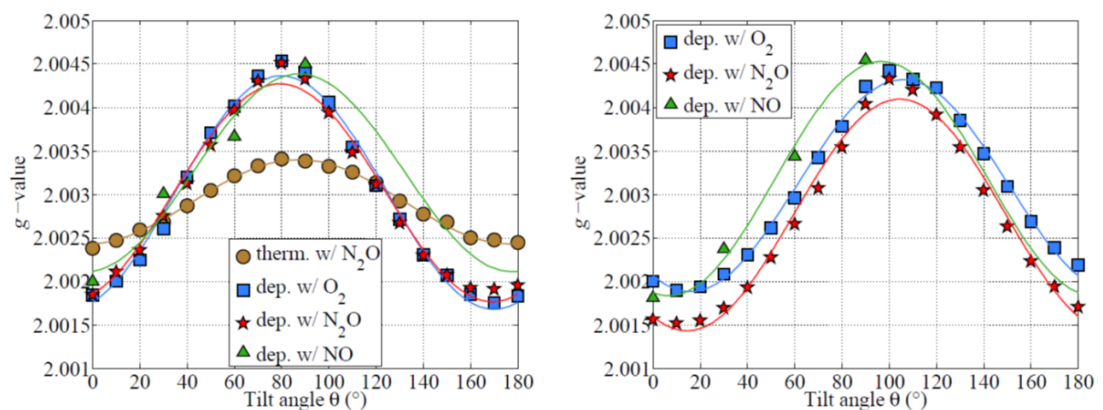


Figure 6.1. a) [11-20] ( $0^\circ$ ) to [0001] ( $90^\circ$ ), b) [1-100] ( $0^\circ$ ) to [0001] ( $90^\circ$ ). Data courtesy of G. Gruber.

From Figure 6.1 there are marked differences between the anisotropy of the devices with thermal and deposited oxides, respectively, with the thermal oxide being the most isotropic. This is interesting to note, as this oxidation approach has been shown to produce extremely rough interfaces and is no longer used. The three deposited oxides show extremely similar defects, and these are present in an

interface that is relevant from a device perspective. Table 6.2 shows the principal  $g$ -factors derived from the tilt series.

Table 6.2. Principal  $g$ -factors from the tilt series in Figure 6.1.

Sample (Anneal)	$g_{xx}$	$g_{yy}$	$g_{zz}$
Thermal (N <sub>2</sub> O)	2.0024	-	2.0034
Deposited (O <sub>2</sub> )	2.0016	2.0019	2.0045
Deposited (N <sub>2</sub> O)	2.0014	2.0018	2.0043
Deposited (NO)	2.0018	2.0021	2.0045

### 6.4.2 Hyperfine Structure

The HF structure of the devices listed above were recorded and considered with B parallel to the [0001] direction. The NO annealed sample required a large amount of signal averaging to elucidate the  $g$ -tensor, which led to the HF interactions being indistinguishable from the noise inherent in the measurement. As a result, the NO defect is neglected from the discussion here, aside from stating that the defect symmetry is extremely similar to N<sub>2</sub>O and O<sub>2</sub> treated systems. Each measurement was recorded at low microwave power (10 mW) and high microwave power (1 W), shown below in Figure 6.2. The final point of note is that the spectra shown below have been shifted and normalised to allow for easier comparison of the HF parameters.

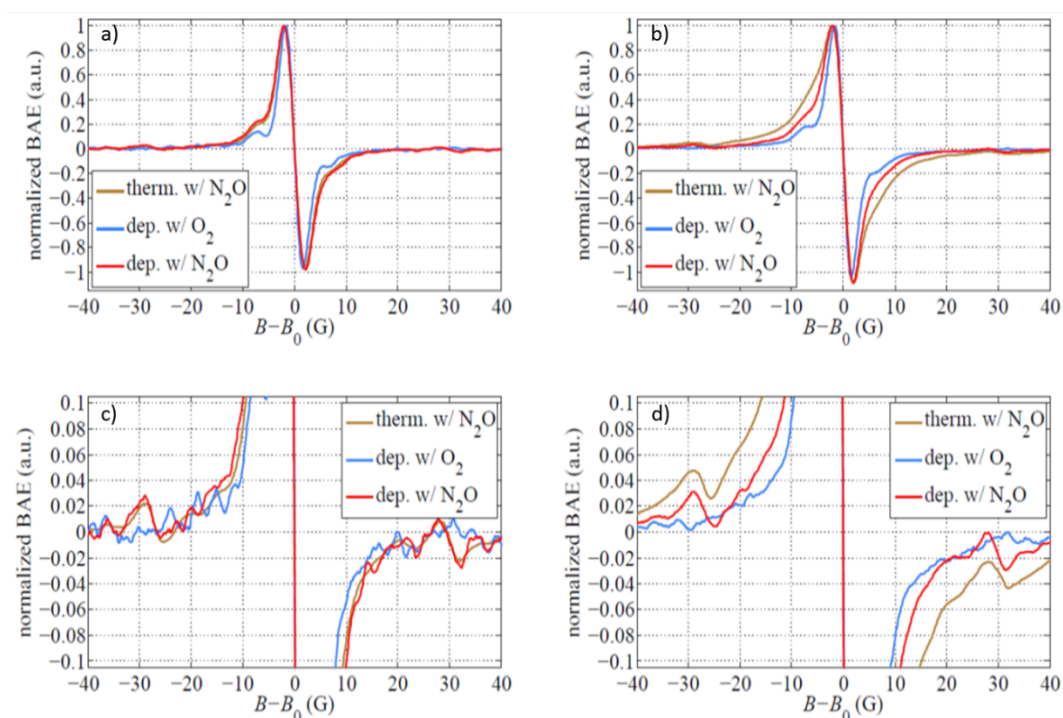


Figure 6.2. A comparison of the HF-interactions of the dominant defect observed with EDMR as a result of the various passivation treatments. a) Shows the EDMR spectra of the indicated devices with a microwave power of  $< 10$  mW. b) Gives the same spectra with a microwave power of  $\approx 1$  W and has the effect of broadening out the features.

The main features that can be extracted from Figure 6.2 is that the low power curves show clearly resolved HF peaks  $\pm 6$  G away from the centre line, with a normalised intensity of 0.15 – 0.2. In the higher power measurements, these peaks are broadened to a point where they are no longer resolved in the  $N_2O$  devices. The  $O_2$  treated device still shows the same peak in the high-power measurement, but with significant broadening. Secondary features of lower intensity are observable in both the  $N_2O$  and the  $O_2$  annealed devices, although the nature of these features appears to be distinct. In the  $N_2O$  devices, a doublet at  $\pm 29$  G is observed. Additionally, by considering the angular behaviour of this doublet, it is independent of the centre line suggesting that it is a separate defect. This can be speculated to be an N-centred or

N-passivated defect, as it is only observed in the N-treated devices, further consideration of this defect is beyond the scope of this thesis. In the O<sub>2</sub> annealed device, a low intensity peak (0.01) is observed at  $\pm 20$  G, this has the same centre line and shows none of the angular quirks that are seen in the N-treated samples.

From consideration of the  $g$ -tensor and the HF behaviour it is possible to extract a ‘fingerprint’ of the defect of interest. The defect shows rotational symmetry about the crystal  $c$ -axis with a slight ( $< 10^\circ$ ) off axis tilt. This gives a defect that is symmetric in the, but highly anisotropic with respect to the  $c$ -axis. Finally, from the HF interaction, there are two pronounced splitting’s of the centre line, at  $\pm 6$  G with an intensity of approximately 15%, and at  $\pm 20$  G with an intensity of 1%.

## 6.5 Theoretical Results

### 6.5.1 Initial Considerations

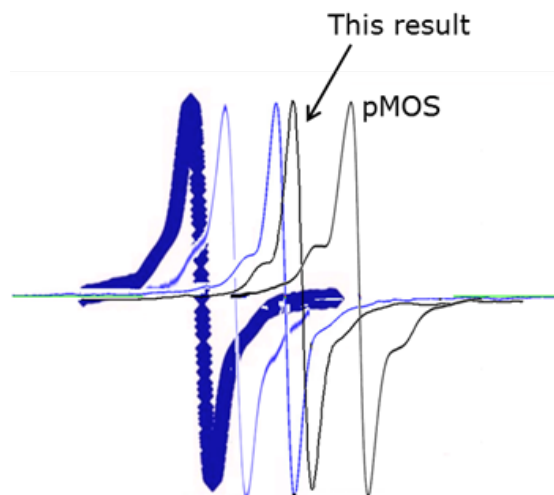


Figure 6.3. A schematic illustration of the  $g$ -tensor shift between the previously measured interface and oxidation defects. Illustrating the similarity in HF and the offset in  $g$ -value between the literature values.

There are several studies in the literature from the groups of Cantin *et al.* and Lenahan *et al.* that have described a number of defects that look extremely similar from a HF perspective to the defects described here (figure 6.3), but show a  $g$ -value shift relative to one another. This is a counter intuitive state of affairs that has led to two schools of thought developing, those that rely upon the description of  $g$ -value and the *fast passage* measurements alone, which, as described before, give a very different spectrum from those shown in Figure 6.2. These defects appear to be most similar to the thermal oxide (with  $N_2O$ ) described above, having the poorest interface quality, highest concentration of traps, and the most isotropic  $g$ -tensor (Table 6.2). This is interpreted to be the  $V_{Si}^-$ , which is an interpretation favoured by the Lenahan group.[141], [145] Their assignment is based on the average of the parallel and perpendicular  $g$ -values being approximately that of the  $V_{Si}$ .

The opposing viewpoint holds that the variation in  $g$ -value is an artefact of field, strain at the interface, or preparation, shifting  $B_{eff}$  and as such leading to the range of values shown above, although it is important to note that the origin of this shift is not well understood. Taking the HF interaction and the angular behaviour of the component parts into account, the alternative interpretation is the  $P_{bC}$  centre or carbon dangling bond.[148] Both candidates will be calculated and compared to the experimental data from the deposited oxide with the  $O_2$  anneal, being as this gives a strong signal free of the secondary defect present in the N-treated devices.

### 6.5.2 Interface Defects

The defects previously postulated in the literature will form the starting point for the theoretical calculations, and were considered using the interface model described in chapter 5. The defect picture of interest is shown schematically in Figure 6.4,

highlighting the orientations of interest and how they are envisaged to fit into the 4H-SiC / SiO<sub>2</sub> interface context.

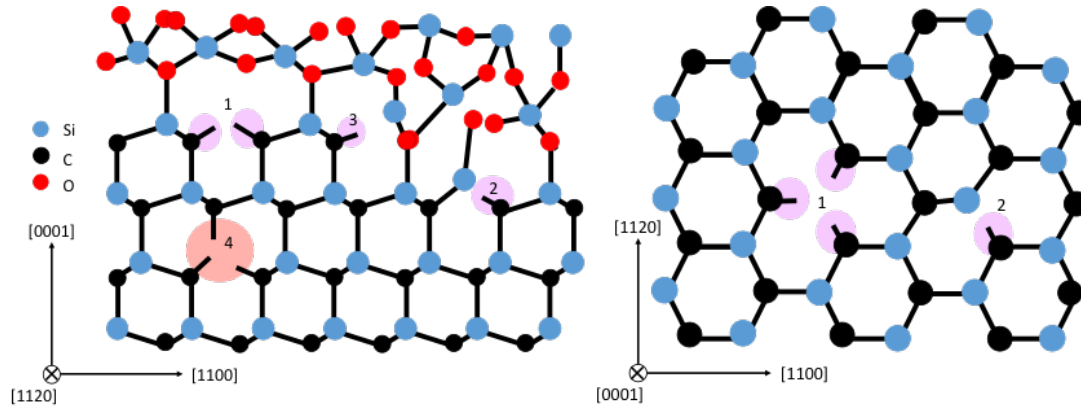


Figure 6.4. Schematic view of the  $V_{Si}$  and the  $P_{bc}$  that are initially considered for comparison with the EDMR measurements. 1)  $V_{Si}$  on a terrace, 2)  $P_{bc}$  at a terrace, 3)  $P_{bc}$  on a step edge, 4)  $V_{Si}$  in the layer beneath the interface. The blue circles represent Si, the black represent C, and red O.

### 6.5.2.1 Silicon Vacancy

The  $V_{Si}$  in the bulk context has been extensively characterised from both a theoretical and experimental perspective. In addition, the assignment of the bulk  $V_{Si}$  is universally agreed upon, described by an isotropic- $g$  at 2.003 with hyperfine splittings  $a_c = 13$  G, and  $a_{si} = 3$  G. Detailed consideration is beyond the scope of this chapter and the  $V_{Si}$  is only considered in the interface and near interface context (1 and 4 from Figure 6.4). Additionally, only the simplest terrace interface morphologies are considered, while the local connection schemes highlighted in chapter 5 will certainly influence the local strain environment and by extension how the defect may be expected to relax. This will be considered more completely in section 6.5.2.2 and 6.6.



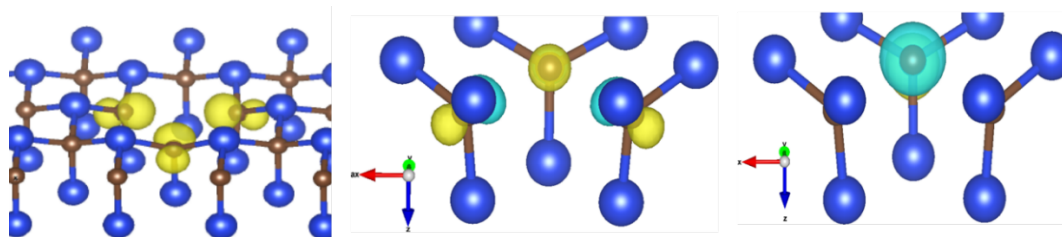


Figure 6.5. a)  $V_{\text{Si}}$  in the neutral charge state at the SiC / SiO<sub>2</sub> interface, b) HOMO state of the  $V_{\text{Si}}$  showing the in phase and out of phase combination of the correlated C-dangling bonds, c) LUMO state of the same defect.

The most pronounced effect the interface has upon the silicon vacancy is to remove the upper most of the 4 C-dangling bonds. It breaks the  $T_d$  site symmetry (equivalent C-relaxation) of the bulk defect and is reduced to either  $C_{3v}$  when the interface allows for equivalent relaxation of the C-dangling bonds, or  $C_1$  with an average symmetry of  $C_{3v}$  when averaged overall all possible arrangements, the principle symmetry axis being aligned along the crystal  $c$ -axis. This describes a defect with 3-fold rotational symmetry around the  $c$ -axis that is symmetric in the  $ab$ -plane and anisotropic with respect to the  $c$ -direction. Geometrically, the C-dangling bonds relax back into the plane of the neighbouring Si, with a displacement of  $\approx 0.1 - 0.2 \text{ \AA}$  compared to the unrelaxed geometry. As a result of this weak interaction between the  $V_{\text{Si}}$  dangling bonds, there is an extremely small energy difference between the low spin (doublet) and the high spin (quartet), of the order of 0.2 eV in the neutral charge state. In the negative charge state, the high spin (triplet) is 0.1 eV lower in energy than the low spin (singlet). This leads to relative populations of 99 % for the 0-doublet and 99.99 % for the -1-triplet at room temperature. The projected density of states (PDOS) plots for the various accessible charge states and multiplicities is shown below in Figure 6.6.

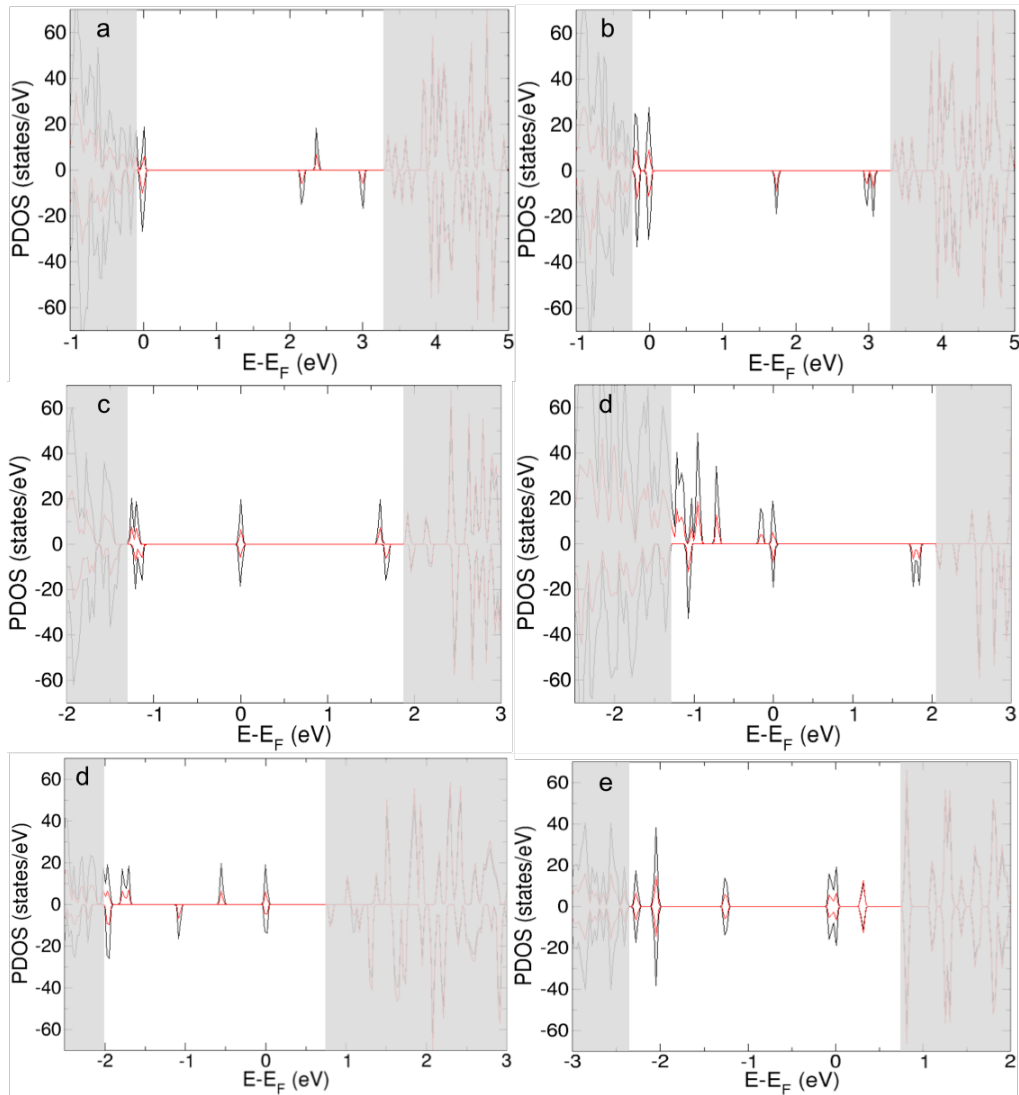


Figure 6.6. Projected density of states plots for the  $V_{Si}$  defect in the a) neutral doublet, b) neutral quartet, c) -1-singlet, d) -1-triplet, e) -2-doublet, f) -3-singlet. The 0 on the x-axis indicates the position of the highest energy electron, those states above the 0 position are unoccupied while those below are occupied. The positive y-values relate to the  $\alpha$ -spin channel, while the negative y-values relate to the  $\beta$ -spin channel. The 4H-SiC band gap is indicated by the non-greyed out area, indicating the number and occupation of the localised gap states associated with the  $V_{Si}$ .

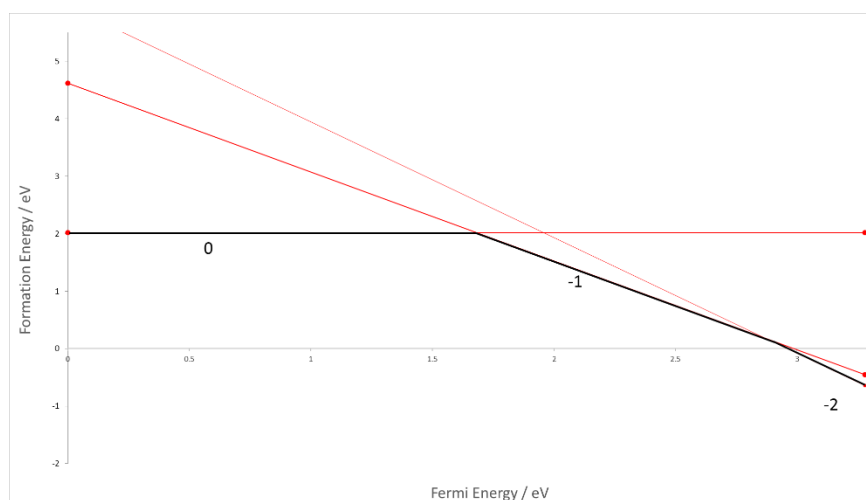


Figure 6.7. Formation energy plot for the interface  $V_{Si}$ , showing the CTL for charge states of interest.

The interface  $V_{Si}$  is accessible in the 0, -1, and -2 charge states in a variety of multiplicities as indicated in Figure 6.6. The doublet, triplet, and quartet states (Figure 6.6a, b, d, and e) are all paramagnetic and as such would be visible to EDMR. The singlet states (c and f) can be excluded as being invisible to EDMR. The -3-charge state is included for completeness although it only becomes favourable at the 4H-SiC CBM. The first observation is that the moving of the  $V_{Si}$  from the bulk to the interface dramatically reduces the formation energy from  $\approx 9$  eV to 2 eV at the VBM. While caution is required in using formation energies in non-equilibrium conditions, the trend is clear. From Figure 6.7, the following CTL's can be extracted; (0/-) at 1.6 eV, and (-/-) at 2.9 eV, this describes a defect that is paramagnetic for the entire 4H-SiC band gap with the 0 / -1 charge states sitting in the observable region.

### 6.5.2.2 Carbon Dangling Bond ( $P_{bc}$ )

The off-axis growth mechanism and the heavily stepped nature of the interface give rise to a large number of sites where the dangling bond could be envisaged to form. These are schematically illustrated in Figure 6.4 as numbers 2 and 3, existing either

at a step edge (3) or a dislocation between the oxide and SiC (2). These defects are a single  $sp^3$  hybridised C-dangling bond with a single electron in the neutral charge state. As with the  $V_{Si}$ , the C-dangling bond relaxes back into the plane of the neighbouring Si-atoms, the magnitude of the relaxation is less pronounced than with a displacement of  $0.08 \text{ \AA}$ . With only a single C-dangling bond there are only 2 accessible charge states, the 0, and -1, with the 0 being favoured for the majority of the SiC band gap. The PDOS are shown in Figure 6.8, with the formation energy plot shown in Figure 6.9. In this case, only the neutral charge state is paramagnetic with a (0/-) CTL at 1.9 eV, as the defect is localised on a single C-atom there are no high spin variants to consider.

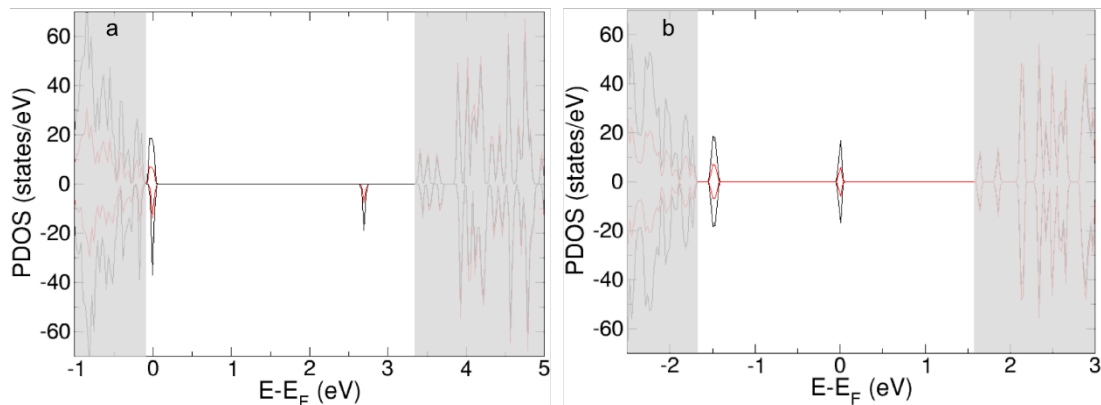


Figure 6.8. DOS plots for the a) neutral doublet, and b) the negative singlet. The 0 on the x-axis indicates the position of the highest energy electron, those states above the 0 position are unoccupied while those below are occupied. The positive y-values relate to the  $\alpha$ -spin channel, while the negative y-values relate to the  $\beta$ -spin channel. The 4H-SiC band gap is indicated by the non-greyed out area, indicating the number and occupation of the localised gap states associated. The black line represents the C-PDOS and the red line the Si-PDOS.

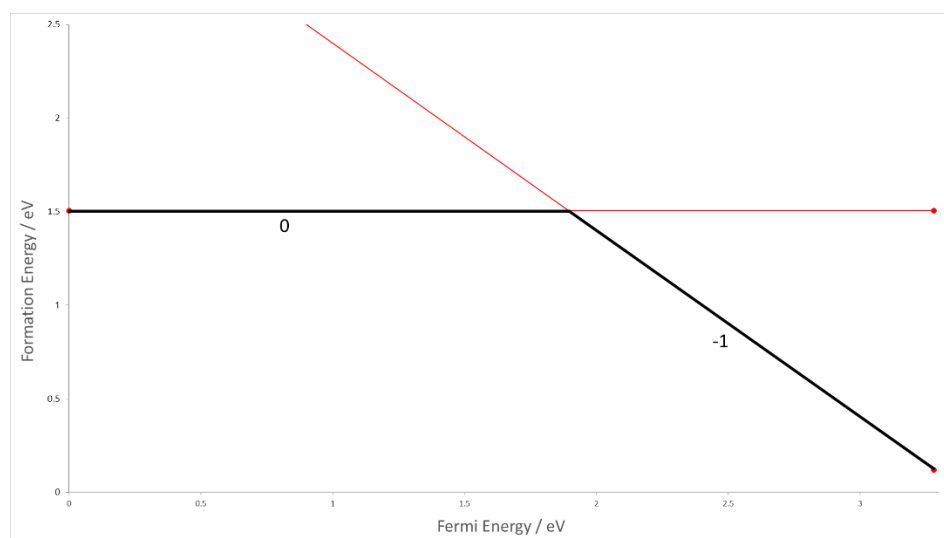


Figure 6.9. Formation energy plot for a single  $P_{bc}$  in configuration a from Figure 6.10a.

As with the  $V_{Si}$  configuration, steric environment, and the local strain play a limited role in the relaxation of the  $P_{bc}$  and the relative stability of the given charge states. The local strain environment affects the two neighbouring Si atoms directly at the interface resulting in only a limited effect for the 3-coordinate C. To make sure a sufficient number of sites were considered, 30 different orientations of the  $P_{bc}$  were calculated, this allows an understanding of the effect of local strain environment on the defect relaxation to be obtained. The variations in HF produced a direct probe of the geometric response of the variation in local strain environment and is highlighted in Appendix B.

From a symmetry perspective, using Figure 6.5 ( $V_{Si}$ ) as a template, there are three degenerate orientations the  $P_{bc}$  may take, each being related by a  $60^\circ$  rotation about the  $c$ -axis. These configurations are energetically equivalent for a given connection scheme, therefore there is no strong direction dependence that would be observed in the EDMR measurements. The average symmetry of the 3-degenerate dangling bonds would be  $C_{3v}$ , and as is the case with  $V_{Si}$ , the peak magnitudes (and

potentially the HF splittings) would be dramatically different as these are based upon the isotopic abundance of the defect atoms.

### 6.5.2.3 Dual Carbon Dangling Bond (Dual- $P_{bc}$ )

The final configuration of interest is the double carbon dangling bond and was found as a result of interface morphology. As described by the TEM results presented in chapter 5, along with previous studies on analogous devices, interface steps propagate in the  $[-1100]$  direction, as this makes a diagonal cut across the surface. This gives rise to both single dangling bonds ( $P_{bc}$ ) and double dangling bonds (dual- $P_{bc}$ ). In considering the genesis of this defect, it can be viewed to have formed in one of two ways, either *via* partial oxidation, or as a result of step bunching. A direct consideration of how this defect may form during the deposition and subsequent oxidative anneal is beyond the scope of this chapter, the understanding of which remains a challenge for the future. The two configurations of this defect are shown in Figure 6.10 and are made up of 2 adjacent weakly correlated  $P_{bc}$  defects, either at a step-edge (Figure 6.10a), or as a result of partial oxidation on a terrace (Figure 6.10b). The step-edge dual- $P_{bc}$  is created by removing the adjacent atoms and then H-capping the facing Si-atoms, creating a single dual- $P_{bc}$  at a step edge.

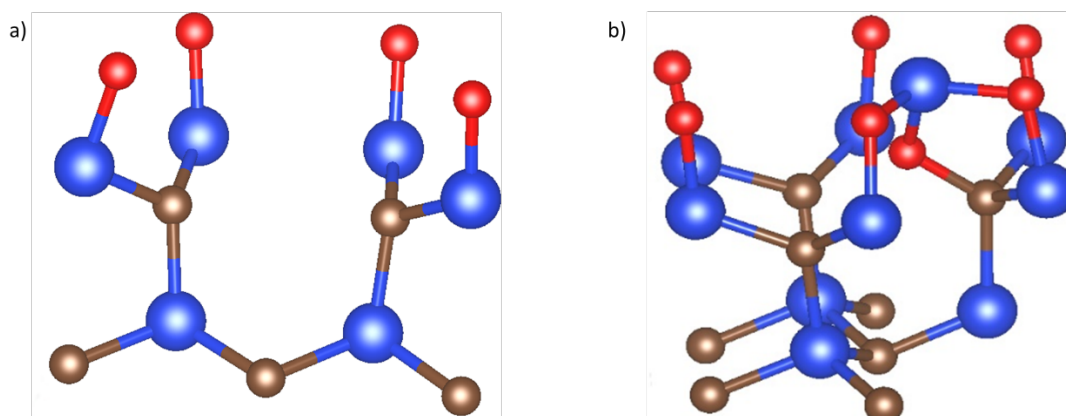


Figure 6.10. The dual- $P_{bc}$  can exist in two forms, that can be viewed as being a result of the stepped interface structure (a), or a result of partial oxidation (b). In each case O is red, Si blue, and C brown.

Both defects have approximately  $C_2$  rotational symmetry individually that when averaged over all sites gives a symmetry of  $C_{3v}$ , which would appear identical to the  $V_{Si}$  and  $P_{bc}$ , giving the angular behaviour described in Figure 6.1. The formation energy plot in Figure 6.12 shows that the defect favours the -1-charge state, for all Fermi level positions but those next to the valence band, where the neutral charge state is favoured, the CTL's are (0/-) at 1.4 eV, and (-/--) at 3.0 eV. The defect configurations shown in Figure 6.10 relax in a similar fashion, which is the same as is described for the  $V_{Si}$  and the  $P_{bc}$ . The two C-dangling bonds relax back into the plane of the neighbouring Si atoms, with a displacement of 0.1 Å compared to the unrelaxed structure.

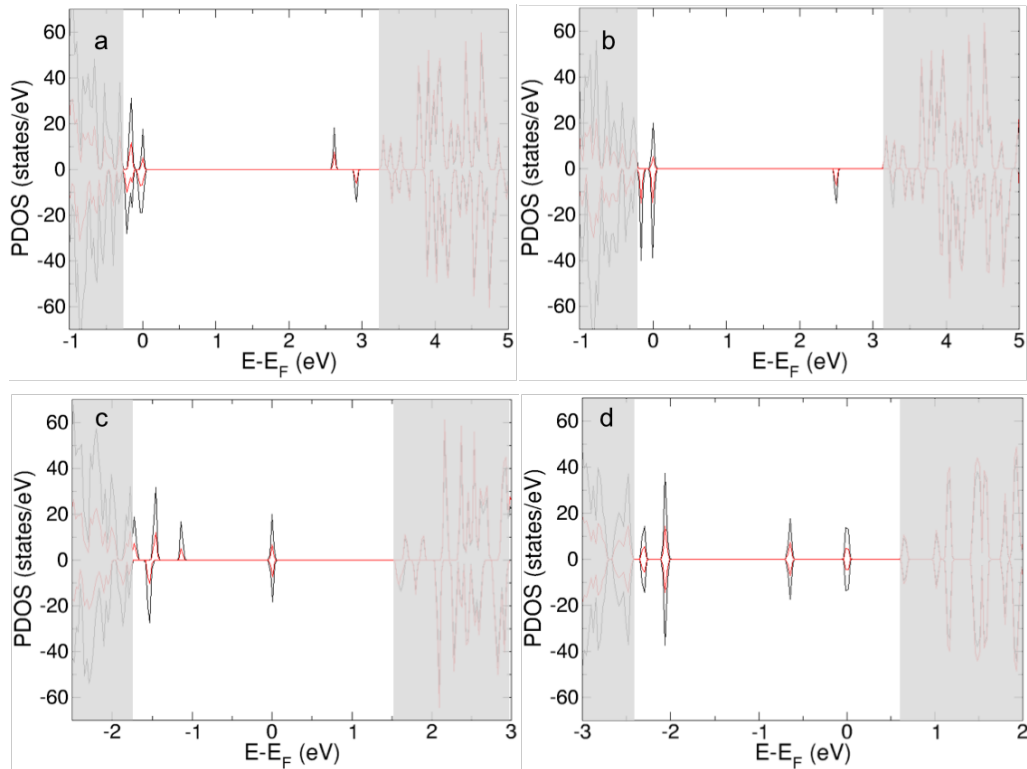


Figure 6.11. PDOS plots for the a) 0-singlet, b) 0-triplet, c) -1-doublet, and d) -2-singlet. The 0 on the x-axis indicates the position of the highest energy electron, those states above the 0 position are unoccupied while those below are occupied. The positive y-values relate to the  $\alpha$ -spin channel, while the negative y-values relate to the  $\beta$ -spin channel. The 4H-SiC band gap is indicated by the non-greyed out area, indicating the number and occupation of the localised gap states associated. The black line represents the C-PDOS and the red line the Si-PDOS.

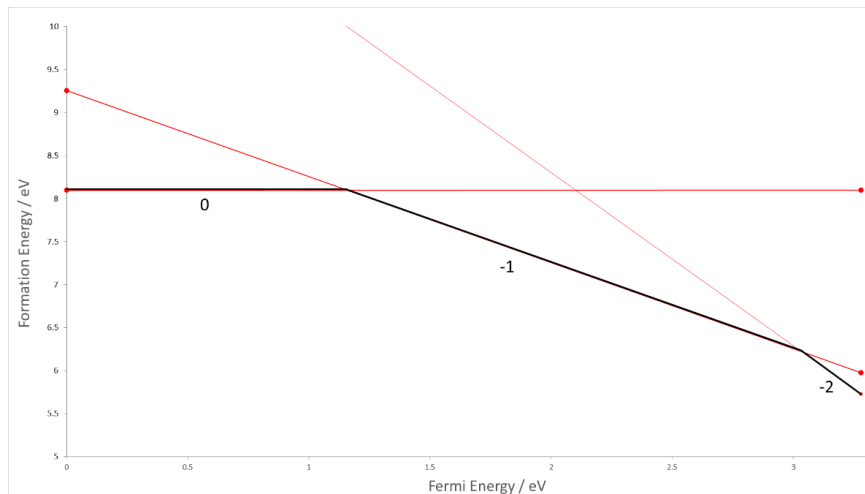


Figure 6.12. Formation energy plot for the double dangling bond defect (dual- $P_{bc}$ ).



The neutral charge state has a low spin (singlet) ground state and as such is diamagnetic and would not be visible to EDMR. However, as with the  $V_{Si}$  the weak interaction between C-dangling bonds leads to an energy difference of 0.04 eV between the singlet and the triplet. As a result, both need to be considered as the relative Boltzmann populations would be 84.4 % and 15.6 % respectively at room temperature. The -1-charge state has a doublet ground state and is paramagnetic and therefore visible to EDMR.

It is important to note that in the case of the dual- $P_{bc}$ , that while the formation energies shown in Figure 6.12 are significantly higher than those for the  $P_{bc}$  and  $V_{Si}$ , these values should be treated with caution. The reason for this is two-fold, firstly, formation energies are only valid for systems that have reached thermodynamic equilibrium, which in the case of deposition and oxidation is far from assured. While the various post-oxidation anneals are expected to move the system closer to equilibrium and significant thermal budgets are provided ( $> 1100$  °C), these temperatures are insufficient to remake the interface. Secondly, the formation energy is very sensitive to the chemical potential selected. In the case of the bulk defect calculations presented in chapter 3 the choice is more straight forward, but at the interface this choice becomes far more complex. This has a meaningful impact on the magnitude of the formation energy ( $y$ -axis), the CTLs are unaffected by this so useful information on the most stable charge state (and multiplicity) for a given Fermi level position can be obtained, whilst defect concentrations in this case cannot.

## 6.6 Comparison between Theory and Experiment

The defects described in the previous section allowed a defect shortlist to be identified for calculation of the HF parameters. These defects are the  $V_{Si}^0$ ,  $V_{Si}^{-1}$ ,  $P_{bc}^0$ , dual- $P_{bc}^0$ ,

dual- $P_{bc}^{-1}$ . The calculated HF for these defects are shown in Table 6.3. These are the mean values averaged over multiple sites for each of the defect configurations, which allows the effect of local strain environment to be understood. Individual plots of the HF parameters of these configurations are presented in Appendix C. As described previously, only the surface Si-atoms show a sensitivity to the local strain environment, the C-dangling bond are accommodated in the layer below the surface leading to only a limited impact. It is important to remember the limitations inherent in the abrupt model presented in this work, and it is possible for strain to have a more significant effect when step bunching is considered.

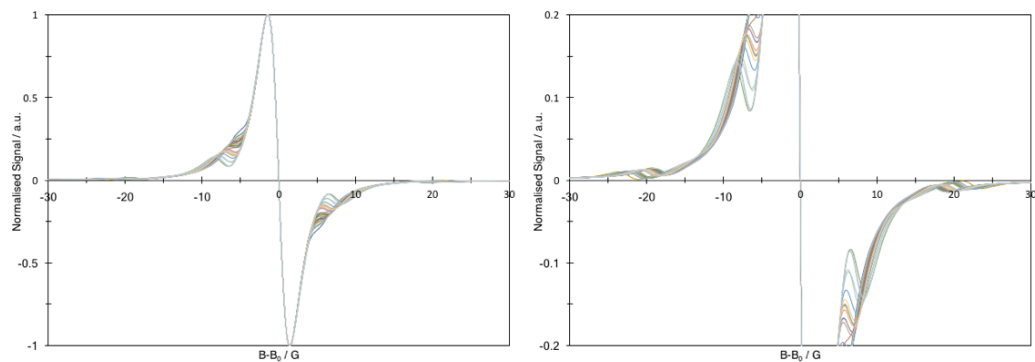


Figure 6.13. The effect  $P_{bc}$  local strain environment has on the calculated HF interaction. The above values sit in a tight range of  $a_c = \pm 4$  G and  $a_{Si} = \pm 2.5$  G.

Figure 6.13 shows the range of HF values that are calculated for the  $P_{bc}$  centre as the local strain environment is varied. This is achieved by placing the defects at different positions at the interface, allowing the proximity to the various connection schemes discussed in chapter 5 to be tested. The C-HF values sit in a tight range between 36 – 44 G with the majority between 37 – 39 G, for the Si-HF values a similar tight range is observed between 9 – 14 G. These values are tabulated in Appendix B along with the individual plots. As is common for all the results here, a Gaussian

broadening of 3 G is added to reflect the experimental conditions, room temperature and an operating device. As there is no robust means of choosing between each of the dangling bond environments, a simple average is taken (Table 6.3).

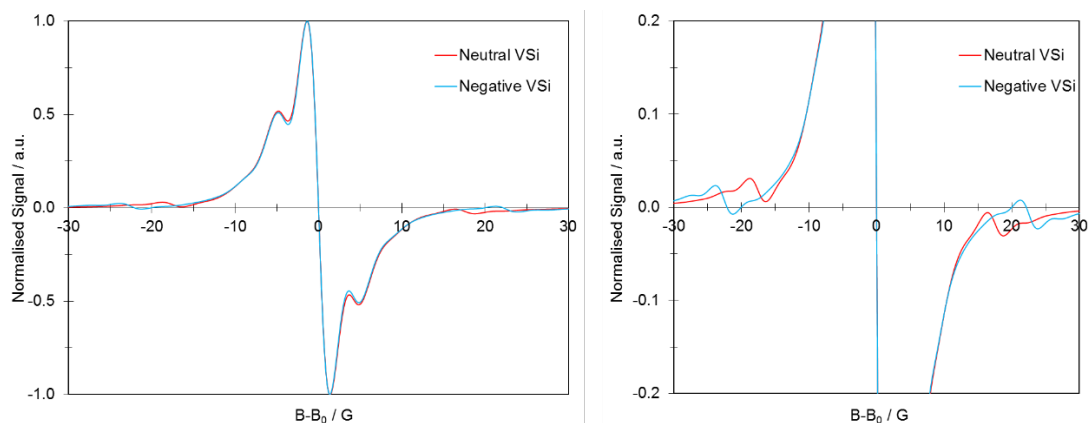


Figure 6.14. HF interaction for the interface  $V_{Si}$  in the neutral and negative charge states showing a similar  $a_{Si}$  regardless of charge state. In the case of the  $a_C$  a more pronounced shift is observed of approximately  $\pm 5$  G between the charge states.

The  $V_{Si}$  shows a similar spectrum to the  $P_{bC}$  (Figure 6.13), the peak intensities are different as this is dictated by the isotopic abundance. The similarities between the defects here are to be expected as they are based upon very similar motifs, with varying numbers of carbon dangling bonds. The HF interactions are shown in Table 6.3, the 5 environments tested varied by less than 1 G showing stability with respect to the different defect configurations shown in Figure 6.8.

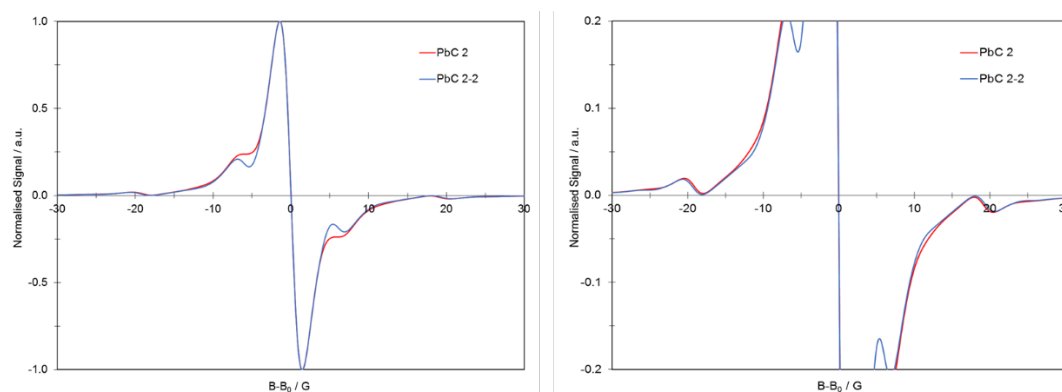


Figure 6.15. HF interactions for the two charge states of the dual- $P_{bc}$ , neutral triplet ( $P_{bc}$  2-2) and negative doublet ( $P_{bc}$  2).

The final configuration considered is the dual- $P_{bc}$  the two accessible charge states show very similar HF interactions with  $<1$  G deviation, Figure 6.15. There are differences between the two configurations, the  $a_{Si}$  show a more pronounced broadening at the step edge (PbC 2-2 from Figure 6.15). This arises from a smaller Si-HF splitting, leading the satellite peaks merge into centre line. In the case of the C-HF, there is next to no deviation between the configurations with less than 0.5 G difference between the two sites. As with the  $P_{bc}$  the two sites are averaged over as shown in Table 6.3, similarly there is no basis to balance between these sites using anything other than an equally weighted mean.

Table 6.3. Average HF splitting's of the shortlisted defects for the defect centre and concentric shells moving radial outwards. In the  $V_{Si}$  case there are 3 x  $C_1$ , 12 x  $Si_2$  and 18 x  $C_3$  the  $C_3$  contribution tends to average to 0. The  $P_{bc}$  has 1 x  $C_1$ , 3 x  $Si_2$ , and 8 x  $C_3$ . The  $P_{bc}^2$  has 2 x  $C_1$ , 6 x  $Si_2$  and 16 x  $C_3$ .

Defect	$C_1 / G$	$Si_2 / G$	$C_3 / G$
$V_{Si}^0$ (Triplet)	35	8.5	1
$V_{Si}^{-1}$ (Doublet)	45	8.0	2
$P_{bc}$ (Doublet)	39	12	2
Dual- $P_{bc}^0$ (Triplet)	40	12	1
Dual- $P_{bc}^{-1}$ (Doublet)	39	10	1

In chapter 3, the defect shortlist could be eliminated based upon an initial inspection of the HF parameters, as each defect is based upon varying numbers of the same motifs. For each of the above defects, plots are shown in Figure 6.16. As before, no fitting parameters are used and 3 G broadening is added to reflect the measurements that were conducted at room temperature on operating devices. No probabilistic cut-offs are required when simulating the EPR spectrum in this case with all lines being considered. All of the spectra share some common features, as they are all based upon extremely similar motifs.

$V_{Si}$ , in either of the charge states (Figure 6.16), shows a HF splitting of approximately the correct magnitude  $a_{Si} = \pm 4.25$  G. This agreement falls apart when the intensity of the peaks are considered, the peak intensity is derived from the isotopic abundance as described in section 3.3.2. Studies that have favoured the  $V_{Si}$  assignment appear to have neglected the peak intensities, and it is hard to understand how this can be reconciled with the data from Table 6.3. This intensity is only altered in samples that have in some way been enriched, which is not the case here. Vague statements are often made about the smearing of peaks to explain away this apparent

discrepancy. The calculated values show that this is not the case here, with the values of  $a_{Si}$  falling into a tight range of  $\pm 2.5$  G.

As a result, the theoretical work calculations have ruled out the interface  $V_{Si}$  in either charge state as a candidate for the defect observed with EDMR. Additionally, as previously discussed, as the *fast passage* measurements identify a defect that is  $V_{Si}$  like, there must be two distinct recombination timescales involved. Only those defects sensitive to the *fast passage* condition ( $1 \ll T_1 \omega_m$ ) are probed by the *fast passage* technique. Defects not meeting this criterion are not probed, even if they represent an efficient recombination path and by extension the dominant recombination defect observed in the non-*fast passage* measurement. The assumption has always been that the non-*fast passage* / *fast passage* measurements are probing the same defect, this need not be the case. From the large differences between the two it would in fact support the view that these defects are distinct and therefore do not both represent the  $V_{Si}$ . The *fast passage* defect is not directly studied here but does appear to match the model for the  $V_{Si}$  proposed by Lenahan *et al.* This is clearly distinct from the defect identified with non-*fast passage* EDMR as this defect cannot be explained using any configuration or combination of configurations of the  $V_{Si}$ . While the magnitude of the HF splittings are reasonable the intensities are 2 – 3 x greater than the observed, which in the absence of isotopic sample enrichment rules out the  $V_{Si}$ . It is beyond the scope of the work presented in this thesis to discuss the genesis of the *fast passage* defect, but it is possible to view the  $P_{bc}$  & dual- $P_{bc}$  as partially oxidised  $V_{Si}$  explaining the presence of both defects at or around the interface.

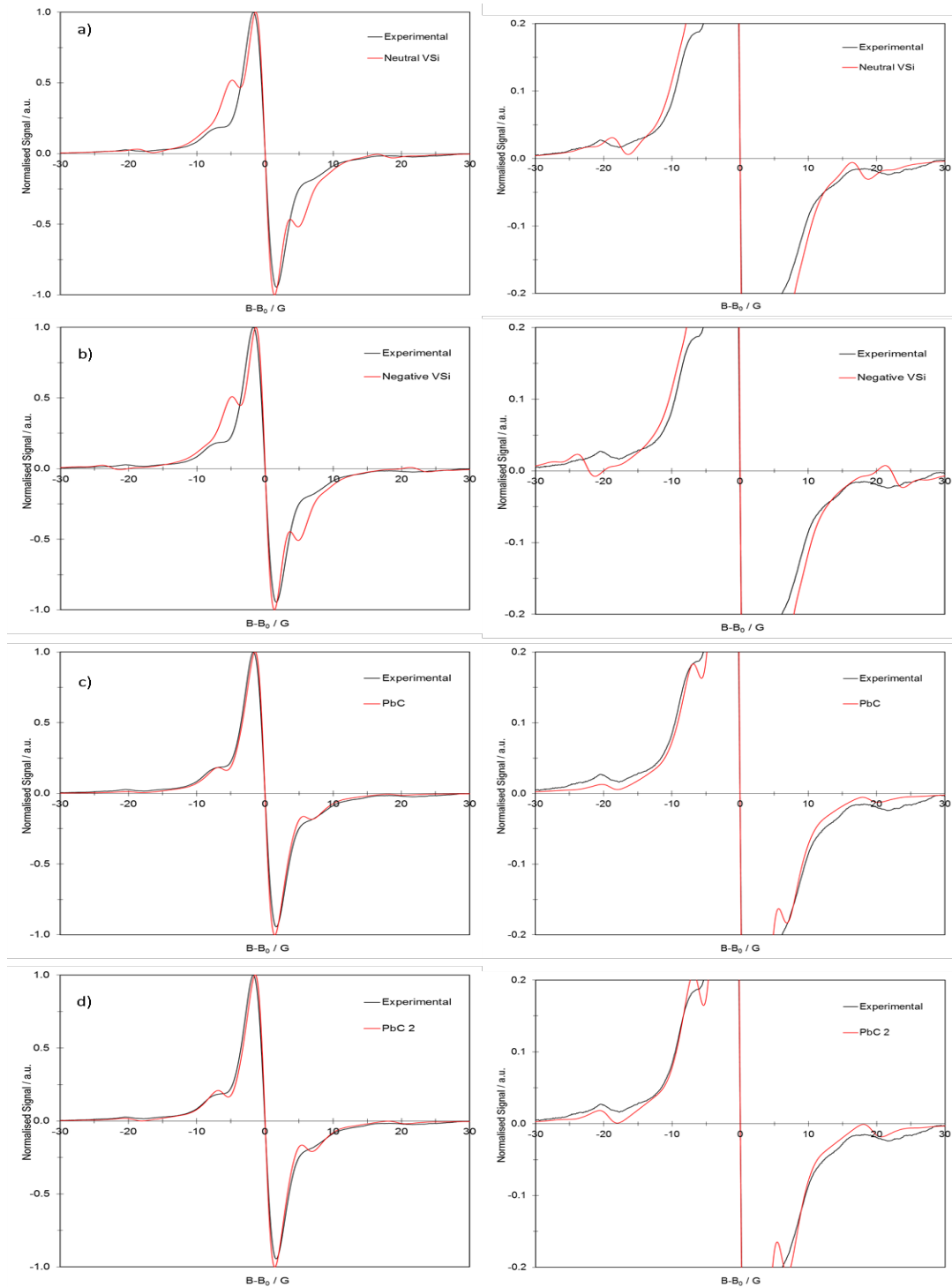


Figure 6.16. A comparison of the EDMR spectra of candidate defects to the EDMR spectrum from the  $O_2$  annealed sample detailed in Figure 6.2 and Table 6.1.

For the  $P_{bc}$  and dual- $P_{bc}$  centres (Figure 6.16) the agreement is much more compelling, once again as with the  $V_{Si}$  the theoretical calculations give atomistic meaning to the experimental features. In this case, the 1 – 2 % intensity features at approximately  $\pm 20$  G relate to the splitting from the 3-coordinate C, accounting for 80 % of the defect spin density. The narrow shoulder features with a 15 – 20 % intensity at  $\pm 6$  G relate to the splitting from the NN Si atoms. The final shell of atoms with non-zero spin relates to the NNN C-atoms, and all of these splitting's are below 1 – 2 G. As such, they contribute to the broadening, but the individual components cannot be resolved.

By considering both the averages (Figure 6.16c and d) and expanding the picture to consider the Max – Min HF interactions (Figure 6.17) both the  $P_{bc}$  and the dual- $P_{bc}$  show excellent agreement with the experimental spectrum. Both the C-HF and the Si-HF interactions are very well reproduced, the broadness relates to the majority of the defects having similar HF values, which are bracketed by the extreme values. This is far more pronounced in the C-HF values as the Si-HF sit in a much narrower range and is illustrated by the C-HF splitting shown in Figure 6.17 where the secondary features of the C-HF are replicated by the extreme values calculated for the  $P_{bc}$ .



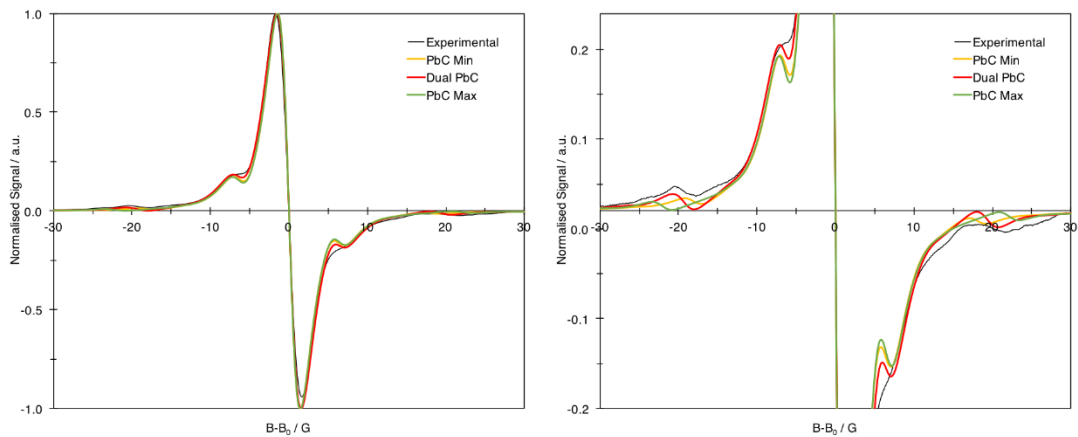


Figure 6.17. A plot of the min-max C-HF interactions, along with the dual- $P_{bC}$  showing an excellent agreement with the observed experimental data. In addition, the secondary features within the C-HF match the magnitude and intensity of the max-min  $P_{bC}$  values.

## 6.7 Conclusion

Through the detailed comparison between the experimental EDMR measurements and *ab initio* calculations, the performance limiting recombination defect observed with EDMR can be identified as a combination of the  $P_{bC}$  and the dual- $P_{bC}$  defects. These defects match the symmetry, HF, and isotopic abundance observed in the experimental spectrum. Critically, these defects are based upon no prior assumptions or fitting to achieve this agreement as is the case with some of the other candidates considered. This identifies a key performance limiting defect that is still prevalent in the current generation of devices. Allowing the  $V_{Si}$  to be discounted and supporting the assignment of Cantin *et al.*[148], [155] for oxidised porous oxides, and the initial assignment of Gruber *et al.*[73], [92], [241] for this system. In the context of the interface described in chapter 5, the highly-stepped nature of the interface can be understood to give rise to a high number of sites where  $P_{bC}$  and dual- $P_{bC}$  could be accommodated. Quantitatively, it is impossible to gauge the concentration of these sites, however, qualitatively from the contrast TEM work of G. Gruber (chapter 5.2)

the interface can be understood to be continuously stepped with a greater area than the observed terraces.

To complete the picture of the  $P_{bc}$  defects presented, an understanding of the deposition oxidation process is needed, and then energetics of formation can be understood in a meaningful context. Once this picture is complete, the logical next step is to extend the approach outlined in chapter 4 to the interface system. This would allow a mechanistic picture of the NO anneal to be developed offering the prospect of making a meaningful impact in the development of the next generation of passivation treatments.

# Chapter 7

## Summary and Future Work

---

### 7.1 Summary

The work presented in this thesis is motivated by the need to identify performance limiting defects within the device context, moving away from the general picture and the laboratory bench. The objective is achieved by starting from the simplest case and then adding complexity in a controlled manner. This has only been possible through the close cooperation of the synthetic, experimental, and theoretical stake holders. This approach allowed for the growth, preparation, and simulation of defects that are directly relevant to technological applications being as the measurements described here were conducted on the highlighted portions of real devices.

Using this approach, in chapter 3 the  $N_C V_{Si}^0$  is identified as the dominant recombination defect in N-implanted *pn*-junctions. This indicates that the high kinetic energies of the implantation process are never entirely healed in the subsequent annealing steps. The implication of this for device performance is two-fold. Firstly, dopant deactivation leads to a significantly lower dopant concentration when compared to the total N-concentration, thereby reducing doping efficiency. Secondly, these defect states introduce deep levels into the band gap of SiC that have implications for both performance and reliability. Having identified the  $N_C V_{Si}^0$  and understanding that directly after implantation the device is subjected to an extremely high temperature anneal, developing an understanding of how the  $N_C V_{Si}$  is formed at the expense of other suggested configurations is a logical next step. This picture is

developed in Chapter 4, taking the  $N_C V_{Si}$  as a starting point and then working backwards to understand how these defects form and accumulate during the dopant activation anneal. This allows a mechanistic understanding of why the  $N_C V_{Si}$  is observed after the post implantation anneal, where the lower energy  $N_C C_{Si}$  is not. The lack of a favourable direct substitution mechanism and limited interstitial diffusion give rise to the formation and accumulation of the  $N_C V_{Si}$ .

In contrast to the implantation defects that can be well approximated by the bulk models used in Chapter 3 and 4, a different approach is required to understand defects at the SiC / SiO<sub>2</sub> interface. The problem of building an appropriate model of the interface is tackled in Chapter 5, where the EELS interface spectrum is deconvoluted using the calculated core-level shifts for a series of abrupt interface motifs. This allows for the interface of interest to be described as abrupt, but highly stepped. The next stage takes these interface motifs and constructs a model system to facilitate defect calculations directly at and just below the interface. This model is then used in chapter 6 to identify the  $P_{bc}$  and double  $P_{bc}$  as the dominant recombination defects observed in the current generation of 4H-SiC MOS devices. This sheds light on an ongoing disagreement in the literature that assigned the same defect to the  $V_{Si}$ . This is demonstrated not to be the case, with the  $V_{Si}$  only being observed with fast passage EDMR, it can thus not be responsible for the main defect observed with EDMR.

## **7.2 Future Work**

The work presented in this thesis shines a light on those defects that are important for the operation and performance of the current and next generation of devices. The findings summarised above are only the start of the story with several logical next

steps from both a modelling and method perspective. The combination of EDMR and *ab initio* calculations is shown to be a powerful tool for defect identification, it does however have a serious limitation only being able to probe paramagnetic defects. All the diamagnetic defects and charge states are as such invisible to EDMR, this makes it vitally important to develop the picture described to encompass diamagnetic defect states. This is a significant challenge requiring the simulation proxies to compare with a variety of experimental techniques (AES, DLTS, and VS).

In a similar vein the model of the interface that is presented here performs extremely well when it comes to interface defect identification. It is however a massive simplification of the interface described by the TEM images, to move towards a model that allows for these features to be described the effects of step bunching would need to be considered and incorporated. This would allow the static picture presented here to be developed along the lines of the N-implantation result presented in Chapter 4, allowing the effect of the post deposition anneals to be described.

# Bibliography

---

- [1] V. Presser and K. G. Nickel, "Silica on Silicon Carbide," *Crit. Rev. Solid State Mater. Sci.*, vol. 33, no. 1, pp. 1–99, Feb. 2008.
- [2] J. Camassel, S. Contreras, and J.-L. Robert, "SiC materials: a semiconductor family for the next century," *Comptes Rendus l'Académie des Sci. - Ser. IV - Phys.*, vol. 1, no. 1, pp. 5–21, 2000.
- [3] F. Bechstedt *et al.*, "Polytypism and Properties of Silicon Carbide," *Phys. Status Solidi*, vol. 202, no. 1, pp. 35–62, 1997.
- [4] H. M. Otte and A. G. Crocker, "Crystallographic Formulae for Hexagonal Lattices," *Phys. Status Solidi*, vol. 9, no. 2, pp. 441–450, 1965.
- [5] T. Kimoto, Z. Y. Chen, S. Tamura, S. Nakamura, N. Onojima, and H. Matsunami, "Surface morphological structures of 4H-, 6H- and 15R-SiC (0001) epitaxial layers grown by chemical vapor deposition," *Jpn. J. Appl. Phys.*, vol. 40, no. 5, pp. 3315–3319, 2001.
- [6] W. Y. Ching, Y. N. Xu, P. Rulis, and L. Ouyang, "The electronic structure and spectroscopic properties of 3C, 2H, 4H, 6H, 15R and 21R polymorphs of SiC," *Mater. Sci. Eng. A*, vol. 422, no. 1–2, pp. 147–156, 2006.
- [7] M. N. Yoder, "Wide bandgap semiconductor materials and devices," *IEEE Trans. Electron Devices*, vol. 43, no. 10, pp. 1633–1636, 1996.
- [8] W. C. Lien, N. Damrongplasit, J. H. Paredes, D. G. Senesky, T. J. K. Liu, and A. P. Pisano, "4H-SiC N-channel JFET for operation in high-temperature environments," *IEEE J. Electron Devices Soc.*, vol. 2, no. 6, pp. 164–167, 2014.
- [9] W. C. Lien, S. Q. Shao, A. Maralani, J. C. Cheng, K. L. Dorsey, and A. P. Pisano, "4H-Silicon Carbide p-n Diode for High Temperature (600°C) Environment Applications," *Silicon Carbide Relat. Mater. 2014*, vol. 821, pp. 636–639, 2015.
- [10] S. Sriram *et al.*, "4H-SiC MESFET's with 42 GHz  $f_{max}$ ," *IEEE Electron Device Lett.*, vol. 17, no. 7, pp. 369–371, 1996.
- [11] B. M. Epelbaum, O. Filip, and A. Winnacker, "Bulk and epitaxial growth of micropipe-free silicon carbide on basal and rhombohedral plane seeds," *Phys. Status Solidi Basic Res.*, vol. 245, no. 7, pp. 1257–1271, 2008.
- [12] Y. M. Tairov and V. F. Tsvetkov, "Investigation of growth processes of ingots of silicon carbide single crystals," *J. Cryst. Growth*, vol. 43, no. 2, pp. 209–212, 1978.
- [13] J. W. Palmour, L. A. Lipkin, R. Singh, D. B. Slater, A. V Suvorov, and C. H. Carter, "SiC device technology : remaining issues," *Diam. Relat. Mater.*, vol. 6, no. 97, pp. 1400–1404, 1997.
- [14] D. Hofmann, M. Bickermann, W. Hartung, and A. Winnacker, "Analysis on the

- Formation and Elimination of Filamentary and Planar Voids in Silicon Carbide Bulk Crystals,” *Mater. Sci. Forum*, vol. 338–342, pp. 445–448, 2000.
- [15] M. Katsuno, N. Ohtani, T. Fujimoto, T. Aigo, and H. Yashiro, “Evolution of Crystal Mosaicity during Physical Vapor Transport Growth of SiC,” *Mater. Sci. Forum*, vol. 389–393, pp. 55–58, 2002.
- [16] R. Singh, “Reliability and performance limitations in SiC power devices,” in *Microelectronics Reliability*, 2006, vol. 46, no. 5–6, pp. 713–730.
- [17] M. Dudley *et al.*, “The mechanism of micropipe nucleation at inclusions in silicon carbide,” *Appl. Phys. Lett.*, vol. 75, no. 6, p. 784, 1999.
- [18] S. Seshadri, G. W. Eldridge, and A. K. Agarwal, “Comparison of the annealing behavior of high-dose nitrogen-, aluminum-, and boron-implanted 4H-SiC,” *Appl. Phys. Lett.*, vol. 72, no. 16, p. 2026, 1998.
- [19] I. G. Ivanov, B. Magnusson, and E. Janzén, “Optical selection rules for shallow donors in 4H-SiC and ionization energy of the nitrogen donor at the hexagonal site,” *Phys. Rev. B - Condens. Matter Mater. Phys.*, vol. 67, no. 16, pp. 1652121–1652125, 2003.
- [20] Y. Negoro, T. Kimoto, and H. Matsunami, “Carrier compensation near tail region in aluminum- or boron-implanted 4H-SiC (0001),” *J. Appl. Phys.*, vol. 98, no. 4, p. 43709, 2005.
- [21] D. Panknin, H. Wirth, A. Mu, and W. Skorupa, “Correlation of electrical and microstructural properties after high dose aluminium implantation into 6H-SiC,” *Mater. Sci. Eng. B*, vol. 62, no. 1999, pp. 363–367, 2000.
- [22] M. A. Capano, J. A. Cooper Jr., M. R. Melloch, A. Saxler, and W. C. Mitchel, “Ionization energies and electron mobilities in phosphorus- and nitrogen-implanted 4H-silicon carbide,” *J. Appl. Phys.*, vol. 87, no. 12, p. 2000, 2000.
- [23] J. B. Tucker *et al.*, “Material and n-p junction characteristics of As- and Sb-implanted SiC,” *Diam. Relat. Mater.*, vol. 9, no. 11, pp. 1887–1896, 2000.
- [24] I. G. Ivanov, A. Henry, and E. Janzén, “Ionization energies of phosphorus and nitrogen donors and aluminum acceptors in 4H silicon carbide from the donor-acceptor pair emission,” *Phys. Rev. B - Condens. Matter Mater. Phys.*, vol. 71, no. 24, p. 241201, 2005.
- [25] A. Nakao, M. Iwaki, H. Sakairi, and K. Terasima, “XPS characterization of nitrogen implanted silicon carbide,” *Nucl. Inst. Methods Phys. Res. B*, vol. 65, no. 1–4, pp. 352–356, 1992.
- [26] D. Åberg, A. Hallén, P. Pellegrino, and B. G. Svensson, “Nitrogen deactivation by implantation-induced defects in 4H-SiC epitaxial layers,” *Appl. Phys. Lett.*, vol. 78, no. 19, pp. 2908–2910, 2001.
- [27] Y. Hirano and T. Inada, “Nitrogen implantation in (100)- $\beta$ -SiC layers grown on

- Si substrate,” *J. Appl. Phys.*, vol. 77, no. 3, pp. 1020–1028, 1995.
- [28] J. Cottom *et al.*, “Recombination centers in 4H-SiC investigated by electrically detected magnetic resonance and ab initio modeling,” *J. Appl. Phys.*, vol. 119, no. 18, 2016.
- [29] J. Cottom, G. Gruber, G. Pobegen, T. Aichinger, and A. L. Shluger, “Identifying Performance Limiting Defects in Silicon Carbide pn- junctions A Theoretical Study,” *Mater. Sci. Forum*, vol. 858, pp. 257–260, 2016.
- [30] G. Pensl *et al.*, “Alternative techniques to reduce interface traps in n-type 4H-SiC MOS capacitors,” *Phys. Status Solidi Basic Res.*, vol. 245, no. 7, pp. 1378–1389, 2008.
- [31] V. V. Afanas’ev, M. Bassler, G. Pensl, and M. Schulz, “Intrinsic SiC/SiO<sub>2</sub> Interface States,” *Phys. Status Solidi*, vol. 162, no. 1, pp. 321–337, 1997.
- [32] K. Ueno, R. Asai, and T. Tsuji, “4H-SiC MOSFET’s utilizing the H<sub>2</sub> surface cleaning technique,” *IEEE Electron Device Lett.*, vol. 19, no. 7, pp. 244–246, 1998.
- [33] J. Rozen, A. C. Ahyi, X. Zhu, J. R. Williams, and L. C. Feldman, “Scaling between channel mobility and interface state density in SiC MOSFETs,” *IEEE Trans. Electron Devices*, vol. 58, no. 11, pp. 3808–3811, 2011.
- [34] F. Roccaforte, P. Fiorenza, and F. Giannazzo, “Impact of the morphological and electrical properties of SiO<sub>2</sub>/4H-SiC interfaces on the behavior of 4H-SiC MOSFETs,” *ECS J. Solid State Sci. Technol.*, vol. 2, no. 8, pp. N3006–N3011, 2013.
- [35] S. Potbhare, N. Goldsman, G. Pennington, A. Lelis, and J. M. McGarrity, “Numerical and experimental characterization of 4H-silicon carbide lateral metal-oxide-semiconductor field-effect transistor,” *J. Appl. Phys.*, vol. 100, no. 4, p. 44515, 2006.
- [36] A. Salinaro *et al.*, “Charge pumping measurements on differently passivated lateral 4H-SiC MOSFETs,” *IEEE Trans. Electron Devices*, vol. 62, no. 1, pp. 155–163, 2015.
- [37] J. Rozen, “ELECTRONIC PROPERTIES AND RELIABILITY OF THE SiO<sub>2</sub>/SiC INTERFACE,” Vanderbilt University, 2008.
- [38] T. Ono and S. Saito, “First-principles study on the effect of SiO<sub>2</sub> layers during oxidation of 4H-SiC,” *Appl. Phys. Lett.*, vol. 106, no. 8, 2015.
- [39] M. Bassler, G. Pensl, and V. V. Afanas’ev, “‘Carbon cluster model’ for electronic states at SiC / SiO<sub>2</sub> interfaces,” *Diam. Relat. Mater.*, vol. 6, no. 10, pp. 1472–1475, 1997.
- [40] G. G. Jernigan, R. E. Stahlbush, and N. S. Saks, “Effect of oxidation and reoxidation on the oxide-substrate interface of 4H-and 6H-SiC,” *Appl. Phys.*



- Lett.*, vol. 77, no. 10, pp. 1437–1439, 2000.
- [41] T. Zheleva, A. Lelis, G. Duscher, F. Liu, I. Levin, and M. Das, “Transition layers at the SiO<sub>2</sub>/SiC interface,” *Appl. Phys. Lett.*, vol. 93, no. 2, p. 22108, 2008.
- [42] T. L. Biggerstaff *et al.*, “Relationship between 4H-SiC/SiO<sub>2</sub> transition layer thickness and mobility,” *Appl. Phys. Lett.*, vol. 95, no. 3, p. 32108, 2009.
- [43] S. Dhar *et al.*, “Effect of nitric oxide annealing on the interface trap density near the conduction bandedge of 4H-SiC at the oxide/(1120) 4H-SiC interface,” *Appl. Phys. Lett.*, vol. 84, no. 9, pp. 1498–1500, 2004.
- [44] J. M. Knaup, P. Deák, T. Frauenheim, A. Gali, Z. Hajnal, and W. J. Choyke, “Theoretical study of the mechanism of dry oxidation of 4H-SiC,” *Phys. Rev. B - Condens. Matter Mater. Phys.*, vol. 71, no. 23, p. 235321, 2005.
- [45] J. M. Knaup, P. Deák, T. Frauenheim, A. Gali, Z. Hajnal, and W. J. Choyke, “Defects in SiO<sub>2</sub> as the possible origin of near interface traps in the SiC SiO<sub>2</sub> system: A systematic theoretical study,” *Phys. Rev. B - Condens. Matter Mater. Phys.*, vol. 72, no. 11, p. 115323, 2005.
- [46] I. Iskandarova, K. Khromov, A. Knizhnik, and B. Potapkin, “The role of neutral point defects in carrier mobility degradation in bulk 4H-SiC and at 4H-SiC/SiO<sub>2</sub> interface: First-principles investigation using Green’s functions,” *J. Appl. Phys.*, vol. 117, no. 17, p. 175703, 2015.
- [47] P. Liu *et al.*, “Roughness of the SiC/SiO<sub>2</sub> vicinal interface and atomic structure of the transition layers,” *J. Vac. Sci. Technol. A Vacuum, Surfaces, Film.*, vol. 32, no. 6, p. 60603, 2014.
- [48] J. A. Taillon *et al.*, “Systematic structural and chemical characterization of the transition layer at the interface of NO-annealed 4H-SiC/SiO<sub>2</sub> metal-oxide-semiconductor field-effect transistors,” *J. Appl. Phys.*, vol. 113, no. 4, p. 44517, 2013.
- [49] J. A. Taillon *et al.*, “Characterization of the Oxide-Semiconductor Interface in 4H-SiC/SiO<sub>2</sub> Structures using TEM and XPS,” *Microsc. Microanal.*, vol. 21, no. S3, pp. 1537–1538, 2015.
- [50] T. Hatakeyama, H. Matsuhata, T. Suzuki, T. Shinohe, and H. Okumura, “Microscopic Examination of SiO<sub>2</sub>/4H-SiC Interfaces,” *Mater. Sci. Forum*, vol. 679–680, pp. 330–333, 2011.
- [51] T. Kimoto, H. Kawano, M. Noborio, J. Suda, and H. Matsunami, “Improved Dielectric and Interface Properties of 4H-SiC MOS Structures Processed by Oxide Deposition and N<sub>2</sub>O Annealing,” *Mater. Sci. Forum*, vol. 527–529, pp. 987–990, 2006.
- [52] Y. Wang *et al.*, “The effect of gate oxide processes on the performance of 4H-SiC MOSFETs and gate-controlled diodes,” *IEEE Trans. Electron Devices*, vol. 55, no. 8, pp. 2046–2053, 2008.

- [53] R. Schörner, P. Friedrichs, D. Peters, and D. Stephani, "Significantly improved performance of MOSFET's on silicon carbide using the 15R-SiC polytype," *IEEE Electron Device Lett.*, vol. 20, no. 5, pp. 241–244, 1999.
- [54] J. J. A. Cooper, M. R. Melloch, R. Singh, A. Agarwal, and J. W. Palmour, "Status and prospects for SiC power MOSFETs," *IEEE Trans. Electron Devices*, vol. 49, no. 4, pp. 658–664, 2002.
- [55] W. Shockley and W. T. Read, "Statistics of the Recombination of Holes and Electrons," *Phys. Rev.*, vol. 87, no. 5, pp. 835–842, 1952.
- [56] R. N. Hall, "Electron-Hole Recombination in Germanium," *Phys. Rev.*, vol. 87, p. 387, 1952.
- [57] P. Deák, J. M. Knaup, T. Hornos, C. Thill, A. Gali, and T. Frauenheim, "The mechanism of defect creation and passivation at the SiC/SiO<sub>2</sub> interface," *J. Phys. D. Appl. Phys.*, vol. 40, no. 20, pp. 6242–6253, Oct. 2007.
- [58] F. Devynck, A. Alkauskas, P. Broqvist, and A. Pasquarello, "Charge transition levels of carbon-, oxygen-, and hydrogen-related defects at the SiC/SiO<sub>2</sub> interface through hybrid functionals," *Phys. Rev. B*, vol. 84, no. 23, p. 235320, Dec. 2011.
- [59] S. Salemi, A. Akturk, S. Potbhare, A. J. Lelis, and N. Goldsman, "Total Near Interface Trap Density Calculation of 4H-SiC/SiO<sub>2</sub> Structures before and after Nitrogen Passivation," *Mater. Sci. Forum*, vol. 717–720, pp. 457–460, May 2012.
- [60] S. Salemi, A. Akturk, S. Potbhare, A. Lelis, and N. Goldsman, "The effect of different passivations on near interface trap density of 4H-SiC/SiO<sub>2</sub> structures," *2011 Int. Semicond. Device Res. Symp. ISDRS*, pp. 1–2, 2011.
- [61] T. E. Rudenko, I. N. Osiyuk, I. P. Tyagulski, H. Ö. Ólafsson, and E. Ö. Sveinbjörnsson, "Interface trap properties of thermally oxidized n-type 4H-SiC and 6H-SiC," *Solid. State. Electron.*, vol. 49, no. 4, pp. 545–553, 2005.
- [62] A.-M. El-Sayed, M. B. Watkins, T. Grasser, V. V. Afanas'ev, and A. L. Shluger, "Hydrogen-Induced Rupture of Strained Si-O Bonds in Amorphous Silicon Dioxide," *Phys. Rev. Lett.*, vol. 114, no. 11, p. 115503, 2015.
- [63] G. Y. Chung *et al.*, "Effect of nitric oxide annealing on the interface trap densities near the band edges in the 4H polytype of silicon carbide," *Appl. Phys. Lett.*, vol. 76, no. 13, pp. 1713–1715, 2000.
- [64] P. Jamet, S. Dimitrijevic, and P. Tanner, "Effects of nitridation in gate oxides grown on 4H-SiC," *J. Appl. Phys.*, vol. 90, no. 10, pp. 5058–5063, 2001.
- [65] G. Liu *et al.*, "Enhanced inversion mobility on 4H-SiC (1120) using phosphorus and nitrogen interface passivation," *IEEE Electron Device Lett.*, vol. 34, no. 2, pp. 181–183, 2013.

- [66] T. Umeda *et al.*, "Behavior of nitrogen atoms in SiC-SiO<sub>2</sub> interfaces studied by electrically detected magnetic resonance," *Appl. Phys. Lett.*, vol. 99, no. 14, p. 142105, 2011.
- [67] J. Houston Dycus, W. Xu, D. J. Lichtenwalner, B. Hull, J. W. Palmour, and J. M. LeBeau, "Structure and chemistry of passivated SiC/SiO<sub>2</sub> interfaces," *Appl. Phys. Lett.*, vol. 108, no. 20, p. 201607, 2016.
- [68] P. Jamet and S. Dimitrijević, "Physical properties of N<sub>2</sub>O and NO-nitrided gate oxides grown on 4H SiC," *Appl. Phys. Lett.*, vol. 79, no. 3, pp. 323–325, 2001.
- [69] Y. Xu *et al.*, "Atomic state and characterization of nitrogen at the SiC/SiO<sub>2</sub> interface," *J. Appl. Phys.*, vol. 115, no. 3, p. 33502, 2014.
- [70] R. Kosugi, T. Umeda, and Y. Sakuma, "Fixed nitrogen atoms in the SiO<sub>2</sub>/SiC interface region and their direct relationship to interface trap density," *Appl. Phys. Lett.*, vol. 99, no. 18, p. 182111, 2011.
- [71] K. C. Chang *et al.*, "High-resolution elemental profiles of the silicon dioxide 4H-silicon carbide interface," *J. Appl. Phys.*, vol. 97, no. 10, p. 104920, 2005.
- [72] H. Shiomi *et al.*, "Electrical and physical characterizations of the effects of oxynitridation and wet oxidation at the interface of SiO<sub>2</sub>/4H-SiC(0001) and (0001)," *Jpn. J. Appl. Phys.*, vol. 55, no. 4, p. 04ER19-1-6, 2016.
- [73] G. Gruber, "Performance and Reliability Limiting Point Defects in SiC Power Devices," Technische Universität Graz, 2016.
- [74] J. Rozen, S. Dhar, M. E. Zvanut, J. R. Williams, and L. C. Feldman, "Density of interface states, electron traps, and hole traps as a function of the nitrogen density in SiO<sub>2</sub> on SiC," *J. Appl. Phys.*, vol. 105, no. 12, p. 124506, 2009.
- [75] H. Yoshioka, T. Nakamura, and T. Kimoto, "Generation of very fast states by nitridation of the SiO<sub>2</sub>/SiC interface," *J. Appl. Phys.*, vol. 112, no. 2, p. 24520, 2012.
- [76] G. Rescher, G. Pobegen, and T. Aichinger, "Impact of Nitric Oxide Post Oxidation Anneal on the Bias Temperature Instability and the On-Resistance of 4H-SiC nMOSFETs," *Mater. Sci. Forum*, vol. 821–823, pp. 709–712, 2015.
- [77] P. Fiorenza *et al.*, "Comparative study of gate oxide in 4H-SiC lateral MOSFETs subjected to post-deposition-annealing in N<sub>2</sub>O and POCl<sub>3</sub>," *Appl. Phys. A Mater. Sci. Process.*, vol. 115, no. 1, pp. 333–339, 2014.
- [78] R. Morishita, H. Yano, D. Okamoto, T. Hatayama, and T. Fuyuki, "Effect of POCl<sub>3</sub> Annealing on Reliability of Thermal Oxides Grown on 4H-SiC," *Mater. Sci. Forum*, vol. 717–720, pp. 739–742, 2012.
- [79] M. Hundhausen, R. Püsche, J. Röhrli, and L. Ley, "Characterization of defects in silicon carbide by Raman spectroscopy," *Phys. Status Solidi Basic Res.*, vol. 245, no. 7, pp. 1356–1368, 2008.

- [80] H. Itoh *et al.*, “Intrinsic Defects in Cubic Silicon Carbide,” *Phys. Status Solidi*, vol. 162, no. 1, pp. 173–198, 1997.
- [81] J. A. Weil, J. R. Bolton, and J. E. Wertz, *Electron Paramagnetic Resonance - Elementary Theory and Practical Applications*. Wiley Interscience, 1994.
- [82] T. Wimbauer, B. K. Meyer, A. Hofstaetter, A. Scharmann, and H. Overhof, “Negatively charged Si vacancy in 4H SiC: A comparison between theory and experiment,” vol. 56, no. 12, pp. 7384–7388, 1997.
- [83] L. Torpo, M. Marlo, T. E. M. Staab, and R. M. Nieminen, “Comprehensive ab initio study of properties of monovacancies and antisites in 4H-SiC,” *J. Phys. Condens. Matter*, vol. 13, no. 13, pp. 6203–6231, 2001.
- [84] L. Torpo, T. E. M. Staab, and R. M. Nieminen, “Divacancy in 3C– and 4H–SiC: An extremely stable defect,” *Phys. Rev. B*, vol. 65, no. 8, p. 85202, 2002.
- [85] M. Bockstedte, A. Mattausch, and O. Pankratov, “Ab initio study of the annealing of vacancies and interstitials in cubic SiC: Vacancy-interstitial recombination and aggregation of carbon interstitials,” *Phys. Rev. B - Condens. Matter Mater. Phys.*, vol. 69, no. 23, pp. 1–13, 2004.
- [86] M. Bockstedte, M. Heid, and O. Pankratov, “Signature of intrinsic defects in SiC: Ab initio calculations of hyperfine tensors,” *Phys. Rev. B*, vol. 67, no. 19, pp. 3–6, 2003.
- [87] T. Umeda, J. Ishoya, T. Ohshima, N. Morishita, H. Itoh, and A. Gali, “Identification of positively charged carbon antisite-vacancy pairs in 4H-SiC,” *Phys. Rev. B - Condens. Matter Mater. Phys.*, vol. 75, no. 24, p. 245202, 2007.
- [88] B. Aradi *et al.*, “Ab initio density-functional supercell calculations of hydrogen defects in cubic SiC,” *Phys. Rev. B*, vol. 63, no. 24, pp. 1–19, May 2001.
- [89] T. Umeda *et al.*, “Identification of the carbon antisite-vacancy pair in 4H-SiC,” *Phys. Rev. Lett.*, vol. 96, no. 14, pp. 14–17, 2006.
- [90] J. Isoya, T. Umeda, N. Mizuochi, N. T. Son, E. Janzén, and T. Ohshima, “EPR identification of intrinsic defects in SiC,” *Phys. Status Solidi Basic Res.*, vol. 245, no. 7, pp. 1298–1314, 2008.
- [91] C. J. Cochrane, P. M. Lenahan, and A. J. Lelis, “An electrically detected magnetic resonance study of performance limiting defects in SiC metal oxide semiconductor field effect transistors,” *J. Appl. Phys.*, vol. 109, no. 1, p. 14506, 2011.
- [92] G. Gruber, P. Hadley, M. Koch, and T. Aichinger, “Electrically detected magnetic resonance study of defects created by hot carrier stress at the SiC/SiO<sub>2</sub> interface of a SiC n-channel metal-oxide-semiconductor field-effect transistor,” *Appl. Phys. Lett.*, vol. 105, no. 4, p. 43506, 2014.
- [93] U. Gerstmann *et al.*, “Nitrogen Donor Aggregation in 4H-SiC: g-Tensor

- Calculations,” *Mater. Sci. Forum*, vol. 556–557, pp. 391–394, 2007.
- [94] K. Szász, X. T. Trinh, N. T. Son, E. Janzén, and A. Gali, “Theoretical and electron paramagnetic resonance studies of hyperfine interaction in nitrogen doped 4H and 6H SiC,” *J. Appl. Phys.*, vol. 115, no. 7, p. 73705, 2014.
- [95] T. Umeda, J. Isoya, N. Morishita, T. Ohshima, and T. Kamiya, “EPR identification of two types of carbon vacancies in 4H-SiC,” *Phys. Rev. B*, vol. 69, p. 121201, 2004.
- [96] J. R. Weber *et al.*, “Defects in SiC for quantum computing,” *J. Appl. Phys.*, vol. 109, no. 10, pp. 12–17, 2011.
- [97] W. F. Koehl, B. B. Buckley, F. J. Heremans, G. Calusine, and D. D. Awschalom, “Room temperature coherent control of defect spin qubits in silicon carbide,” *Nature*, vol. 479, p. 84, 2011.
- [98] L. Gordon, A. Janotti, and C. G. Van de Walle, “Defects as qubits in 3C- and 4H-SiC,” *Phys. Rev. B*, vol. 92, no. 4, p. 45208, 2015.
- [99] M. Widmann *et al.*, “Coherent control of single spins in silicon carbide at room temperature,” *Nat. Mater.*, vol. 14, no. 2, p. 164, 2015.
- [100] H. J. von Bardeleben, J. L. Cantin, E. Rauls, and U. Gerstmann, “Identification and magneto-optical properties of the NV center in 4H-SiC,” *Phys. Rev. B*, vol. 92, no. 6, p. 64104, 2015.
- [101] M. Bockstedte, A. Gali, A. Mattausch, O. Pankratov, and J. W. Steeds, “Identification of intrinsic defects in SiC: Towards an understanding of defect aggregates by combining theoretical and experimental approaches,” *Phys. Status Solidi Basic Res.*, vol. 245, no. 7, pp. 1281–1297, 2008.
- [102] S. B. Zhang and J. E. Northrup, “Chemical potential dependence of defect formation energies in GaAs: Application to Ga self-diffusion,” *Phys. Rev. Lett.*, vol. 67, no. 17, pp. 2339–2342, 1991.
- [103] P. G. Baranov, I. V. Ilyin, A. A. Soltamova, and E. N. Mokhov, “Identification of the carbon antisite in SiC: EPR of C13 enriched crystals,” *Phys. Rev. B - Condens. Matter Mater. Phys.*, vol. 77, no. 8, pp. 1–5, 2008.
- [104] N. T. Son, P. N. Hai, and E. Janzén, “Silicon Antisite in 4H SiC,” *Phys. Rev. Lett.*, vol. 87, no. 4, p. 45502, 2001.
- [105] T. Liao, O. N. Bedoya-Martínez, and G. Roma, “Stoichiometric Defects in Silicon Carbide,” *J. Phys. Chem. C*, vol. 114, no. 51, pp. 22691–22696, 2010.
- [106] A. Mattausch, “Ab initio-Theory of Point Defects and Defect Complexes in SiC,” Friedrich-Alexander-Universität, 2007.
- [107] A. Mattausch, M. Bockstedte, and O. Pankratov, “Self Diffusion in SiC: the Role of Intrinsic Point Defects,” *Mater. Sci. Forum*, vol. 353–356, pp. 323–326, 2001.

- [108] M. Bockstedte, A. Gali, T. Umeda, N. T. Son, J. Isoya, and E. Janzén, “Signature of the Negative Carbon Vacancy-Antisite Complex,” vol. 529, pp. 539–542, 2006.
- [109] T. Umeda *et al.*, “EPR and theoretical studies of positively charged carbon vacancy in 4H-SiC,” *Phys. Rev. B - Condens. Matter Mater. Phys.*, vol. 70, no. 23, pp. 1–6, 2004.
- [110] T. Umeda *et al.*, “EPR and theoretical studies of negatively charged carbon vacancy in 4H-SiC,” *Phys. Rev. B*, vol. 71, no. 19, p. 193202, 2005.
- [111] N. T. Son *et al.*, “The Carbon Vacancy Related E14 Defect in 4H-SiC,” *Mater. Sci. Forum*, vol. 645–648, pp. 399–402, 2010.
- [112] N. T. Son, P. N. Hai, and E. Janzén, “Carbon vacancy-related defect in 4H and 6H SiC,” *Phys. Rev. B*, vol. 63, no. 20, p. 201201, 2001.
- [113] K. Kawahara, X. Thang Trinh, N. T. Son, E. Janzén, J. Suda, and T. Kimoto, “Quantitative comparison between Z1/2 center and carbon vacancy in 4H-SiC,” *J. Appl. Phys.*, vol. 115, no. 14, 2014.
- [114] E. Rauls, T. Lingner, Z. Hajnal, S. Greulich-Weber, T. Frauenheim, and J.-M. Spaeth, “Metastability of the Neutral Silicon Vacancy in 4H-SiC,” *Phys. Stat. Sol.*, vol. 217, pp. R1–R3, 2000.
- [115] E. Rauls, T. Frauenheim, A. Gali, and P. Deák, “Theoretical study of vacancy diffusion and vacancy-assisted clustering of antisites in SiC,” *Phys. Rev. B*, vol. 68, no. 15, p. 155208, Oct. 2003.
- [116] E. Sörman, N. Son, W. Chen, O. Kordina, C. Hallin, and E. Janzén, “Silicon vacancy related defect in 4H and 6H SiC,” *Phys. Rev. B*, vol. 61, no. 4, pp. 2613–2620, 2000.
- [117] N. Mizuochi *et al.*, “Continuous-wave and pulsed EPR study of the negatively charged silicon vacancy with S=3/2 and C3v symmetry in n-type 4H-SiC,” *Phys. Rev. B*, vol. 66, no. 23, p. 235202, 2002.
- [118] P. G. Baranov *et al.*, “Silicon vacancy in SiC as a promising quantum system for single-defect and single-photon spectroscopy,” *Phys. Rev. B - Condens. Matter Mater. Phys.*, vol. 83, no. 12, pp. 1–12, 2011.
- [119] V. A. Soltamov, A. A. Soltamova, and P. G. Baranov, “Room Temperature Coherent Spin Alignment of Silicon Vacancies in 4H- and 6H-SiC,” *Phys. Rev. Lett.*, vol. 108, p. 226402, 2012.
- [120] T. Umeda, N. Morishita, T. Ohshima, H. Itoh, and J. Isoya, “Electron Paramagnetic Resonance Study of Carbon Antisite-Vacancy Pair in p-Type 4H-SiC,” *Mater. Sci. Forum*, vol. 556–557, no. c, pp. 453–456, 2007.
- [121] P. Carlsson *et al.*, “EPR and ab initio calculation study on the E14 center in 4H - And 6H-SiC,” *Phys. Rev. B - Condens. Matter Mater. Phys.*, vol. 82, no. 23,

- pp. 1–11, 2010.
- [122] A. Gali, A. Gällström, N. T. Son, and E. Janzén, “Theory of Neutral Divacancy in SiC: A Defect for Spintronics,” *Mater. Sci. Forum*, vol. 645–648, pp. 395–397, 2010.
- [123] N. T. Son *et al.*, “Divacancy in 4H-SiC,” *Phys. Rev. Lett.*, vol. 96, no. 5, pp. 8–11, 2006.
- [124] A. Gali, T. Hornos, M. Bockstedte, and T. Frauenheim, “Point Defects and their Aggregation in Silicon Carbide,” *Mater. Sci. Forum*, vol. 556–557, pp. 439–444, 2007.
- [125] O. V. Zwier, D. O’Shea, A. R. Onur, and C. H. van der Wal, “All-optical coherent population trapping with defect spin ensembles in silicon carbide,” *Sci. Rep.*, vol. 5, p. 10931, 2015.
- [126] U. Gerstmann, E. Rauls, T. Frauenheim, and H. Overhof, “Formation and annealing of nitrogen-related complexes in SiC,” *Phys. Rev. B*, vol. 67, no. 20, pp. 1–8, 2003.
- [127] M. Bockstedte, A. Mattausch, and O. Pankratov, “The Solubility and Defect Equilibrium on the n-Type Dopants Nitrogen and Phosphorus in 4H-SiC: A Theoretical Study,” *Mater. Sci. Forum*, vol. 457–460, pp. 715–718, 2004.
- [128] B. R. Tuttle, T. Aichinger, P. M. Lenahan, and S. T. Pantelides, “Theory of Hyperfine Active Nitrogen Complexes Observed in 4H-SiC Diodes,” *J. Appl. Phys.*, vol. 114, p. 113712, 2013.
- [129] M. Bockstedte, A. Mattausch, and O. Pankratov, “Solubility of nitrogen and phosphorus in 4H-SiC: A theoretical study,” *Appl. Phys. Lett.*, vol. 85, no. 1, p. 58, 2004.
- [130] T. Aichinger, P. M. Lenahan, B. R. Tuttle, and D. Peters, “A nitrogen-related deep level defect in ion implanted 4H-SiC pn junctions - A spin dependent recombination study,” *Appl. Phys. Lett.*, vol. 100, no. 11, 2012.
- [131] H. Woodbury and G. Ludwig, “Electron Spin Resonance Studies in SiC,” *Phys. Rev.*, vol. 124, no. 4, pp. 1083–1089, 1961.
- [132] S. Greulich-Weber, “EPR and ENDOR Investigations of Shallow Impurities in SiC Polytypes,” *Phys. Status Solidi A Appl. Mater. Sci.*, vol. 162, p. 95, 1997.
- [133] E. N. Kalabukhova *et al.*, “EPR, ESE and Pulsed ENDOR Study of Nitrogen Related Centers in 4H-SiC Wafers Grown by Different Technologies,” *Mater. Sci. Forum*, vol. 556–557, pp. 355–358, 2007.
- [134] M. E. Zvanut and J. van Tol, “Nitrogen-related Point Defect in 4H and 6H SiC,” *Phys. B*, vol. 401–402, p. 73, 2007.
- [135] D. V. Savchenko *et al.*, “Spin-coupling in Heavily Nitrogen-doped 4H-SiC,”

- Mater. Sci. Forum*, vol. 615–617, p. 343, 2009.
- [136] H. J. von Bardeleben, J. L. Cantin, S. Hamon, K. Khazen, U. Gerstmann, and E. Rauls, “Experimental and theoretical study of the NV Center in 4H-SiC,” *Phys. Rev. B*, vol. 92, no. 2009, p. 64104, 2015.
- [137] V. V. Afanas’ev, F. Ciobanu, S. Dimitrijević, G. Pensl, and A. Stesmans, “Band alignment and defect states at SiC/oxide interfaces,” *J. Phys. Condens. Matter*, vol. 16, no. 17, pp. S1839–S1856, 2004.
- [138] P. Deák, J. M. Knaup, T. Hornos, C. Thill, A. Gali, and T. Frauenheim, “The mechanism of defect creation and passivation at the SiC/SiO<sub>2</sub> interface,” *J. Phys. D. Appl. Phys.*, vol. 40, no. 20, pp. 6242–6253, 2007.
- [139] V. V. Afanas’ev, F. Ciobanu, S. Dimitrijević, G. Pensl, and A. Stesmans, “SiC/SiO<sub>2</sub> Interface States: Properties and Models,” *Mater. Sci. Forum*, vol. 483–485, pp. 563–568, 2005.
- [140] T. Hornos, N. T. Son, E. Janzén, and A. Gali, “Theoretical study of small silicon clusters in 4H-SiC,” *Phys. Rev. B*, vol. 76, no. 16, p. 165209, Oct. 2007.
- [141] D. J. Meyer, P. M. Lenahan, and A. J. Lelis, “Observation of trapping defects in 4H -silicon carbide metal-oxide-semiconductor field-effect transistors by spin-dependent recombination,” *Appl. Phys. Lett.*, vol. 86, no. 2, p. 23503, 2005.
- [142] M. S. Dautrich, P. M. Lenahan, and A. J. Lelis, “Identification of trapping defects in 4H -silicon carbide metal-insulator-semiconductor field-effect transistors by electrically detected magnetic resonance,” *Appl. Phys. Lett.*, vol. 89, no. 22, p. 223502, 2006.
- [143] B. C. Bittel, P. M. Lenahan, J. T. Ryan, J. Fronheiser, and A. J. Lelis, “Spin dependent charge pumping in SiC metal-oxide-semiconductor field-effect-transistors,” *Appl. Phys. Lett.*, vol. 99, no. 8, p. 83504, 2011.
- [144] P. M. Lenahan, M. S. Dautrich, and C. J. Cochrane, “Performance Limiting Defects in SiC Based Transistors,” *Conf. Pap.*, 2006.
- [145] C. J. Cochrane, P. M. Lenahan, and A. J. Lelis, “Identification of a silicon vacancy as an important defect in 4H SiC metal oxide semiconducting field effect transistor using spin dependent recombination,” *Appl. Phys. Lett.*, vol. 100, no. 2, p. 23509, 2012.
- [146] C. J. Cochrane, P. M. Lenahan, and A. J. Lelis, “Direct observation of lifetime killing defects in 4 H SiC epitaxial layers through spin dependent recombination in bipolar junction transistors,” *J. Appl. Phys.*, vol. 105, p. 64502, 2009.
- [147] C. J. Cochrane, “Development of new atomic scale defect identification schemes in micro / nanoelectronics incorporating digital signal processing methods for investigating zero/low field spin dependent transport and passage effects in electrically detected magnetic resona,” Pennsylvania State



University, 2013.

- [148] J. L. Cantin, H. J. von Bardeleben, Y. Shishkin, Y. Ke, R. P. Devaty, and W. J. Choyke, "Identification of the Carbon Dangling Bond Center at the 4H-SiC/SiO<sub>2</sub> Interface by an EPR Study in Oxidized Porous SiC," *Phys. Rev. Lett.*, vol. 92, no. 1, p. 15502, 2004.
- [149] H. J. von Bardeleben, J. L. Cantin, L. Ke, Y. Shishkin, R. P. Devaty, and W. J. Choyke, "Interface Defects in n-type 3C-SiC/SiO<sub>2</sub>: An EPR Study of Oxidized Porous Silicon Carbide Single Crystals," *Mater. Sci. Forum*, vol. 4853–485, pp. 273–276, 2005.
- [150] H. J. von Bardeleben, J. L. Cantin, M. G. Mynbaeva, and S. E. Sadow, "EPR Studies of Interface Defects in n-Type 6H-SiC/SiO<sub>2</sub> Using Porous SiC," *Mater. Sci. Forum*, vol. 433–436, pp. 495–498, 2003.
- [151] J. Isoya, R. Kosugi, K. Fukuda, and S. Yamasaki, "ESR characterization of SiC bulk crystals and SiO<sub>2</sub>/SiC interface," *Mater. Sci. Forum*, vol. 389–393, no. 2, pp. 1025–1028, 2002.
- [152] P. J. Macfarlane and M. E. Zvanut, "Characterization of paramagnetic defect centers in three polytypes of dry heat treated, oxidized SiC," *J. Appl. Phys.*, vol. 88, no. 7, p. 4122, 2000.
- [153] T. Umeda *et al.*, "Electrically detected ESR study of interface defects in 4H-SiC metal-oxide-semiconductor field effect transistor," *Silicon Carbide Relat. Mater. 2010*, vol. 679–680, pp. 370–373, 2011.
- [154] M. A. Anders, P. M. Lenahan, and A. J. Lelis, "Are dangling bond centers important interface traps in 4H-SiC metal oxide semiconductor field effect transistors?," *Appl. Phys. Lett.*, vol. 109, no. 14, p. 142106 (2016);, 2016.
- [155] J. L. Cantin, H. J. Von Bardeleben, Y. Ke, R. P. Devaty, and W. J. Choyke, "Hydrogen passivation of carbon P b like centers at the 3C- and 4H-SiC SiO<sub>2</sub> interfaces in oxidized porous SiC," *Appl. Phys. Lett.*, vol. 88, no. 9, pp. 7–9, 2006.
- [156] G. Pensl *et al.*, "Defect-engineering in SiC by ion implantation and electron irradiation," *Microelectron. Eng.*, vol. 83, no. 1 SPEC. ISS., pp. 146–149, 2006.
- [157] G. Pensl *et al.*, "Implantation-induced defects in silicon carbide," *Phys. B*, vol. 340–342, p. 121, 2003.
- [158] G. Pensl *et al.*, "(Nitrogen-Vacancy)-Complex Formation in SiC: Experiment and Theory," *Mater. Sci. Forum*, vol. 556–557, pp. 307–312, 2007.
- [159] C. Strenger *et al.*, "Comparative Study of Electrical and Microstructural Properties of 4H-SiC MOSFETs," *Mater. Sci. Forum*, vol. 717–720, pp. 437–440, 2012.
- [160] R. Schneider, J. Woltersdorf, and O. Lichtenberger, "Phase identification in

- composite materials by EELS fine-structure analysis," *J. Microsc.*, vol. 183, no. 1, pp. 39–44, 1996.
- [161] P. Deák, T. Hornos, C. Thill, J. Knaup, A. Gali, and T. Frauenheim, "The Mechanism of Interface State Passivation by NO," *Mater. Sci. Forum*, vol. 556–557, pp. 541–544, 2007.
- [162] P. Hohenberg and W. Kohn, "Inhomogeneous Electron Gas," *Phys. Rev. B*, vol. 136, no. 3B, pp. 864–871, 1964.
- [163] W. Kohn and L. J. Sham, "Self-consistent equations including exchange and correlation effects," *Phys. Rev.*, vol. 140, no. 4A, 1965.
- [164] J. C. Slater, "The theory of complex spectra," *Phys. Rev.*, vol. 34, no. 10, pp. 1293–1322, 1929.
- [165] G. Lippert, J. Hutter, and M. Parrinello, "A hybrid Gaussian and plane wave density functional scheme," *Mol. Phys.*, vol. 92, no. 3, pp. 477–488, 1997.
- [166] J. D. Pack and H. J. Monkhorst, "special points for Brillouin-zone integrations—a reply," *Phys. Rev. B*, vol. 16, no. 4, pp. 1748–1749, 1977.
- [167] P. E. Blöchl, O. Jepsen, and O. K. Andersen, "Improved tetrahedron method for Brillouin-zone integrations," *Phys. Rev. B*, vol. 49, no. 23, pp. 16223–16233, 1994.
- [168] N. Troullier and J. L. Martins, "Efficient pseudopotentials for plane-wave calculations. II. Operators for fast iterative diagonalization," *Phys. Rev. B*, vol. 43, no. 11, pp. 8861–8869, 1991.
- [169] S. Goedecker, M. Teter, and J. Hutter, "Separable dual-space Gaussian pseudopotentials," *Phys. Rev. B*, vol. 54, no. 3, pp. 1703–1710, Jul. 1996.
- [170] J. VandeVondele, M. Krack, F. Mohamed, M. Parrinello, T. Chassaing, and J. Hutter, "Quickstep: Fast and accurate density functional calculations using a mixed Gaussian and plane waves approach," *Comput. Phys. Commun.*, vol. 167, no. 2, pp. 103–128, 2005.
- [171] D. M. Ceperley and B. J. Alder, "Ground state of the electron gas by a stochastic model," *Phys. Rev. Lett.*, vol. 45, no. 7, pp. 566–569, 1980.
- [172] J. P. Perdew, K. Burke, and M. Ernzerhof, "Generalized Gradient Approximation Made Simple- ERRATA," *Phys. Rev. Lett.*, vol. 77, no. 18, pp. 3865–3868, 1996.
- [173] J. P. Perdew, K. Burke, and M. Ernzerhof, "Generalized Gradient Approximation Made Simple," *Phys. Rev. Lett.*, vol. 77, no. 18, pp. 3865–3868, 1996.
- [174] J. P. Perdew and A. Zunger, "Self-interaction correction to density-functional approximations for many-electron systems," *Phys. Rev. B*, vol. 23, no. 10, pp.

- 5048–5079, 1981.
- [175] S. H. Vosko, L. Wilk, and M. Nusair, “Accurate spin-dependent electron liquid correlation energies for local spin density calculations: a critical analysis,” *Can. J. Phys.*, vol. 58, no. 8, pp. 1200–1211, 1980.
- [176] J. P. Perdew and Y. Wang, “ACCURATE AND SIMPLE ANALYTIC REPRESENTATION OF THE ELECTRON-GAS CORRELATION-ENERGY,” *Phys. Rev. B*, vol. 45, no. 23, pp. 13244–13249, 1992.
- [177] J. P. Perdew, “Local density and gradient-corrected functionals for short-range correlation: Antiparallel-spin and non-RPA contributions,” *Int. J. Quantum Chem.*, vol. 48, no. 27 S, pp. 93–100, 1993.
- [178] A. D. Becke, “Density-functional exchange-energy approximation with correct asymptotic behavior,” *Phys. Rev. A*, vol. 38, no. 6, pp. 3098–3100, 1988.
- [179] A. D. Becke, “A new mixing of Hartree–Fock and local density-functional theories,” *J. Chem. Phys.*, vol. 98, no. 2, p. 1372, 1993.
- [180] S. Ivanov, S. Hirata, and R. J. Bartlett, “Exact exchange treatment for molecules in finite-basis-set Kohn-Sham theory,” *Phys. Rev. Lett.*, vol. 83, no. 26, pp. 5455–5458, 1999.
- [181] J. Heyd, G. E. Scuseria, and M. Ernzerhof, “Erratum: ‘Hybrid functionals based on a screened Coulomb potential’ [J. Chem. Phys. 118, 8207 (2003)],” *J. Chem. Phys.*, vol. 124, no. 21, p. 219906, 2006.
- [182] J. Heyd, G. E. Scuseria, and M. Ernzerhof, “Hybrid functionals based on a screened Coulomb potential,” *J. Chem. Phys.*, vol. 118, no. 18, p. 8207, 2003.
- [183] M. Guidon, J. Hutter, and J. VandeVondele, “Auxiliary Density Matrix Methods for Hartree–Fock Exchange Calculations,” *J. Chem. Theory Comput.*, vol. 6, no. 8, pp. 2348–2364, 2010.
- [184] A. D. Becke, “Density-functional thermochemistry. III. The role of exact exchange,” *J. Chem. Phys.*, vol. 98, no. 7, p. 5648, 1993.
- [185] J. P. Perdew, M. Ernzerhof, and K. Burke, “Rationale for mixing exact exchange with density functional approximations,” *J. Chem. Phys.*, vol. 105, no. 22, p. 9982, 1996.
- [186] J. F. Janak, “Proof that  $dE/dn_i = \epsilon_i$  in density-functional theory,” *Phys. Rev. B*, vol. 18, no. 2, pp. 7165–7168, 1978.
- [187] R. Fletcher and C. M. Reeves, “Function minimization by conjugate gradients,” *The Computer Journal*, vol. 7, no. 2, pp. 149–154, 1964.
- [188] J. D. Head and M. C. Zerner, “A Broyden-Fletcher-Goldfarb-Shanno optimization procedure for molecular geometries,” *Chem. Phys. Lett.*, vol. 122, no. 3, pp. 264–270, 1985.

- [189] G. P. Francis and M. C. Payne, "Finite basis set corrections to total energy pseudopotential calculations," *J. Phys. Condens. Matter*, vol. 2, no. 19, pp. 4395–4404, 1990.
- [190] G. Henkelman, B. P. Uberuaga, and H. Jónsson, "Climbing image nudged elastic band method for finding saddle points and minimum energy paths," *J. Chem. Phys.*, vol. 113, no. 22, pp. 9901–9904, 2000.
- [191] D. Sheppard, R. Terrell, and G. Henkelman, "Optimization methods for finding minimum energy paths," *J. Chem. Phys.*, vol. 128, no. 13, pp. 1–10, 2008.
- [192] A. Heyden, A. T. Bell, and F. J. Keil, "Efficient methods for finding transition states in chemical reactions: Comparison of improved dimer method and partitioned rational function optimization method," *J. Chem. Phys.*, vol. 123, no. 22, 2005.
- [193] H. Jónsson, G. Mills, and K. W. Jacobsen, "Nudged elastic band method for finding minimum energy paths of transitions," *Class. Quantum Dyn. Condens. Phase Simulations*, 1998.
- [194] G. Mills and H. Jónsson, "Reversible Work Transition State Theory: Application to Dissociative Adsorption of Hydrogen," *Surf. Sci.*, vol. 324, no. 2–3, p. 42, 1994.
- [195] G. Henkelman and H. Jónsson, "Improved tangent estimate in the nudged elastic band method for finding minimum energy paths and saddle points," *J. Chem. Phys.*, vol. 113, no. 22, pp. 9978–9985, 2000.
- [196] F. Bloch, "Über die Quantenmechanik der Elektronen in Kristallgittern," *Zeitschrift für Phys.*, vol. 52, no. 7–8, pp. 555–600, 1929.
- [197] M. Leslie and N. J. Gillan, "The energy and elastic dipole tensor of defects in ionic crystals calculated by the supercell method," *J. Phys. C Solid State Phys.*, vol. 18, no. 5, p. 973, 1985.
- [198] G. Makov and M. Payne, "Periodic boundary conditions in ab initio calculations," *Phys. Rev. B*, vol. 51, no. 7, pp. 4014–4022, 1995.
- [199] S. Lany and A. Zunger, "Accurate prediction of defect properties in density functional supercell calculations," *Model. Simul. Mater. Sci. Eng.*, vol. 17, no. 8, p. 84002, 2009.
- [200] E. Zavoisky, "Paramagnetic Relaxation of Liquid Solutions for Perpendicular Fields," *J. Phys.*, vol. 9, pp. 211–216, 1945.
- [201] E. Zavoisky, "Spin-Magnetic Resonance in Paramagnetics," *J. Phys. USSR*, vol. 9, pp. 211–245, 1945.
- [202] A. Lund, M. Shiotani, and S. Shimada, "Principles of ESR," in *Principles and Applications of ESR Spectroscopy*, Dordrecht: Springer Netherlands, 2011, pp. 3–28.

- [203] J. J. Davies, "Optically-detected magnetic resonance and its applications," *Contemp. Phys.*, vol. 17, no. 3, pp. 275–294, 1976.
- [204] M. Stutzmann, M. S. Brandt, and M. W. Bayerl, "Spin-dependent processes in amorphous and microcrystalline silicon: a survey," *J. Non. Cryst. Solids*, vol. 266–269, P, pp. 1–22, 2000.
- [205] D. J. Lépine, "Spin-dependent recombination on silicon surface," *Phys. Rev. B*, vol. 6, no. 2, pp. 436–441, 1972.
- [206] D. Kaplan, I. Solomon, and N. F. Mott, "Explanation of the Large Spin-Dependent Recombination Effect in Semiconductors," *Le J. Phys. - Lettres*, vol. 39, pp. 51–54, 1978.
- [207] M. Stutzmann, M. S. Brandt, and M. W. Bayerl, "Spin-dependent processes in amorphous and microcrystalline silicon: a survey," *J. Non. Cryst. Solids*, vol. 266–269, pp. 1–22, 2000.
- [208] G. D. Watkins, "Chapter 1 EPR and ENDOR Studies of Defects in Semiconductors," *Semicond. Semimetals*, vol. 51, pp. 1–43, 1998.
- [209] G. D. Watkins, "Chapter 1 EPR and ENDOR Studies of Defects in Semiconductors," *Semicond. Semimetals*, vol. 51, no. PART A, pp. 1–43, 1998.
- [210] B. Stich, S. Greulich-Weber, and J. -M. Spaeth, "Electrical detection of electron paramagnetic resonance: New possibilities for the study of point defects," *J. Appl. Phys.*, vol. 77, no. 4, pp. 1546–1553, 1995.
- [211] T. Aichinger and P. M. Lenahan, "Giant amplification of spin dependent recombination at heterojunctions through a gate controlled bipolar effect," *Appl. Phys. Lett.*, vol. 101, no. 8, p. 83504, 2012.
- [212] D. B. Williams, C. B. Carter, and C. Barry, *Transmission Electron Microscopy: A Textbook for Materials Science*. Springer, 2009.
- [213] M. A. Jupina and P. M. Lenahan, "A Spin Dependent Recombination Study of Radiation Induced Defects at and near the Si/SiO<sub>2</sub> Interface," *IEEE Trans. Nucl. Sci.*, vol. 36, no. 6, pp. 1800–1807, 1989.
- [214] S. M. Sze and K. K. Ng, *Physics of Semiconductor Devices*, 3rd ed. John Wiley & Sons, 2007.
- [215] C. J. Pickard and F. Mauri, "First principles theory of the EPR g-tensor in solids: defects in quartz," *Phys. Rev. Lett.*, vol. 88, p. 86403, 2002.
- [216] F. Jensen, "The basis set convergence of spin-spin coupling constants calculated by density functional methods," *J. Chem. Theory Comput.*, vol. 2, no. 5, pp. 1360–1369, 2006.
- [217] S. T. Murphy and N. D. M. Hine, "Anisotropic charge screening and supercell size convergence of defect formation energies," *Phys. Rev. B - Condens.*

- Matter Mater. Phys.*, vol. 87, no. 9, pp. 1–18, Mar. 2013.
- [218] A. Gali, “Time-dependent density functional study on the excitation spectrum of point defects in semiconductors,” *Phys. Status Solidi B*, vol. 248, no. 6, pp. 1337–1346, 2011.
- [219] A. Gali, “Excitation spectrum of point defects in semiconductors studied by time-dependent density functional theory,” *J. Mater. Res.*, vol. 27, no. 6, pp. 897–909, 2012.
- [220] K. Szász, Viktor Ivády, I. A. Abrikosov, E. Janzén, M. Bockstedte, and A. Gali, “Spin and photophysics of carbon-antisite vacancy defect in 4H silicon carbide: A potential quantum bit,” *Phys. Rev. B*, vol. 91, p. 121201, 2015.
- [221] S. Lee *et al.*, “Localized Tail States and Electron Mobility in Amorphous ZnON Thin Film Transistors,” *Sci. Rep.*, vol. 5, p. 13467, 2015.
- [222] T. Hornos, A. Gali, R. P. Devaty, and W. J. Choyke, “Doping of phosphorus in chemical-vapor-deposited silicon carbide layers: A theoretical study,” *Appl. Phys. Lett.*, vol. 87, no. 21, pp. 1–3, 2005.
- [223] P. Deák, B. Aradi, M. Kaviani, T. Frauenheim, and A. Gali, “Formation of NV centers in diamond: A theoretical study based on calculated transitions and migration of nitrogen and vacancy related defects,” *Phys. Rev. B*, vol. 89, no. 7, p. 75203, Feb. 2014.
- [224] R. Jones, J. P. Goss, H. Pinto, and D. W. Palmer, “Diffusion of nitrogen in diamond and the formation of A-centres,” *Diam. Relat. Mater.*, vol. 53, no. June, pp. 35–39, 2015.
- [225] R. W. Schmude and K. a Gingerich, “Thermodynamic Study of Small Silicon Carbide Clusters with a Mass Spectrometer,” *J. Phys. Chem. A*, vol. 101, no. 14, pp. 2610–2613, 1997.
- [226] T. Hornos, A. Gali, N. T. Son, and E. Janzén, “A Theoretical Study on Aluminium-Related Defects in SiC,” *Mater. Sci. Forum*, vol. 556–557, pp. 445–448, 2007.
- [227] M. Scheffler and J. Dabrowski, “Parameter-free calculations of total energies, interatomic forces and vibrational entropies of defects in semiconductors,” *Philos. Mag. A*, vol. 58, no. 1, pp. 107–121, 1988.
- [228] A. Gali, T. Hornos, N. T. Son, and E. Janzén, “New Type of Defects Explored by Theory: Silicon Interstitial Clusters in SiC,” *Mater. Sci. Forum*, vol. 600–603, pp. 413–416, 2009.
- [229] T. Hiyoshi and T. Kimoto, “Elimination of the major deep levels in n- and p-type 4H-SiC by two-step thermal treatment,” *Appl. Phys. Express*, vol. 2, no. 9, pp. 1–3, 2009.
- [230] K. Kawahara, J. Suda, and T. Kimoto, “Elimination of Deep Levels in Thick SiC

- Epilayers by Thermal Oxidation and Proposal of the Analytical Model,” *Mater. Sci. Forum*, vol. 717–720, pp. 241–246, 2012.
- [231] B. Zippelius, J. Suda, and T. Kimoto, “High temperature annealing of n-type 4H-SiC: Impact on intrinsic defects and carrier lifetime,” *J. Appl. Phys.*, vol. 111, no. 3, 2012.
- [232] H. Miyake, T. Kimoto, and J. Suda, “Enhanced Current Gain (>250) in 4H-SiC Bipolar Junction Transistors by a Deep-Level-Reduction Process,” *Mater. Sci. Forum*, vol. 717–720, pp. 1117–1122, 2012.
- [233] G. Alfieri and T. Kimoto, “Resolving the EH6/7 level in 4H-SiC by Laplace-transform deep level transient spectroscopy,” *Appl. Phys. Lett.*, vol. 102, no. 15, 2013.
- [234] F. Devynck, F. Giustino, and A. Pasquarello, “Abrupt model interface for the 4H(1000)SiC-SiO<sub>2</sub> interface,” *Microelectron. Eng.*, vol. 80, pp. 38–41, Jun. 2005.
- [235] F. Devynck, F. Giustino, P. Broqvist, and A. Pasquarello, “Structural and electronic properties of an abrupt 4H-SiC(0001)/SiO<sub>2</sub> interface model: Classical molecular dynamics simulations and density functional calculations,” *Phys. Rev. B*, vol. 76, no. 7, pp. 1–9, Aug. 2007.
- [236] E. Pippel, J. Woltersdorf, J. Gegner, and R. Kirchheim, “EVIDENCE OF OXYGEN SEGREGATION AT Ag / MgO INTERFACES,” *Acta Mater.*, vol. 48, pp. 2571–2578, 2000.
- [237] M. J. Frisch *et al.*, “Gaussian09.” Gaussian, Inc., Wallingford CT, 2009.
- [238] S. J. Clark *et al.*, “First principles methods using CASTEP,” *Zeitschrift für Krist.*, vol. 220, pp. 567–570, 2005.
- [239] S. Plimpton, “Fast Parallel Algorithms for Short – Range Molecular Dynamics,” *J. Comput. Phys.*, vol. 117, pp. 1–19, 1995.
- [240] B. W. H. van Beest, G. J. Kramer, and R. A. van Santen, “Force fields for silicas and aluminophosphates based on ab initio calculations,” *Phys. Rev. Lett.*, vol. 64, no. 16, pp. 1955–1958, Apr. 1990.
- [241] G. Gruber, P. Hadley, M. Koch, D. Peters, and T. Aichinger, “Interface defects in SiC power MOSFETs - An electrically detected magnetic resonance study based on spin dependent recombination,” *Int. Conf. DEFECTS Semicond. 2013 Proc. 27th Int. Conf. Defects Semicond. ICDS-2013*, vol. 1583, no. 1, pp. 165–168, 2014.
- [242] J. S. Hyde and L. Dalton, “Very slowly tumbling spin labels: adiabatic rapid passage,” *Chem. Phys. Lett.*, vol. 16, no. 3, pp. 568–572, Oct. 1972.
- [243] M. Weger, “Passage Effects in Paramagnetic Resonance Experiments,” *Bell Syst. Tech. J.*, vol. 39, no. 4, pp. 1013–1112, Jul. 1960.

# Appendix A

## Hyperfine Dependence on Defect Symmetry

---

In 4H-SiC there are sites that are either quasi-hexagonal or quasi-cubic as described in section 1.2. In the context of simple point defects, this requires the consideration of two symmetry sites. In the case of small defect clusters, such as the  $N_C V_{Si}$ , the picture is more complex. In this case, the two components of the defect ( $N_C$  or  $V_{Si}$ ) need to be considered at the different symmetry sites they can occupy, leading to several possible arrangements for the  $N_C V_{Si}$  centre. The pure symmetry defect (hh and kk) where the  $N_C$  and the  $V_{Si}$  occupy sites of the same symmetry, in the mixed symmetry defect (hk and kh) the  $N_C$  and  $V_{Si}$  sit at sites of different symmetry. The pure symmetry sites are singly degenerate having only one potential configuration, the mixed symmetry defects are triply degenerate with three energetically equivalent configurations. The calculated HF parameters for the various configurations that form components of the Boltzmann sum for the final comparison presented in Chapter 3 are presented here.



*Appendix A: Hyperfine Dependence on Defect Symmetry*

Table A. 1. Initial comparison of hyperfine parameters (excluding N), hh symmetry.

	0/Doublet	0/Quartet	1/Triplet	-2/Doublet
C1	38.36	44.64	45.72	6.78
C2	37.93	14.20	45.11	11.58
C3	-29.00	39.46	45.11	48.00
Si1	11.47	11.76	7.61	0.87
Si2	10.95	12.74	7.62	0.45
Si3	11.06	11.59	9.28	1.21
Si4	-9.83	4.36	7.94	0.82
Si5	-10.09	4.97	7.17	1.75
Si6	-9.76	2.77	8.95	1.87
Si7	10.77	11.85	7.95	11.09
Si8	10.67	12.48	7.19	10.93
Si9	10.39	12.12	8.95	10.87
C5	0.33	0.44	0.52	0.64
C6	-0.35	0.71	0.52	0.25
C7	0.30	0.99	0.53	0.10
C8	0.56	0.57	0.61	0.10
C9	0.42	0.91	0.62	0.09
C10	0.47	0.32	0.54	0.56
C11	6.47	7.49	5.42	6.68
C12	6.73	5.94	5.64	1.20
C13	5.82	6.84	4.80	6.65
C14	0.45	0.93	0.30	0.30
C15	-5.45	3.15	5.78	0.11
C16	6.24	8.04	5.64	0.2
C17	-5.51	0.92	4.8	1.27
C18	0.03	0.26	0.3	0.15
C19	0.02	1.23	0.3	0.45
C20	5.48	5.41	4.00	5.63
C21	0.05	0.77	0.07	0.30
C22	-5.12	2.57	3.99	0.60
C23	0.02	0.63	0.15	0.50
C24	5.77	5.82	4.36	0.35

*Appendix A: Hyperfine Dependence on Defect Symmetry*

---

Table A.2. Hyperfine parameters for hh family in neutral charge state with HSE06.

Site Sym	hh	HF/G	kh1	HF/G	kh2	HF/G	kh3	HF/G
h	N	0.70	C	14.17	C	13.89	C	14.37
k	Si	-0.18	Si	2.04	Si	2.75	Si	3.82
k	Si	0.45	Si	2.54	Si	2.44	Si	3.78
k	Si	0.47	Si	2.32	Si	2.18	Si	4.03
k	C	39.84	C	1.99	N	0.10	C	40.89
h	Si	11.22	Si	-0.14	Si	-0.05	Si	10.54
h	Si	10.47	Si	-0.91	Si	0.20	Si	11.32
k	Si	11.05	Si	-0.37	Si	0.09	Si	10.42
k	C	-38.14	N	0.09	C	39.02	C	-1.99
h	Si	-9.94	Si	0.30	Si	10.70	Si	-0.19
h	Si	-10.18	Si	0.22	Si	10.77	Si	-0.26
k	Si	-9.78	Si	0.11	Si	10.55	Si	-0.22
k	C	40.99	C	39.03	C	2.03	N	0.10
h	Si	11.09	Si	10.97	Si	0.23	Si	-0.14
h	Si	10.46	Si	11.28	Si	-0.11	Si	0.16
k	Si	10.86	Si	10.92	Si	-0.12	Si	0.04

Table A.3. Hyperfine parameters for kk family in neutral charge state with HSE06.

Site Sym	kk	HF/G	hk1	HF/G	hk2	HF/G	hk3	HF/G
k	N	-0.07	C	18.71	C	-3.19	C	39.72
h	Si	0.11	Si	4.43	Si	-2.75	Si	11.25
h	Si	0.14	Si	3.78	Si	-2.27	Si	10.26
h	Si	0.15	Si	4.62	Si	-2.02	Si	10.57
h	C	39.18	C	39.83	N	0.34	C	-3.64
k	Si	10.25	Si	10.97	Si	0.016	Si	-1.18
k	Si	10.19	Si	11.19	Si	0.02	Si	-1.18
h	Si	10.63	Si	10.32	Si	0.46	Si	-1.09
h	C	11.02	N	0.05	C	40.00	C	19.53
k	Si	1.88	Si	0.30	Si	11.54	Si	4.86
k	Si	1.85	Si	0.03	Si	11.56	Si	4.28
h	Si	2.19	Si	0.15	Si	11.17	Si	4.84
h	C	40.23	C	-3.42	C	18.70	N	0.45
k	Si	11.74	Si	-1.85	Si	4.43	Si	0.24
k	Si	11.43	Si	-2.42	Si	4.49	Si	0.02
h	Si	11.60	Si	-2.06	Si	4.52	Si	-0.02

Table A.4. Hyperfine parameters for hh family in -1 charge state with HSE06.

Site Sym	hh	HF/G	kh1	HF/G	kh2	HF/G	kh3	HF/G
h	N	-0.72	C	42.37	C	41.80	C	41.72
k	Si	0.29	Si	6.14	Si	6.82	Si	6.61
k	Si	0.29	Si	6.57	Si	6.83	Si	6.17
k	Si	0.31	Si	6.61	Si	6.49	Si	6.64
k	C	41.40	C	40.44	N	-0.56	C	40.31
h	Si	5.94	Si	7.29	Si	-0.08	Si	5.68
h	Si	5.71	Si	5.69	Si	-0.08	Si	7.29
k	Si	7.44	Si	6.01	Si	0.06	Si	6.00
k	C	40.53	N	-0.47	C	39.77	C	40.75
h	Si	6.20	Si	0.22	Si	6.31	Si	7.43
h	Si	5.50	Si	-0.06	Si	7.19	Si	5.80
k	Si	7.14	Si	0.02	Si	5.94	Si	6.16
k	C	40.62	C	40.89	C	39.48	N	-0.48
h	Si	5.52	Si	5.81	Si	7.11	Si	-0.07
h	Si	6.22	Si	7.43	Si	6.22	Si	0.22
k	Si	7.16	Si	6.16	Si	5.84	Si	0.01

*Appendix A: Hyperfine Dependence on Defect Symmetry*

Table A.5. Hyperfine parameters for kk family in -1 charge state with HSE06.

Site Sym	kk	HF/G	hk1	HF/G	hk2	HF/G
k	N	-0.71	C	41.71	C	42.20
h	Si	0.02	Si	4.58	Si	4.91
h	Si	0.02	Si	6.17	Si	4.91
h	Si	-0.01	Si	4.50	Si	6.48
h	C	35.11	C	36.85	N	-0.35
k	Si	6.47	Si	6.89	Si	0.11
k	Si	6.47	Si	7.96	Si	0.11
h	Si	7.85	Si	6.45	Si	0.19
h	C	35.10	N	-0.26	C	36.89
k	Si	6.93	Si	0.35	Si	7.35
k	Si	6.24	Si	0.12	Si	7.84
h	Si	7.70	Si	0.22	Si	6.43
h	C	34.98	C	37.51	C	37.00
k	Si	6.92	Si	8.12	Si	7.38
k	Si	6.22	Si	6.97	Si	7.87
h	Si	7.68	Si	6.70	Si	6.46

*Appendix A: Hyperfine Dependence on Defect Symmetry*

---

Table A.6. Hyperfine parameters for hh family in -2 charge state with HSE06.

Site Sym	hh	HF/G	kh1	HF/G	kh2	HF/G	kh3	HF/G
h	N	-0.33	C	8.94	C	7.62	C	37.88
k	Si	0.32	Si	1.01	Si	0.81	Si	7.76
k	Si	0.09	Si	1.41	Si	1.27	Si	7.63
k	Si	0.05	Si	0.95	Si	0.97	Si	7.74
k	C	5.29	C	11.24	N	-0.29	C	7.41
h	Si	-0.69	Si	1.54	Si	0.07	Si	1.18
h	Si	0.69	Si	-0.45	Si	-0.21	Si	1.40
k	Si	1.11	Si	1.27	Si	0.14	Si	-0.07
k	C	36.93	N	-0.20	C	12.48	C	11.61
h	Si	7.65	Si	0.09	Si	0.72	Si	1.84
h	Si	7.55	Si	0.09	Si	1.97	Si	1.76
k	Si	7.57	Si	0.12	Si	1.73	Si	0.40
k	C	14.80	C	38.56	C	36.42	N	-0.19
h	Si	2.34	Si	7.89	Si	7.80	Si	0.02
h	Si	1.13	Si	8.11	Si	7.73	Si	0.10
k	Si	2.42	Si	8.04	Si	7.77	Si	-0.17

Table A.7. Hyperfine parameters for kk family in -2 charge state with HSE06.

Site	kk	HF/G	hk	HF/G
k	N	-0.33	C	6.16
h	Si	-0.12	Si	-0.30
h	Si	0.06	Si	1.12
h	Si	0.10	Si	0.79
h	C	5.67	C	8.59
k	Si	0.11	Si	0.98
k	Si	0.99	Si	2.16
h	Si	1.55	Si	2.19
h	C	10.11	N	-0.06
k	Si	1.48	Si	0.15
k	Si	2.12	Si	0.10
h	Si	2.39	Si	0.30
h	C	31.84	C	33.19
k	Si	8.03	Si	8.20
k	Si	7.84	Si	8.00
h	Si	7.92	Si	7.96

# Appendix B

## Hyperfine Parameters for Interface Defects

---

This section presents the HF parameters for the configurations that are combined to calculate the average figures that are compared to the experimental results in chapter 6. These configurations act as a probe of the local strain environment for each of the connection schemes described in chapter 5. The HF is very sensitive to defect geometry being as the magnitude of the Fermi contact interaction (section 2.3.3), depends directly upon the degree of s-character of the defect wave function. In addition to the tabulated values individual plots for the  $P_{bc}$  configurations are included for completeness.



Table B.1. Hyperfine parameters (G) for the various  $P_{bc}$  environments.

$P_{bc}$ Environment	C	Si	Si	Si
1	35.92	10.59	10.19	10.27
2	41.30	10.79	9.29	10.66
3	37.90	10.99	11.31	11.16
4	44.56	12.05	12.17	12.68
5	36.74	10.91	9.95	10.61
6	36.31	9.46	9.29	10.26
7	36.01	9.06	9.06	9.06
8	36.89	10.58	12.95	10.34
9	36.20	9.67	11.06	10.37
10	41.87	11.27	10.87	11.10
11	41.95	10.76	10.81	10.75
12	41.35	11.47	10.90	10.49
13	40.80	12.35	11.47	11.98
14	40.86	10.00	11.71	10.03
15	42.74	11.60	12.13	11.65
16	37.64	9.82	10.31	10.01
17	36.11	12.00	13.16	13.42
18	36.33	15.59	13.69	14.44
19	37.18	11.69	11.29	10.75
20	37.42	12.73	11.58	12.26
21	42.25	14.50	13.91	14.46
22	38.64	12.95	12.01	12.54
23	42.74	12.50	11.89	12.65
24	40.75	10.33	9.84	10.14
25	37.38	10.31	9.23	10.25
26	38.54	11.83	11.50	12.37
27	35.44	9.85	9.45	9.32
28	38.01	12.49	12.13	12.15
29	39.04	14.26	12.37	14.24
30	39.14	13.68	12.99	13.99
Average	38.95	11.62	11.38	11.58

## Appendix B: Hyperfine Parameters for Interface Defects

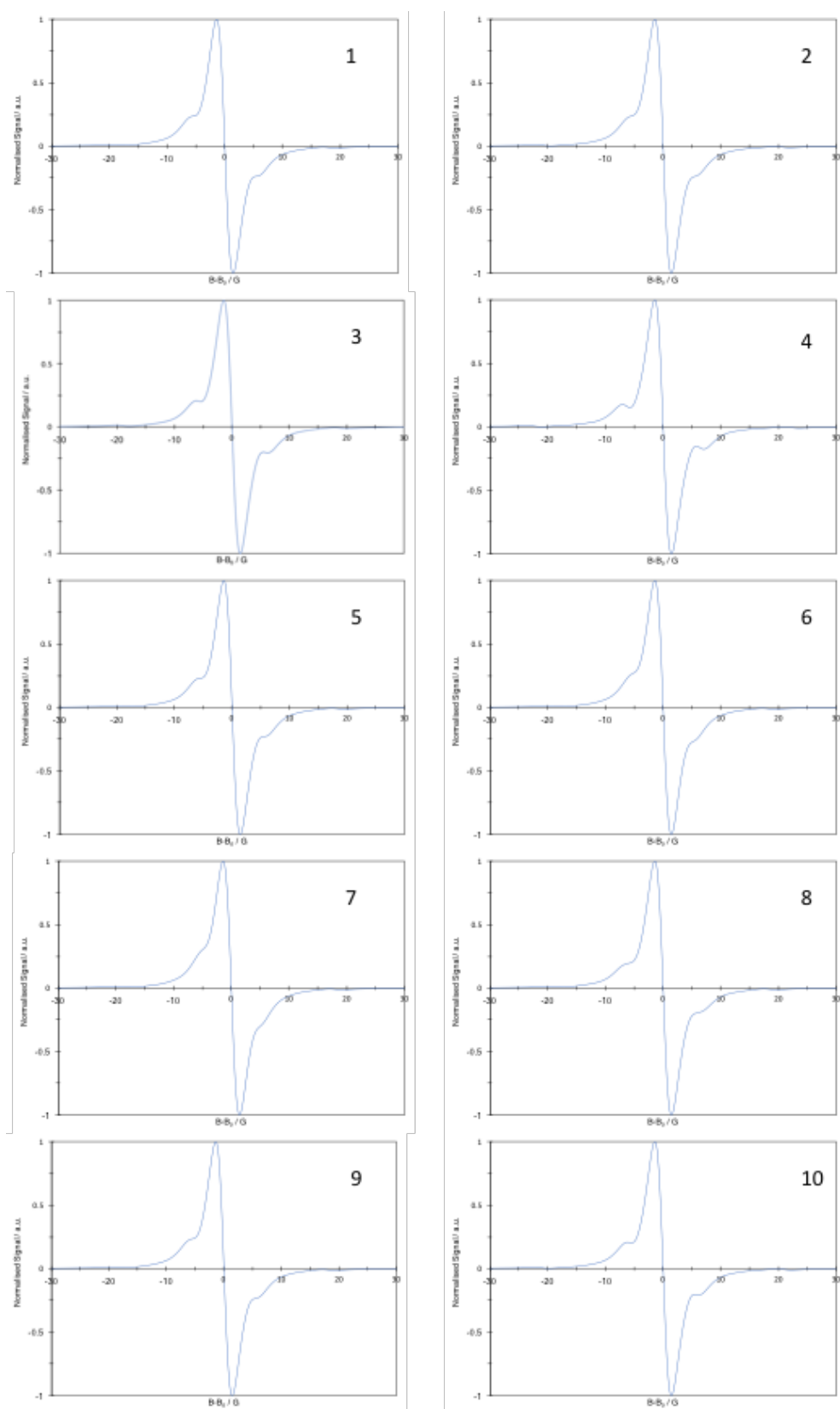


Figure B.1. Hyperfine plots corresponding to  $P_{bc}$  environments 1-10 in table B.1.

Appendix B: Hyperfine Parameters for Interface Defects

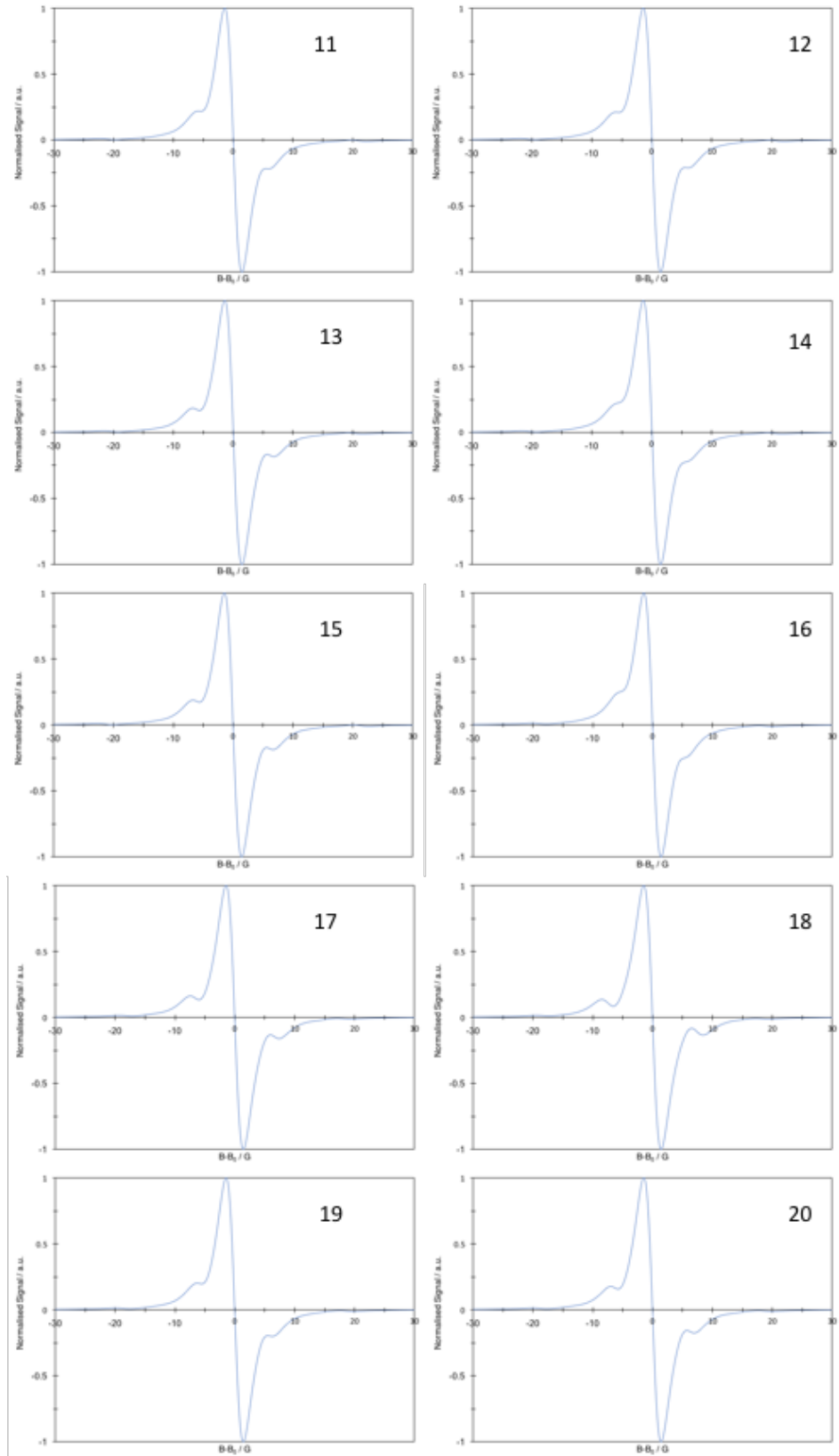


Figure B.2. Hyperfine plots corresponding to P<sub>bc</sub> environments 11-20 in table B.1.

## Appendix B: Hyperfine Parameters for Interface Defects

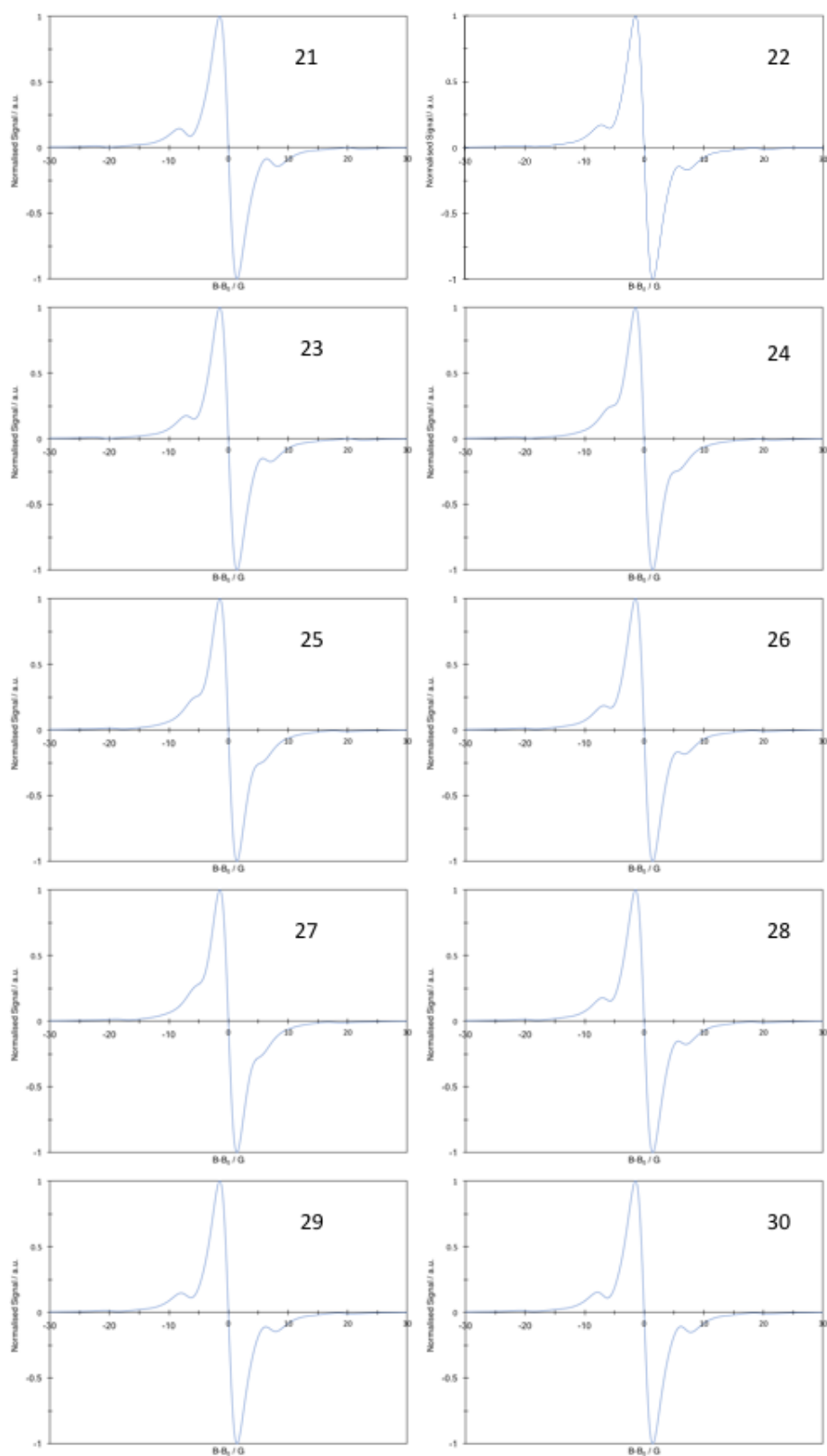


Figure B.3. Hyperfine plots corresponding to  $P_{bc}$  environments 21-30 in table B.1.

Table B.2. Hyperfine parameters (G) for the Dual-P<sub>bc</sub> Neutral Triplet.

	C1	Si	Si	Si	C2	Si	Si	Si
1	38.56	12.75	12.13	12.83	38.67	9.99	10.02	9.27
2	37.20	13.28	11.93	12.69	41.64	10.10	10.33	9.72
3	39.54	12.64	12.19	12.62	40.47	9.89	9.76	9.54
4	40.24	13.44	15.99	14.81	39.70	11.04	11.09	11.0 2
Average	38.89	13.03	13.06	13.24	40.12	10.25	10.30	9.89

Table B.3. Hyperfine parameters (G) for the Dual-P<sub>bc</sub> negative triplet.

	C2	Si	Si	Si
1	37.70	9.74	9.77	9.04
2	40.60	9.85	10.07	9.48
3	39.46	9.45	9.32	9.30
4	38.71	10.76	10.81	10.75
Average	39.12	9.95	9.99	9.64

# Appendix C

## Convergence Tests – SiC / SiO<sub>2</sub>

---

### C.1 Cell Size Convergence

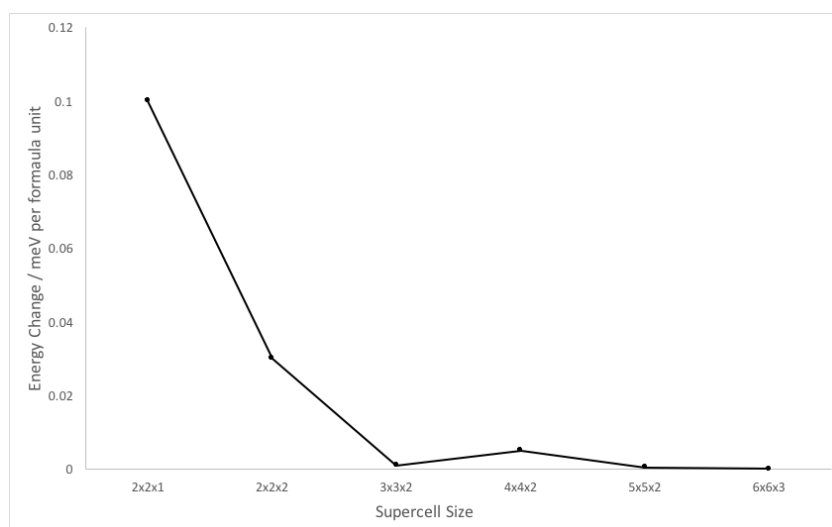


Figure C.1. Cell size convergence for hexagonal cell.

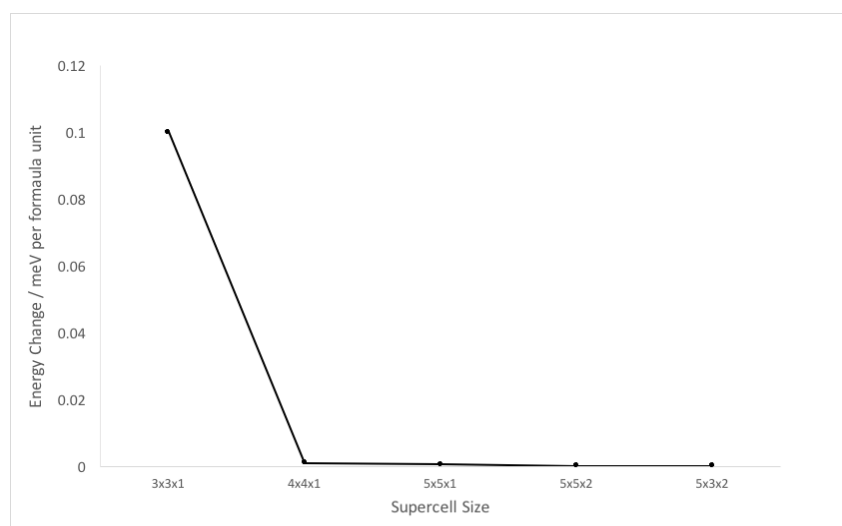


Figure C.2. Cell size convergence for orthorhombic cell.

## C.2 Plane Wave Cut Off Convergence

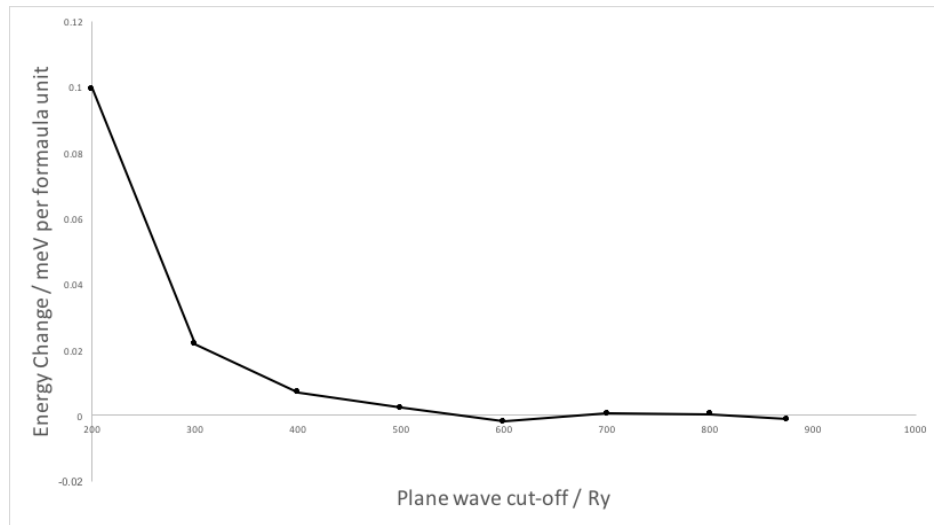


Figure C.3. Plane wave cut off convergence for orthorhombic cell.

## C.3 Plane Wave Cut off: SiC / SiO<sub>2</sub> interface system

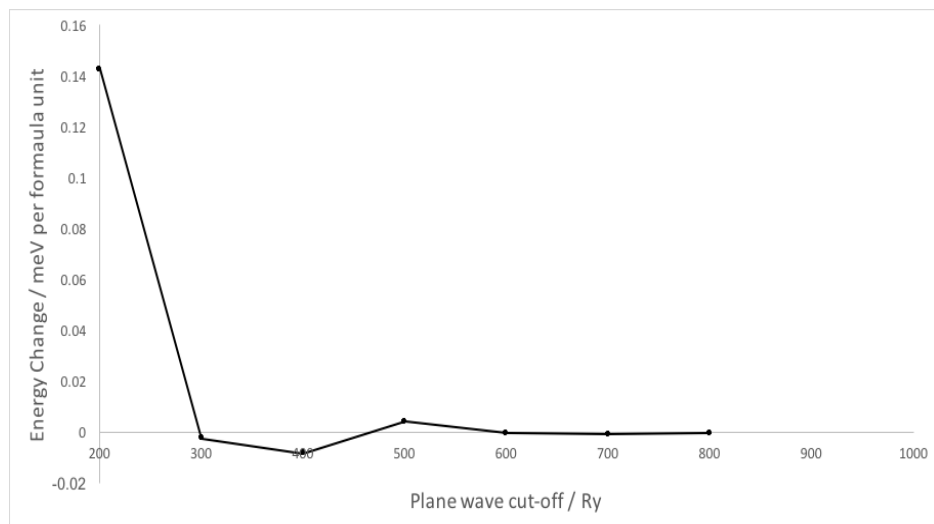


Figure C.1. Plane wave cut off convergence, SiC / SiO<sub>2</sub> interface system.